



# Motion analysis of suspended jacket transport with the Heerema SSCV Sleipnir

Comparison of model jacket motions vs actual jacket motions  
based on motion measurements and exploration of crane fatigue

Mark Johan van Geel



MARINE  
CONTRACTORS



Motion analysis of suspended jacket transport  
with the Heerema SSCV Sleipnir  
Comparison of model jacket motions vs actual jacket motions  
based on motion measurements and exploration of crane fatigue

Mark Johan van Geel

Dissertation submitted to the  
University of Delft  
in partial fulfillment of the requirements for the degree of

Master of Science  
in  
Offshore and Dredging Engineering

Prof. dr. ir. Andrei Metrikine, Chair  
Dr. ir. Bart Ummels  
Ir. Radboud van Dijk

July 30, 2021  
Delft, Zuid-Holland

Keywords: Suspended Transport, Fatigue Cranes, RAO's  
Copyright 2021, Mark Johan van Geel

# **Motion analysis of suspended jacket transport with the Heerema SSCV Sleipnir**

## **Comparison of model jacket motions vs actual jacket motions based on motion measurements and exploration of crane fatigue**

Mark Johan van Geel

### **ABSTRACT**

This research explores the development of an accurate yet fast methodology to use measured vessel motions for a fatigue damage calculation in the cranes during suspended transport. First, the kinematics, definitions and particulars of the system of interest – the vessel including crane and suspended jacket - are provided. Then, literature research is done on the main two problems with any transport at sea: the inconvenient draft problem, and the forward speed problem. To remove the inaccuracies introduced by both problems, the novel TF A2B Method is introduced. The method can be used to find the required force transmissibility functions at location of the cranes that are most prone to fatigue: the welds at the crane boom pivots. It is mathematically proven that the TF A2B Method can be used and with validation tests set up for unrestrained suspended transport it is shown that the required RAO's can be obtained from in-house modeling software Liftdyn. Overall, it is concluded that the TF A2B Method works in principle, removing the need to consider inconvenient draft and forward speed.

The hypotheses proposed in this research are further validated by the proposed validation tests in combination with a synthetic data model created in software tool Liftdyn. The Synthetic Data Model (SDM) uses a Jonswap Spectrum to obtain the motions at the Motion Reference Unit (MRU, 'A') and the Control Point ('B') at the modelled SSCV Sleipnir, which is assumed as a rigid body. After successful validation, the SDM model is then used to calculate the motions at the Jacket Sensor ('B'). Further validation of the found responses is done and it is confirmed that the location 'B' can in fact be located on another rigid body as the MRU, which in this research was the location of the jacket sensor. It is also shown that the transmissibility functions (TFs) between A and B are almost equal for different draft, resulting in that the TFs between A and B are not significantly dependent on the hydrodynamic properties of the modelled system. Therefore, it is concluded that the TF A2B Method can correctly find motions at location B by using the motions of location A in combination with the corresponding TFs between A and B.

The TF A2B Method is then applied to calculate the jacket motions using measured vessel motions. Data obtained from the X suspended transport were processed and applied using the Measured Data Model. The calculated jacket motions are compared to the measured jacket motions during the X suspended transport to the accuracy of the TF A2B Method with real data. An approximate 70% accuracy match with the measured suspended jacket motions, Roll and Pitch during the X Suspended Jacket transport was found. It is noted that not all data was found to be suitable for use.

Suggestions for improving this have been made and are expected to further improve accuracy of the match. The validated Liftodyn model of the X transport is then used to model the suspended transport of X. From the Liftodyn model Force RAO's can be obtained at the selected fatigue location of the cranes. A Fatigue Data Model using the TF A2B Method is proposed to find the stress cycles and thereby the fatigue damage during suspended transport.

Concluding, the TF A2B Method developed in this research shows positive results overall. The method can in principle be used to translate vessel measurements during suspended transport into fatigue life consumption of the crane. Further research is needed to improve the Measured Data Model, for which the use of a Surge and Sway motion sensor at the MRU is recommended. Furthermore, smaller vessel motions and more data samples should be used to further validate the accuracy of the method which is required to validate the Liftodyn model of the transport. Finally, to verify the results of the Fatigue Data Model, it is suggested to install strain gauges at the welds of the crane boom pivots for validation.

*Dedicated to TU Delft.*

# Acknowledgments

Throughout the writing of this dissertation I have received a great deal of support and assistance. I hereby would like to thank anyone who has shown time and interest in my research. On this long ride to the finish line there were many ups and downs. The enthusiasm of all people showing interest in my research has been a great support during my work. I feel grateful to thank each one.

First of all, I would like to thank my esteemed chairman, professor Andrei Metrikine for his invaluable supervision and support during the course of my master thesis. I feel grateful and honoured to be able to graduate under your name. Your passion for science always amazed me. To be able to make intricate problems graspable for students like me, has inspired me to work harder and to learn more.

I would also like to thank Bart whose expertise was invaluable in formulating the research questions and methodology. Your insightful feedback pushed me to sharpen my thinking and brought my work to a higher level. It was a great pleasure to work together and I particularly enjoyed the walks and coffee breaks through Delft in which we discussed the findings of my thesis and talked about other things in life during these weird times.

Furthermore, I would like to thank Joscha for all his help during my thesis. You helped me understand all software used within HMC and helped me numerous times explaining difficult problems or helped me find information that I by myself would never be able to find.

Radboud, I would like to thank you for all your time and patience with me. Your contributions to the Matlab code really improved the quality of the work. You are sometimes a strict teacher, but this pushed me to work even harder to deliver a better result. Your knowledge about every small detail of every step really amazed me and helped me greatly in finding meaningful results. I know there is still a long way to go to once code like you, but I am certain I will make it some day.

In addition, I would like to thank Job and Pandu for their contributions in the weekly meetings. I enjoyed all the discussion we had and I think they provided me with the tools that I needed to choose the right direction and successfully complete my dissertation.

Lastly, I want to show my deep gratitude to my family, friends and girlfriend for helping me through these, unusual times. You always support me in every aspect of life and made me the person I am today.

# Contents

<b>List of Figures</b>	<b>viii</b>
<b>List of Tables</b>	<b>xi</b>
<b>List of Abbreviations</b>	<b>xii</b>
<b>1 Introduction</b>	<b>1</b>
1.1 Decommissioning . . . . .	1
1.2 Suspended transport . . . . .	1
1.3 Crane specification . . . . .	4
1.4 Fatigue damage . . . . .	4
1.5 Current fatigue calculation suspended transport . . . . .	5
1.6 Heerema Marine Contractors . . . . .	8
1.7 Problem statement . . . . .	8
1.8 Research objectives . . . . .	9
1.9 Scope & research approach . . . . .	10
1.10 Thesis layout . . . . .	11
<b>2 Theoretical background</b>	<b>13</b>
2.1 Kinematics system . . . . .	13
2.2 Ocean waves . . . . .	22
2.3 The frequency domain . . . . .	25
2.4 Multi-body dynamics . . . . .	29
2.5 RAO's . . . . .	34
2.6 Overview fatigue requirements . . . . .	43
2.7 Miner's damage rule . . . . .	45
<b>3 Modelling approach</b>	<b>48</b>
3.1 TF A2B Method . . . . .	48
3.2 Overview hypotheses & validation tests . . . . .	50
3.3 Prove of hypotheses . . . . .	51
3.4 The Synthetic Data Model . . . . .	56
3.5 X Synthetic Data Model (SDM) . . . . .	64
3.6 TF A2B Method with SDM . . . . .	68
<b>4 Validation SDM using Liftdyn</b>	<b>69</b>
4.1 Validation: X with Synthetic Data Model . . . . .	69
4.2 Results SDM at control point . . . . .	72
4.3 Results jacket sensor . . . . .	77
<b>5 The Measured Data Model</b>	<b>84</b>
5.1 Background information X . . . . .	85
5.2 Data selection X transport . . . . .	85
5.3 Data processing . . . . .	87

5.4	Vessel motions X . . . . .	89
5.5	Jacket motions X . . . . .	94
5.6	Mode shape analysis . . . . .	98
5.7	Model adjustment for real data MDM . . . . .	101
5.8	TF A2B Method with MDM X . . . . .	102
<b>6</b>	<b>Fatigue calculation input data</b>	<b>114</b>
6.1	Fatigue Data Model . . . . .	114
6.2	Forcing on welds boom pivots . . . . .	115
6.3	Force distribution to the boom pivots . . . . .	115
6.4	TF A2B Method with Fatigue Data Model . . . . .	117
6.5	Rayleigh counting . . . . .	118
6.6	Resistance weld . . . . .	121
6.7	Damage during suspended transport . . . . .	122
<b>7</b>	<b>Conclusion &amp; recommendations</b>	<b>124</b>
	<b>Bibliography</b>	<b>128</b>
	<b>Appendices</b>	<b>133</b>
	<b>Appendix A Potential theory</b>	<b>134</b>
	<b>Appendix B Limiting criteria X transport</b>	<b>137</b>
	<b>Appendix C TFs independent of draft</b>	<b>138</b>
	<b>Appendix D Synthetic Data Model X</b>	<b>141</b>
	<b>Appendix E TFs MRU2JS X</b>	<b>144</b>
	<b>Appendix F Synthetic data: response jacket sensor</b>	<b>150</b>
	<b>Appendix G MDM model X</b>	<b>151</b>
	<b>Appendix H MDM model responses jacket X</b>	<b>152</b>
	<b>Appendix I Overview measured motions jacket</b>	<b>155</b>
	<b>Appendix J FDM model X part 1</b>	<b>156</b>
	<b>Appendix K Additional information</b>	<b>157</b>

# List of Figures

1.1	Iteration loop suspended transport [1]	2
1.2	Top two figures: Unrestrained suspended transport. Bottom two figures: Restrained suspended transport	3
1.3	Load curves of the cranes. The allowable crane load at 60m radius is shown with a red cross [2]	7
1.4	Overview research	12
2.1	Location MRU, control point and jacket sensor of X suspended transport	14
2.2	Global axis system Liftdyn and wave directions [3]	15
2.3	A simple pendulum [4]	17
2.4	Thialf Roll RAO and the respective SDA response to unidirectional JON-SWAP Spectra of Hs: 1m, gamma: 3.3, and various Tp's [1]	18
2.5	Combination of many simple, regular harmonic wave components to describe the irregular sea [5]	22
2.6	A snapshot of a harmonic wave. Left: fixed in space Right: fixed in time [5].	23
2.7	Left two plots: two regular waves with different directions [6] Right: three regular waves with different directions [5].	26
2.8	From irregular waves in wave record to energy density spectrum by Fourier analysis [5]	27
2.9	Rayleigh probability density function with explanation of the significant wave height [7].	27
2.10	Superposition of hydro-mechanic loads and wave loads on body [5].	31
2.11	Solving equations of motion in the frequency domain	35
2.12	Solving equations of motion in the frequency domain [8]	35
2.13	Hull SSCV discretized into panels [8]	36
2.14	A moving vessel encounters frequencies differently due to a translating coordinate system [5]	39
2.15	Top figure: adjust wave forces to original frequency Bottom figure: vessel oscillates with encounter frequency [9]	40
2.16	Left figure: adjusted Heave RAO and encounter spectrum for head waves Right figure: adjusted Heave RAO and encounter spectrum for stern waves [9]	41
2.17	Overview of the requirements for a fatigue calculation at a point of interest [10]	43
2.18	Crack growth development for three different S-N curves [11]	46
3.1	Steps required to obtain the force TFs at the boom pivots	48
3.2	Overview Synthetic Data Model	56
3.3	Liftdyn model of Y suspended transport	57
3.4	The transmissibility functions for all six DOF at the CP (B) due to a Roll motion of the vessel at the MRU (A)	58

3.5	The transmissibility functions phases for all six DOF at the CP(B) due to a Roll motion of the vessel at the MRU(A) . . . . .	60
3.6	The transmissibility functions for all six DOF at the JS (B) due to a Roll motion of the vessel at the MRU (A) . . . . .	61
3.7	The transmissibility functions phases for all six DOF at the JS (B) due to a Roll motion of the vessel at the MRU (A) . . . . .	61
3.8	Mode shape of Y draft 19m at 1.99 rad/s in which big roll motions of the jacket occur . . . . .	62
4.1	The X transport modeled in Liftdyn [12] . . . . .	69
4.2	Liftdyn model of X suspended transport . . . . .	70
4.3	The Jonswap spectrum used to simulate vessel and jacket motions . . . . .	71
4.4	Reconstruction of $RAO_{\zeta, idof_{CP}}$ following 3.1 [6] . . . . .	72
4.5	Responses of all degrees of freedom at the control point . . . . .	73
4.6	Response in Surge at the CP due to Surge, Pitch and Yaw at the MRU . . . . .	75
4.7	Phases of TFs, Surge, Pitch, Yaw at the MRU to Surge motion at the CP . . . . .	76
4.8	Reconstruction of $RAO_{\zeta, DOFs_{JS}}$ following 3.1[6] . . . . .	77
4.9	Small errors in Surge and Pitch TF from restrained RAO's at 0.28-0.3 rad/s . . . . .	78
4.10	Responses DOFs jacket W2JS vs TF MRU2JS * DFT MRU . . . . .	79
4.11	The Jonswap spectrum used as input for the SDM . . . . .	80
4.12	Transmissibility functions for the Yaw motion at the JS due to motions at the MRU . . . . .	80
4.13	Yaw constraint at the SB main block of the crane . . . . .	81
4.14	Transmissibility functions which contribute to a Surge motion at the JS . . . . .	82
4.15	Main contributions to the Surge motion at the JS . . . . .	83
5.1	The Measured Data Model (MDM) . . . . .	84
5.2	Sailing route from site to the decommissioning yard (Vats) [12] . . . . .	85
5.3	An overview of parameters during the X Transport and the selected sample between the red vertical lines . . . . .	87
5.4	A picture of the jacket sensor and the proposed axis system [13] . . . . .	88
5.5	Roll & Pitch of the vessel . . . . .	90
5.6	Yaw & Heave of the vessel . . . . .	90
5.7	Surge at the MRU, obtained from GPS data . . . . .	92
5.8	Sway at the MRU, obtained from GPS data . . . . .	92
5.9	Left figure: waiting on weather Right figure: suspended X jacket . . . . .	93
5.10	Roll of the jacket at the JS . . . . .	94
5.11	Pitch of the jacket at the JS . . . . .	95
5.12	Yaw of the jacket at the JS . . . . .	95
5.13	Surge of the jacket at the JS . . . . .	96
5.14	Sway of the jacket at the JS . . . . .	96

5.15	Heave of the jacket at the JS . . . . .	97
5.16	Important mode shapes X suspended transport . . . . .	100
5.17	Incorrect responses all 6 DOF at jacket sensor by using all six vessel motions measured at the MRU. . . . .	102
5.18	Surge response of the jacket at the jacket sensor calculated by using all measured vessel motions at the MRU, except Surge and Sway vs measured Surge at the jacket sensor . . . . .	103
5.19	Sway response of the jacket at the jacket sensor calculated by using all measured vessel motions at the MRU, except Surge and Sway vs measured Surge at the jacket sensor . . . . .	104
5.20	Heave response of the jacket at the jacket sensor calculated by using all measured vessel motions at the MRU, except Surge and Sway vs measured Heave at the jacket sensor vs measured vessel Heave . . . . .	105
5.21	Roll response of the jacket at the jacket sensor calculated by using all measured vessel motions at the MRU, except Surge and Sway vs measured Roll at the jacket sensor vs measured vessel Roll . . . . .	106
5.22	Left: RAO from waves to roll at the MRU and JS Right: RAO from waves to pitch at the MRU and JS . . . . .	107
5.23	Pitch response of jacket at the jacket sensor calculated by using all measured vessel motions at the MRU, except Surge and Sway vs measured Pitch at the jacket sensor vs measured vessel Pitch . . . . .	108
5.24	Phases of the TFs between vessel Surge & Pitch and the Pitch motion at the jacket sensor and phase between Pitch and Surge motion of the vessel . . . . .	110
5.25	Contribution of vessel Surge & Pitch to Pitch at the JS . . . . .	110
5.26	Yaw response of jacket at the jacket sensor calculated by using all measured vessel motions at the MRU except Surge and Sway vs measured Yaw at the jacket sensor vs measured Yaw vessel . . . . .	111
5.27	Responses all 6 DOF at the jacket sensor by using all vessel motions except Surge and Sway measured at the MRU vs measured jacket motions vs measured vessel motions . . . . .	112
6.1	The Fatigue Data Model (FDM) . . . . .	114
6.2	Off- & side-lead, decomposition of forces and the suspension point of the crane	116
6.3	Axial and shear boom loading, transferred to the crane boom pivots resulting in Fx and Fy at the boom pivots . . . . .	116
6.4	S-N curves in air as defined in [11] D-air curve in red . . . . .	122

# List of Tables

2.1	Vessel particulars X suspended transport . . . . .	16
2.2	Jacket particulars X suspended transport . . . . .	16
3.1	Mode shapes in which the Y jacket moves heavily with small motions of the vessel for different draft . . . . .	63
5.1	Overview measured parameters during transport . . . . .	88
5.2	Overview off all SDA's during the X transport . . . . .	97
6.1	Location boom pivots [14] . . . . .	117
6.2	Fatigue analysis Huisman [15] . . . . .	119
6.3	Adjusted LC 64 obtaining less conservative weld stresses . . . . .	120

# List of Abbreviations

BP	Boom Pivots
CoG	Center of Gravity
DAF	Dynamic Amplification Factor
DFE	Design Fatigue Factor
DOF	Degree of Freedom
DOFs	Degrees of Freedom
DP	Dynamic Positioning
FDM	Fatigue Data Model
FEM	Finite Element Method
FFD	Full Frequency Domain
GCS	Global Coordinate System
HMC	Heerema Marine Contractors
LFD	Low Frequency Domain
MDM	Measured Data Model
MRU	Motion Reference Unit
Nm	Nautical miles
OSCLA	The Outer Continental Shelf Lands Act
OSPAR	Convention Protection of the Marine Environment of the North-East Atlantic
PS	Portside
RAO	Response Amplitude Operator
SB	Starboard
SCF	Stress Concentration Factor
SDA	Significant Double Amplitude
SDM	Synthetic Data Model
SMPM	Single amplitude Most Probable Maximum
SSCV	Semi-submersible Crane Vessel
t	Ton
TFs	Transmissibility Functions
T <sub>p</sub>	Peak Period
UK	United Kingdom
ULS	Ultimate Limit Strength
UTC	Coordinate Universal Time
WFD	Wave Frequency Domain

# Chapter 1: Introduction

## 1.1 Decommissioning

Decommissioning in the offshore industry is the process of removing existing infrastructure of offshore oil and gas operations at an offshore platform and returning the ocean and seafloor to its previous condition. The first international removal standard may be found in the 1958 Geneva Convention on the Continental Shelf, which provides in Article 5 that: "Any installations which are abandoned or disused must be entirely removed" [16].

Since 1992, operators in territorial waters of the European Union are obliged to decommission production facilities nearing the end of their economic life under the OSPAR convention, whilst in the USA since 1989 Offshore facilities have to be removed under the Outer Continental Shelf Lands Act (OCSLA) [17] [18], [19]. There are some other international texts covering the decommissions of offshore oil and gas installations, namely [20], [21], [22], [23], [24]. Until now there is no specific common legal framework in this area. Moreover, these conventions deal only with minimum standards. Individual countries may impose more stringent conditions.

Just in the UK, Oil and Gas has counted 1,630 wells set to be dismantled in the next decade in British waters. This is the equivalent of nearly one rig every two days and requires more than 1.2 million tonnes of concrete and steel to be removed [25]. The removal of these construction installations has become of paramount importance due to the aging of the oil platforms that can harm the environment [26]. Offshore decommissioning and abandonment has therefore matured over the years, becoming a considerable part of the portfolio of many offshore contractors with many years to come. Decommissioning typically takes several years of careful planning before execution starts. It takes many steps involving different stakeholders such as the community, regulatory agencies, the federal state, local governments, private investors, academia, non-governmental organizations and contractors. Often the operator relies on technical and logistical services from the service industry of which Heerema Marine Contractors is part of. During the decommissioning of offshore installations like oil platforms, the topsides are typically cut and lifted from the supporting structure by large crane vessels. The supporting structures (mostly jackets) are then separately lifted from the seabed and transported together with the topsides either for re-use elsewhere, or back to shore for dismantling and recycling. Afterwards, the site is restored to its original state.

## 1.2 Suspended transport

As every decommissioning project is unique, there is a continuous effort to find innovative methods to create more economical and sustainable ways of working. One of the areas of development is the optimization of use of available equipment and crane capacity.

About a decade ago, Heerema Marine Contractors introduced an new, unconventional method to remove and transport large jackets. The jackets are lifted as one single piece and transported to the recycling yard whilst being suspended from one or both cranes of one of Heerema's Semi-Submersible Crane Vessels. These transports are named suspended transports. A suspended transport is shown in figure 1.2b. In this research, a suspended transport starts the moment the ship is deballasted after lift off of the jacket. The vessel will deballast to a lower draft for transit and sails away. The suspended transport ends the moment the ship has to be ballasted again to safely transport the suspended object to shore. There are two variations of suspended transports, a restrained suspended transport and an unrestrained suspended transport. During an unrestrained suspended transport the jacket can freely move horizontally, see figure 1.2a & 1.2b. The restrained suspended transport uses two purpose built gripper structures at the bow of the vessel to restrain the jackets from horizontal motions during transport, see figure 1.2c & 1.2d. Major advantages of a suspended transport over a conventional decommissioning operation are:

- A shorter offshore project duration due to a reduced subsea cutting scope
- Substantial cost savings due to reduction of subsea lifting tools and marine spread requirements.
- Risk on weather downtime is reduced
- Improved safety during operation due to fewer offshore activities and prevention of back loading operations to a barge at open sea.

During the project analysis the appropriate method can be selected. A typical engineering analysis for the selection of a restraint or unrestrained suspended transport is shown in figure 1.1.

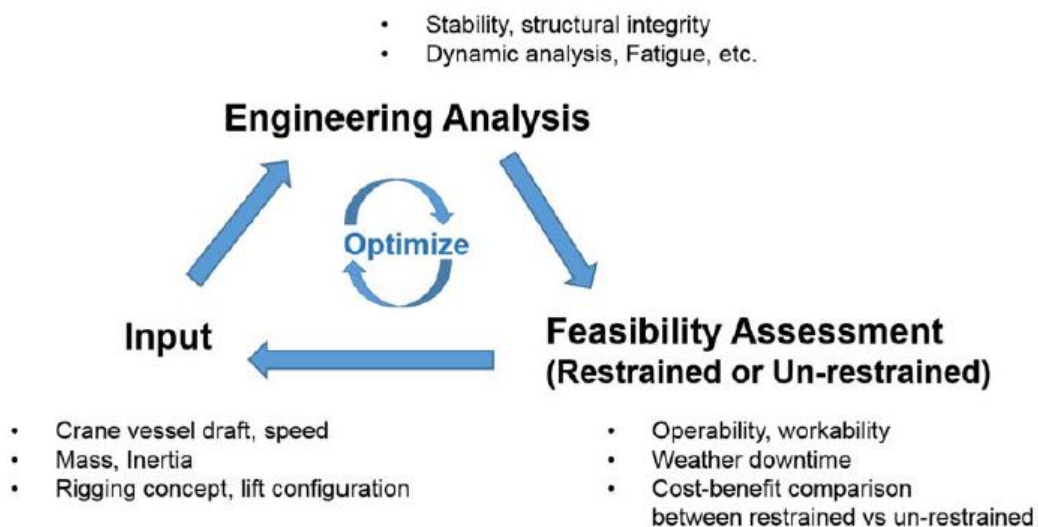
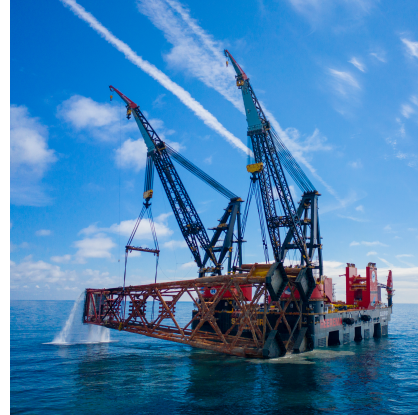


Figure 1.1: Iteration loop suspended transport [1]



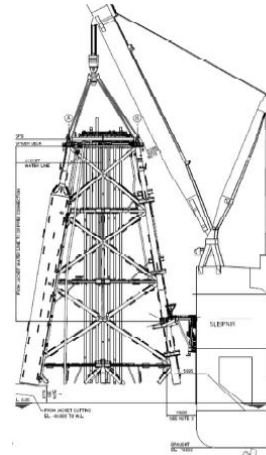
(a) Lift off unrestrained suspended transport by Sleipnir [27]



(b) Unrestrained suspended transport by Sleipnir[27]



(c) Gripper Frame used for restrained transports [1]



(d) Design sketch Gripper Frame restrained suspended transport [2]

Figure 1.2: Top two figures: Unrestrained suspended transport.

Bottom two figures: Restrained suspended transport

As every jacket is unique, adjustments have to be made to the gripper structure if a restrained suspended transport is the only option. Other disadvantages of restrained suspended transport are that structural strong points to attach the grippers are not always easily accessible due to protruding platforms and walkways. Omitting the restraints therefore sounds like the more favourable option, but brings other implications. Opposed to a load which is horizontally restrained, a load freely suspended in the cranes significantly influences the vessel's motion behaviour. This makes the transportation more weather sensitive.

To ensure that the loads stay within the capacity of the cranes, numerous hydrodynamic calculations and simulations are performed to investigate the effect of expected environmental conditions on the behaviour of vessel and load. The result is an effective removal method which is predictable, safe and time efficient. The method has been successfully applied for the removal of a number of structures (weighing up to 7000t) in the North Sea.

### 1.3 Crane specification

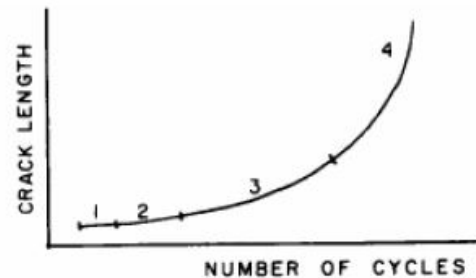
During a suspended transport, the time a jacket is suspended in the crane is much longer than during a regular heavy lift. This may result in that there is an impact on the overall life time of the crane as cranes are designed with a specific fatigue life. In design certain assumptions are applied regarding the use of the cranes (e.g. number of CSTs, environmental conditions). In practice the use of the crane will most often be different.

With their effectiveness, suspended transports are planned to occur more frequently in the future as more oil platforms reach their end of their lifespan. This brings implications to the certification of the cranes, as the design life of the crane can be negatively impacted by more frequent suspended transport. Therefore, it is necessary to accurately quantify the impact of suspended transports on the fatigue life of cranes.

### 1.4 Fatigue damage

Fatigue in material science, is the progressive structural damage that a material experiences when it is subjected to cyclic loading. The loads are not large enough to cause failure in a single application (Ultimate Strength) but failure can occur if the loads are repeated long enough. It may also occur at stresses less than the yield stress. The process of fatigue consists out of the following events [28]:

1. Crack initiation
2. Crack growth
3. Crack propagation
4. Final rupture



The fatigue life of a material is determined by the number of cycles of a certain loading that a material can undergo before failing. The fatigue life mainly depends on [28]:

- The shape of the connection
- The magnitude of the stress cycles
- The material of the object

Fatigue failure will only occur if the following essential conditions are present: cyclic tensile loads, stress levels above a threshold value, fatigue susceptible material and a flaw in the material [29].

The initiation of fatigue cracks primarily happens due to stress concentrations introduced by constructional details. Discontinuities such as welds and other local or general changes in geometrical form will set up such stress concentrations from which fatigue cracks may be initiated. The cracks may subsequently propagate through the member or through a connection. Typically, one therefore will find a pattern of distinct lines in the surface of a fracture caused by fatigue. These lines, which are called 'rest lines', indicate the progress of the crack until a final breakage occurs. This breakage is either a brittle or ductile fracture [29]. Connected with strength evaluation of cranes, one might in general claim that [29]:

- Static calculations are accurate
- Dynamic calculations are fairly accurate
- Fatigue calculations are inaccurate

Found from S-N curves, the fatigue life (allowable amount of cycles  $N$ ) of a steel detail is inversely proportional to the cube (or higher) of the stress range implying its high dependence on the magnitude of stress [11].

$$\begin{aligned} \log(N) &= \log(\bar{a}) - m \cdot \log(\Delta\sigma) \\ N &= \bar{a} \cdot \Delta\sigma^{-m} \quad (m_{steel} \geq 3) \end{aligned} \tag{1.1}$$

Furthermore, in the analysis of the fatigue life of a structural detail, many uncertainties are involved. These include the material dependent factors such as the geometry and size, but also residual stress and defects. Even the laboratory tests to determine the S-N curves, which are a measure of the ability to resist stress cycles, show considerable scatter [11]. This makes the prediction of fatigue life an uncertain process.

## 1.5 Current fatigue calculation suspended transport

Within HMC, currently fatigue assessment in the design phase of a suspended transport is done by a basic calculation. The manufacturer of the crane, Huisman has done an in-depth fatigue assessment of the crane. It was a probabilistic study in which in-house FEM models of the cranes with suspended load were used. Based on a previous in-house fatigue analysis of Huisman, the most critical welds in the boom of the cranes were determined to be the welds between the pivot bush and the pivot leg [15]. In their analysis the following assumptions were made:

- Fatigue life and stresses are calculated for:
  - The welds of the boom pivots as a function of the vertical load fluctuation
  - The welds of the boom pivots as a function of the side-lead fluctuation
  - The welds of the boom pivots as a function of the combined vertical and side lead fluctuation

- The stress is assumed to be linear with load and side-lead angles. The cycle time is taken as 10s
- A dynamic amplification factor of 1.1 is taken
- A side-lead of 1.0 degree is taken
- The D-Air S-N curve is used
- A Design Fatigue Factor (DFF) of 1 is used.

In the Huisman fatigue analyses [15] & [30] quite some conservatism was adopted:

- For the operational load cases, max values for heel, trim, roll and pitch of the vessel are applied. The ‘soft’ operational limits set during the designing phase of all suspended transports is lower .
- For the environmental load cases, the vessel motion accelerations are all applied in phase [30]. This is not realistic as maximum motions in the x-plane don’t occur with maximum motions in the y-plane of the vessel.
- For the environmental cases, equivalent accelerations are used. The resulting damage is based on a single segment S-N curve with  $m=5$ . In practice however, a typical S-N curve consists out of two segments. One steeper segment ( $m=3$ ) at a low amount of cycles which allows for a more gradual increase in higher stresses for an decreasing amount of cycles and a less steep segment ( $m=5$ ) at a higher amount of cycles which allows for a smaller gradual increase of stress for an increasing number of cycles. By taking the less steep  $m=5$  curve over the whole spectrum of obtained stress cycles, a lower amount of cycles is allowed which results in higher damage. This will result in a more conservative fatigue damage answer than if a two segment S-N curve would be used [30].

To make a prediction of the occurring fatigue damage during a suspended transport, currently HMC linearly scales reduced weld stresses at the boom pivots, obtained from the Huisman suspended transport analysis [15] with a scaling factor that takes into account the actual DAF (Dynamic Amplification Factor), crane moment utilization and crane load of the suspended transport [2]. This is show in equation 1.3.

$$u = \frac{\text{crane load}}{\text{max SWL}} \quad u_{ref} = \frac{\text{crane load Huisman}}{\text{max SWL Huisman}} \quad \text{Factor}_{Stress} = \frac{\text{crane load}}{5000t} \quad (1.2)$$

$$\text{Scaling factor} = \frac{DAF}{1.1} \cdot \frac{u}{u_{ref}} \cdot \frac{\text{crane load}}{5000t} \quad (1.3)$$

$u$  in equation 1.2 gives the crane load during suspended transport over the maximum Safe Working Load (SWL) which is defined by the load curves of the cranes. The load curve of the cranes can be found in figure 1.3. Besides these factors, a scaling factor to account for the DAF during transport over the DAF in the Huisman case and a scaling factor to account

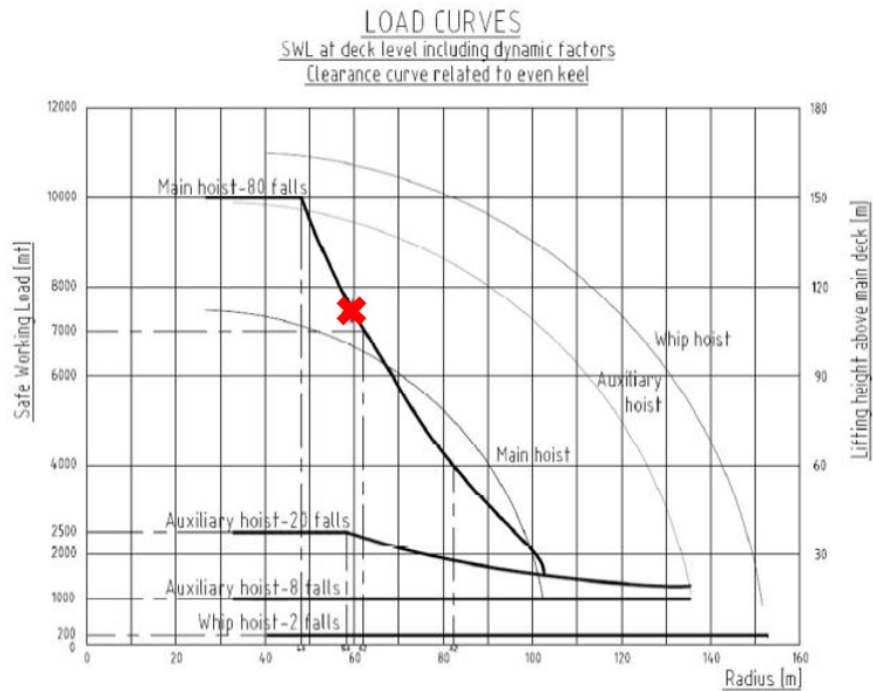


Figure 1.3: Load curves of the cranes. The allowable crane load at 60m radius is shown with a red cross [2]

for the increase in stresses in the crane are multiplied to find the scaling factor used to scale the weld stresses of the Huisman case as shown in equation 1.3.

With this prediction method, substantial fatigue life degradation during suspended transports has been found (0.5% fatigue life degradation 1 transport) [2]. Considering the limited duration of these transports and conservatism's in the assessment this has been accepted until now. However, this predication method will no longer be sufficiently accurate in case of more frequent use of the cranes for suspended transports, as is currently foreseen by Heerema.

## 1.6 Heerema Marine Contractors

Since its foundation in 1948, Heerema Marine Contractors (HMC) has grown to become one of the world leading marine contractors in the international offshore oil and gas industry. HMC transports, installs and removes all types of offshore facilities. Heerema's main fleet consists out of four heavy lift vessels.

- Sleipnir is a new-generation Semi Submersible Crane Vessel (SSCV) with a pair of revolving cranes that can lift 20,000t in tandem. No other existing crane vessel has this capacity. This is the vessel analysed in this research.
- SSCV Thialf is the second world's largest crane vessel and is capable of a tandem lift of 14,200t. This multi-functional dynamic positioned SSCV is tailored for the transportation, installation and decommissioning of foundations, moorings, SPARs, TLPs, integrated topsides, turbines, AC substations and DC convertor stations.
- Balder is a SSCV and is capable to execute a tandem lift of 4000t ton. The vessel has unique capabilities to work at water depths from 70ft and beyond. Balder is tailored for the installation of foundations, jackets, moorings, SPARs, TLPs, and integrated topsides. The vessel has extensive ROV capabilities and can lower 300t structures down to 9000ft of water depth.
- Aegir is a fast sailing heavy lift vessel, optimized for fast transit speed. Aegir is a monohull vessel with the capability to execute the transportation, installation and decommissioning of offshore facilities for both the oil & gas and offshore wind market. The Heavy Lift Crane has a capacity of 5,000t.

## 1.7 Problem statement

As decommissioning projects are more and more becoming a considerable part of the portfolio of offshore contractors due to the amount of offshore projects reaching the end of their life span, innovative methods as suspended transports are becoming increasingly important. Due to their effectiveness over conventional decommissioning methods, suspended transports are foreseen to be done more frequently in the future, which could potentially exceed the number of suspended transports the cranes were designed for. Thus far HMC estimated the risk of higher fatigue life consumption, to be low. Currently, HMC linearly scales reduced weld stresses at the most fatigue sensitive area, the welds of the boom pivots of the cranes. These weld stresses are obtained from the Huisman suspended transport analysis [15]. The weld stresses are linearly scaled with a scaling factor that takes into account the actual DAF (Dynamic Amplification Factor), crane moment utilization and crane load of the suspended transport [2]. Within this scaling method, no stress and motions measurements obtained from the analysed suspended transport are used to verify the results of this fatigue calculation. Besides the three terms in the scaling factor, no other details of the suspended transport are taken into account for the fatigue calculation. For example, the actual occurred wave climate is not taken into account.

This is different for every suspended transport. It therefore remains questionable how accurate it is to linearly scale Huisman's fatigue assessment to all future suspended transports operated by HMC. At the same time, as more suspended transports are foreseen, this means that the cranes are getting closer to the fatigue limits estimated by the current method. Besides this, in the 30y design life of the cranes, suspended transports are only taken into account assuming a load of 8000t suspended in each crane with exposure to the applicable environmental conditions for the main hoist for a period of four days, occurring three times each year. The question therefore arises how much fatigue really occurs in the cranes during different suspended transports. As there is currently no fast and accurate methodology available within HMC to obtain stresses during past suspended transports, there is at this moment in time, no input available for a fatigue damage calculation at the boom pivots of the cranes during past suspended transports.

## 1.8 Research objectives

The **goal** of this research is to develop an accurate yet fast methodology that uses measured vessel motions during suspended transport to obtain stresses at the boom pivots of the cranes, which can be used as input for a fatigue damage calculation.

- **Method:** Post processing of available measured vessel and jacket motions during the suspended transport of X.
- **Validation:** By comparing the measured jacket motions obtained from the suspended transport of X with calculated jacket motions of the suspended transport, created with Liftodyn models in combination with Matlab scripts
- **Deliverable:** An accurate and fast methodology that uses measured vessel motions during suspended transport to obtain stresses at the boom pivots of the cranes, which can be used as input for a fatigue damage calculation. A recommendation on how to find the fatigue damage in the cranes with the proposed method.

To achieve this deliverable, the following research questions were set up.

- Is it possible to provide input for a fatigue damage calculation of the cranes, based on the vessel and jacket motions or are there more measurements required?
- How can the available data of vessel and jacket motions correctly be translated into accurate fatigue life consumption estimates?
- How does the computed fatigue compare to Huisman's predictive fatigue analysis and is this accurate enough?
- Is it possible to expand this method to a wider range of vessels in the industry?
- Can the proposed methodology be used for either restrained and unrestrained suspended transport?

## 1.9 Scope & research approach

The main focus of this thesis is the post-processing of vessel and jacket motions of the unrestrained suspended transport of the X jacket. The main reason for choosing this more recent suspended transport are the notable vessel motions due to the waves. In most cases a suspended transport is performed during good weather conditions as the limiting criteria for operability defined during the design phase are rather tight. To obtain the most confidence that the models capture the motions of the jacket correctly, the best starting point of the analysis therefore is to choose a suspended transport with the most notable vessel motions. Most vessel motions occurred during the suspended transport of the X jacket which makes it the best suspended transport to start the analysis from.

In this research it is assumed that all flows are non-viscous, in-compressible, continuous and homogeneous. There are no cavitation holes or gas bubbles in the fluid. During the analysis, use is made of data measured by the Motion Reference Unit (MRU) of the vessel and data measured by a motion sensor mounted on the jacket. It is assumed that this data is correct after removing some erroneous data points. Besides data from these data sensors, HMC provided Liftodyn models of the suspended transports and a few Matlab functions which after some adjustments are also assumed to be correct.

Liftdyn is an in-house developed computer program that is designed to model and solve general linear hydrodynamic problems in the frequency domain. The program can solve systems consisting of rigid bodies connected to each other or to the earth by springs, dampers and hinges. This way, all linear dynamic systems can be modeled irrespective of the number of bodies or connectors. The bodies may have frequency dependent (added) mass, damping and frequency depended exciting forces which can be calculated by any diffraction code. Linear damping may be added to represent viscous damping not calculated by the diffraction analysis software. The resulting Response Amplitude Operators (RAOs) calculated by Liftdyn can be post-processed to a motion, velocity or acceleration RAO at any desired point relative to any other point. A RAO of the force in a connector can also be calculated. The main advantages of Liftdyn are:

- Able to analyze linear or linearised response.
- Flexible in modelling complex lift configuration.

Some disadvantages of Liftdyn are:

- Unable to analyze non-linear response.
- Unable to analyze non-stationary processes.
- Only simplified modelling of hydrodynamic data (only first order wave forces)

As only small motions of the suspended jacket are allowed during transport ( $1^\circ =$  soft limit for off-lead and side-lead hoist wires [12]), the suspended transport can be assumed linear and solved with LiftDyn. For this research it is assumed that force RAO's obtained from LiftDyn can be used to obtain stresses at the boom pivots as strain gauges are not installed during suspended transport. In this thesis, arguments are given as to why this assumption can be taken.

## 1.10 Thesis layout

The approach taken in this research to answer the research questions stated above, is to first dive into the required literature to better understand the problem. This is done in chapter 2. Besides this, also definitions and system particulars as coordinate systems and wave directions are presented. The theory comes together further in the chapter, where the inconvenient draft and forward speed problem are presented. These form the boundary conditions for the proposed method. At the end of the chapter, an overview of all required input for a fatigue calculation is given.

In chapter 3 the main assumptions and hypotheses for the proposed TF A2B Method are presented. The chosen approach is explained in more depth and some of the hypotheses are proven. Validation tests required for the validation of the Synthetic Data Model are presented. At the end of the chapter the full Synthetic Data Model is mathematically delivered. In chapter 4, the validation tests presented in chapter 3 are validated with the Synthetic Data Model (SDM). This model uses a Jonswap spectrum as input to simulate the vessel motions at location A, which is the MRU of the vessel (W2A). In combination with RAO's obtained from the LiftDyn model of the X suspended transport, the motions at location B are calculated (A2B). This is either the control point (same rigid body) or the location of the jacket sensor (other rigid body). These are compared to the simulated motions at location B, which are directly obtained from the Jonswap spectrum (W2B).

In chapter 5, the TF A2B Method is validated with the Measured Data Model (MDM). The MDM is an adjustment of the SDM. The MDM is using measured vessel motions obtained from the X suspended transport as input. A sample of the X suspended transport is used to validate if the MDM can calculate the correct Jacket motions (B) using transmissibility functions and the measured vessel motions at the MRU (A). In chapter 6, a Fatigue Data Model is presented which uses the TF A2B Method to obtain stress spectra at the boom pivots of the cranes during suspended transport. The stress spectra are required to obtain the occurred stress cycles during suspended transport. This is the missing input required for a fatigue damage calculation at the welds of the boom pivots during suspended transport. At the end of this thesis conclusions and recommendations for further research are given. This is visualised in figure 1.4.

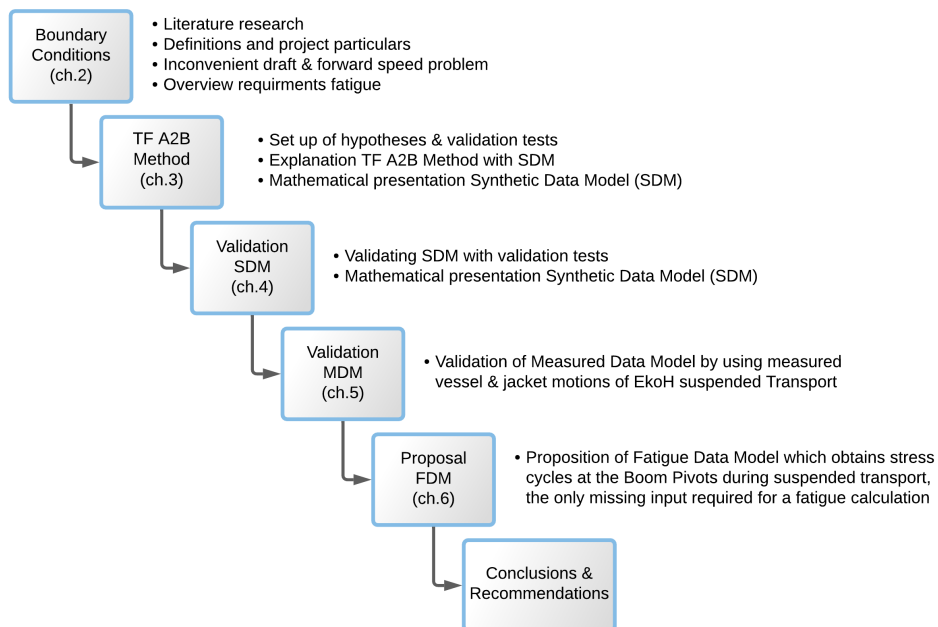


Figure 1.4: Overview research

# Chapter 2: Theoretical background

## 2.1 Kinematics system

The suspended transport of X is modeled as five different rigid bodies in LiftDyn, namely:

1. The Sleipnir body
2. The crane boom
3. The crane main block
4. The SPF platform on top of the jacket
5. The suspended jacket

The rigid body assumption assumes that the bodies do not deform under the action of applied forces. This will reduce the amount of parameters which are required to describe the configuration of the system [31]. The motions of a body can therefore be described by 6 degrees of freedom. These 6 degrees of freedom consist out of three translations and three rotations. The six degrees of freedom of the vessel motion are described as for a right handed axis system [5]:

- 3 translations of the ships centre of gravity in the direction of the x-, y- and z-axes:
  - Surge is in the longitudinal x-direction and is positive forwards (DOF 1).
  - Sway is in the lateral y-direction, positive to portside (DOF 2).
  - Heave is in the vertical z-direction, positive upwards (DOF 3).  
The gravity force is therefore working in the negative z-direction.
- 3 rotations about the x-, y- and z-axes:
  - Roll about the x axis, positive right turning (DOF 4).
  - Pitch about the y axis, positive right turning (DOF 5).
  - Yaw about the z axis, positive right turning (DOF 6).

A modeled representation of the X suspended transport can be seen in figure 2.1. The global, fixed to earth axis system in LiftDyn can be seen in figure 2.2. It is a right handed axis system with the Z axis pointing upwards. The axis system is located at the **aft** of the vessel. All wave directions used by LiftDyn are also shown with blue arrows. The wave directions are therefore defined as follows:

- 0° is from aft to forward: following seas
- 90° is from starboard to port-side: beam waves
- 180° is from forward to aft: head waves

In this thesis all data is presented in a right handed axis system with the Z axis pointing upwards. All local axis systems are aligned with the global axis system as seen in figure 2.1 & 2.2, so that all motions can be handled equally.

Three locations on the vessel and jacket will be used during this research, namely:

- The MRU of the vessel: This is the location where the vessel measures most of its motions. It is located at the 5th floor of the accommodation deck at the aft of the vessel in room INST RM 5A14. The location of the MRU is fixed. Coordinates in the global coordinate system (GCS): X: 35.625 Y: -12.5 Z: 68.5 [m]
- The control point: The location in which the DP system is keeping the vessel at its position. The control point technically changes slightly for every draft but it is assumed in this research that this point doesn't move. This is on the same rigid body as the MRU and is a point mid-ship between the floaters. Coordinates GCS X: 92.5 Y: 0 Z: 33.64 [m]
- The jacket sensor: The location in which the jacket motions are recorded during suspended transport. The location varies for every transport and is therefore modelled specifically for every transport. The jacket sensor is located **not** on the same rigid body as the MRU. For the X transport the jacket is mounted on top of the jacket. Coordinates GCS X: 210.56 Y: -25.5 Z: 121.67 [m]

The location of the MRU, control point and jacket sensor during the X suspended transport are shown in figure 2.1. The MRU is shown with a blue cross, the control point with a yellow triangle and the location of the jacket sensor is shown with a green square.

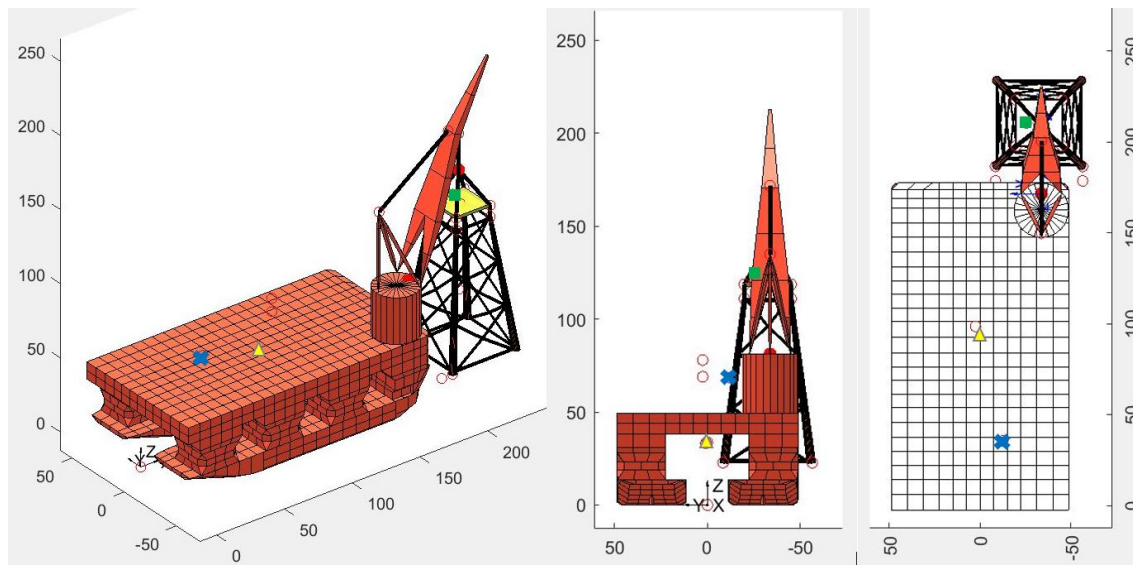


Figure 2.1: Location MRU, control point and jacket sensor of X suspended transport

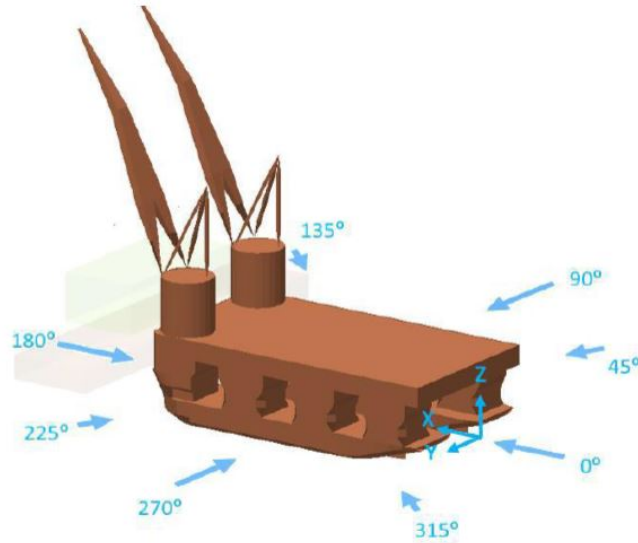


Figure 2.2: Global axis system Liftdyn and wave directions [3]

### 2.1.1 Vessel particulars

The total mass of a vessel as well as its distribution over the body is considered to be constant with time. This assumption is normally valid during a time which is large relative to the period of the motions. This results in that small effects, such as for instance a decreasing mass due to fuel consumption, can be ignored [5].

$$\text{Solid mass matrix : } m = \begin{pmatrix} \rho \nabla & 0 & 0 & 0 & 0 & 0 \\ 0 & \rho \nabla & 0 & 0 & 0 & 0 \\ 0 & 0 & \rho \nabla & 0 & 0 & 0 \\ 0 & 0 & 0 & I_{xx} & 0 & -I_{xz} \\ 0 & 0 & 0 & 0 & I_{yy} & 0 \\ 0 & 0 & 0 & -I_{zx} & 0 & I_{zz} \end{pmatrix}. \quad (2.1)$$

The solid mass matrix of a vessel is then given as in equation 2.1, in which the moments of inertia are often expressed in terms of the radii of inertia and the solid mass of the structure. Since Archimedes law is valid for a floating structure this results in equation 2.2.

$$\begin{aligned} I_{xx} &= k_{xx}^2 \cdot \rho \nabla \\ I_{yy} &= k_{yy}^2 \cdot \rho \nabla. \\ I_{zz} &= k_{zz}^2 \cdot \rho \nabla \end{aligned} \quad (2.2)$$

With the loading condition sheet of Sleipnir the vessel can be ballasted so that the actual mass, CoG and Radii of Gyration for a specific project (crane load, boom angle, etc) can be found. The stability criteria of the vessel are evaluated for a specific draft, making sure that the trim and heel of the vessel stay within favourable work-ability ranges.

### 2.1.2 Particulars Sleipnir during X suspended transport

The main particulars of Sleipnir during the X suspended transport are presented in table 2.1. The main particulars of the suspended jacket are presented in table 2.2.

Sleipnir parameters	Unit	Value
Design transport draft	m	16.8
Length overall	m	220
Breadth	m	97.5
Main deck height	m	49.5
Hook-load	t	4000

Table 2.1: Vessel particulars X suspended transport

X jacket body	Unit	
Hookload	4000	t

Table 2.2: Jacket particulars X suspended transport

### 2.1.3 Pendulum motion

The suspended jacket can move 'freely' in the cranes during unrestrained suspended transport. The jacket can therefore move with pendulum like motions. In its simplest form a pendulum consists of a ball (point-mass)  $m$  hanging from a (mass-less) string of length  $L$  and fixed at a pivot point  $P$  without friction as seen in figure 2.3. When displaced to an initial angle and released, the pendulum will swing back and forth with periodic motion. Since in this model there is no frictional energy loss, when given an initial displacement it will swing back and forth at a constant amplitude. By applying Newton's second law for rotational systems, the equation of motion for the pendulum may be obtained as in equation 2.3.

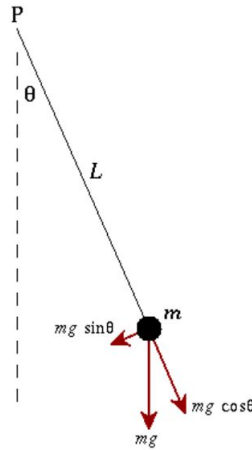


Figure 2.3: A simple pendulum [4]

$$\tau = I \cdot \alpha \rightarrow -m \cdot g \cdot \sin(\theta)L = mL^2 \frac{d^2\theta}{dt^2} \quad (2.3)$$

$$\text{Rearrange : } \frac{d^2\theta}{dt^2} + \frac{g}{L} \sin(\theta) = 0$$

Where:

$\tau$  = Torque [ $kg \cdot m^2 \cdot s^{-2}$ ]

$I$  = Moment of inertia [ $kg \cdot m^2$ ]

$\alpha$  = Angular acceleration [rad/s]

$\theta$  = angle of pendulum [rad]

$L$  = Length of string [m]

$g$  = Gravitational constant of earth 9.81 [ $m \cdot s^2$ ]

With the small angle approximation  $\sin(\theta) = \theta$  the equations of motion for a pendulum simplify into equation 2.4. As only small motions of the suspended jacket are allowed during transport ( $1^\circ$ = soft limit for off-lead and side-lead [12]) the small angle assumption also holds within this research.

$$\frac{d^2\theta}{dt^2} + \frac{g}{L}\theta = 0 \quad (2.4)$$

The harmonic solution can be written as

$$\theta(t) = \theta_0 \cdot \cos(\omega t) \quad (2.5)$$

With:

$$\theta_0 = \text{Initial angular displacement [rad]}$$

$$\omega_0 = \sqrt{\frac{g}{L}} = \text{Natural frequency [rad/s]}$$

$$T = \frac{2\pi}{\omega} = 2\pi \sqrt{\frac{L}{g}} = \text{Period [s]}$$

### 2.1.4 Literature pendulum motions

[1] shows that due to the unrestrained suspended jacket, mode shapes are introduced which show heavy pendulum motions of the suspended jacket. These natural frequencies of the pendulum mode shapes typically have a relatively high natural period and the occurring pendulum motions at these mode shapes can be in phase or out of phase in respect to the vessel motions. These pendulum mode shapes of the suspended jacket are however designed to be outside of the wave frequency domain and are therefore not excited much during suspended transport. [1] also shows that for restrained suspended transport only one pendulum mode shape exist within the low frequency domain. For frequencies in the wind-waves area, the responses between unrestrained and restrained suspended transport are however quite similar. To illustrate this, in figure 2.4, the Roll RAO of Thialf is shown for a restrained and unrestrained transport in which the extra mode shape due to unrestrained transport can clearly be seen [1].

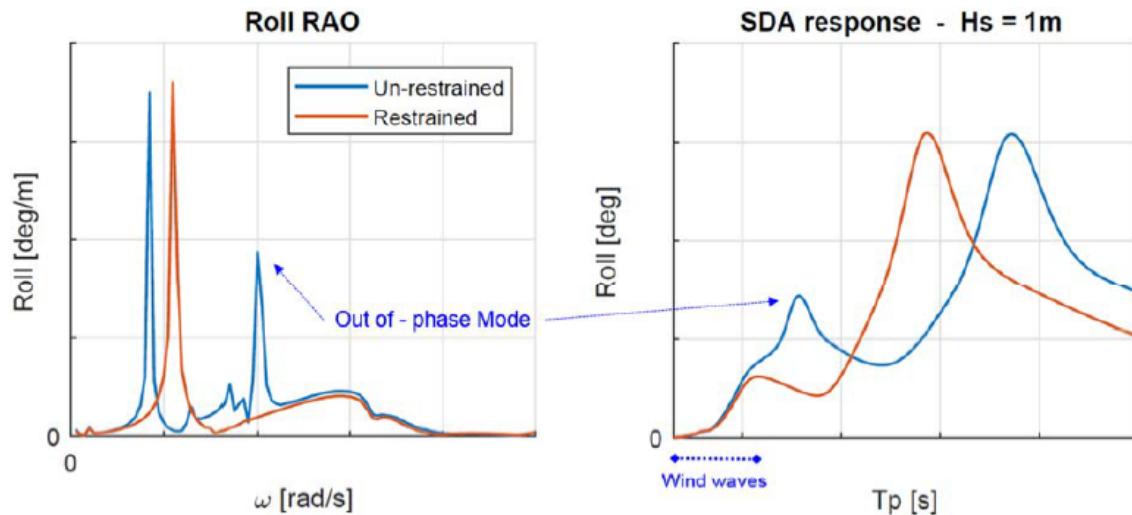


Figure 2.4: Thialf Roll RAO and the respective SDA response to unidirectional JONSWAP Spectra of Hs: 1m, gamma: 3.3, and various Tp's [1]

If one of the pendulum modes would be heavily excited, the assumed linear pendulum motions becomes non-linear as the small angle approximation does not hold anymore. If due to any unforeseen reason the suspended jacket obtains big motions during transport, the linear model used during the design phase will not be able to describe the motions correctly. This could lead to different resonant response with big(ger) motions of the jacket as result.

[32] examined the non-linearity's involved in the dynamic response of a boom crane first. They modeled the cable-payload assembly in a ship-mounted boom crane as a conical pendulum subject to base excitation's applied at the boom tip. They found a resonant response when the excitation frequency is near the natural frequency (primary resonance) or one-half the natural frequency (secondary resonance) of the assembly. [33]&[34] examined the weakly nonlinear response of a lightly damped, spherical pendulum. The pendulum was excited by a simple harmonic, planar displacement of the point of suspension. [34] found that non-planar motions could be excited due to the nonlinear interaction between the two modes.

Criteria for avoiding unstable crane load swinging motions have been presented [35]&[36]. Both papers generate crane operability diagrams by mapping instability regions of the Mathieu chart on to a plot of encountered wave period vs crane sling length. The main criticism of these diagrams is that they are based on harmonic forcing. Given that excitation due to the Mathieu instability results in a gradually increasing amplitude of motion, the assumption of regular seas with harmonic forcing is physically unrealistic, except for certain swell conditions. In [37], instead a Pierson-Moskowitz wave spectrum is used to describe a fully developed moderate sea state. [37] shows that the governing equations of motion for a crane vessel and its suspended crane load are non-linear as well as parametric if line tension variations are taken into account. The response of this system is therefore highly complex and exponential in growth, limit cycle (sustained oscillations without decay or growth) responses and sub-harmonic responses are all evident for harmonic excitation. There are therefore conditions in which large amplitude oscillations of a suspended load can occur due to parametric excitation.

Large swinging motions will be generated when the dominant period of the incident waves is approximately equal to the natural period of the load or approximately equal to one half times the natural period. Limit cycles are distinguishable from linear oscillations in that their amplitude of oscillation is independent of initial conditions.

The suspended line length is the dominant parameter and it is therefore advised to be adjusted by the crane operator so that parametric excitation is avoided in the prevailing sea conditions. With wave excitation representative of realistic moderate sea states however a more modest behaviour is observed since the development of the parametric instability is significantly reduced with the spread of wave excitation frequencies. Therefore, dramatic responses are unlikely to occur in realistic sea states. [37] however still shows that and around the unstable regions, the displacement amplitudes were always greater when the time-varying stiffness matrix was used instead of using conventional linear analysis. These enhanced motions of the crane load as a result of parametric excitation can reduce crane operability and therefore could lead to downtime during lifting operations.

In [37] however, a crane load of 1000t is used whilst during the suspended transport of X a hook load of 4000t is found. As explained in [37], larger incident waves are required to trigger the instability for increased damping values just as for an increase in lift load. This would result in that a parametric instability as in [37] would be unlikely during a suspended transport of a jacket as X, but does give clarity that non-linear behaviour of for instance pendulum motions, could potentially be incorrectly described by only using linearized models during the dynamic analysis of a suspended transport. [38], [39] & [40] also conclude that non-linear behaviour of pendulum motions is fairly different than linear behaviour of a suspended load in the crane. Note that this is shown for crane loads a few magnitudes smaller than that of a suspended jacket as X and mostly for different vessels than semi-submersibles. Many non-linear models are inspected which could better describe the non-linear behaviour of pendulum motions of the (cargo) load. For small pendulum motions linear theory should however be adequate to describe the motion of the suspended jacket. In this thesis, in-house linear modelling software Liftdyn is used to model the behaviour of the suspended jacket & vessel system during the dynamic analysis.

Interesting of [37] is that the non-linear phenomena can be avoided by changing the suspended line length by the operator of the crane. [41] modeled a boom crane as a spherical pendulum allowing for cable length changes and elastic stretch in the cable. [41] found out that a parametric excitation at twice the natural frequency leads to a sudden jump in the response as the cable is unreeled. They also demonstrated that introducing a harmonic change in the cable length at the same at frequency as the excitation's can suppress this dynamic instability and result in a smooth response. [42] however found that a planar direct base excitation near the natural frequency can produce in-plane and out-of-plane motions, sudden jumps in the response and a chaotic response as the cable length is changed. It is found that the load-swing amplitude depends on the reeling or unreeling speed of the cable length. Following [37] & [41] changing the cable length is probably the best way to correct instability if this would occur. Following [41] this change of cable length should be done with an harmonic change at the same frequency as the excitation's. Following [42], changing the cable length can however still give a chaotic response and remains a hard task for the crane operator if instability occurs.

[43] showed that for a shear-leg crane ship, hook load response strongly coupled with ship motions was mainly influenced by first order wave forces. Low frequency response due to second-order wave drift forces generally did not affect hook load response. A 9 DOF dynamic non-linear model with incorporated hull motions, non-linear large-angle load swing and elastic stretch of the hoisting wires was accounted for. A shear-leg crane ship is however a different lift vessel compared to a SSCV as Sleipnir, used in this research. Besides this, again much smaller loads (242t & 300t) were used. Normally a suspended transport is designed so that modes which induce big motions of the suspended jacket are not in the wave frequency domain of the first order wave forces. It is however helpful that the influence of second order wave drift forces in the lower frequency domain as shown by [43] could be of minor influence on the jacket response.

[44] shows that coupling between the cargo and the ship can be unilateral; the cargo oscillations are strongly dependent on the ship motion but the ship motions are not influenced much by the motions of the cargo. A nonlinear crane-ship dynamic model was developed which also takes nonlinear large load-swing angles of the cargo into account. Further investigations are however required for large cargo-to-ship mass ratios. The reason for this weak effect of the cargo on the ship is that for a large vessel, the hydrodynamic forces are much larger than the coupled dynamic forces exerted by the swinging load. This was also found by [45]. Unilateral coupling can also be true for suspended transports as the cargo to ship mass ratio of the suspended transport is found as 0.020 [2]. This is even smaller than found in [44] (ratio was 0.1).

[39] & [40] show the the existence of nonlinear phenomena such as sub-harmonic response for a barge and a mono-hull vessel with a 4 DOF 2D model in the x-z plane. Sub-harmonic response is the periodic response of a system at a frequency that is a sub multiple of the excitation frequency. The system in this case is a crane vessel with a load in the crane. Both show that if wave frequency approaches the system's eigenfrequency corresponding to a strongly coupled surge-swing motion, large resonant oscillations can occur. The main cause of this is small modal damping in that mode. It was also shown that for perfectly balanced vessels, the heave motion is coupled with other degrees-of-freedom only through non-linear terms. The result of this is that heave does not affect the primary resonances of surge, pitch, and swing motions of the researched vessels. However, it can act under certain circumstances as a para-metrical excitation on the swinging load and thus influence the period-2 motion of the researched floating cranes. Besides this it was also shown that large period-3 surge motions of the vessels may be excited by regular waves. These motions may occur at wave frequencies which are greater than the triple the eigenfrequency of the surge motion.

All of these findings could be of interest during a suspended transport of a jacket. Small modal damping in a mode during the X suspended transport could be a possible explanation for bigger motions, possibly even in the coupled surge - jacket motion modes or sway - roll jacket motions modes as there is less damping in the y plane of the vessel. These non-linear sub-harmonic responses would not be captured by the linear model. The researched vessels in [39]&[40] are however not a semi-submersible. The mass of the suspended jacket and Sleipnir is also a few magnitudes bigger than the payload and vessel as described in [39] (3592.8t & 180296t vs 0.1t & 55.3t respectively).

### 2.1.5 Literature double pendulum motion

Another interesting phenomena is described in [46]. A pendulum motion which should be taken into account during the design phase of a suspended transport is the double-pendulum phenomenon. If the payload is suspended by hook(s) through long steel cables, the payload cannot be simply considered as the same mass point as the hook at all. In such situations, the hook will swing around the suspension point of the crane, whilst the payload could potentially swing around the hook.

When the double-pendulum phenomenon is triggered, it will be notably challenging to suppress the resulting double-pendulum swing angles, even for experienced operators. Most control strategies designed based upon single-pendulum cranes are not applicable in such cases because in the case of improper control, much more severe double-pendulum effects may be excited [46]. During the design phase of a suspended transport this can be avoided by keeping the suspended jacket relatively close to the hook of the main block of Sleipnir.

## 2.2 Ocean waves

The most common way to describe ocean waves is by using ocean wave theory. To describe the irregularity of the ocean it is assumed that the irregular sea consists out of many simple, regular harmonic wave components. Every harmonic components has its own amplitude, length, period or frequency and direction of propagation but together can represent the irregularity of the ocean [7]. This is called the superposition principle and makes it possible to predict the complex irregular behaviour of sea waves with regular harmonics. The superposition principle is shown in figure 2.5. With the superposition principle the irregular sea surface can be decomposed into regular harmonics of which different relations between parameters are known. A snapshot of a harmonic wave fixed in space and fixed in time can be found in figure 2.6. The wave profile (the shape of the water surface) of a progressive harmonic wave in positive x direction can be described by equation 2.6. In this equation the wave number  $k$ , the circular wave frequency  $\omega$  and wave amplitude  $\zeta_a$  can be described by the equations in 2.7.

$$\zeta = \zeta_a \cdot \cos(kx - \omega t) \quad (2.6)$$

$$k = \frac{2\pi}{\lambda} \text{ [rad/m]} \quad \omega = \frac{2\pi}{T} \text{ [rad/s]} \quad H = 2 \cdot \zeta_a \text{ [m]} \quad \lambda = \frac{2\pi}{k} \text{ [m]} \quad (2.7)$$

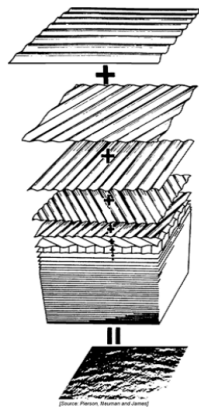


Figure 2.5: Combination of many simple, regular harmonic wave components to describe the irregular sea [5]

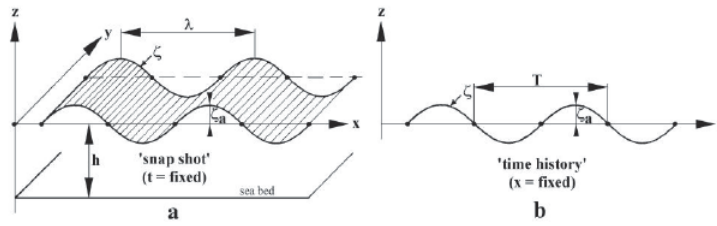


Figure 2.6: A snapshot of a harmonic wave. Left: fixed in space Right: fixed in time [5].

### 2.2.1 Wave motions

To describe the motions of harmonic waves, potential flow theory is used. To be able to use this linear theory it is assumed that the water surface slope is small. It is therefore assumed that the wave steepness is small enough so that terms in the equations of waves with a magnitude in the order of the steepness-squared can be ignored. This will result in that harmonic displacements, velocities and accelerations of the water particles and harmonic pressures all have a linear relation with the sea surface elevation, originated by the waves [5]. This is the reason why the profile of a simple wave with a small steepness looks like the harmonic wave in figure 2.6. The motions of water particles depend on the distance below the still water level. The velocity potential of harmonic waves can be described if it fulfills four requirements. The velocity potential of harmonic waves has to fulfil:

- The Laplace equation or Continuity equation
- The seabed boundary condition
- The free surface dynamic boundary condition
- The free surface kinematic boundary condition.

For an explanation of the boundary conditions I refer to [5], pages 5-4 to 5-9. If the boundary conditions are satisfied the velocity potential of harmonic waves can be written as in equation 2.8, where 0 corresponds with the mean surface elevation and  $z =$  positive in the upward direction.

$$\Phi_w = \frac{\zeta_a g}{\omega} \cdot \frac{\cosh(k(h+z))}{\cosh(kh)} \cdot \sin(kx - \omega t) \quad (2.8)$$

Where:

- $k$  = Wave number  $[\frac{2\pi}{m}]$
- $h$  = Water depth [m]
- $\zeta_a$  = Wave amplitude [m]
- $\omega$  = Radial frequency [rad/s]
- $g$  = Gravitational constant of earth 9.81  $[m \cdot s^{-2}]$
- $z$  =  $z$  location for which the potential can be found.

Offshore activities are most often in deep water, also referred to as short waves. The water is considered deep if the water depth  $h$  is more than half the wave length (left eq 2.9). This will result in that the relatively short waves do not feel the sea floor and are therefore not influenced by it. The potential in equation 2.8 will for deep water simplify into the right equation of 2.9.

$$\frac{h}{\lambda} > 0.5 \quad \Phi_w = \frac{\zeta_a g}{\omega} \cdot e^{kz} \cdot \sin(kx - \omega t) \quad (2.9)$$

### 2.2.2 First order wave forces

The multi-body system in this thesis is a vessel with a suspended jacket in the cranes. To describe the dynamic behaviour of the system, the main external excitation forces are required. As the multi-body system in this thesis is mostly active at sea, the main exciting forces are ocean waves. The ocean waves excite a pressure on the hull of the vessel. The pressure of ocean waves follows from the Bernoulli equation. The Bernoulli equation for an unstationary irrotational flow is given in equation 2.10. The velocity is given in terms of its three components  $u, v, w$ .

$$\frac{\partial \Phi_w}{\partial t} + \frac{1}{2}(u^2 + v^2 + w^2) + \frac{p}{\rho} + gz = C^* \quad (2.10)$$

Where:

- $\frac{\partial \Phi_w}{\partial t}$  = Derivative Wave Potential
- $t$  = Time [s]
- $u, v, w$  = Velocity component in x-, y-, z direction
- $p$  = Pressure [ $\frac{N}{m^2}$ ]
- $\rho_w$  = Density of water [ $\frac{kg}{m^3}$ ]
- $g$  = Gravitational constant of earth 9.81 [ $m \cdot s^2$ ]
- $z$  = z location [m]
- $C^*$  = meaning, is constant

In combination with the wave potential for deep water 2.9, the pressure due to ocean waves in deep water is gives as in equation 2.11.

$$p = -\rho g z + \frac{1}{2} \rho g \zeta_a^2 \omega^2 + \rho g \zeta_a \cdot e^{kz} \cdot \cos(kx - \omega t) \quad (2.11)$$

The first term is the hydro-static part of the equation. The time-independent non-linear second term is the radiation pressure. The radiation pressure causes second order wave drift loads on the structure. These are particularly important for anchored or moored floating structures. The harmonic third term causes the first order wave loads on a system. The time averaged contribution is 0. These first order forces are the most important and determine the linearised motions of the system [5].

As small wave steepness is assumed (linearization),  $u$  and  $w$  in the Bernoulli equation 2.10 are small. In two dimensions ( $v=0$ ) the Bernoulli equation therefore simplifies to the linearized Bernoulli equation in 2.12.

$$\frac{\partial \Phi_w}{\partial t} + \frac{p}{\rho} + gz = C^* \quad (2.12)$$

Therefore the pressure in deep water as in equation 2.11 simplifies into the linearised pressure in deep water as in equation 2.13.

$$p = -\rho gz + \rho g \zeta_a \cdot e^{kz} \cdot \cos(kx - \omega t) \quad (2.13)$$

## 2.3 The frequency domain

The motion and pressure potential of a progressive harmonic wave have now been described. The sea surface however doesn't consist out of one progressive harmonic wave. It is the superposition of many harmonic waves that is required to obtain a more accurate description of the irregular sea surface. The sea surface is therefore not described by one progressive harmonic wave as in equation 2.6, but by many as in equation 2.14. The wave number  $k$ , the circular wave frequency  $\omega$  and wave amplitude  $\zeta_a$  are now described for  $n$  amount of harmonic waves. Due to the combination of harmonics, now also a phase angle  $\epsilon_n$  is present for every harmonic, as they can be in or out of phase with each other. To decompose the irregular sea surface into regular wave components a Fourier series analysis is required at the location of the system. A full explanation of the Fourier Analysis can be found in [5] chapter 15. A time wave record sample can be taken which contains many waves. By measuring the water surface at the required location for a period of at least 30 minutes, a wave record is obtained. The wave record has to be short enough to be stationary, but long enough to obtain reliable statistics. It is assumed that the signal being studied repeats itself after each (long) interval even though a wave record does not do this exactly.

The wave elevation in the time domain of a long-crested irregular sea, propagating along the positive  $x$ -axis, can then be written as the sum of a large number of regular wave components in the frequency domain as in equation 2.14. Combining two or three regular waves with different directions already show a more irregular sea surface. This is shown in figure 2.7.

$$\zeta(t) = \sum_{n=1}^N \zeta_{a_n} \cos(k_n x - \omega_n t + \epsilon_n) \quad (2.14)$$

In the frequency domain, stationary linear processes can be analysed. All the wave amplitudes  $\zeta_{a_n}$  can be combined in a wave spectrum  $S_\zeta(\omega_n)$  as in equation 2.15.  $\Delta\omega$  the step size between two consecutive frequencies.

$$S_\zeta(\omega_n) \cdot \Delta\omega = \sum_{\omega_n}^{\omega_n + \Delta\omega} \frac{1}{2} \zeta_{a_n}^2(\omega) \quad (2.15)$$

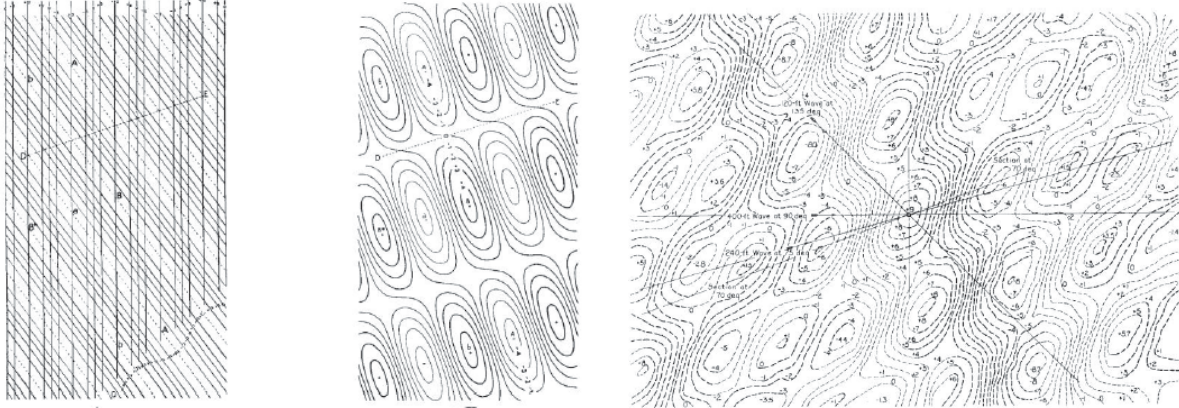


Figure 2.7: Left two plots: two regular waves with different directions [6]  
 Right: three regular waves with different directions [5].

If the wave spectrum is multiplied by  $\rho g$  and  $\Delta\omega \rightarrow 0$ , the wave energy spectrum  $S_\zeta(\omega_n)$  is defined as in equation 2.16.

$$S_\zeta(\omega_n) \cdot d\omega = \frac{1}{2} \zeta_{a_n}^2 \quad (2.16)$$

Within HMC the following three frequency ranges are approximately used:

- Ultra low frequency =  $T \gg 30s$ ,  $\omega < 0.014$  rad/s (crane slew etc)
- Low frequency =  $T \approx 18-45s$ .  $0.14 < \omega < 0.35$   
 2nd order waves, LF-wind, thruster response, possible long swells: For Roll/Pitch/Heave response there can already be a substantial contribution at periods in the 18-45s range.
- Wave frequency:  $T = 0-18s$ ,  $\omega > 0.35$  rad/s

The relation between a measured wave record, Fourier series and energy density spectrum is shown in figure 2.8. Phase information  $\epsilon_n$  is lost when transforming a Fourier series to a wave energy spectrum. The statistical properties of the harmonic components in terms of both frequency and amplitude are however often what is important to further analyse the decomposed irregular sea.

A narrow banded frequency wave spectrum is a spectrum with not too many frequencies. Generally waves in a sea or swell satisfy this condition. If a narrow banded frequency spectrum is present and the water surface elevation is treated as a stationary, Gaussian distribution, then wave amplitude statistics can be obtained from a Rayleigh distribution. A more elaborate explanation about the origin of the Rayleigh distribution can be found in [7] chapter 4. The Rayleigh probability density function is shown in figure 2.9. The Rayleigh distribution has only one parameter, which in this case is the zeroth-order moment  $m_{0\zeta}$  of the energy density spectrum (not the zeroth-order moment of the Rayleigh distribution). Since all statistical characteristics of the wave heights are determined by this distribution, they can all be expressed in terms of this spectral zeroth-order moment  $m_{0\zeta}$  alone, provided that the spectrum is narrow.

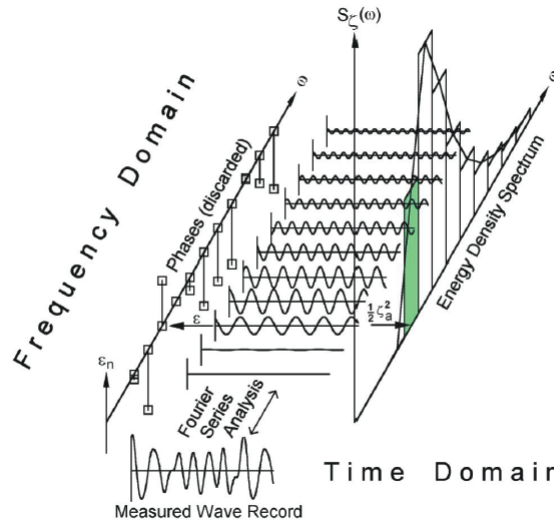


Figure 2.8: From irregular waves in wave record to energy density spectrum by Fourier analysis [5]

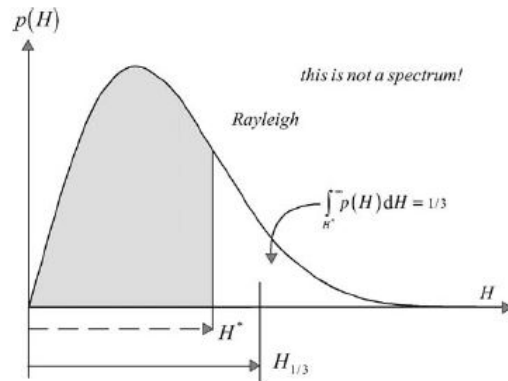


Figure 2.9: Rayleigh probability density function with explanation of the significant wave height [7].

A common used statistic in the Offshore Industry is the significant wave height. The significant wave height is defined as the mean value of the highest one-third of wave heights. This fraction of the waves can be identified in the Rayleigh distribution, which results in that the significant wave height can be determined from that distribution. The wave heights that are taken into account in this definition are located in the highest third of the Rayleigh distribution are  $H > H^*$  with  $H^*$  as in figure 2.9 and in which the significant wave height is noted as  $H_{1/3}$ . The significant wave height can be determined as an expected value from the zeroth and first-order moments of the highest third of the Rayleigh distribution. After substituting the wave heights that are involved in the significant wave height (the equation in figure 2.9) and the analytical expression for the Rayleigh distribution the significant wave height can be found as in equation 2.17. For the elaboration, see [7] pages 68 to 70.

$$H_{1/3} = H_{m0} \approx 4\sqrt{m_0} \tag{2.17}$$

In equation 2.17,  $m_0$  is the zeroth-order moment of the energy density spectrum  $E(\omega)$ . The significant wave height  $H_{m0}$  can therefore be estimated from the spectrum, which in turn can be obtained from a time series of the sea-surface elevation.

Other statistical properties of an energy density spectrum can also be found by using the spectral moments of the area under the spectral curve with respect to the vertical axis at which  $\omega = 0$ . The spectral moments can be found as in equation 2.18.

$$M_{n\zeta} = \int_0^{\infty} \omega^n \cdot S_{\zeta}(\omega) \cdot d\omega \quad (2.18)$$

$M_{0\zeta}$  is an indication of the variance of the water surface elevation, whilst  $M_{1\zeta}$  is the first order moment (static moment) and  $M_{2\zeta}$  the second order moment (moment of inertia). This way significant wave amplitudes, -heights and -periods can be found in the frequency domain which can be used to further analyze the dynamic behaviour of the sea at the chosen location. In combination with the Rayleigh distribution also probability of exceedances of for instance the significant wave height ( $H_{1/3}$ ) by a chosen wave height can be found. For all other formulas see, [5] & [7].

Nowadays there are three common standard wave spectrum's frequently used to describe different sea states within a frequency domain analysis. These are Bretschneider, Pierson-Moskowitz and JONSWAP spectra. All three spectra have different factors and are more accurate for different sea states. The JONSWAP spectrum is a spectrum where most of the spectral energy comes from fetch-limited or coastal wind waves generated by local weather. The JONSWAP spectrum is frequently used in the North Sea as most waves here are generated by local weather.

A Bretschneider or Pierson-Moskowitz spectrum is used for fully developed seas in which a part of the wave energy comes from swell. Swell is generated by distant weather systems. The gravity surface waves (swell) disperse through the ocean. When swell arrives in different weather systems, it is hardly affected by the local weather. The wave period of swell waves is longer than that of local wind waves and is therefore found at the beginning of a wave spectrum (high period means low frequency). Swell has a narrower range of frequencies and direction due to dispersion from their area of generation and dissipation. This gives swell waves a more defined shape and makes them less random than local wind waves [7].

The main advantage of a frequency domain analysis is that is very quick. It can be applied when:

- Hydrodynamic properties are constant in time
- Forces are linear depended motion, velocity and acceleration
- The forces are harmonic

In the next section it will be explained that hydrodynamic properties could depend on frequency but are constant in time. With Newton's laws in section 2.4.1 it is explained how forces linearly depend on motion, velocity and acceleration. The decomposition of the irregular sea in regular harmonics validates the third entry. The result of a frequency domain analysis is that the equations of motion reduce to linear second order differential equations. This is important as equations of motion are used to describe the dynamic behaviour of the vessel and payload. With the superposition principle it is possible to find the total response of the vessel. For a specific sea state, the total response of the vessel is the sum of responses of the vessel to every harmonic.

In many cases the vessel motions mainly have a linear behaviour. This means that, at each frequency, the different ratios between the motion amplitudes and the wave amplitudes and also the phase shifts between the motions and the waves are constant. The Significant Double Amplitude can therefore be calculated in the same way as the significant wave height  $H_{1/3}$ , as the phase shifts between output and input does not change. As a result of linear theory, the resulting vessel motions in irregular waves can be obtained by adding together results from regular waves of different amplitudes, frequencies and propagation directions (superposition principle). With known wave energy spectra and the calculated frequency characteristics of the responses of the ship, therefore the response spectra and the statistics of these responses can be found [5].

## 2.4 Multi-body dynamics

Complicated dynamical behaviour of structures is often modelled with multi-body dynamic theory. These bodies are connected with each other or the world by connectors. Because these bodies are connected, their motions are influenced by each other. Connectors which are frequently used within dynamics are springs and dampers.

The connector applies a force on the connection points due to a relative motion and/or velocity between the connection points. Besides connectors, restraints are frequently used within dynamics to describe the motion of coupled bodies. Restraints restrict the relative motions, velocities or accelerations of the bodies. Frequently used constraints are hinges. This is a joint which fixes all motions and two of the three rotations.

The five rigid bodies modeled in LiftDyn as shown in figure 2.1 move as five connected rigid bodies. The rigid bodies are excited by external forces and moments. As all bodies are connected to each other by springs and dampers, there is interaction between the bodies. If the relative motion & velocity between the bodies change, forces are transmitted through the springs which are connected to the bodies. This happens because the springs are compressed or stretched. The forces in the springs are calculated by multiplying the spring stiffness with the relative extension/compression of the spring whilst the dampers dissipate energy proportional to the velocity of the mass in the opposite direction of the motion. All motions, velocities, accelerations and forces are calculated in a LiftDyn model as shown in figure 2.1 which can describe the total dynamic behaviour of the modeled system.

The dynamic behaviour results from the equilibrium of applied forces and a change in momentum. There are external forces acting on the system and internal forces which are a result from the stiffness and the damping in the system. With Newtons laws of motion a relation between the external forcing acting on the system can be developed to describe the changes in the state of motion of the system.

### 2.4.1 Equations of motion

The equations of motions of a rigid body in a space fixed coordinate system follow from Newton's second law. The vector equations for the translations and the rotations about the centre of gravity are given in equation 2.19.

$$\vec{F} = \frac{d}{dt}(m\vec{U}) \quad \text{and} \quad \vec{M} = \frac{d}{dt}(m\vec{H}) \quad (2.19)$$

Where:

- $\vec{F}$  = Resulting external force acting in the centre of gravity (CoG) [N]
- $m$  = Mass of the rigid body [kg]
- $\vec{U}$  = Instantaneous velocity of the centre of gravity [m/s]
- $\vec{M}$  = Resulting external moment acting about the centre of gravity [Nm]
- $\vec{H}$  = Instantaneous angular momentum about the centre of gravity [ $kgm^2s^{-1}$ ]
- $t$  = Time [s]

Newton's second law describes how the acceleration  $\frac{d}{dt}\vec{U}$  of a body (m) changes due to external forcing  $\vec{F}$  or how the angular momentum  $\vec{H}$  changes in time due to an external moment. The body can be pulled or pushed which changes the motion of the body. Together with the constraints and connectors in the system the equations of motion of the system can be set up. The equations of motion of the system describe the dynamic behaviour of the system due to internal and external forcing. In its simplest form a mass-damper-spring system can be described by equation 2.20.

$$M \cdot \ddot{x} + B \cdot \dot{x} + C \cdot x = F \quad (2.20)$$

M is the mass of the body, B is the damping added to the body and C is the stiffness added to the body.  $\ddot{x}$ ,  $\dot{x}$  and x are the acceleration, velocity and displacement of the body respectively. The motion of the body should equal the external forcing F as Newtons second law describes.

The example above is a single bodied system. If M, B and C are extended from scalar values to matrices and  $\ddot{x}$ ,  $\dot{x}$  and x are extended into vectors, more bodies can be described. This is the base for linear multi body dynamics and the foundation of how Liftdyn calculates the resulting motions, velocities, accelerations and forces of the modeled system [3].

As the system is active at sea the main excitation forces are the waves at sea. The linearised pressure of the waves cause first order loads on the system. The time-averaged value of the wave loads and the resulting motion component are zero. The resulting linear motions with harmonic character can be described by equations of motions of the system. The equations of motion are described by linear second order differential equations. This makes it possible to apply the superposition principle. For one body the resulting motion in waves of the body is the superposition of the motions of the body in still water and the motion of the restrained body excited by the waves. This will result into two categories of forces and moments. These are:

- Hydro-mechanic forces and moments which are induced by the harmonic oscillations of the rigid body which is moving in the undisturbed surface of the fluid.
- Wave exciting forces and moments (first order wave forces) from waves coming in on the restrained body.

In figure 2.10 the superposition of hydro-mechanic and wave loads is shown on a rigid body. For a vessel it works the same only now the problem is 3 dimensional. Since the system is linear, hydro-mechanic forces and wave exciting forces can be added up to obtain the total loads on the system. As the vessel and payload will oscillate vertically it will generate waves that will propagate radial from it. The radiated waves transport energy and will therefore withdraw energy from the system, the motions of the system would die out. This is called wave or potential damping and is proportional to the velocity in a linear system. Within equations of motion the wave damping can be found in the damping coefficient  $b[\frac{kg}{s}]$ . Besides potential damping from radiation of waves there is also friction present in a viscous fluid. Friction causes damping, vortices and separation phenomena. Frictional damping is highly non-linear and is often linearized within the equations of motion.

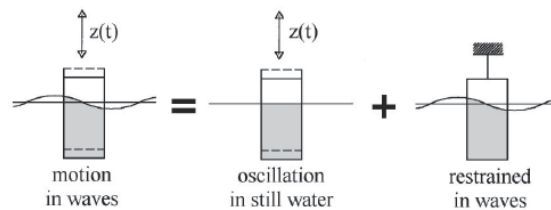


Figure 2.10: Superposition of hydro-mechanic loads and wave loads on body [5].

The second part of the hydro-mechanic reaction force is proportional to the vertical acceleration of the system. The force is the result of acceleration of water particles near the system due to the oscillating motion of the system. This part of the hydro-mechanic force does not dissipate energy and will show as a standing wave system on the sides of the vessel and payload. This is called the added mass. In the equations of motion this can be found as the added mass coefficient  $a[kg]$ .

For free floating bodies, restoring forces are found in heave, pitch and roll motions. These restoring act as 'springs'. When the system is for example pushed in heave, pitch or roll, the system wants to return back to its original position. It acts just as a spring and are therefore called restoring spring forces. They can be found by performing linearized static stability calculations in which use is made of Archimedes Law, Scribanti and the metacentric height. See [5], chapter two. The restoring spring forces are given as in equation 2.21.

$$\begin{aligned}
 \text{Heave} : c_{zz} &= \rho g A_{WL} \\
 \text{Roll} : c_{\phi\phi} &= \rho g \nabla \cdot \overline{GM} \\
 \text{Pitch} : c_{\theta\theta} &= \rho g \nabla \cdot \overline{GM}_L
 \end{aligned} \tag{2.21}$$

## 2.4.2 Coupled motions

Generally, a theoretical ship has a vertical-longitudinal plane of symmetry, which results in that its motions can be split into symmetric and anti-symmetric components. On this theoretical symmetric vessel, Surge, Heave and Pitch motions are symmetric motions. This means that a point to starboard has the same motion as the mirrored point to port side. The motions Sway, Roll and Yaw - are anti-symmetric motions. Symmetric and anti-symmetric motions are not coupled for a perfect symmetric vessel. This means that they don't have any influence to each other. In reality vessels are not perfectly symmetric so there is still some coupling. This coupling is often less strong than the coupling with motions in the same plane. In this explanation the symmetry is however assumed for explanation purposes.

Because of this symmetry and anti-symmetry, two sets of three coupled equations of motion can be found for perfectly symmetric vessels. The fully written out equations of motion for coupled Surge, Sway and Pitch for a perfect symmetric can be found in equation 2.22. The coupled Sway, Roll and Yaw equations of motion for a perfect symmetric ship can be found in 2.23 [5]. In reality a vessel is however not perfectly symmetric and therefore there is no perfect uncoupling of motions. This result that all 6 motions of the vessel in reality can influence each other.

$$\left. \begin{aligned}
 (\rho \nabla + a_{11}) \cdot \ddot{x} + b_{11} \cdot \dot{x} + c_{11} \cdot x \\
 + a_{13} \cdot \ddot{z} + b_{13} \cdot \dot{z} + c_{13} \cdot z \\
 + a_{15} \cdot \ddot{\theta} + b_{15} \cdot \dot{\theta} + c_{15} \cdot \theta \\
 a_{31} \cdot \ddot{x} + b_{31} \cdot \dot{x} + c_{31} \cdot x \\
 + (\rho \nabla + a_{33}) \cdot \ddot{z} + b_{33} \cdot \dot{z} + c_{33} \cdot z \\
 + a_{35} \cdot \ddot{\theta} + b_{35} \cdot \dot{\theta} + c_{35} \cdot \theta \\
 a_{51} \cdot \ddot{x} + b_{51} \cdot \dot{x} + c_{51} \cdot x \\
 + a_{53} \cdot \ddot{z} + b_{53} \cdot \dot{z} + c_{53} \cdot z \\
 + (I_{yy} + a_{55}) \cdot \ddot{\theta} + b_{55} \cdot \dot{\theta} + c_{55} \cdot \theta
 \end{aligned} \right\} \begin{array}{l} = X_{w1} \text{ Surge} \\ = X_{w3} \text{ Heave} \\ = X_{w5} \text{ Pitch} \end{array} \text{Symmetric Motions} \tag{2.22}$$

$$\left. \begin{aligned}
(\rho \nabla + a_{22}) \cdot \ddot{y} + b_{22} \cdot \dot{y} + c_{22} \cdot y \\
+ a_{24} \cdot \ddot{\phi} + b_{24} \cdot \dot{\phi} + c_{24} \cdot \phi &= X_{w2} \text{ Sway} \\
+ a_{26} \cdot \ddot{\psi} + b_{26} \cdot \dot{\psi} + c_{26} \cdot \psi \\
a_{42} \cdot \ddot{y} + b_{44} \cdot \dot{y} + c_{44} \cdot y \\
+(I_{xx} + a_{44}) \cdot \ddot{\phi} + b_{33} \cdot \dot{\phi} + c_{33} \cdot \phi &= X_{w4} \text{ Roll} \\
+(-I_{xz} + a_{46}) \cdot \ddot{\psi} + b_{46} \cdot \dot{\psi} + c_{46} \cdot \psi \\
a_{62} \cdot \ddot{y} + b_{62} \cdot \dot{y} + c_{62} \cdot xy \\
+(-I_{zx} + a_{64}) \cdot \ddot{\phi} + b_{64} \cdot \dot{\phi} + c_{64} \cdot \phi &= X_{w6} \text{ Yaw} \\
+(I_{zz} + a_{66}) \cdot \ddot{\psi} + b_{66} \cdot \dot{\psi} + c_{66} \cdot \psi
\end{aligned} \right\} \text{Anti - Symmetric Motions} \quad (2.23)$$

- $\rho$  = Density of water [ $\frac{kg}{m^3}$ ]  
 $\nabla$  = Volume of displacement of the water [ $m^3$ ]  
 $I_{ij}$  = Mass moment of inertia of vessel in i due to an acceleration vessel in j [ $kgm^2$ ]  
 $a_{ij}$  = Added mass for force on vessel in i due to an acceleration of vessel in j [kg]  
 $b_{ij}$  = Damping for the force on vessel in i due to an velocity of vessel in j [kgs]  
 $c_{ij}$  = Spring stiffness for the force on vessel in i due to an motion of vessel in j [ $\frac{N}{m}$ ]  
 $X_{h1}, X_{h2}, X_{h3}$  = Exciting wave forces in the x-, y- and z directions [N]  
 $X_{h4}, X_{h5}, X_{h6}$  = Exciting wave moments about the x-, y- and z axes [Nm]

It is now possible to set up the equations of motion of the vessel and payload:

$$F_{ext}(t) + F_{wave}(t) - (k_{hyd} + k_{other}) \cdot x(t) - b_{visc} \cdot \dot{x}(t) \cdot |\dot{x}(t)| - b_{hyd} \cdot \dot{x}(t) = (m + a_{hyd}) \cdot \ddot{x}(t) \quad (2.24)$$

For every degree of freedom there is an equation of motion. This results in 6 coupled equations of motion. After rearranging the equations of motion in matrix notation this will result in equation 2.25. In which  $M$ ,  $A_{hyd}$ ,  $B_{visc}$ ,  $B_{hyd}$ ,  $K_{hyd}$  and  $K_{other}$  are 6x6 matrices.  $X(t)$ ,  $F_{wave}(t)$  and  $F_{ext}(t)$  are 6x1 vectors.

$$(M + A_{hyd}) \cdot \ddot{X}(t) + B_{visc} \cdot \dot{X}(t) \cdot |\dot{X}(t)| + B_{hyd} \cdot \dot{X}(t) + (K_{hyd} + K_{other}) \cdot X(t) = F_{ext}(t) + F_{wave}(t) \quad (2.25)$$

To apply a frequency domain analysis, the frictional damping has to be linearized and all forces need to be harmonic. The following external forces are therefore not included in a frequency domain analysis:

- Wind forces
- Current forces
- Other external forces
- Other spring forces (mooring, dynamic positioning)

This results in that  $F_{ext}(t)$  is removed from equation 2.25. The frictional damping is linearized.

The linearization of the frictional damping is shown in equation 2.26. This equivalent linear damping coefficient  $B_{add}$  depends on the frequency and the amplitude of oscillation [5]. The equations of motion in matrix form will change to equation 2.27. The equation of motions can be solved for regular waves. A regular wave can be written as 2.28.

$$B_{visc} \cdot \dot{X}(t) \cdot |\dot{X}(t)| \rightarrow B_{add} \cdot \dot{X}(t) \quad (2.26)$$

$$(M + A_{hyd}) \cdot \ddot{X}(t) + (B_{add} + B_{hyd}) \cdot \dot{X}(t) + (K_{hyd} + K_{other}) \cdot X(t) = F_{wave}(t) \quad (2.27)$$

$$\zeta(\omega, t) = \zeta_a \sin(\omega t) \quad (2.28)$$

The wave forcing can therefore be written as 2.29.

$$F_{wave(t)} = F_a(\omega) \sin(\omega t + \epsilon_{\zeta, F}) \quad (2.29)$$

The equations of motion can be solved by searching for a solution in the form as in equation 2.30 in which  $X_a(\omega)$  is the motion amplitude and  $\epsilon_{\zeta, X}(\omega)$  is the phase difference between the motion and wave respectively. It is now possible to rewrite the equation of motion 2.27 into the form 2.31. In which  $i$  is the degrees of freedom (1 to 6) as explained in 2.1.

$$\begin{aligned} X(t) &= X_a(\omega) \cdot \sin(\omega t + \epsilon_{\zeta, X}(\omega)) \\ \dot{X}(t) &= \omega X_a(\omega) \cdot \cos(\omega t + \epsilon_{\zeta, X}(\omega)) \\ \ddot{X}(t) &= -\omega^2 \cdot X_a(\omega) \cdot \sin(\omega t + \epsilon_{\zeta, X}(\omega)) \end{aligned} \quad (2.30)$$

$$[(K_{hyd} + K_{other}) + i \cdot (B_{hyd} + B_{add})\omega - (M + A_{hyd}) \cdot \omega^2] \cdot X_{a,i} = F_{a,i} \quad (2.31)$$

## 2.5 RAO's

The equations of motion 2.31 are often rewritten in the form of a response amplitude operator (RAO) 2.32.

$$RAO(\omega) = \frac{F_{a,i}}{[(K_{hyd} + K_{other}) + i \cdot (B_{hyd} + B_{visc})\omega - (M + A_{hyd}) \cdot \omega^2]} \quad (2.32)$$

$\frac{X_a}{\zeta_a}$  = Motion amplitude per unit wave amplitude ( $|RAO|$ )

$\epsilon_X$  = Phase difference between motion and wave ( $\angle(RAO)$ )

The response amplitude operator (RAO) is the transfer function between input (waves) and output (response). To solve the equations of motion in the frequency domain for a particular system and location, several pieces of information are required. This is summed up in figure 2.11. For a certain wave amplitude acting on the system a motion amplitude of the system in the degree of freedom for which the equation of motion is solved can be found.

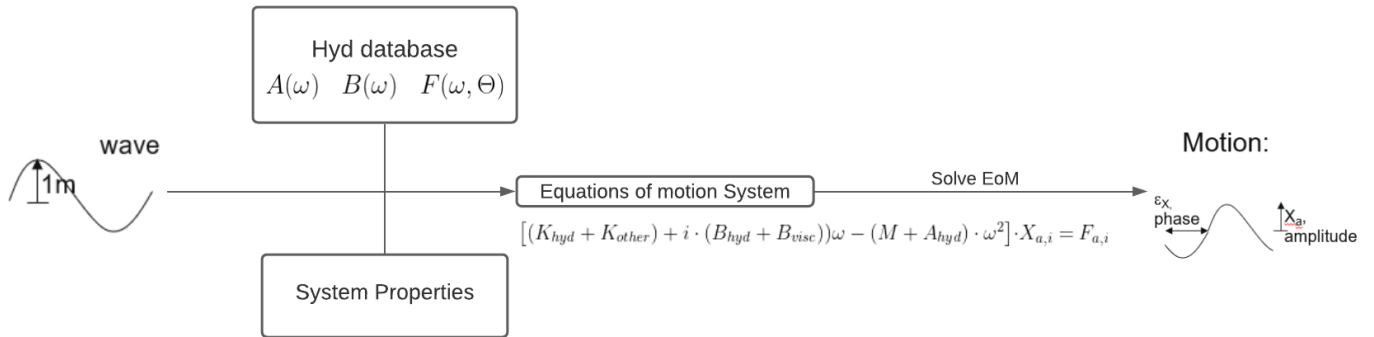


Figure 2.11: Solving equations of motion in the frequency domain

There are however a lot of waves acting on the vessel which have different amplitudes, frequencies and directions. As the system is linear, RAOs can be added for different amplitudes and frequencies as shown in equation 2.33 (superposition principle).

$$\begin{aligned}
 \zeta_w(\zeta_a = 1m, \omega = \omega_1) &\rightarrow RAO(\omega_1) \\
 \zeta_w(\zeta_a = 2m, \omega = \omega_1) &\rightarrow 2 \cdot RAO(\omega_1) \quad \rightarrow RAO(\omega_1) + 2 \cdot RAO(\omega_1) + 1.5 \cdot RAO(\omega_2) \quad (2.33) \\
 \zeta_w(\zeta_a = 1.5m, \omega = \omega_2) &\rightarrow 1.5 \cdot RAO(\omega_2)
 \end{aligned}$$

For a complete wave spectrum this finally results in that the RAO's can be used in the frequency domain as in equation 2.34.

$$\begin{aligned}
 S_w \cdot d\omega &= \frac{1}{2} \cdot \zeta_a^2(\omega) \\
 S_{response} \cdot d\omega &= \frac{1}{2} \cdot X_a^2(\omega) = \frac{1}{2} \cdot (RAO(\omega) \cdot \zeta_a(\omega))^2 \cdot d\omega = RAO^2(\omega) \cdot S_w(\omega) \cdot d\omega \quad (2.34) \\
 S_{response} &= RAO^2(\omega) \cdot S_w(\omega)
 \end{aligned}$$

Solving the equations of motions in the frequency domain is therefore in practice using the obtained RAO's in combination with a wave spectrum to find the response spectra of the vessel motions in the frequency domain. This is shown in figure 2.12.

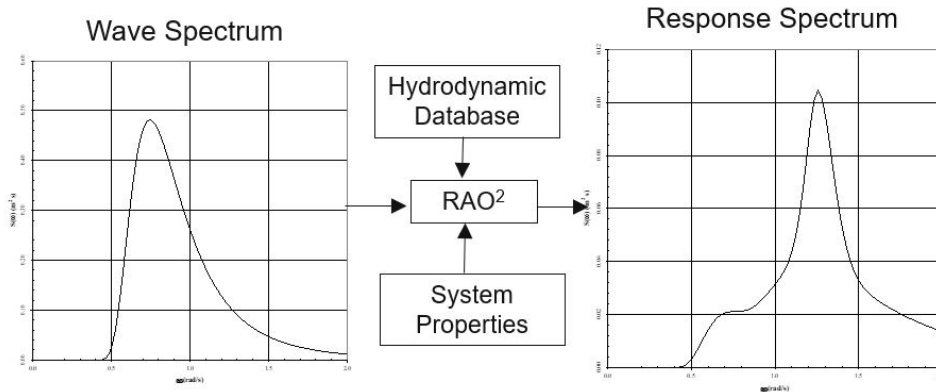


Figure 2.12: Solving equations of motion in the frequency domain [8]

The frequency depended added mass, damping and frequency and direction dependent wave forcing of the system are however required to solve the equations of motions and thus to obtain the RAO's. These hydrodynamic properties can be derived by different methods. The most common theories are [8]:

- Model tests: expensive and time consuming
- Morison's theory: suitable for structures with slender members. Example: jackets
- Strip theory: suitable for slender vessels, but not applicable for complicated shapes
- Panel method: suitable for general vessel shapes

Strip theory is only suitable for slender vessels which are vessels that can cruise at significant forward speeds. SSCV's don't belong in this category of ships so the panel method is used. The panel method is based on potential theory. An explanation of potential theory is presented in appendix A.

### 2.5.1 Panel method

To obtain the hydrodynamic properties of vessel hull shapes the panel method can be used. With the panel method the flow around a body is calculated based on Green's integral theorem [47] [48] [49]. Following Green's integral theorem, it is possible to transform a three-dimensional linear homogeneous differential equation into a two dimensional integral equation. In the context of the panel method this is used to transform Laplace's three-dimensional potential equation to a surface integral equation. This is known as Green's identity. The body surface is divided in N panels small enough to assume that the sources and dipoles strength and the fluid pressure is constant over each element, see figure 2.13. For every panel a source or dipole strength has to be found. A dipole is a source and a sink for which the distance between the source and sink approaches zero.

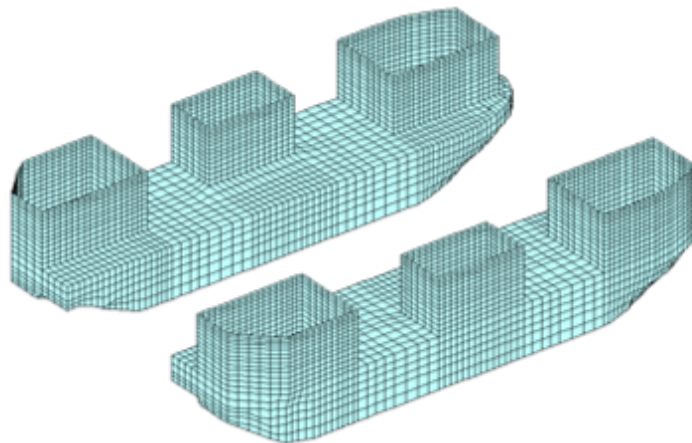


Figure 2.13: Hull SSCV discretized into panels [8]

The following requirements and boundary conditions have to be satisfied [5]:

- Conservation of mass: satisfaction of the Mass Continuity equation
- The seabed is watertight
- The vessel is watertight
- Free surface dynamic boundary condition: pressure at the free surface is equal to the atmospheric pressure
- Free surface kinematic boundary condition (no leak condition): the vertical velocity of a water particle at the free surface of the fluid is identical to the vertical velocity of the free surface itself; a water particle at the surface will stay at the surface
- The potential values tends to zero far away from the body

For derivations of the boundary conditions, a reference is made to [5], chapter 5, 7, 8. For a more elaborate explanation of potential theory, see appendix A. By using the boundary condition of tangential flow, the no-slip boundary condition: The normal component of velocity is fixed at zero, and the tangential component is set equal to the velocity of the hull [50], the unknown strength of the sources and dipoles can be solved. If the strength of each dipole or source is found, the velocities and the resulting forces can be determined on the hull surface. To find the velocities on the hull surface, generally the problem is split up in two parts. The radiation problem: The vessel oscillates in still water and the wave/diffraction problem: The vessel is restrained in the waves. Together they give the motion of the vessel in the waves. This was shown in figure 2.10 for a more general shape.

The hydro-mechanic loads are found by letting the vessel move in still water. This results in a radiation of waves from the vessel. The resulting hydrodynamic loads are the dynamic forces and moments caused by the fluid on the oscillating body. These forces can be calculated by solving the radiation potential. This will result in the added mass and potential damping of the vessel which is required to solve the equations of motion of the vessel as explained in chapter 2.4.1.

To find the wave forces, the vessel is held still in the waves. The exciting forces and moments are produced by waves coming in on the restrained body. The wave force consist out of the Froude-Krilov wave force and the diffracted wave force. The first order wave forces follow from the linearised pressure in the fluid. The pressure in the fluid follows can be found with the linearised Bernoulli as shown in equation 2.12. The Froude-Krilov force or moment is calculated by an integration of the directional pressure gradient in the undisturbed wave over the cross sectional area of every panel on the hull. A part of the waves however, will be diffracted due to the shape of the vessel. This requires a correction of this Froude-Krilov force. As the diffraction potential is not known, this is still hard to solve.

However, Green's second theorem provides a relation between the diffraction and radiation potential, which results in the Haskind relations. The relations underlie the relative motion (displacement - velocity - acceleration) hypothesis. These relations are only valid for a floating body with a zero time averaged speed in all directions [51].

With the Haskind relations, the first order wave forces and moments on the restrained body in waves are only depended on the wave- and radiation potential which makes the problem solvable. A more elaborate explanation of the wave-, radiation- and diffraction potentials can be found in [5] chapter 7.

The main advantage of the panel method therefore is that the problem is reduced to a two-dimensional (surface) problem instead of a three-dimensional (volume) problem. Besides this the creation of the grid is also reduced to a 2D problem: the panel grid only has to be created on the hull of the body. This results in faster computation time as now instead of  $N^3$  equations only  $N^2$  equations have to be solved to determine the velocity field. The quality of the results depends on the size and the number of panels used to simulate the vessel hull. As it is assumed that source and dipole densities are constant over each element, also the fluid pressure is constant over each element. Therefore, for areas where the flow changes rapidly there are more panels required to correctly simulate the flow changes.

A few disadvantages of the panel method are:

- The numerical solution for the velocities at a panel located at a sharp corner is never satisfactory. The assumption of constant source/dipole density and velocity potential over an element at a sharp corner is not true in reality.
- The panel method has trouble with extreme waves. However, given the low weather limits for suspended transports, this is not considered to be an issue.
- The panel method has trouble with large volumes just above/below the waterline and has problems with large volumes near the seabed. This will be addressed in 2.5.3.
- Another problem with the standard panel method is that it is only suitable for 0 forward speed. The reason is that in general potential coefficients are determined in a coordinate system in which the origin(O) and CoG (G) is in the waterline. This results in a required correction with a lever arm  $\overline{OG}$  between CoG of the moving vessel(G) and the origin of the potentials in the waterline [5]. This will be accounted for in this research by omitting the need of a diffraction analysis which is addresses in the next chapter.

## 2.5.2 The forward speed problem

A vessel with forward speed 'feels' the waves differently than a stationary vessel. This is called a Doppler Shift: the change in frequency of a wave in relation to an observer (the vessel) who is moving relative to the wave source. The steadily translating coordinate system  $O(x, y, z)$  is moving forward at the ship's speed  $V$ , instead of staying stationary. This is shown in figure 2.14. This has implications for an analysis of a moving vessel in the frequency domain. For the different wave directions this results in:

$\omega_e > \omega$  = Sailing into the waves, head waves (higher frequency)

$\omega_e = \omega$  = Sailing perpendicular to the waves, beam waves (frequency unchanged)

$\omega_e < \omega$  = Sailing along the waves, stern waves (lower frequency)

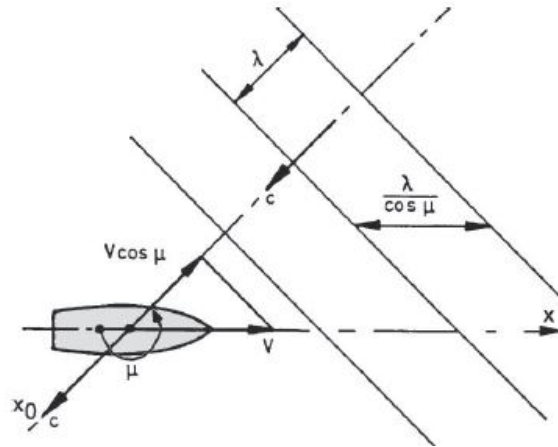


Figure 2.14: A moving vessel encounters frequencies differently due to a translating coordinate system [5]

For deep water the encounter frequency can be found following equation 2.35.

$$\omega_e = \omega - \frac{\omega^2}{g} \cdot V \cdot \cos\mu = \omega \cdot \left(1 - \frac{V}{c} \cos\mu\right) \quad (2.35)$$

*using  $c = \frac{g}{\omega}$*

With:

- $\omega$  = Wave frequency in a fixed reference frame [rad/s]
- $\omega_e$  = Frequency of encounter in a moving reference frame [rad/s]
- $V$  = Forward speed vessel [m/s]
- $c$  = Wave celerity [m/s]
- $\mu$  = Ship heading relative to wave direction [rad]

Within HMC, the panel method is used in the diffraction software of WAMIT (appendix K.2). As explained in chapter 2.5.1, a vessel with forward speed means that the diffraction analysis has to be adjusted for forward speed of the vessel. Within HMC, a way (unproven) to take the forward speed into account is to let the vessel stay in position and adjust the wave spectrum and wave forces, so that the sailing of the vessel is 'mimicked' instead of letting the vessel actually sail.

To do this the following steps are taken:

- Move the wave energy from the original frequency to the encounter frequency
- Take the wave force equal to the original frequency of the wave spectrum. Only the oscillation period in which the wave is felt changed. The geometry of the wave didn't change so it is assumed the wave force didn't change. This is shown in the top figure of 2.15. It is noted that the added mass and damping don't need to be corrected. The vessel will be oscillating with the encounter frequency, so the radiation forces should be taken for this frequency. This is shown in the bottom figure of 2.15

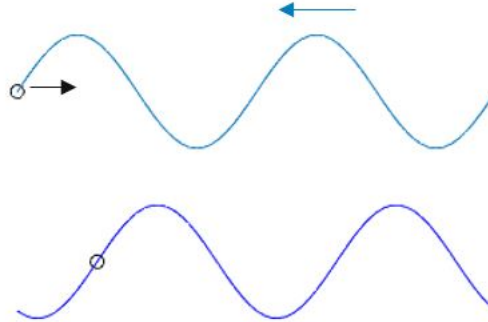


Figure 2.15: Top figure: adjust wave forces to original frequency  
 Bottom figure: vessel oscillates with encounter frequency [9]

The energy over the wave spectrum should not change by transforming the original wave spectrum to the encounter wave spectrum. In combination with the formula for the encounter frequency in deep water this results in a solution to transform the original wave spectrum to the encounter wave spectrum of the vessel with forward speed as in equation 2.36.

$$S_{\zeta}(\omega_e) \cdot d\omega_e = S_{\zeta}(\omega) \cdot d\omega \rightarrow S_{\zeta}(\omega_e) = \frac{S_{\zeta}(\omega)}{\frac{d\omega_e}{d\omega}} \quad (2.36)$$

$$\text{Deep water : } \omega_e = \omega - \frac{\omega^2}{g} V \cdot \cos\mu \rightarrow \frac{d\omega_e}{d\omega} = 1 - \frac{2\omega V \cdot \cos\mu}{g}$$

The adjustments of the wave forcing in the diffraction analysis and the shifting of the wave energy results in adjusted RAOs and an adjusted wave spectrum for forward speed. The difference between not adjusting the RAOs and wave spectrum is shown in an example in figure 2.16 for head waves and stern waves to the vessel. It can clearly be seen that the 'mimicking' of the vessel speed influences the wave spectrum and in this case the RAO of heave of the vessel.

A concern with this method is that it assumes that the wave forces, added mass and potential damping don't change for a moving vessel in respect to a stationary vessel. The vessel acquires forward speed and as a result another potential has to be taken into account, an approximately steady flow potential. Therefore, the wave forces, the added mass and the radiation damping are expected to be different from the case in which the vessel is not sailing [52] [5]. Besides this, the standard panel method is still used which is only suitable for 0 forward speed. The required correction with a lever arm  $\overline{OG}$  between CoG of the moving vessel (G) and the origin of the potentials in the waterline (O) is therefore not applied [5]. It is also still not common practice within HMC to fully apply this method to take into account the forward speed effect. The adjustment of the wave forces obtained from the diffraction analysis is often not applied and only the wave spectrum is adjusted to take into account the forward speed of the vessel.

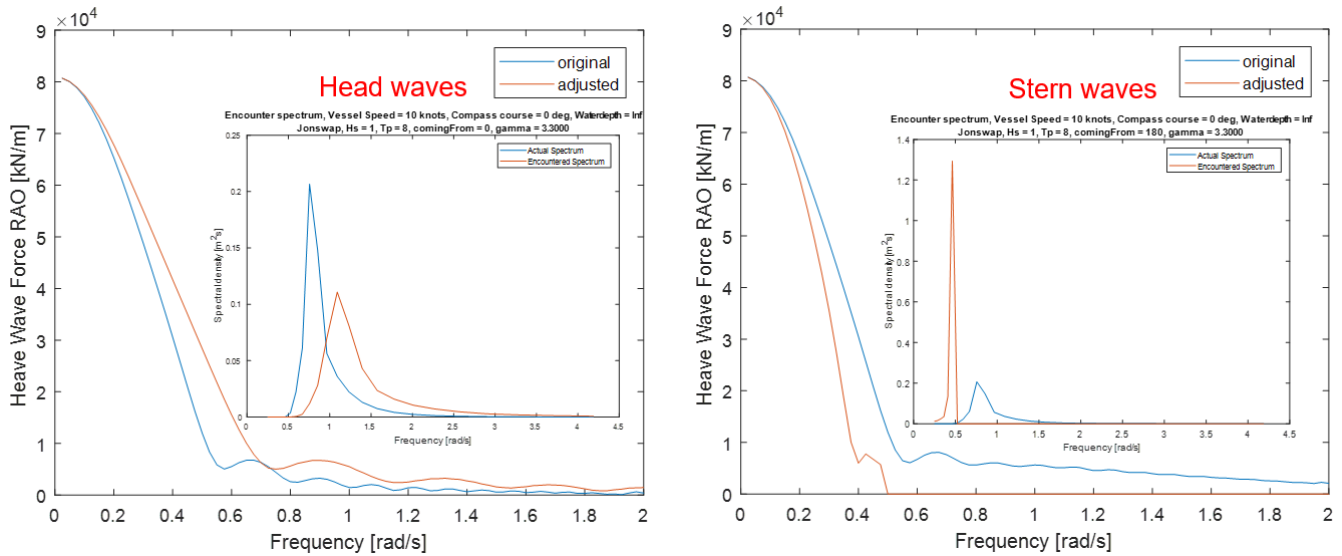


Figure 2.16: Left figure: adjusted Heave RAO and encounter spectrum for head waves  
 Right figure: adjusted Heave RAO and encounter spectrum for stern waves [9]

With or without adjustment of the wave spectra and RAO's, stronger non-linear viscous effects due to a sailing vessel are still not captured within the panel method as it uses linear potential flow theory and therefore assumes no viscous effects.

More severe drag is expected for a moving vessel due to more flow separation while sailing. After the flow separation point, the flow no longer adheres the surface of the body which results in that the skin friction drag is almost zero. At the same time, however, the pressure drops considerably due to the energy dissipation in the turbulent wake. This leads to a significant increase in pressure drag, which is far greater than the reduction in skin friction drag. Therefore, the total drag thus increases very strongly in the event of more flow separation [5].

Due to the more severe effects of drag it is harder to model moving vessels in respect to stationary vessels [53] [54]. These viscous non-linear effects can be obtained from model tests and added in linearized form to Liftdyn models by spring and damping matrices. These are however not always readily available for every situation and are often obtained for a vessel that is stationary.

Due to the combination of all these possible inaccuracies due to the forward speed effect it is therefore preferred to find a method which omits the translation from waves to vessel motions. This method is proposed in chapter 3.

### 2.5.3 Inconvenient draft problem

During most suspended transports, HMC vessels are sailing on a relatively high draft for fuel efficiency purposes. During the X suspended transport, Sleipnir mostly sailed at a draft of 16.8m, whilst the maximum draft is approximately 32m and the minimum draft is approximately 12m. For SSCVs, the hull of the vessels consists out of two pontoons (fig 2.13).

Due to the high sailing draft during suspended transport, the pontoons are relatively close to the water surface and there is therefore only a shallow water layer on the pontoons of the vessel. The panel method using potential theory finds that resonances in the fluid occur due to this shallow water layer. Within the diffraction analysis therefore very high wave heights and resulting high wave forces on the vessel are predicted. The over-prediction of the wave forces on the vessel hull in turn over-predict the motions of the vessel. Depending on the wave climate, the 'inconvenient draft' of Sleipnir in which the diffraction software over-predicts the wave heights, lays approximately between 12-19m draft of the vessel. In reality, non-linear phenomena such as wave breaking and turbulence are apparent. These limit the actual wave height on top of the pontoons and causing a different behavior of the fluid at the specific domain.

In addition, the pontoons can also be fully or partly submerged depending on the instantaneous surface elevation and the vessel displacements. This results in that the water-plane area is not constant and non-linearity's appear in the stiffness terms of the equations of motion. Under these specific circumstances, technically speaking there is no set of RAO's able to correctly describe the vessel behavior because the system is nonlinear instead of linear.

To solve the problem in a linear system, the resonance in the fluid found by the panel method can be suppressed using a damping lid [55] [56]. The damping parameter  $\epsilon$  does not correspond to a tabulated physical property of water. The value used, should therefore be informed by experimental or measured data in a similar system to that being modelled. Within HMC there is currently no diffraction software available that includes a damping lid into the diffraction analysis. These calculations are therefore outsourced and there are currently only two diffraction analyses with damping lid available (draft = 14.5m & 16.8m). This greatly reduces the availability of sailing drafts during suspended transport as only two sailing drafts can be modelled with enough accuracy. Besides this, the selected strength of the damping lid influences the results and currently within HMC the exact accuracy of the diffraction analysis with damping lid is unknown.

Due to the inaccuracies that the forward speed problem and inconvenient draft problem induce on the system it is therefore preferred that a method is created which can obtain motions and forces at locations of the system which is not depended on the hydrodynamic properties of the vessel during suspended transport. This method is proposed in chapter 3.

## 2.6 Overview fatigue requirements

Fatigue calculations require two main inputs. The first is the actual loading at the point of interest (boom pivots) and the second is the resistance strength of that point of interest to the loading. In practice this results in the following steps which are required to determine the fatigue damage at a point of interest:

1. The weight of the suspended jacket generate stresses at the point of interest.
2. The stresses are evaluated by their magnitude and number of cycles by a counting method
3. The resistance of the object is defined by an S-N Curve which is a measure of the materials ability to resist the amount of stress cycles at a certain magnitude
4. The stress cycles and S-N curves are evaluated by Miner's Rule to give an indication of the induced fatigue damage

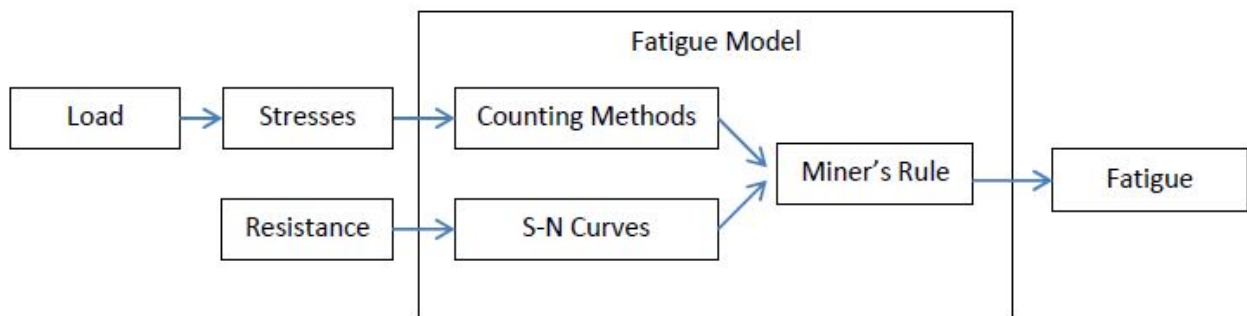


Figure 2.17: Overview of the requirements for a fatigue calculation at a point of interest [10]

### 2.6.1 Rayleigh counting method

The Rayleigh counting method can be used in the frequency domain. The Rayleigh method assumes that the stress cycles only cover a narrow range of frequencies. When applied to a broadband spectra, the Rayleigh method will predict the damage value of an equivalent ideal narrow process with the same variance and a number of peaks equal to the number of up-crossings of the mean level of the real broadband process [57].

While doing so, it over estimates the fatigue damage. This mainly originates from an over-estimation of the probability of large stress cycles [58]. Some therefore propose to apply a correction (mostly reduction) factor to better approximate the rain-flow damage intensity [59].

The Rayleigh distribution assumes that the probability density of the stress range  $\sigma_r$  only depends on the zeroth spectral moment of the stress spectrum and is given in equation 2.37 [7].

$$\begin{aligned}
 p_{RAY}(\sigma_r) &= \frac{\sigma_r}{4m_0} \cdot \exp\left(-\frac{\sigma_r^2}{8m_0}\right) \\
 m_n &= \int_0^\infty \omega^n \cdot S_{\sigma\sigma}(\omega) d\omega = n^{th} \text{ spectral moment of stress} \\
 \sigma_0 &= \sqrt{m_0} \\
 Cdf_{RAY}(\sigma_r) &= 1 - \exp\left(-\frac{\sigma_r^2}{8m_0}\right)
 \end{aligned} \tag{2.37}$$

## 2.6.2 S-N curve

The resistance of the boom pivots can be quantified with an S-N curve. The S-N curve dictates the number of cycles the boom pivots which have a certain geometry can take before failing. S-N curves are derived by fatigue testing of small specimens in test laboratories where they are tested at constant stress levels until failure occurs. Failure is defined as being crack growth going fully through the thickness. It is however more complex to derive design S-N curves for real structures than by simple mathematical regression of test data for derivation of S-N curves. The main reason for this is the lack of relevant fatigue test data for structures [11]. Test specimens do not have the same amount of residual stresses as a full scale structure. The test data may also belong to different R-ratios  $R = \frac{\sigma_{min}}{\sigma_{max}}$  [11].

Furthermore, the small scale test specimens are most often more perfect (having less defects) than real structures [11]. To account for this, the design S-N curves in [11] are based on the mean-minus-two-standard-deviation curves for relevant experimental data. This result in that the The S-N curves are thus associated with a 97.7 % probability of survival.

The basic design S-N curve is given as in equation 2.38:

$$\log(N) = \log(\bar{a}) - m \cdot \log(\Delta\sigma) \tag{2.38}$$

Where:

- $N$  = Predicted number of cycles to failure for stress range
- $\Delta\sigma$  = Stress range [MPa]
- $m$  = Negative inverse slope of S-N curve
- $\log(\bar{a})$  = Intercept of log N-axis by S-N curve

$$\log(\bar{a}) = \log(a) - 2 \cdot s_{\log(N)} \tag{2.39}$$

Where:

- $\log(a)$  = Intercept of mean S-N curve with the log N axis
- $2 \cdot s_{\log(N)}$  = Standard deviation of log N

The fatigue strength of welded joints is also to some extent dependent on plate thickness. This effect is coming from the local geometry of the weld toe in relation to thickness of the ad-joint plates. The fatigue strength of welded joints is also dependent on the stress gradient over the thickness. The thickness effect is accounted for by a modification of the stress range such that the design S-N curve for thickness larger than the reference thickness (in this case 25mm) can be found as in equation 2.40:

$$\log(N) = \log(\bar{a}) - m \cdot \log\left(\Delta\sigma\left(\frac{t}{t_{ref}}\right)^k\right) \quad (2.40)$$

Where:

- $\log(a)$  = Intercept of mean S-N curve with the log N axis
- $t_{ref}$  = Reference thickness equal 25 mm for welded connections other than tubular joints. For tubular joints the reference thickness is 16 mm
- $t$  = Thickness through which a crack will most likely grow.  $t = t_{ref}$  is used for thickness less than  $t_{ref}$
- $k$  = Thickness exponent on fatigue strength as given in [11] Table 2-1, Table 2-2, Table 2-3 and Table 2-4.

The thickness exponent therefore accounts for different size of plate through which a crack will most likely grow. To some extent the thickness exponent also accounts for local geometry at the weld toe. What should be noted is that it does not account for a different weld length or different length of the component than tested [11]. The D S-N curve allows for the least amount of undercuts at the weld toes. This is therefore a safe curve, as most fatigue cracks are initiated from undercuts at weld toes [11]. It is therefore always recommended to prepare a good welding procedure to avoid large undercuts during production welding.

An example of crack growth through a plate thickness of 25 mm is shown for S-N curve F, C and D in figure 2.18. It is observed that larger surface defects can be accepted for an F curve detail than for a D- and C curve detail. This shows the importance of the correct selection of the detail class in [11], to obtain the correct SN curve which represents the resistance of detail.

## 2.7 Miner's damage rule

The S-N curves are based on constant stress amplitude tests. The counting method has determined the amount of times stress cycles with different stress amplitudes have occurred. The S-N curves can therefore not directly be used with the counting method. In order to still be able to quantify the fatigue damage, Palmgren-Miner's rule for linear fatigue damage accumulation is used, which combines both the S-N curves and the counted cycles [60]. In the counting method the random stress signal has been reduced to information on how many times a cycle of a certain stress level has occurred.

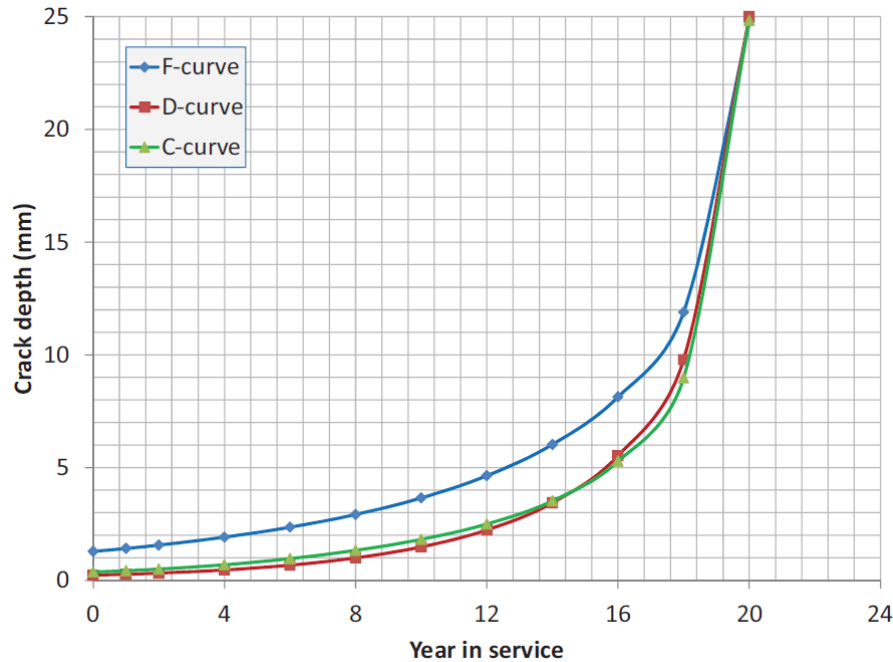


Figure 2.18: Crack growth development for three different S-N curves [11]

The linear damage rule, developed by Palmgren in 1924 and adapted by Miner in 1954, states that the total damage a structure is experiencing, may be expressed as the accumulated damage from each load cycle at different stress levels, independent of the sequence in which the stress cycles occur [60]. The rule evaluates how much each stress block, containing a certain number of cycles with a certain magnitude, consumes from the allowed number of cycles for each stress block and sums that over the total number of stress blocks. When the accumulated damage  $D$  reaches the usage factor (mostly 1), the structure fails.

The rule is given in equation 2.41 [11].

$$D = \sum_{i=1}^k \frac{n_i}{N_i} \leq \eta \quad (2.41)$$

With:

$D$  = Accumulated fatigue damage

$k$  = Number of stress blocks

$n_i$  = Number of stress cycles in stress block  $i$  found by counting method

$N_i$  = Number of cycles to failure at constant stress range  $\Delta\sigma_i$  from S-N curve

$\eta$  = Usage factor, mostly 1 but may vary

= 1/design fatigue

There are however several major limitations to Miner's rule:

- The rule doesn't take the probabilistic nature of fatigue into account and there is also no simple way to relate fatigue life predicted by the rule with the characteristics of a probability distribution. Therefore industry analysts often use design curves which are adjusted for scatter to calculate  $N_i$  [11]
- The rule implies that damage accumulation is independent of the mean stress level. This does not correspond to observed behavior. In reality stress cycles at mean tensile stress will cause more fatigue than the same cycle at mean compressive stress [61]
- The rule does not account for the sequence in which high and low stress cycles are applied to a structure. This however does affect the fatigue life of the structure. In some circumstances, cycles of low stress followed by high stress cause more damage than would be predicted by the rule [62]. The rule does not consider the effect of an overload or high stress which may result in a compressive residual stress that may delay crack growth. High stress followed by low stress may therefore have less damage due to the presence of a compressive residual stress [62].

Despite these limitations, Miner's Rule is still the standard in the Offshore Industry [11] as it is able to solve the assumed linear cumulative damage efficiently.

# Chapter 3: Modelling approach

## 3.1 TF A2B Method

The only way to obtain the occurred forces at the boom pivots during a past suspended transport, is to use a validated Liftdyn model of that suspended transport to obtain force RAO's at the boom pivots. The reason for this is that no strain gauges were installed at the boom pivots during any suspended transport. To validate the Liftdyn model of a past suspended transport, measured vessel and jacket motions during the analysed suspended transport can be used to verify calculated results by a proposed method. One of the goals during this research is therefore to create a method which in combination with a model is able to calculate the motions of the suspended jacket. These calculated jacket motions can then be compared to the measured jacket motions recorded during the suspended transport. The Liftdyn model of the selected suspended transport is validated if the results of this comparison match quite accurately. With this validation it is possible to extract the required force RAO's at the boom pivots out of the Liftdyn model. It is assumed that these force RAO's are then also correct (indirectly proven). An overview of this total process is shown in figure 3.1

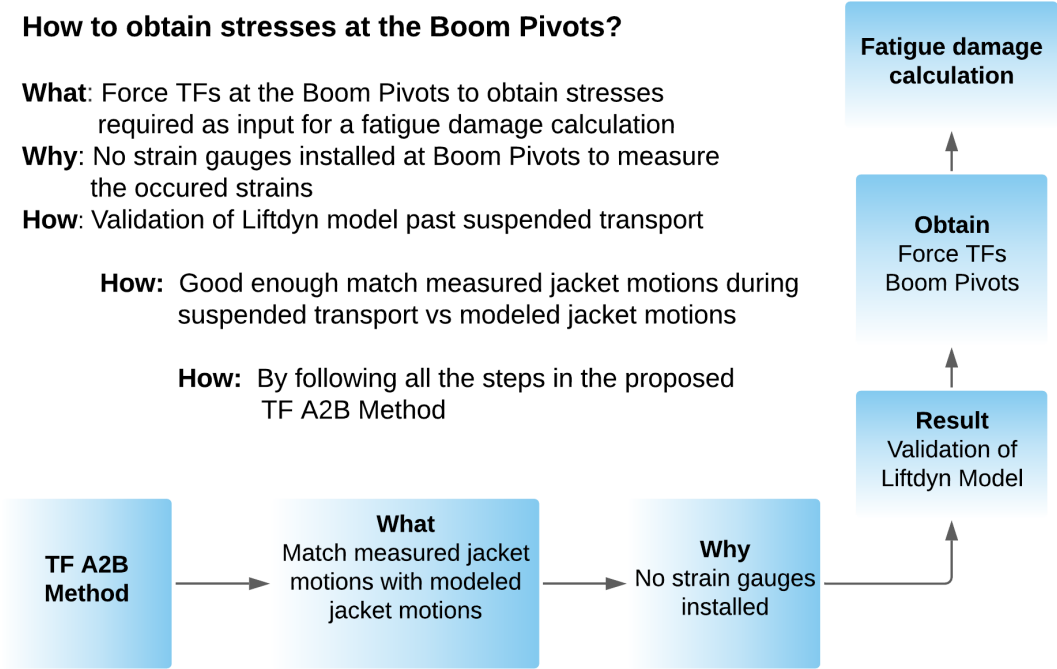


Figure 3.1: Steps required to obtain the force TFs at the boom pivots

Before the measured jacket motions during suspended jacket can be used, a method needs to be proposed. The forward speed and inconvenient draft problem make a common approach method with wave forecasted data and corresponding wave loads as input potentially inaccurate. There is low confidence that due to the many uncertainties at play at the same time, the model would be able to calculate the real measured jacket motions correctly as all the uncertainties influencing the hydrodynamic properties of the vessel cannot yet be fully captured by HMC. Therefore, it has been decided to instead develop a method which is using measured vessel motions as main input for the model instead of wave forecasted data and corresponding wave loads which rely on the hydrodynamic properties of the system. This method is called the TF A2B Method. This method will have a few advantages:

- The first advantage is that if fully validated, it is possible to use Sleipnir's measured motions to make a prediction of the jacket motions, without having to measure the jacket motions for every transport. This would save time offshore, which saves money.
- Already created Liftdyn models of the suspended transport can be used instead of complicated, unavailable FEM models of the suspended transport. This also saves time and money. Besides this, run-times of Liftdyn are rather quick (1 min) making it an efficient tool. In combination with efficient Matlab scripts this can save a lot of time during every design phase of a suspended transport.
- More motions can be captured. The motion sensors on the vessel (MRU) capture any motion of the vessel in the degree of freedom for which the sensor is designed for within the capabilities of the sensor. If a wave spectrum and diffraction analysis is used to find the vessel motions, only motions due to first order wave forces are found as these are the only wave forces captured by the diffraction analysis. Besides this, the uncertainty of the actual wave spectrum is not relevant anymore.
- The hydrodynamic properties of the vessel are not required for the method as it directly uses the measured vessel motions. The step from wave to vessel response is therefore omitted. The inaccuracies due to the inconvenient draft problem are therefore solved for this problem. This result in that the uncertain accuracy of the damping lid diffraction analysis is omitted
- The effect of the forward speed on the hydrodynamic properties of the vessel is omitted:
  - More severe nonlinear viscous effects of drag due to flow separation don't have to be taken into account. Therefore, no model tests are required which saves money.
  - The standard panel method used within HMC which is only suitable for 0 forward speed doesn't have to be adjusted.
  - The steady flow potential due to the forward speed doesn't have to be accounted for.
  - The unproven method within HMC to take into account the forward speed is not required: the wave spectra don't have to be adjusted for forward speed. The wave forces in the diffraction analysis don't have to be adjusted for forward speed.

## 3.2 Overview hypotheses & validation tests

The TF A2B Method assumes that a suspended transport can be considered as a stationary and linear condition, i.e. the system's behavior does not significantly change in time. Any non-linear effects, such as frictional damping, and nonlinear pendulum motions can be adequately accounted for by a linear representation having almost the same effect. This justifies the use of frequency domain analysis approach, which allows for the dynamic behavior to be described by transfer functions (RAO's) and provides valuable insight in the dynamic behavior through a mode shape analysis. To accept that the method works, several hypotheses (H) have to be proven. Also several validation tests (VT) are set up. An overview of all hypotheses and validation tests that will be used discussed in this chapter is given below:

- A set of transmissibility functions can be found for an unrestrained vessel which can correctly transfer motions from location A to motions at location B by using RAO's obtained from Liftodyn. [H1]
- A set of transmissibility functions can be found for a restrained vessel which can correctly transfer motions from location A to motions at location B by using RAO's obtained from Liftodyn.. [H2]
- The set of restrained transmissibility functions are not significantly dependent on the hydrodynamic properties of the system [H3] and are therefore almost equal for every draft. [VT1]
- The created, restrained set of transmissibility functions [6x6] between point A and B (TFs A2B) multiplied with the unrestrained set of RAO's [6x1] from waves to A (W2A), results in the set of RAO's [6x1] from waves to B (W2B) for point A and B on the same rigid body. [VT2]
- The response of all six motions at B on the same rigid body as A, found by using the restrained transmissibility functions [6x6] (TFs A2B) in combination with the response at A, is equal to the set of responses at B found by the unrestrained set of RAO's [6x1] from waves to B in combination with the wave spectrum (W2B) [VT3]
- The created, restrained set of transmissibility functions [6x6] between point A and B (TFs A2B) multiplied with the unrestrained set of RAO's [6x1] from waves to A (W2A), results in the set of RAO's [6x1] from waves to B (W2B) for point A and B **not** on the same rigid body. [VT4]
- The response of all six motions at B **not** on the same rigid body as A, found by using the restrained transmissibility functions [6x6] (TFs A2B) in combination with the response at A, is equal to the set of responses at B found by the unrestrained set of RAO's [6x1] from waves to B (W2B) in combination with the wave spectrum [VT5]

After proving the hypotheses and perform the validation tests it is assumed that the TF A2B Method can accurately describe motions at location B by using motions at location A.

## 3.3 Prove of hypotheses

### 3.3.1 Unrestrained transmissibility functions [H1]

To obtain jacket motions from vessel motions, the mathematical theory in equations 3.1 is used as the basis of the method. In this example, the response of the z motion of the generic points A and B are found. The theory in 3.1 must be true for any chosen point A or B on the vessel. In this thesis, location A is the MRU of the vessel. This is the location on the vessel where most motions are measured. Location B can be any other point on the vessel. In this thesis location B is either the control point (CP) of the vessel or the jacket sensor (JS) located on the jacket (see 2.1).

$$\begin{aligned}
 S_{\zeta}(\omega) \cdot RAO_{\zeta, z_A}^2 &= S_{z_A}(\omega) [1] \\
 S_{\zeta}(\omega) \cdot RAO_{\zeta, z_B}^2 &= S_{z_B}(\omega) [2] \\
 S_{z_A}(\omega) \cdot TF_{z_A, z_B}^2 &= S_{z_B}(\omega) [3] \\
 S_{\zeta}(\omega) \cdot RAO_{\zeta, z_A}^2 \cdot TF_{z_A, z_B}^2 &= S_{\zeta}(\omega) \cdot RAO_{\zeta, z_B}^2 [4] \\
 TF_{z_A, z_B} &= \frac{RAO_{\zeta, z_B}}{RAO_{\zeta, z_A}} [5] \\
 RAO_{\zeta, z_B} &= TF_{z_A, z_B} \cdot RAO_{\zeta, z_A} [6]
 \end{aligned} \tag{3.1}$$

1. In equation 3.1 [1], first the response of the z motion of A (MRU) is found. A created Jonswap spectrum is multiplied with the RAO from waves to z motion at A (MRU) squared, to obtain the response of the z motion at A (MRU) in the frequency domain. This is a standard frequency domain calculation used in the offshore industry to obtain the response in a degree of freedom of a point of interest.
2. In equation 3.1 [2], a created Jonswap spectrum is multiplied with the RAO from wave to z motion at B (CP or JS) squared, to obtain the response of the z motion at B (CP or JS) in the frequency domain.
  - As the proposed method is using vessel motions as input to finally obtain the jacket motions, a set of transmissibility functions is required from location A to location B.
3. In equation 3.1 [3], the response spectrum of z at A (MRU) is multiplied with the transmissibility function z at A (MRU) to z at B (CP or JS) squared. This results in the same response of z at B as in [2]. This is the basis of the TF A2B Method. The motions at A are known and the motions at B are known. To find the motion in z at B by using the response in z at A, the unknown transmissibility function between those responses has to be found.
4. This results in that equation [3] has to be rewritten to find the unknown TF z at A (MRU) to z at B (CP or JS). The left hand-side of equation [1] can be inserted for the response of z at A (MRU) in equation [3] and the left hand-side of equation [2] can be inserted in the right hand side of equation [3] for the response of z at B. This results in equation [4]. The only unknown in this equation is the TF z at A (MRU) to z at B.

5. The required transmissibility function [5] from  $z$  at A (MRU) to  $z$  at B can then be found from rearranging equation [4]. It should be noted that after rearranging, the influence of the hydrodynamic properties of the vessel are removed from the equation of the TF [5]. The influence of the hydrodynamic properties of the vessel on this TF is therefore removed.
6. Equation [6] is a rearrangement of [5] used to prove that a model should be able to re-obtain the RAO from waves to  $z$  at B by using the new, transmissibility function, multiplied with the RAO from waves to  $z$  at A (MRU).

The TF A2B Method just described, can be used for any point A related to another point B on the ship or jacket. The method described in equation 3.1 must however be expanded to be used with measured data.

### 3.3.2 The TF A2B Method [H2]

To find the response of any degree of freedom at location B (DOF B), the response of a degree of freedom at location A (DOF A) is multiplied with the transmissibility function squared (TF A2B), see equation 3.2.

$$S_{DOF_B} = TF_{DOF_A, DOF_B}^2 \cdot S_{DOF_A} \quad (3.2)$$

To get a better grasp on which motion at location A is influencing a motion at location B, it is required to restrain all other motions of the vessel in location A, **except** for the chosen degree of freedom at A. The reason for this is the coupling of motions within the system. Normally, a vessel moves in all six degree of freedom at the same time. Due to the interaction between the sea and the vessel this results in that in every motion of the vessel there is also a contribution of other motions of the system (2.4.2). See equation 2.22 for the coupling of symmetric motions Surge, Heave and Pitch and equation 2.23 for anti-symmetric coupled motions Sway, Roll and Yaw due to the waves acting on a vessel with a vertical-longitudinal plane of symmetry.

The motions of the suspended jacket in 1 degree of freedom can be influenced by six degrees of freedom of the vessel as it is a system with multiple rigid bodies connected with springs, dampers and hinges. By restraining five of the six motions at the MRU it is possible to find how much the unrestrained motion at the MRU influences the six motions at the jacket sensor as all coupling terms with other motions at the MRU are removed. The following steps have to be taken in Liftdyn to obtain the restrained transmissibility functions:

1. The motions are uncoupled by placing a restraint at location A. This restrains the vessel from moving in every motion, except for the motion which is chosen in the joint section of Liftdyn at location A.
2. This motion at A can then be used to describe the six motions of location B. This results in that the TFs of the chosen unrestrained degree of freedom are fully uncoupled.

3. To fully capture all motions of location B, the restraint has to be changed six times, namely for every degree of freedom at location A. This will finally result in 2\*6x6 matrices with all possible RAO's. One 6x6 matrix for all RAO's from waves to DOFs at location A and one 6x6 matrix for all RAO's from waves to DOFs location B.
4. To obtain the transmissibility functions between A and B, the set of RAO's have to be divided as in equation 3.1 [5]. This will result in a transmissibility function matrix as in equation 3.3.

$$TFs_{A2B} = \begin{pmatrix} \begin{array}{c} \text{Vessel unrestrained in X} \\ \frac{RAO_{\zeta,x_B}}{RAO_{\zeta,x_A}} \\ \frac{RAO_{\zeta,y_B}}{RAO_{\zeta,y_A}} \\ \frac{RAO_{\zeta,z_B}}{RAO_{\zeta,z_A}} \\ \frac{RAO_{\zeta,rx_B}}{RAO_{\zeta,rx_A}} \\ \frac{RAO_{\zeta,ry_B}}{RAO_{\zeta,ry_A}} \\ \frac{RAO_{\zeta,rz_B}}{RAO_{\zeta,rz_A}} \\ \frac{RAO_{\zeta,x_A}}{RAO_{\zeta,x_B}} \end{array} & \begin{array}{c} \text{Vessel unrestrained in Y} \\ \frac{RAO_{\zeta,x_B}}{RAO_{\zeta,y_A}} \\ \frac{RAO_{\zeta,y_B}}{RAO_{\zeta,y_A}} \\ \frac{RAO_{\zeta,z_B}}{RAO_{\zeta,y_A}} \\ \frac{RAO_{\zeta,rx_B}}{RAO_{\zeta,ry_A}} \\ \frac{RAO_{\zeta,ry_B}}{RAO_{\zeta,ry_A}} \\ \frac{RAO_{\zeta,rz_B}}{RAO_{\zeta,ry_A}} \\ \frac{RAO_{\zeta,y_A}}{RAO_{\zeta,x_B}} \end{array} & \begin{array}{c} \text{Vessel unrestrained in Z} \\ \frac{RAO_{\zeta,x_B}}{RAO_{\zeta,z_A}} \\ \frac{RAO_{\zeta,y_B}}{RAO_{\zeta,z_A}} \\ \frac{RAO_{\zeta,z_B}}{RAO_{\zeta,z_A}} \\ \frac{RAO_{\zeta,rx_B}}{RAO_{\zeta,rz_A}} \\ \frac{RAO_{\zeta,ry_B}}{RAO_{\zeta,rz_A}} \\ \frac{RAO_{\zeta,rz_B}}{RAO_{\zeta,rz_A}} \\ \frac{RAO_{\zeta,z_A}}{RAO_{\zeta,x_B}} \end{array} & \begin{array}{c} \text{Vessel unrestrained in Rx} \\ \frac{RAO_{\zeta,x_B}}{RAO_{\zeta,rx_A}} \\ \frac{RAO_{\zeta,y_B}}{RAO_{\zeta,rx_A}} \\ \frac{RAO_{\zeta,z_B}}{RAO_{\zeta,rx_A}} \\ \frac{RAO_{\zeta,rx_B}}{RAO_{\zeta,rx_A}} \\ \frac{RAO_{\zeta,ry_B}}{RAO_{\zeta,rx_A}} \\ \frac{RAO_{\zeta,rz_B}}{RAO_{\zeta,rx_A}} \\ \frac{RAO_{\zeta,rx_A}}{RAO_{\zeta,x_B}} \end{array} & \begin{array}{c} \text{Vessel unrestrained in Ry} \\ \frac{RAO_{\zeta,x_B}}{RAO_{\zeta,ry_A}} \\ \frac{RAO_{\zeta,y_B}}{RAO_{\zeta,ry_A}} \\ \frac{RAO_{\zeta,z_B}}{RAO_{\zeta,ry_A}} \\ \frac{RAO_{\zeta,rx_B}}{RAO_{\zeta,ry_A}} \\ \frac{RAO_{\zeta,ry_B}}{RAO_{\zeta,ry_A}} \\ \frac{RAO_{\zeta,rz_B}}{RAO_{\zeta,ry_A}} \\ \frac{RAO_{\zeta,ry_A}}{RAO_{\zeta,x_B}} \end{array} & \begin{array}{c} \text{Vessel unrestrained in Rz} \\ \frac{RAO_{\zeta,x_B}}{RAO_{\zeta,rz_A}} \\ \frac{RAO_{\zeta,y_B}}{RAO_{\zeta,rz_A}} \\ \frac{RAO_{\zeta,z_B}}{RAO_{\zeta,rz_A}} \\ \frac{RAO_{\zeta,rx_B}}{RAO_{\zeta,rz_A}} \\ \frac{RAO_{\zeta,ry_B}}{RAO_{\zeta,rz_A}} \\ \frac{RAO_{\zeta,rz_B}}{RAO_{\zeta,rz_A}} \\ \frac{RAO_{\zeta,rz_A}}{RAO_{\zeta,x_B}} \end{array} \end{pmatrix} \quad (3.3)$$

To finally find the response at location B using the transmissibility functions as in 3.1 [3], the proof given in 3.1 [3] has to be adapted slightly. The most clear way to obtain the correct responses of all 6 degrees of freedom (DOFs) at location B is instead of using the response of location A (MRU) multiplied with the TFs A2B (MRU2CP or MRU2JS) squared as in 3.1 [3], is to use the Discrete Fourier Transform of a degree of freedom at location A (MRU) multiplied with the corresponding transmissibility functions A2B (MRU2CP or MRU2JS).

The main reason for this is that: *"The square of the sum is not equal to the sum of the squares."* The total response of 1 degree of freedom at location B is now build up out of 6 restrained, separate motions of the vessel at location A. Ergo, 6 TFs are required for 1 motion at B. In matrix 3.3, the third row of TFs is for example required to find the Z motion at B. Every transmissibility function in that third row of 3.3 has to be squared and then multiplied with the corresponding response at A. The sum of all six contributions is than the total response in Z at B. This is shown in equation 3.4.

$$S_{z_B} = \begin{pmatrix} \text{Vessel unrestrained in X} & \text{Vessel unrestrained in Y} & \text{Vessel unrestrained in Z} & \text{Vessel unrestrained in Rx} & \text{Vessel unrestrained in Ry} & \text{Vessel unrestrained in Rz} \\ \frac{RAO_{\zeta,z_B}}{RAO_{\zeta,x_A}} & \frac{RAO_{\zeta,z_B}}{RAO_{\zeta,y_A}} & \frac{RAO_{\zeta,z_B}}{RAO_{\zeta,z_A}} & \frac{RAO_{\zeta,z_B}}{RAO_{\zeta,rx_A}} & \frac{RAO_{\zeta,z_B}}{RAO_{\zeta,ry_A}} & \frac{RAO_{\zeta,z_B}}{RAO_{\zeta,rz_A}} \end{pmatrix} \cdot \begin{pmatrix} S_{x_A} \\ S_{y_A} \\ S_{z_A} \\ S_{rx_A} \\ S_{ry_A} \\ S_{rz_A} \end{pmatrix} \quad (3.4)$$

This however would **not** result in the same answer as if the response at B for z would be obtained from the TF from the unrestrained vessel [6x1], which would be squared with the response of z at location A. Again, the reason for this is that: *"The square of the sum is not equal to the sum of the squares."* For example,  $2^2 + 2^2 = 8 \neq 4^2 = 16$ . To make this work, all cross correlation spectra between motions A and B have to be added: For each DOF of B, the following has to be calculated (eq 3.5).

$$S_{z_B} = RAO_z \cdot RAO_x \cdot S_{zx} + RAO_z \cdot RAO_y \cdot S_{zy} + RAO_z \cdot RAO_z \cdot S_{zz} + \dots \quad (3.5)$$

By using the Discrete Fourier Transform (DFT) of every DOF at location A, this can be omitted. By using the DFT of the motions of location A, the transmissibility functions don't have to be squared but only multiplied. This results in that *"The square of the sum is not equal to the sum of the squares."* problem doesn't occur and not all cross correlation spectra have to be found. This results in the TF A2B Method in which the response at location B is found, by using the transmissibility functions A2B multiplied with the DFT of the chosen DOF at A. The full TF A2B Method applicable for the Synthetic Data Model (SDM) is shown in section 3.6 and will be explained in more depth in section 3.5. Finding the DFT of the 6 DOFs at B is shown in equation 3.6.

$$\begin{pmatrix} DFT_{A_6DOF \rightarrow x_B} \\ DFT_{A_6DOF \rightarrow y_B} \\ DFT_{A_6DOF \rightarrow z_B} \\ DFT_{A_6DOF \rightarrow rx_B} \\ DFT_{A_6DOF \rightarrow ry_B} \\ DFT_{A_6DOF \rightarrow rz_B} \end{pmatrix} = \begin{pmatrix} DFT_{x_A} \\ DFT_{y_A} \\ DFT_{z_A} \\ DFT_{rx_A} \\ DFT_{ry_A} \\ DFT_{rz_A} \end{pmatrix} \cdot \begin{pmatrix} \text{Vessel unrestrained in X} & \text{Vessel unrestrained in Y} & \text{Vessel unrestrained in Z} & \text{Vessel unrestrained in Rxx} & \text{Vessel unrestrained in Ryy} & \text{Vessel unrestrained in Rzz} \\ \frac{RAO_{\zeta, x_B}}{RAO_{\zeta, x_A}} & \frac{RAO_{\zeta, x_B}}{RAO_{\zeta, y_A}} & \frac{RAO_{\zeta, x_B}}{RAO_{\zeta, z_A}} & \frac{RAO_{\zeta, x_B}}{RAO_{\zeta, rx_A}} & \frac{RAO_{\zeta, x_B}}{RAO_{\zeta, ry_A}} & \frac{RAO_{\zeta, x_B}}{RAO_{\zeta, rz_A}} \\ \frac{RAO_{\zeta, y_B}}{RAO_{\zeta, x_A}} & \frac{RAO_{\zeta, y_B}}{RAO_{\zeta, y_A}} & \frac{RAO_{\zeta, y_B}}{RAO_{\zeta, z_A}} & \frac{RAO_{\zeta, y_B}}{RAO_{\zeta, rx_A}} & \frac{RAO_{\zeta, y_B}}{RAO_{\zeta, ry_A}} & \frac{RAO_{\zeta, y_B}}{RAO_{\zeta, rz_A}} \\ \frac{RAO_{\zeta, z_B}}{RAO_{\zeta, x_A}} & \frac{RAO_{\zeta, z_B}}{RAO_{\zeta, y_A}} & \frac{RAO_{\zeta, z_B}}{RAO_{\zeta, z_A}} & \frac{RAO_{\zeta, z_B}}{RAO_{\zeta, rx_A}} & \frac{RAO_{\zeta, z_B}}{RAO_{\zeta, ry_A}} & \frac{RAO_{\zeta, z_B}}{RAO_{\zeta, rz_A}} \\ \frac{RAO_{\zeta, rx_B}}{RAO_{\zeta, x_A}} & \frac{RAO_{\zeta, rx_B}}{RAO_{\zeta, y_A}} & \frac{RAO_{\zeta, rx_B}}{RAO_{\zeta, z_A}} & \frac{RAO_{\zeta, rx_B}}{RAO_{\zeta, rx_A}} & \frac{RAO_{\zeta, rx_B}}{RAO_{\zeta, ry_A}} & \frac{RAO_{\zeta, rx_B}}{RAO_{\zeta, rz_A}} \\ \frac{RAO_{\zeta, ry_B}}{RAO_{\zeta, x_A}} & \frac{RAO_{\zeta, ry_B}}{RAO_{\zeta, y_A}} & \frac{RAO_{\zeta, ry_B}}{RAO_{\zeta, z_A}} & \frac{RAO_{\zeta, ry_B}}{RAO_{\zeta, rx_A}} & \frac{RAO_{\zeta, ry_B}}{RAO_{\zeta, ry_A}} & \frac{RAO_{\zeta, ry_B}}{RAO_{\zeta, rz_A}} \\ \frac{RAO_{\zeta, rz_B}}{RAO_{\zeta, x_A}} & \frac{RAO_{\zeta, rz_B}}{RAO_{\zeta, y_A}} & \frac{RAO_{\zeta, rz_B}}{RAO_{\zeta, z_A}} & \frac{RAO_{\zeta, rz_B}}{RAO_{\zeta, rx_A}} & \frac{RAO_{\zeta, rz_B}}{RAO_{\zeta, ry_A}} & \frac{RAO_{\zeta, rz_B}}{RAO_{\zeta, rz_A}} \end{pmatrix} \quad (3.6)$$

### 3.3.3 Restrained transmissibility functions A2B are not significantly dependent on hydrodynamic properties system [H3]

The waves are the main excitation forces on the system during the suspended transport. The elegance of the TF A2B Method however is that the motions of point B are obtained using the motions of point A in combination with the transmissibility functions A2B. By knowing the motions of point A (caused by the waves) the motions of point B are calculated without the need of having to know the interaction between the vessel and the waves, as this interaction is already captured in the motions of the vessel (eq 3.1 [3]).

This results in that the transmissibility functions that transfer motions from location A to location B are not significantly dependent on the hydrodynamic properties of the system; first order wave forces, added mass, potential damping, viscous damping and hydrodynamic stiffness.

### 3.4 The Synthetic Data Model

To prove that the TF A2B Method works by using RAO's obtained from Liftdyn, the proposed hypotheses have to be validated. The hypotheses will be validated by the validation tests proposed in 3.2. To perform the validation tests the Synthetic Data Model (SDM) is created. A Jonswap spectrum will be used to simulate the motions of the vessel and the suspended jacket. Liftdyn models of the X suspended transport are used to obtain the required RAO's. An overview of the Synthetic Data Model is given in figure 3.2

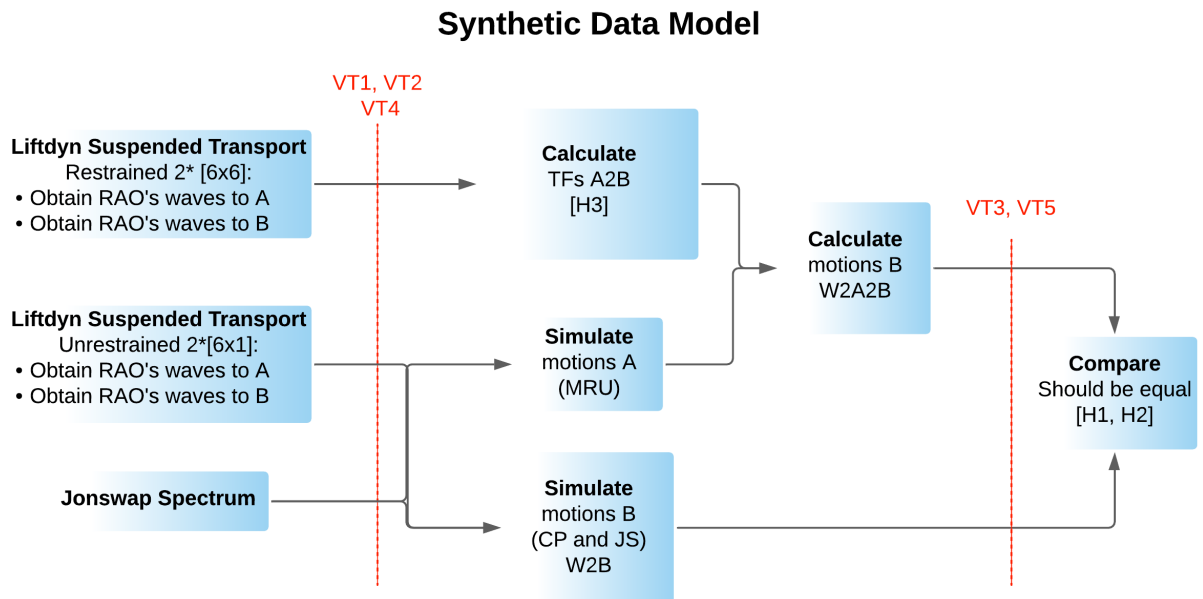


Figure 3.2: Overview Synthetic Data Model

#### 3.4.1 Restrained transmissibility functions are almost equal for every draft [VT1]

To prove that the transmissibility functions not significantly depended on the hydrodynamic properties of the vessel it can be shown that the transmissibility functions between A and B are almost equal for different drafts. This is done by using four Liftdyn models with different drafts of the same suspended transport. The result of a diffraction analysis is different for every draft as the submerged hull surface is different. Therefore first order wave forces, added mass and potential damping are different for the system. Besides the different results of the diffraction analyses, the different mass, centre of gravity, radii of gyrations of the vessel are taken into account for every draft just as free surface corrections and correct additional spring and damping matrices. The properties of springs and dampers between the vessel and jacket just as the mass of the jacket don't change. The drafts selected are 32, 19, 16.8 and 12m. 32m is the lowest draft achievable for Sleipnir, whilst 12m is the highest draft possible. The two other drafts are drafts frequently used during lifting and transport.

For this validation test, the Liftodyn models of the Y suspended transport are used. The main reason for this is that X was not yet transported at this period during this thesis. Following 3.1 [1] to [5], hypothesis [H3] must however be independent of the selected suspended transport. The Liftodyn model of Y is shown in 3.3. The blue cross again shows the MRU, the yellow triangle the control point and the green square the jacket sensor.

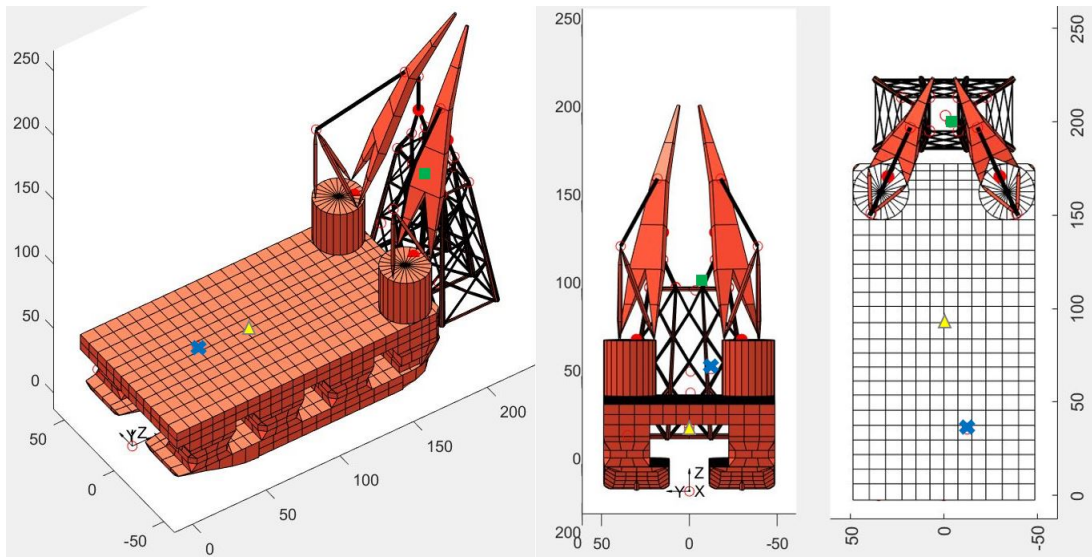


Figure 3.3: Liftodyn model of Y suspended transport

From the Liftodyn models all required RAO's are obtained. This is done in the following way for every draft (so 4 times):

- The restrained Liftodyn models of Y: Obtain the restrained RAO's for location A and B. In this case that is again the MRU (A), The control point (B) & the location of the jacket sensor (B) These are obtained from six edited Liftodyn models of the selected suspended transport. To every model a joint has to be added to location A. This to restrain the other 5 degrees of freedom and only let the vessel move in the selected degree of freedom. For every model this results in 6 RAO's at all three locations, 3 times [6x1] RAO's. As there are 6 models with a restraint, this results in 3 times [6x6] RAO's.
- The transmissibility functions are then obtained by dividing the RAO's of point A and B as in matrix 3.3. Matrix 3.3 shows that for every degree of freedom of the vessel at A (every column), a contribution is given to a degree of freedom at location B. It can also be said the other way around: Every degree of freedom at B (every row), has a contribution of the 6 degrees of freedom at A. This results in a 6x6 matrix with transmissibility functions for every draft, 4 times [6x6].

### 3.4.2 Transmissibility functions for the control point

To compare if the transmissibility functions are equal, the same transmissibility functions for every draft are plotted on top of each other. In figure 3.4, all six transmissibility functions of the control point (B) due to a Roll motion of the vessel at the MRU (A) are plotted.

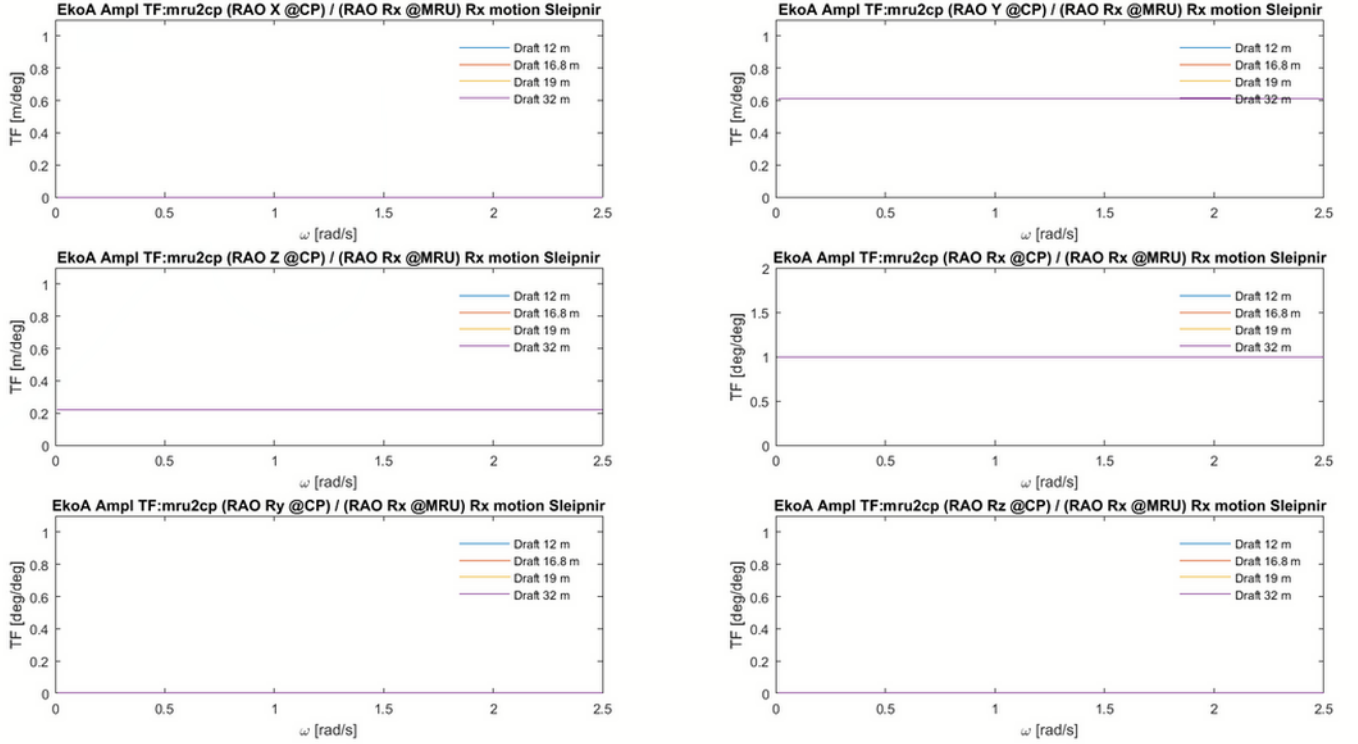


Figure 3.4: The transmissibility functions for all six DOF at the CP (B) due to a Roll motion of the vessel at the MRU (A)

In figure 3.4, it can be seen that three of the six transmissibility functions are 0. This follows from a transformation matrix shown in 3.7. This transformation matrix shows how to transform a motion at point A to a motion at point B on the same rigid body. For example, to find the motion of Y at B, the second row of the first matrix is required. It shows that to find the Y motion at B: the Y at A is multiplied with 1 - the relative distance in z between B and A multiplied with Roll at A (in rad) + the relative distance in x between B and A multiplied with Yaw at A (in rad).

$$T_{Mshift}(b-a) = \begin{pmatrix} 1 & 0 & 0 & 0 & (b_z - a_z) & -(b_y - a_y) \\ 0 & 1 & 0 & -(b_z - a_z) & 0 & (b_x - a_x) \\ 0 & 0 & 1 & (b_y - a_y) & -(b_x - a_x) & 0 \\ 0 & 0 & 0 & 1 & 0 & 0 \\ 0 & 0 & 0 & 0 & 1 & 0 \\ 0 & 0 & 0 & 0 & 0 & 1 \end{pmatrix} \cdot \begin{pmatrix} X_a(m) \\ Y_a(m) \\ Z_a(m) \\ RX_a(rad) \\ RY_a(rad) \\ RZ_a(rad) \end{pmatrix} \quad (3.7)$$

In this example however, the ship can only move in Rx (due to the modelling of restraints). So, if the transformation matrix is used to find the motions at B (CP), but only by accepting a Roll motion at location A due to the restraints, the transformation matrix will look like as in equation 3.8. In the vector, only a roll motion of 1 rad at A is shown. From equation 3.8 it becomes clear that there is no motion in X, Ry and Rz at location B, as the transformation matrix will give 0. This is as seen in figure 3.4, top left plot (X), bottom left plot (Ry) and bottom right plot (Rz).

$$T_{Mshift}(b-a) = \begin{pmatrix} 1 & 0 & 0 & 0 & (b_z - a_z) & -(b_y - a_y) \\ 0 & 1 & 0 & -(b_z - a_z) & 0 & (b_x - a_x) \\ 0 & 0 & 1 & (b_y - a_y) & -(b_x - a_x) & 0 \\ 0 & 0 & 0 & 1 & 0 & 0 \\ 0 & 0 & 0 & 0 & 1 & 0 \\ 0 & 0 & 0 & 0 & 0 & 1 \end{pmatrix} \cdot \begin{pmatrix} 0 \\ 0 \\ 0 \\ 1 \\ 0 \\ 0 \end{pmatrix} \quad (3.8)$$

The relative RAO for Y at CP (B) divided by Rx at the MRU (A) gives a value of 0.61 as can be seen in figure 3.4, top right plot. The Y position at the control point in respect to it's starting position changes due to a Roll motion at the MRU, namely 0.6m for every degree. This also follows from the transformation matrix 3.8 in which the vessel can only move in Rx at A (MRU) (due to the restraint). The Y motion at point B (CP) due to the Roll motion of point A (MRU) in 3.8 (2nd row first matrix) is only influenced by the relative distance in z between point A(MRU) and B(CP):  $-(b_z - a_z)$ . The relative distance is found as  $-(33.64(CP_z) - 68.5(MRU_z)) = 34.86$  [m/rad]. Converting this value to [m/deg] by multiplying this with  $\pi/180$  results in 0.61 [m/deg] as shown in figure 3.4, top right plot.

The same analogy and transformation matrix 3.8 can be used for the Z motion at B, due to a Roll motion at the MRU (A). The Z location of the CP changes 0.21m for every degree as seen in figure 3.4, middle left plot. As a Roll motion of the vessel gives the same Roll RAO for any point on the rigid body, all distances stay equal and the relative RAO for (Rx @CP/Rx @MRU) becomes 1 over the whole frequency domain. This is shown in figure 3.4, middle right plot. The corresponding phases to the TFs for Sleipnir moving in only roll are shown in figure 3.5. It can be seen that three TFs show random phases, namely:

$$\frac{RAOX_{cp}}{RAORX_{mru}}, \frac{RAORY_{cp}}{RAORX_{mru}}, \frac{RAORZ_{cp}}{RAORX_{mru}} \quad (3.9)$$

There are no motion components in Surge, Pitch and Yaw at the CP, due to Roll of the vessel at the MRU. This results in random phases (noise) as there is no motion, which is expected following the taken assumptions. A motion in Sway, Heave and Roll at the CP due to a Roll motion at the MRU are all in phase. For an X motion the transmissibility functions for the control point with four different drafts can be found in appendix C.1. Also here it can be seen that all transmissibility functions for every draft are on top of each other (so almost equal) and therefore don't change much for different draft. This validates that the transmissibility functions are not significantly dependent of the hydrodynamic properties of the vessel when the to points are on the same rigid body. To keep the report concise the transmissibility functions for the other motions at the control point are not included in the appendix.

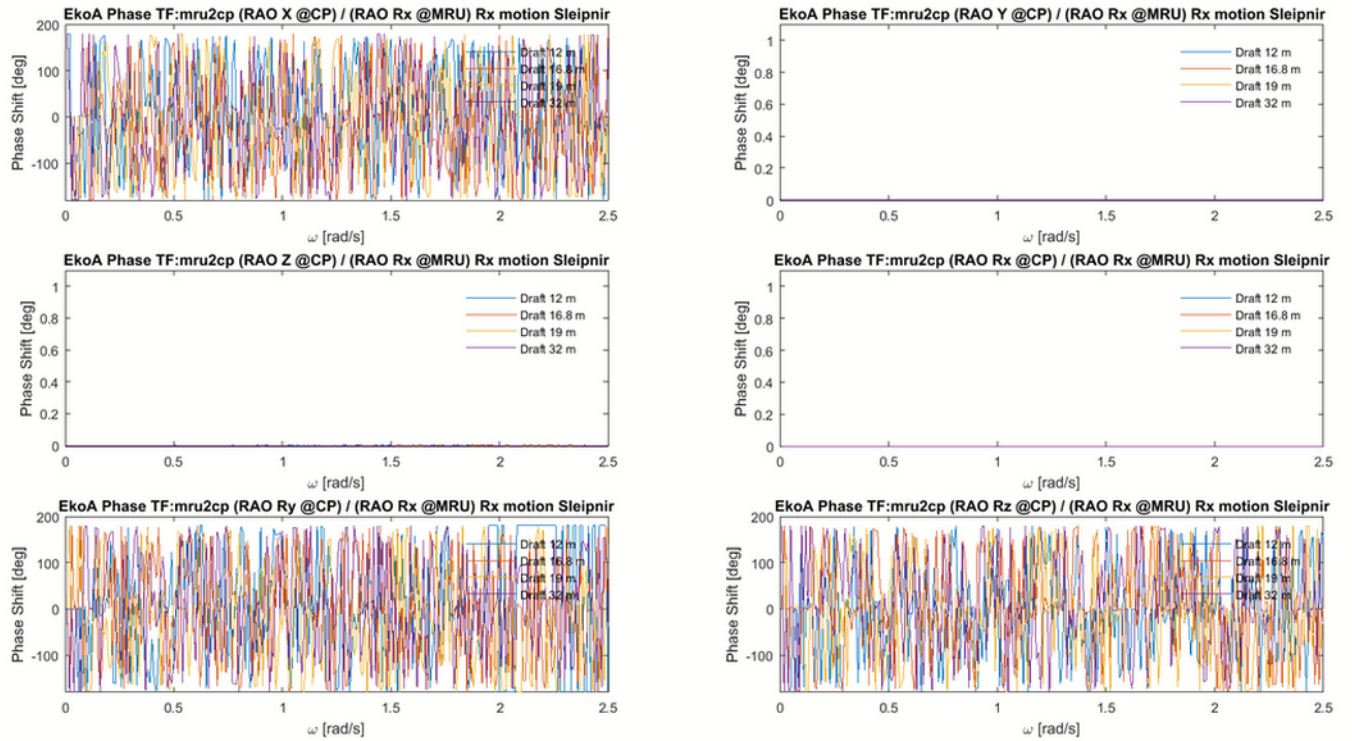


Figure 3.5: The transmissibility functions phases for all six DOF at the CP(B) due to a Roll motion of the vessel at the MRU(A)

### 3.4.3 Restrained TFs 6for the jacket sensor

For the jacket sensor the transmissibility functions which contribute to the motions at the jacket sensor (B) due to a motion at the MRU (A) can also be plotted. The six transmissibility functions for all six motions at the JS (B) due to a Roll motion at the MRU are shown in figure 3.6. Their phases are shown in figure 3.7. It is now however not possible to directly use a transformation matrix like in equation 3.7, as the jacket sensor is not on the same rigid body as the MRU which can be clearly seen in figure 2.1. In the Liftdyn models of Y, there are 10 connected rigid bodies, all connected with springs and dampers. The most prominent 6 rigid bodies are:

1. The Sleipnir body
2. The PS crane boom
3. The PS crane main block
4. The SB crane boom
5. The SB crane main block
6. The suspended jacket

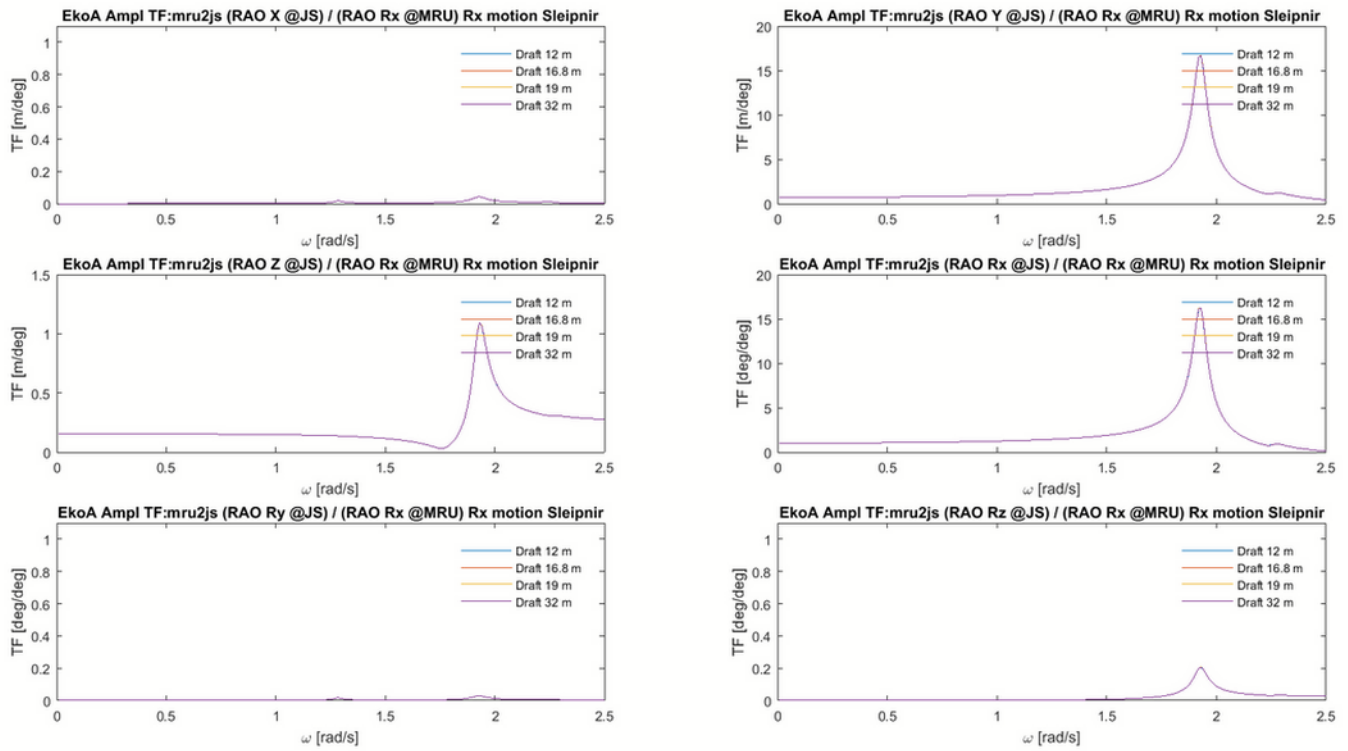


Figure 3.6: The transmissibility functions for all six DOF at the JS (B) due to a Roll motion

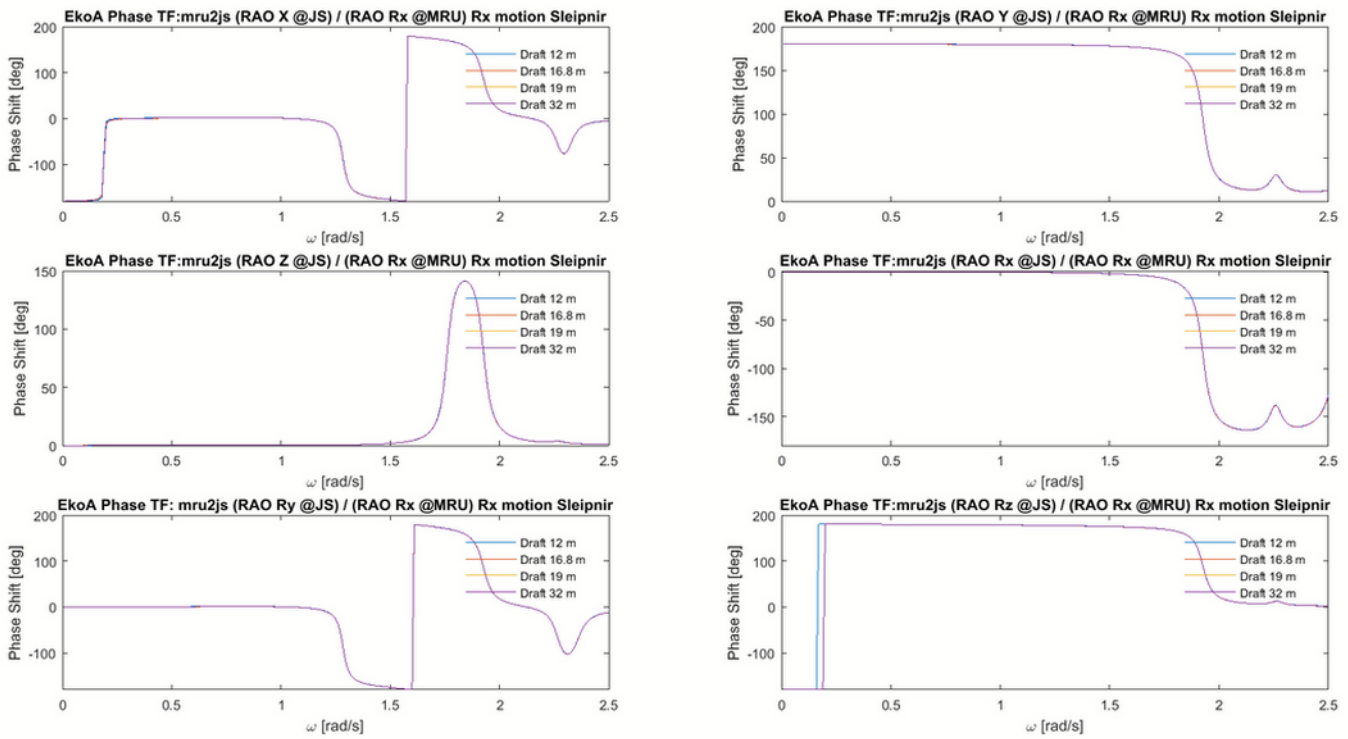


Figure 3.7: The transmissibility functions phases for all six DOF at the JS (B) due to a Roll motion of the vessel at the MRU (A)

The amount of rigid bodies makes it more complicated to show direct coupling between bodies. As can be seen in figure 3.6, the Roll motion at the MRU still mostly amplifies the in-plane motions Sway, Heave and Roll at the jacket sensor, which is also what is expected. A motion at the MRU would most likely still induce motions in-plane with the selected motion, as there is the strongest coupling. What is also found is that there is a slight coupling with the motions out of plane with Roll, namely Surge, Pitch and Yaw at the jacket sensor. This is different in comparison with the control point as here this coupling doesn't exist. This can be explained as in its most simplest form the jacket-vessel interaction can be seen as a vessel with two cranes in which a jacket is suspended. This jacket acts like a pendulum, which can move freely in every degree of freedom. The control point on the other side is located on the same rigid body as the MRU and can therefore not move freely.

What can also be seen is that the contribution of Roll at the MRU to a degree of freedom at the JS is now also influenced by the frequency. This is also expected. At certain frequencies (here approximately at 1.99 rad/s) bigger amplification of motions is expected. This can be explained by the fact that around this frequency a natural frequency of the system is excited, which induces a mode shape with big Sway, Heave and Roll motions of the jacket. This mode shape is shown figure 3.8.

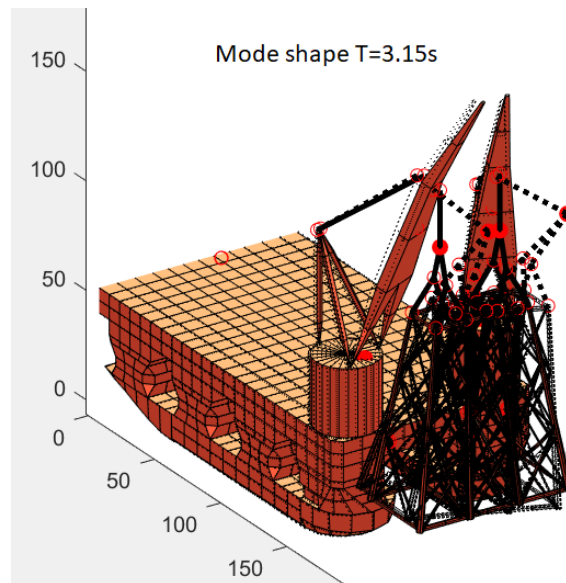


Figure 3.8: Mode shape of Y draft 19m at 1.99 rad/s in which big roll motions of the jacket occur

Most importantly, for the proof that *'The restrained transmissibility functions are almost equal for different draft'*, figure 3.6 shows that also the TFs between a vessel motion of roll at the MRU and the resulting amplification of motions in the six degrees of freedom at the jacket sensor are almost equal for the four selected drafts. In figure 3.7 it can be seen that the phases of the transmissibility functions of Roll at the MRU to the six degrees of freedom at the JS are also equal for every draft. The motions at the jacket sensor due to Heave and Pitch motions at the MRU are found in appendix C.2.

That the transmissibility functions between the vessel and jacket don't change much can be explained by the fact that the weight of the vessel in comparison to the jacket is way bigger (ratio  $\approx 2\%$ ). Changes in mass, added mass and hydrodynamic stiffness of the vessel due to different draft also do not affect the ratio between the weight of the vessel and jacket much so significantly that the transmissibility functions between the vessel and jacket change much. The jacket weight in comparison to the vessel weight remains rather small. This can be seen in table 3.1. This results in that the transmissibility functions for different draft between the vessel and jacket are almost equal which was shown for the restrained TFs between the six motions of the jacket due to a Roll motion of the vessel in figure 3.6

<b>Draft 12 m</b>	<b>Draft 16.8 m</b>	<b>Draft 19 m</b>	<b>Draft 32 m</b>	<b>Description mode shape</b>
1.31 rad/s	1.32 rad/s	1.3 rad/s	1.3 rad/s	Jacket Pitch
2 rad/s	2.01 rad/s	1.99 rad/s	1.98 rad/s	Jacket Roll
2.27 rad/s	2.27 rad/s	2.27 rad/s	2.27 rad/s	Jacket Roll + hoist wires

Table 3.1: Mode shapes in which the Y jacket moves heavily with small motions of the vessel for different draft

Some minor differences can be found in the phases for the selected drafts at the transmissibility functions with a Z motion as input at the MRU (fig C.4) and for the transmissibility functions with a Pitch motion as input at the MRU (fig C.6). There are small phase differences which can be explained as that in the domain where the differences are the amplitude TFs are 0 resulting in noise. The amplitude transmissibility functions of these motions are however almost equal for every draft. All other transmissibility functions between vessel and jacket for different drafts are equal, but for the purpose of keeping this research concise are not included in the appendix.

As it is shown in 3.4.2 that the transmissibility functions of the control point are almost equal for different draft, which can also be explained with the transformation matrix 3.7, and that it is shown that the transmissibility functions that transfer motions between the MRU and the jacket sensor are also almost equal for different draft, it is validated that the transmissibility functions between any point A and B in the system are not significantly dependent on hydrodynamic properties of the system. To keep the report concise the transmissibility functions for the other motions between the MRU and the jacket sensor are not included in the appendix. These were however equal for every draft.

### 3.5 X Synthetic Data Model (SDM)

To validate that the TF A2B Method works with RAO's obtained from Liftodyn, the validation tests have to be performed. These can be performed with the Synthetic Data Model

In this model, synthetic data is used which can easily be changed by changing the parameters of the input. This means that a Jonswap Spectrum is used to simulate the motions of the system at the MRU, CP and JS. The RAO's for the MRU, CP and JS are obtained from the Liftodyn model of the X suspended transport. The following steps have to be taken in Liftodyn to obtain the RAO's:

1. The unrestrained RAO's have to be obtained for the Liftodyn model of X without any restraints. These are three sets of [6x1] vectors, containing the 6 RAO's of the 6 degrees of freedom for three locations: the MRU, the control point and the location of the jacket sensor.
2. Then a restraint has to be placed at the location of the MRU by adding a joint in the modelling mode of Liftodyn. The joint in the Liftodyn model has to be changed 6 times; there can only be 1 unrestrained motion at the same time. As the model allows the vessel to only move in one direction at the same time, this finally results in a 6x6 matrix of RAO's for all three locations 3\*[6x6].
3. To obtain the transmissibility functions between 2 locations A (MRU) and B (either CP or JS), the RAO's of those locations have to be divided as shown in matrix 3.10. This way the contribution of a motion at location B due to a motion at location A can more easily be found, as all coupling of motions is removed.

$$TFs_{A2B} = \begin{pmatrix} \begin{matrix} \text{Vessel unrestrained in X} \\ \text{Vessel unrestrained in Y} \\ \text{Vessel unrestrained in Z} \\ \text{Vessel unrestrained in Rx} \\ \text{Vessel unrestrained in Ry} \\ \text{Vessel unrestrained in Rz} \end{matrix} & \begin{matrix} \frac{RAO_{\zeta,x_B}}{RAO_{\zeta,x_A}} \\ \frac{RAO_{\zeta,y_B}}{RAO_{\zeta,y_A}} \\ \frac{RAO_{\zeta,z_B}}{RAO_{\zeta,z_A}} \\ \frac{RAO_{\zeta,rx_B}}{RAO_{\zeta,rx_A}} \\ \frac{RAO_{\zeta,ry_B}}{RAO_{\zeta,ry_A}} \\ \frac{RAO_{\zeta,rz_B}}{RAO_{\zeta,rz_A}} \end{matrix} & \begin{matrix} \frac{RAO_{\zeta,x_B}}{RAO_{\zeta,y_A}} \\ \frac{RAO_{\zeta,y_B}}{RAO_{\zeta,y_A}} \\ \frac{RAO_{\zeta,z_B}}{RAO_{\zeta,z_A}} \\ \frac{RAO_{\zeta,rx_B}}{RAO_{\zeta,rx_A}} \\ \frac{RAO_{\zeta,ry_B}}{RAO_{\zeta,ry_A}} \\ \frac{RAO_{\zeta,rz_B}}{RAO_{\zeta,rz_A}} \end{matrix} & \begin{matrix} \frac{RAO_{\zeta,x_B}}{RAO_{\zeta,z_A}} \\ \frac{RAO_{\zeta,y_B}}{RAO_{\zeta,z_A}} \\ \frac{RAO_{\zeta,z_B}}{RAO_{\zeta,z_A}} \\ \frac{RAO_{\zeta,rx_B}}{RAO_{\zeta,rx_A}} \\ \frac{RAO_{\zeta,ry_B}}{RAO_{\zeta,ry_A}} \\ \frac{RAO_{\zeta,rz_B}}{RAO_{\zeta,rz_A}} \end{matrix} & \begin{matrix} \frac{RAO_{\zeta,x_B}}{RAO_{\zeta,rx_A}} \\ \frac{RAO_{\zeta,y_B}}{RAO_{\zeta,rx_A}} \\ \frac{RAO_{\zeta,z_B}}{RAO_{\zeta,rx_A}} \\ \frac{RAO_{\zeta,rx_B}}{RAO_{\zeta,rx_A}} \\ \frac{RAO_{\zeta,ry_B}}{RAO_{\zeta,rx_A}} \\ \frac{RAO_{\zeta,rz_B}}{RAO_{\zeta,rx_A}} \end{matrix} & \begin{matrix} \frac{RAO_{\zeta,x_B}}{RAO_{\zeta,ry_A}} \\ \frac{RAO_{\zeta,y_B}}{RAO_{\zeta,ry_A}} \\ \frac{RAO_{\zeta,z_B}}{RAO_{\zeta,ry_A}} \\ \frac{RAO_{\zeta,rx_B}}{RAO_{\zeta,ry_A}} \\ \frac{RAO_{\zeta,ry_B}}{RAO_{\zeta,ry_A}} \\ \frac{RAO_{\zeta,rz_B}}{RAO_{\zeta,ry_A}} \end{matrix} & \begin{matrix} \frac{RAO_{\zeta,x_B}}{RAO_{\zeta,rz_A}} \\ \frac{RAO_{\zeta,y_B}}{RAO_{\zeta,rz_A}} \\ \frac{RAO_{\zeta,z_B}}{RAO_{\zeta,rz_A}} \\ \frac{RAO_{\zeta,rx_B}}{RAO_{\zeta,rz_A}} \\ \frac{RAO_{\zeta,ry_B}}{RAO_{\zeta,rz_A}} \\ \frac{RAO_{\zeta,rz_B}}{RAO_{\zeta,rz_A}} \end{matrix} \end{pmatrix} \quad (3.10)$$

There are several checks that have to be done to prove that the sub-steps in the model work correctly. The validation tests that have to be done are:

- Prove that the created, restrained set of transmissibility functions  $[6 \times 6]$  between MRU to control point (MRU2CP) multiplied with the unrestrained set of RAO's  $[6 \times 1]$  from waves to MRU (W2MRU), result in the unrestrained set of RAO's  $[6 \times 1]$  from waves to control point (W2CP). The MRU is used as location A and the control point as location B. The control point is located on the same rigid body as the MRU. Following the theory in 3.1 [6], this should be true. [VT2]
- Prove that the response of all six motions at the control point, found by using the restrained transmissibility functions  $[6 \times 6]$  (MRU2CP) is equal to the set of responses for the six motions at the control point, found with the unrestrained set of RAO's  $[6 \times 1]$  from waves to CP (W2CP). [VT3]
- Prove that the created, restrained set of transmissibility functions  $[6 \times 6]$  for location MRU to jacket sensor (MRU2JS) multiplied with the unrestrained set of RAO's  $[6 \times 1]$  from waves to MRU (W2MRU), results in the unrestrained set of RAO's  $[6 \times 1]$  from waves to jacket sensor (W2JS). The MRU is used as location A and the location of the jacket sensor as location B. The jacket sensor is **not** located on the same rigid body as the MRU. Following the theory in 3.1 [6], this should be true. [VT4]
- Prove that the response of all six motions at the jacket sensor, found by using the restrained transmissibility functions  $[6 \times 6]$  (MRU2JS), is equal to the set of responses at the jacket sensor found by the unrestrained set of RAO's  $[6 \times 1]$  from waves to JS (W2JS). [VT5]

After successfully performing these validation tests with the SDM, it is shown that the TF A2B Method works with RAO's obtained from LiftDyn. In the next subsections on the following pages the steps which have to be performed with the SDM are mathematically presented.

### 3.5.1 TF(A2B)\*RAO(W2A) equals RAO(W2B) [VT2] & [VT4]

To validate proof [VT2] & [VT4], the theory with the restrained TFs in 3.3.2 is used. This is shown in equation 3.11. The difference between equations 3.1 [6] and 3.11 is that now that the uncoupled TFs [6x6] between A and B are used instead of the coupled transmissibility functions [6x1]. This to see how the motions at A contribute to motions at B.

$$\begin{array}{c} \text{Vessel unrestrained in X} \\ \text{Vessel unrestrained in Y} \\ \text{Vessel unrestrained in Z} \\ \text{Vessel unrestrained in Rx} \\ \text{Vessel unrestrained in Ry} \\ \text{Vessel unrestrained in Rz} \end{array} \begin{pmatrix} \frac{RAO_{\zeta, x_B}}{RAO_{\zeta, x_A}} & \frac{RAO_{\zeta, x_B}}{RAO_{\zeta, y_A}} & \frac{RAO_{\zeta, x_B}}{RAO_{\zeta, z_A}} & \frac{RAO_{\zeta, x_B}}{RAO_{\zeta, rx_A}} & \frac{RAO_{\zeta, x_B}}{RAO_{\zeta, ry_A}} & \frac{RAO_{\zeta, x_B}}{RAO_{\zeta, rz_A}} \\ \frac{RAO_{\zeta, y_B}}{RAO_{\zeta, x_A}} & \frac{RAO_{\zeta, y_B}}{RAO_{\zeta, y_A}} & \frac{RAO_{\zeta, y_B}}{RAO_{\zeta, z_A}} & \frac{RAO_{\zeta, y_B}}{RAO_{\zeta, rx_A}} & \frac{RAO_{\zeta, y_B}}{RAO_{\zeta, ry_A}} & \frac{RAO_{\zeta, y_B}}{RAO_{\zeta, rz_A}} \\ \frac{RAO_{\zeta, z_B}}{RAO_{\zeta, x_A}} & \frac{RAO_{\zeta, z_B}}{RAO_{\zeta, y_A}} & \frac{RAO_{\zeta, z_B}}{RAO_{\zeta, z_A}} & \frac{RAO_{\zeta, z_B}}{RAO_{\zeta, rx_A}} & \frac{RAO_{\zeta, z_B}}{RAO_{\zeta, ry_A}} & \frac{RAO_{\zeta, z_B}}{RAO_{\zeta, rz_A}} \\ \frac{RAO_{\zeta, rx_B}}{RAO_{\zeta, x_A}} & \frac{RAO_{\zeta, rx_B}}{RAO_{\zeta, y_A}} & \frac{RAO_{\zeta, rx_B}}{RAO_{\zeta, z_A}} & \frac{RAO_{\zeta, rx_B}}{RAO_{\zeta, rx_A}} & \frac{RAO_{\zeta, rx_B}}{RAO_{\zeta, ry_A}} & \frac{RAO_{\zeta, rx_B}}{RAO_{\zeta, rz_A}} \\ \frac{RAO_{\zeta, ry_B}}{RAO_{\zeta, x_A}} & \frac{RAO_{\zeta, ry_B}}{RAO_{\zeta, y_A}} & \frac{RAO_{\zeta, ry_B}}{RAO_{\zeta, z_A}} & \frac{RAO_{\zeta, ry_B}}{RAO_{\zeta, rx_A}} & \frac{RAO_{\zeta, ry_B}}{RAO_{\zeta, ry_A}} & \frac{RAO_{\zeta, ry_B}}{RAO_{\zeta, rz_A}} \\ \frac{RAO_{\zeta, rz_B}}{RAO_{\zeta, x_A}} & \frac{RAO_{\zeta, rz_B}}{RAO_{\zeta, y_A}} & \frac{RAO_{\zeta, rz_B}}{RAO_{\zeta, z_A}} & \frac{RAO_{\zeta, rz_B}}{RAO_{\zeta, rx_A}} & \frac{RAO_{\zeta, rz_B}}{RAO_{\zeta, ry_A}} & \frac{RAO_{\zeta, rz_B}}{RAO_{\zeta, rz_A}} \end{pmatrix} \begin{pmatrix} RAO_{\zeta, x_A} \\ RAO_{\zeta, y_A} \\ RAO_{\zeta, z_A} \\ RAO_{\zeta, rx_A} \\ RAO_{\zeta, ry_A} \\ RAO_{\zeta, rz_A} \end{pmatrix} = \begin{pmatrix} RAO_{\zeta, x_B} \\ RAO_{\zeta, y_B} \\ RAO_{\zeta, z_B} \\ RAO_{\zeta, rx_B} \\ RAO_{\zeta, ry_B} \\ RAO_{\zeta, rz_B} \end{pmatrix} \quad (3.11)$$

### 3.5.2 $S_{DOF_B}$ from $S_{DOF_A}$ and TFs (A2B) [VT3] & [VT5]

To prove that the response of all six motions at B found by using the restrained transmissibility functions [6x6] (A2B), is equal to the set of responses at B found by the unrestrained set of RAO's [6x1] from waves to B (W2B), the following steps have to be taken within the Synthetic Data Model:

1. In the Synthetic Data Model, the DFTs of the degrees of freedom (DOF) at A (MRU) are first obtained from an inverse DFT of a Jonswap spectrum. See equation 3.12. Random phases are created for an N amount of samples as there is no phase information within a spectrum.

$$S_{\zeta}(\omega) \xrightarrow{Spec2DFT} \begin{pmatrix} DFT_{\zeta} \\ DFT_{\zeta} \\ DFT_{\zeta} \\ DFT_{\zeta} \\ DFT_{\zeta} \\ DFT_{\zeta} \end{pmatrix} \cdot \begin{pmatrix} RAO_{\zeta, x_A} \\ RAO_{\zeta, y_A} \\ RAO_{\zeta, z_A} \\ RAO_{\zeta, rx_A} \\ RAO_{\zeta, ry_A} \\ RAO_{\zeta, rz_A} \end{pmatrix} = \begin{pmatrix} DFT_{x_A} \\ DFT_{y_A} \\ DFT_{z_A} \\ DFT_{rx_A} \\ DFT_{ry_A} \\ DFT_{rz_A} \end{pmatrix} \quad \begin{array}{l} \zeta = \sqrt{2 \cdot S_{\zeta} \cdot \Delta\omega} \\ \epsilon = \epsilon \cdot \frac{\pi}{180} \\ DFT = N \cdot \zeta \cdot (\cos(\epsilon) + i \cdot \sin(\epsilon)) \end{array} \quad (3.12)$$

2. The DFTs of the DOFs at A are then multiplied with the transmissibility functions (A2B) to obtain the DFTs at B (either CP or & JS), see equation 3.13.

$$\begin{pmatrix} DFT_{A_{6DOF} \rightarrow x_B} \\ DFT_{A_{6DOF} \rightarrow y_B} \\ DFT_{A_{6DOF} \rightarrow z_B} \\ DFT_{A_{6DOF} \rightarrow rx_B} \\ DFT_{A_{6DOF} \rightarrow ry_B} \\ DFT_{A_{6DOF} \rightarrow rz_B} \end{pmatrix} = \begin{pmatrix} DFT_{x_A} \\ DFT_{y_A} \\ DFT_{z_A} \\ DFT_{rx_A} \\ DFT_{ry_A} \\ DFT_{rz_A} \end{pmatrix} \cdot \begin{pmatrix} \text{Vessel unrestrained in X} & \text{Vessel unrestrained in Y} & \text{Vessel unrestrained in Z} & \text{Vessel unrestrained in } R_{xx} & \text{Vessel unrestrained in } R_{yy} & \text{Vessel unrestrained in } R_{zz} \\ \hline \frac{RAO_{\zeta, x_B}}{RAO_{\zeta, x_A}} & \frac{RAO_{\zeta, x_B}}{RAO_{\zeta, y_A}} & \frac{RAO_{\zeta, x_B}}{RAO_{\zeta, z_A}} & \frac{RAO_{\zeta, x_B}}{RAO_{\zeta, rx_A}} & \frac{RAO_{\zeta, x_B}}{RAO_{\zeta, ry_A}} & \frac{RAO_{\zeta, x_B}}{RAO_{\zeta, rz_A}} \\ \frac{RAO_{\zeta, y_B}}{RAO_{\zeta, x_A}} & \frac{RAO_{\zeta, y_B}}{RAO_{\zeta, y_A}} & \frac{RAO_{\zeta, y_B}}{RAO_{\zeta, z_A}} & \frac{RAO_{\zeta, y_B}}{RAO_{\zeta, rx_A}} & \frac{RAO_{\zeta, y_B}}{RAO_{\zeta, ry_A}} & \frac{RAO_{\zeta, y_B}}{RAO_{\zeta, rz_A}} \\ \frac{RAO_{\zeta, z_B}}{RAO_{\zeta, x_A}} & \frac{RAO_{\zeta, z_B}}{RAO_{\zeta, y_A}} & \frac{RAO_{\zeta, z_B}}{RAO_{\zeta, z_A}} & \frac{RAO_{\zeta, z_B}}{RAO_{\zeta, rx_A}} & \frac{RAO_{\zeta, z_B}}{RAO_{\zeta, ry_A}} & \frac{RAO_{\zeta, z_B}}{RAO_{\zeta, rz_A}} \\ \frac{RAO_{\zeta, rx_B}}{RAO_{\zeta, x_A}} & \frac{RAO_{\zeta, rx_B}}{RAO_{\zeta, y_A}} & \frac{RAO_{\zeta, rx_B}}{RAO_{\zeta, z_A}} & \frac{RAO_{\zeta, rx_B}}{RAO_{\zeta, rx_A}} & \frac{RAO_{\zeta, rx_B}}{RAO_{\zeta, ry_A}} & \frac{RAO_{\zeta, rx_B}}{RAO_{\zeta, rz_A}} \\ \frac{RAO_{\zeta, ry_B}}{RAO_{\zeta, x_A}} & \frac{RAO_{\zeta, ry_B}}{RAO_{\zeta, y_A}} & \frac{RAO_{\zeta, ry_B}}{RAO_{\zeta, z_A}} & \frac{RAO_{\zeta, ry_B}}{RAO_{\zeta, rx_A}} & \frac{RAO_{\zeta, ry_B}}{RAO_{\zeta, ry_A}} & \frac{RAO_{\zeta, ry_B}}{RAO_{\zeta, rz_A}} \\ \frac{RAO_{\zeta, rz_B}}{RAO_{\zeta, x_A}} & \frac{RAO_{\zeta, rz_B}}{RAO_{\zeta, y_A}} & \frac{RAO_{\zeta, rz_B}}{RAO_{\zeta, z_A}} & \frac{RAO_{\zeta, rz_B}}{RAO_{\zeta, rx_A}} & \frac{RAO_{\zeta, rz_B}}{RAO_{\zeta, ry_A}} & \frac{RAO_{\zeta, rz_B}}{RAO_{\zeta, rz_A}} \\ \frac{RAO_{\zeta, x_A}}{RAO_{\zeta, x_A}} & \frac{RAO_{\zeta, y_A}}{RAO_{\zeta, y_A}} & \frac{RAO_{\zeta, z_A}}{RAO_{\zeta, z_A}} & \frac{RAO_{\zeta, rx_A}}{RAO_{\zeta, rx_A}} & \frac{RAO_{\zeta, ry_A}}{RAO_{\zeta, ry_A}} & \frac{RAO_{\zeta, rz_A}}{RAO_{\zeta, rz_A}} \end{pmatrix} \quad (3.13)$$

3. Then the DFTs at B (CP or JS) are converted to the corresponding responses of every DOF in the frequency domain for location B, see equation 3.14. In which N is the number of time steps,  $\zeta$  is the amplitude,  $\Delta\omega$  is the frequency step and  $\epsilon$  are the phases in degrees.

$$\begin{pmatrix} DFT_{A_{6DOF} \rightarrow x_B} \\ DFT_{A_{6DOF} \rightarrow y_B} \\ DFT_{A_{6DOF} \rightarrow z_B} \\ DFT_{A_{6DOF} \rightarrow rx_B} \\ DFT_{A_{6DOF} \rightarrow ry_B} \\ DFT_{A_{6DOF} \rightarrow rz_B} \end{pmatrix} \xrightarrow{DFT2Spec} \begin{pmatrix} S_{A_{6DOF} \rightarrow x_B} \\ S_{A_{6DOF} \rightarrow y_B} \\ S_{A_{6DOF} \rightarrow z_B} \\ S_{A_{6DOF} \rightarrow rx_B} \\ S_{A_{6DOF} \rightarrow ry_B} \\ S_{A_{6DOF} \rightarrow rz_B} \end{pmatrix} \quad \begin{aligned} \zeta_{DOF_B} &= \frac{\|DFT_{DOF_B}\|}{N} \\ S_{DOF_B} &= \frac{\zeta_{DOF_B}^2 \cdot \Delta\omega}{2} \\ \epsilon &= \angle(DFT_{DOF_B}) \cdot \frac{180}{\pi} \end{aligned} \quad (3.14)$$

4. These responses are then compared to the responses of the DOFs at B (CP or JS), obtained by multiplying the Jonswap Spectrum with the square of the unrestrained RAOs from waves to motions DOFs at B (W2B), see equation 3.15.

$$\begin{pmatrix} S_{A_{6DOF} \rightarrow x_B} \\ S_{A_{6DOF} \rightarrow y_B} \\ S_{A_{6DOF} \rightarrow z_B} \\ S_{A_{6DOF} \rightarrow rx_B} \\ S_{A_{6DOF} \rightarrow ry_B} \\ S_{A_{6DOF} \rightarrow rz_B} \end{pmatrix} = \begin{pmatrix} S_{x_B} \\ S_{y_B} \\ S_{z_B} \\ S_{rx_B} \\ S_{ry_B} \\ S_{rz_B} \end{pmatrix} \leftarrow \begin{pmatrix} RAO_{\zeta, x_b}^2 \cdot S_{\zeta} \\ RAO_{\zeta, y_b}^2 \cdot S_{\zeta} \\ RAO_{\zeta, z_b}^2 \cdot S_{\zeta} \\ RAO_{\zeta, rx_b}^2 \cdot S_{\zeta} \\ RAO_{\zeta, ry_b}^2 \cdot S_{\zeta} \\ RAO_{\zeta, rz_b}^2 \cdot S_{\zeta} \end{pmatrix} \quad (3.15)$$

5. Following the theory in equation 3.1 [2] & [3], with [3] adjusted for the use of restrained TFs as in 3.3.2, the responses found by using the TFs between A and B and the responses found directly from waves to B should be identical. In section 3.6 the full method for the Synthetic Data Model is displayed.

### 3.6 TF A2B Method with SDM

$$S_{\zeta}(\omega) \xrightarrow{IDFT} \begin{pmatrix} DFT_{\zeta} \\ DFT_{\zeta} \\ DFT_{\zeta} \\ DFT_{\zeta} \\ DFT_{\zeta} \\ DFT_{\zeta} \end{pmatrix} \cdot \begin{pmatrix} RAO_{\zeta,x_A} \\ RAO_{\zeta,y_A} \\ RAO_{\zeta,z_A} \\ RAO_{\zeta,rx_A} \\ RAO_{\zeta,ry_A} \\ RAO_{\zeta,rz_A} \end{pmatrix} = \begin{pmatrix} DFT_{x_A} \\ DFT_{y_A} \\ DFT_{z_A} \\ DFT_{rx_A} \\ DFT_{ry_A} \\ DFT_{rz_A} \end{pmatrix} \quad \text{Spec2DFT :} \quad \zeta = \sqrt{2 \cdot S_{\zeta} \cdot \Delta\omega}$$

$$\epsilon = \epsilon \cdot \frac{\pi}{180} \quad DFT = N \cdot \zeta \cdot (\cos(\epsilon) + i \cdot \sin(\epsilon)) \quad (3.16)$$

$$\begin{pmatrix} DFT_{A_{6DOF} \rightarrow x_B} \\ DFT_{A_{6DOF} \rightarrow y_B} \\ DFT_{A_{6DOF} \rightarrow z_B} \\ DFT_{A_{6DOF} \rightarrow rx_B} \\ DFT_{A_{6DOF} \rightarrow ry_B} \\ DFT_{A_{6DOF} \rightarrow rz_B} \end{pmatrix} = \begin{pmatrix} DFT_{x_A} \\ DFT_{y_A} \\ DFT_{z_A} \\ DFT_{rx_A} \\ DFT_{ry_A} \\ DFT_{rz_A} \end{pmatrix} \cdot \begin{pmatrix} \text{Vessel unrestrained in X} & \text{Vessel unrestrained in Y} & \text{Vessel unrestrained in Z} & \text{Vessel unrestrained in Rxx} & \text{Vessel unrestrained in Ryy} & \text{Vessel unrestrained in Rzz} \\ \frac{RAO_{\zeta,x_B}}{RAO_{\zeta,x_A}} & \frac{RAO_{\zeta,x_B}}{RAO_{\zeta,y_A}} & \frac{RAO_{\zeta,x_B}}{RAO_{\zeta,z_A}} & \frac{RAO_{\zeta,x_B}}{RAO_{\zeta,rx_A}} & \frac{RAO_{\zeta,x_B}}{RAO_{\zeta,ry_A}} & \frac{RAO_{\zeta,x_B}}{RAO_{\zeta,rz_A}} \\ \frac{RAO_{\zeta,y_B}}{RAO_{\zeta,x_A}} & \frac{RAO_{\zeta,y_B}}{RAO_{\zeta,y_A}} & \frac{RAO_{\zeta,y_B}}{RAO_{\zeta,z_A}} & \frac{RAO_{\zeta,y_B}}{RAO_{\zeta,rx_A}} & \frac{RAO_{\zeta,y_B}}{RAO_{\zeta,ry_A}} & \frac{RAO_{\zeta,y_B}}{RAO_{\zeta,rz_A}} \\ \frac{RAO_{\zeta,z_B}}{RAO_{\zeta,x_A}} & \frac{RAO_{\zeta,z_B}}{RAO_{\zeta,y_A}} & \frac{RAO_{\zeta,z_B}}{RAO_{\zeta,z_A}} & \frac{RAO_{\zeta,z_B}}{RAO_{\zeta,rx_A}} & \frac{RAO_{\zeta,z_B}}{RAO_{\zeta,ry_A}} & \frac{RAO_{\zeta,z_B}}{RAO_{\zeta,rz_A}} \\ \frac{RAO_{\zeta,rx_B}}{RAO_{\zeta,x_A}} & \frac{RAO_{\zeta,rx_B}}{RAO_{\zeta,y_A}} & \frac{RAO_{\zeta,rx_B}}{RAO_{\zeta,z_A}} & \frac{RAO_{\zeta,rx_B}}{RAO_{\zeta,rx_A}} & \frac{RAO_{\zeta,rx_B}}{RAO_{\zeta,ry_A}} & \frac{RAO_{\zeta,rx_B}}{RAO_{\zeta,rz_A}} \\ \frac{RAO_{\zeta,ry_B}}{RAO_{\zeta,x_A}} & \frac{RAO_{\zeta,ry_B}}{RAO_{\zeta,y_A}} & \frac{RAO_{\zeta,ry_B}}{RAO_{\zeta,z_A}} & \frac{RAO_{\zeta,ry_B}}{RAO_{\zeta,rx_A}} & \frac{RAO_{\zeta,ry_B}}{RAO_{\zeta,ry_A}} & \frac{RAO_{\zeta,ry_B}}{RAO_{\zeta,rz_A}} \\ \frac{RAO_{\zeta,rz_B}}{RAO_{\zeta,x_A}} & \frac{RAO_{\zeta,rz_B}}{RAO_{\zeta,y_A}} & \frac{RAO_{\zeta,rz_B}}{RAO_{\zeta,z_A}} & \frac{RAO_{\zeta,rz_B}}{RAO_{\zeta,rx_A}} & \frac{RAO_{\zeta,rz_B}}{RAO_{\zeta,ry_A}} & \frac{RAO_{\zeta,rz_B}}{RAO_{\zeta,rz_A}} \end{pmatrix} \quad (3.17)$$

$$\begin{pmatrix} DFT_{A_{6DOF} \rightarrow x_B} \\ DFT_{A_{6DOF} \rightarrow y_B} \\ DFT_{A_{6DOF} \rightarrow z_B} \\ DFT_{A_{6DOF} \rightarrow rx_B} \\ DFT_{A_{6DOF} \rightarrow ry_B} \\ DFT_{A_{6DOF} \rightarrow rz_B} \end{pmatrix} \xrightarrow{DFT2Spec} \begin{pmatrix} S_{A_{6DOF} \rightarrow x_B} \\ S_{A_{6DOF} \rightarrow y_B} \\ S_{A_{6DOF} \rightarrow z_B} \\ S_{A_{6DOF} \rightarrow rx_B} \\ S_{A_{6DOF} \rightarrow ry_B} \\ S_{A_{6DOF} \rightarrow rz_B} \end{pmatrix} \quad \zeta_{DOFB} = \frac{\|DFT_{DOFB}\|}{N}$$

$$DFT2spec : S_{DOFB} = \frac{\zeta_{DOFB}^2 \cdot \Delta\omega}{2} \quad \epsilon = \angle(DFT_{DOFB}) \cdot \frac{180}{\pi} \quad (3.18)$$

$$\begin{pmatrix} S_{A_{6DOF} \rightarrow x_B} \\ S_{A_{6DOF} \rightarrow y_B} \\ S_{A_{6DOF} \rightarrow z_B} \\ S_{A_{6DOF} \rightarrow rx_B} \\ S_{A_{6DOF} \rightarrow ry_B} \\ S_{A_{6DOF} \rightarrow rz_B} \end{pmatrix} = \begin{pmatrix} S_{x_B} \\ S_{y_B} \\ S_{z_B} \\ S_{rx_B} \\ S_{ry_B} \\ S_{rz_B} \end{pmatrix} \leftarrow \begin{matrix} RAO_{\zeta,x_b}^2 \cdot S_{\zeta} \\ RAO_{\zeta,y_b}^2 \cdot S_{\zeta} \\ RAO_{\zeta,z_b}^2 \cdot S_{\zeta} \\ RAO_{\zeta,rx_b}^2 \cdot S_{\zeta} \\ RAO_{\zeta,ry_b}^2 \cdot S_{\zeta} \\ RAO_{\zeta,rz_b}^2 \cdot S_{\zeta} \end{matrix} \quad (3.19)$$

# Chapter 4: Validation SDM using Liftdyn

## 4.1 Validation: X with Synthetic Data Model

The Sleipnir and X jacket are modelled in Liftdyn during the design phase of the X suspended transport. The vessel and jacket are modeled as rigid bodies, connected to each other by springs, dampers and hinges representing tie downs to crane assembly and rigging arrangement. This can be seen in figure 4.1.

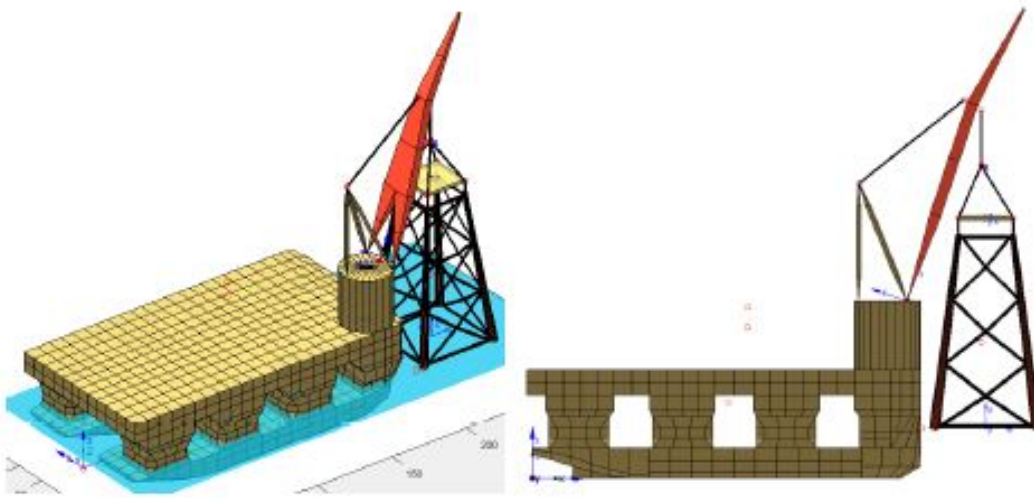


Figure 4.1: The X transport modeled in Liftdyn [12]

Each body is defined by a mass matrix representing the mass and mass moments of inertia. The effect of the dynamic positioning system has been represented by a linear spring between vessel and earth, approximating the combined stiffness of the DP system. The stiffness values for the springs have been chosen such that the modes associated with the low frequency motions in the system have a period higher than 100s.

The hydrodynamic properties of the Sleipnir for the analyzed transit draft (16.8 m) are derived from the MARIN provided hydrodynamic database. The database was based on diffraction analysis in DIFFRAC software whereby a damping lid was applied on top of and in the space between the floaters. This to better assess the inconvenient draft problem as described in 2.5.3. The hydrodynamic databases contains added mass, potential damping and first order wave forcing as function of the wave frequency. Viscous damping has been assessed based on in-house available data, such as model test results, and are linearized for the analyzed wave height.

The SDM proposed in 3.6 is tested with the following input:

- A Jonswap spectrum with a significant wave height of 4m and a peak period of 11s is selected, as this resembles a sea state with high waves in the wave frequency domain to make sure no noise is analysed.
- Unrestrained RAO's obtained from a Liftodyn model of the X transport without any restraints. This results in three sets of 6 RAO's [6x1]. One for every degree of freedom (in total 6) at three locations. Namely, at the MRU (A), the control point (B) and the jacket sensor (B). The locations of the 3 points are shown in figure 4.2.
- Restrained RAO's obtained from six edited Liftodyn models of the X transport. Every model has a joint placed at the MRU (A), to restrain the other 5 degrees of freedom. This results in three sets of 6x6 RAO's.

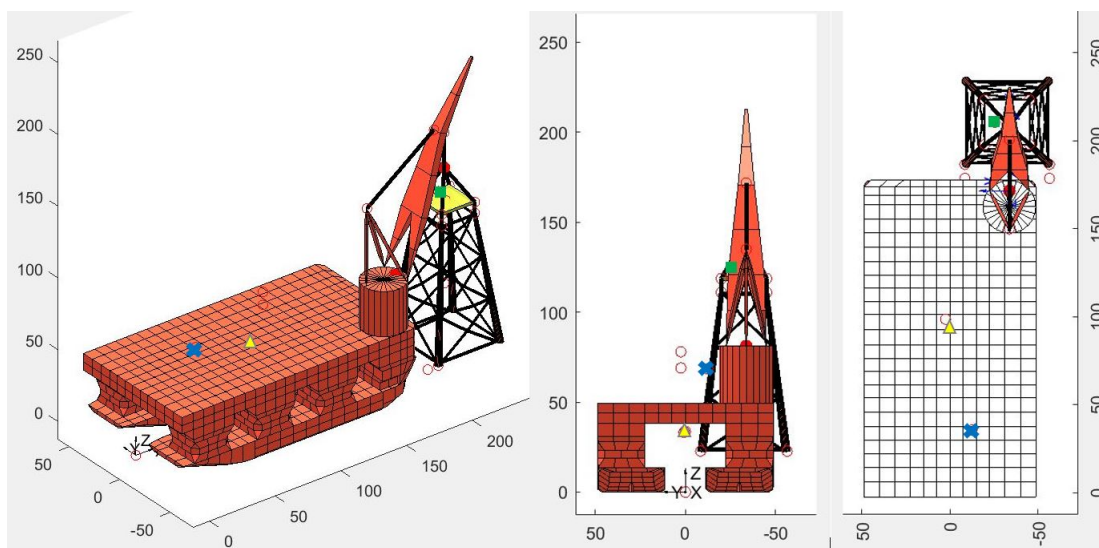


Figure 4.2: Liftodyn model of X suspended transport

### 4.1.1 Nyquist frequency

In the model the frequency grid of the RAO's should be equal to the frequency grid of the Jonswap Spectrum. If this is not the case the data with the biggest  $\Delta\omega$  should be interpolated to the smallest data grid. This is the easiest way to prevent aliasing. The Nyquist frequency states that two samples per frequency (period) are required to capture the signal of that frequency [7]. So for a 1 Hz (1s) signal it is required to sample with at least 2 Hz ( $T_{sample} \leq 0.5s$ ). However, when looked to such a signal, this will show a poor definition of a signal and realistically therefore more samples are required for every period of oscillation. Hence the rule of thumb within HMC,  $f_{sample} \geq 10 \cdot f_{signal}$ .

If a signal is under sampled, aliasing will occur. This means that frequencies above the Nyquist frequency will show up as virtual low frequencies (mirrored around the Nyquist frequency). To avoid this a low pass filter has to be applied and only then down sample the signal. To check this a spectrum can be made to see if the energy close to the Nyquist is zero. By up-sampling the signal from the biggest to the smallest frequency grid aliasing cannot occur.

Currently, there are no sensors that directly measure the Surge and Sway of the vessel. Therefore, it is interesting to see what the influence of the Surge and Sway motion of the vessel are on the jacket motions and on the motions of the control point. To be able to find the response at B (either JS or CP) without contributions of Surge and Sway of the vessel, the contributions of the first two columns of the transmissibility function matrix in 3.13 are set to 0. This results in the response at B (CP or JS) in all six degrees of freedom without the contribution of Surge and Sway of the vessel at A (MRU). The benefit of this approach is that if the calculated Surge and Sway of the vessel are too inaccurate, the model can still find a partial response of jacket motions at the jacket sensor. The results are expected to be less accurate as now no coupling between Surge and Sway at the vessel and all 6 DOFs at the jacket sensor is taken into account.

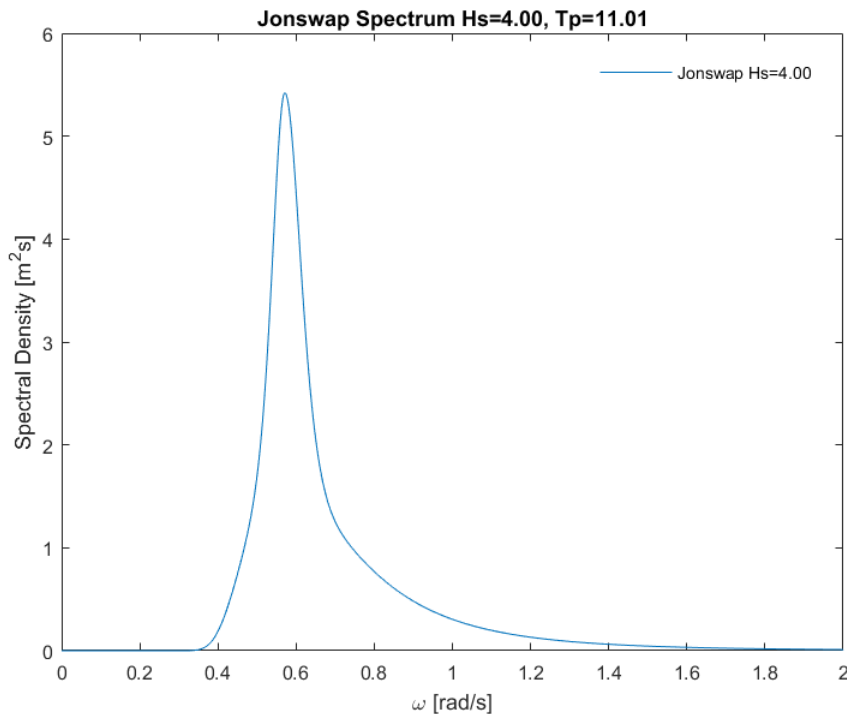


Figure 4.3: The Jonswap spectrum used to simulate vessel and jacket motions

## 4.2 Results SDM at control point

### 4.2.1 $TF(MRU2CP) \cdot RAO(W2MRU) = RAO(W2CP)$ [VT2]

Within HMC, transmissibility functions have never been obtained by using RAO's from Liftodyn. To partly verify that the transmissibility functions between the MRU and the CP can correctly be obtained from Liftdyn and used with Matlab, it must be shown that the restrained set of transmissibility functions [6x6] from the MRU to control point (MRU2CP) multiplied with the unrestrained set of RAO's [6x1] from waves to MRU (W2MRU), result in the set of RAO's [6x1] from waves to control point (W2CP) (eq 4.1). To verify this, simulations with the SDM model are done. In figure 4.4 it is shown that for all six degrees of freedom at the control point the RAO, W2CP can be reconstructed. As can be observed, in every plot of figure 4.4 the orange line ( $TF(MRU2CP) \cdot RAO(W2MRU)$ ) is on top of the blue line (RAO W2JS). This proves that the transmissibility functions between the MRU and the JS are correctly found [VT2].

$$TF_{s_{DOF_{MRU}, DOF_{CP}}} = \frac{RAO_{\zeta, DOF_{CP}}}{RAO_{\zeta, DOF_{MRU}}} \quad (4.1)$$

$$RAO_{\zeta, DOF_{CP}} = TF_{s_{DOF_{MRU}, DOF_{CP}}} \cdot RAO_{\zeta, DOF_{MRU}}$$

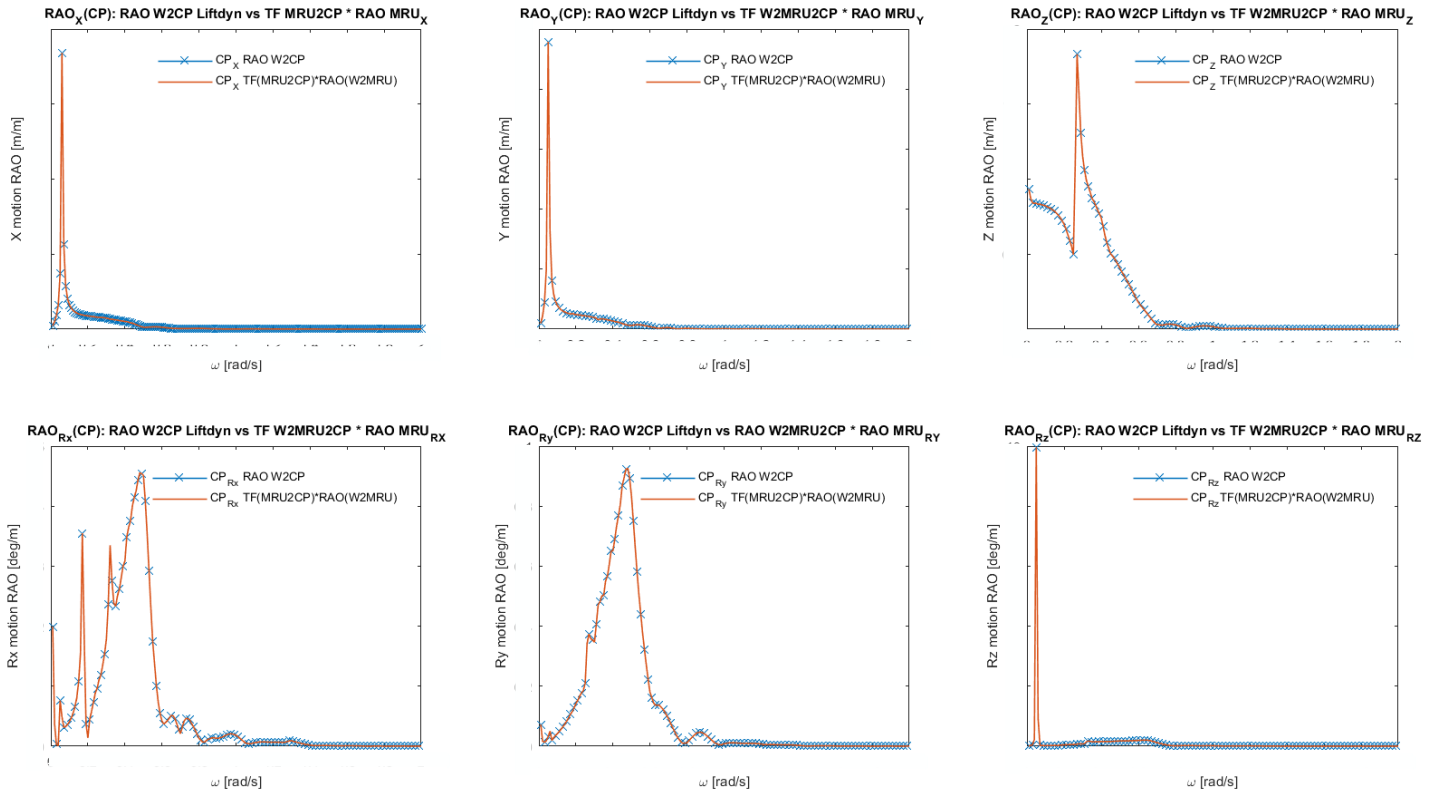


Figure 4.4: Reconstruction of  $RAO_{\zeta, idof_{CP}}$  following 3.1 [6]

### 4.2.2 $S_{DOF_{CP}}$ from $S_{DOF_{MRU}}$ & TFs (MRU2CP) [VT3]

To prove that the transmissibility functions between the MRU and the CP can be used with Liftdyn and Matlab to find the correct response at the CP, it must be shown that the response of all six motions at the CP on the same rigid body as the MRU, found by using the restrained transmissibility functions [6x6] (TF MRU2CP), is equal to the set of responses at the CP found by the unrestrained set of RAO's [6x1] from waves to the CP (W2CP) (eq 4.2). To verify this, simulations with the SDM model are done. In figure 4.5 the responses at the control point are shown for a relative wave direction of 150°. In the SDM, the motions at the MRU are dependent on the wave direction.

$$S_{\zeta}(\omega) \cdot RAO_{\zeta,DOF_{CP}}^2 = S_{DOF_{CP}}(\omega)$$

$$DFT_{DOF_{MRU}}(\omega) \cdot TF_{DOF_{MRU},DOF_{CP}} = DFT_{DOF_{CP}}(\omega) \xrightarrow{DFT2Spec} S_{DOF_{CP}}(\omega) \quad (4.2)$$

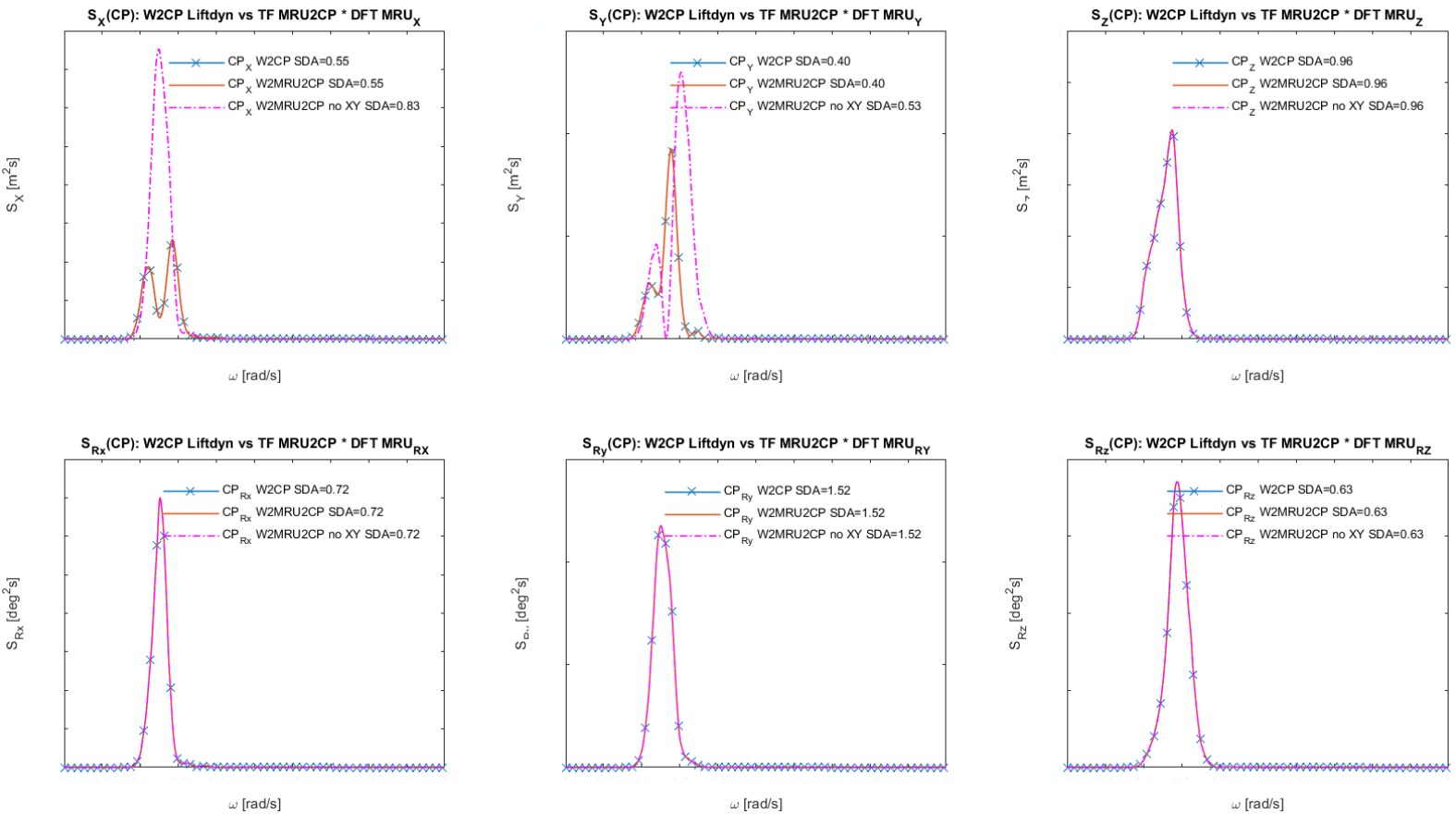


Figure 4.5: Responses of all degrees of freedom at the control point

All six responses at the CP in figure 4.5 are within the wave frequency domain. This is expected as the input of the model currently is a Jonswap spectrum (figure 4.3) the waves with no spectral energy before 0.36 rad/s. This then results in no response in any DOF of the vessel below this frequency, which is also what can be seen in all six plots of figure 4.5. What can also be seen is that the TF A2B Method W2MRU2CP (orange line) results in the same response in every degree of freedom as if the direct approach W2CP (blue line) is used. The blue lines are not visible as the orange line (W2MRU2CP) is exactly on top of the blue line (W2CP). This proves that the transmissibility functions between the MRU (A) and the CP (B) can be used to find the correct response at the CP (B), which lays on the same rigid body as the MRU (A) [VT3].

This verifies that the Matlab script `tf_a2b_method_w2mr_u2cp` which follows all steps in 3.6 in combination with the RAO's from Liftdyn can be used. It can also be seen that if the Surge and Sway motion of the vessel at the MRU are not included in the calculation (magenta lines), the response in Surge and Sway at the CP is different. This can be explained by the fact that motions that contribute to the response in a degree of freedom at the CP can be in anti-phase to each other. The response of one degree of freedom at the CP is built up out of 6 degrees of freedom at the MRU. As the control point is on the same rigid body as the MRU, not all motions at the MRU contribute to every degree of freedom at the CP. How much a motion of the MRU contributes to a motion to another location B (CP) depends on a combination of two things, namely:

- The magnitude of the response of a motion at location A (MRU) at a certain frequency
- The magnitude of the required transmissibility functions at a certain frequency

For example: there could be a significant response in Sway of the vessel at the MRU. This however does not contribute to a response in Surge of the vessel at the control point, as these are uncoupled motions as found from the transformation matrix 3.7. The motions at the MRU that do contribute to a Surge motion at the control point are a Surge, Pitch and Yaw motion at the MRU. This can again be explained with the Transformation Matrix shown in 4.3. To translate a Surge motion from location A (MRU) to a Surge motion at location B (CP) on the same rigid body, a Surge, Pitch and Yaw motion component are required at location A (MRU). This is found from the first row of the Transformation Matrix in 4.3.

$$T_{Mshift}(b-a) = \begin{pmatrix} 1 & 0 & 0 & 0 & (b_z - a_z) & -(b_y - a_y) \\ 0 & 1 & 0 & -(b_z - a_z) & 0 & (b_x - a_x) \\ 0 & 0 & 1 & (b_y - a_y) & -(b_x - a_x) & 0 \\ 0 & 0 & 0 & 1 & 0 & 0 \\ 0 & 0 & 0 & 0 & 1 & 0 \\ 0 & 0 & 0 & 0 & 0 & 1 \end{pmatrix} \cdot \begin{pmatrix} X_a(m) \\ Y_a(m) \\ Z_a(m) \\ RX_a(rad) \\ RY_a(rad) \\ RZ_a(rad) \end{pmatrix} \quad (4.3)$$

The contributions of the transmissibility functions at the MRU to the Surge motion at the CP, can also be found from the SDM. The response in X at the control point due to a Surge, Pitch and Yaw motion at the MRU is shown in figure 4.6, together with the required transmissibility functions.

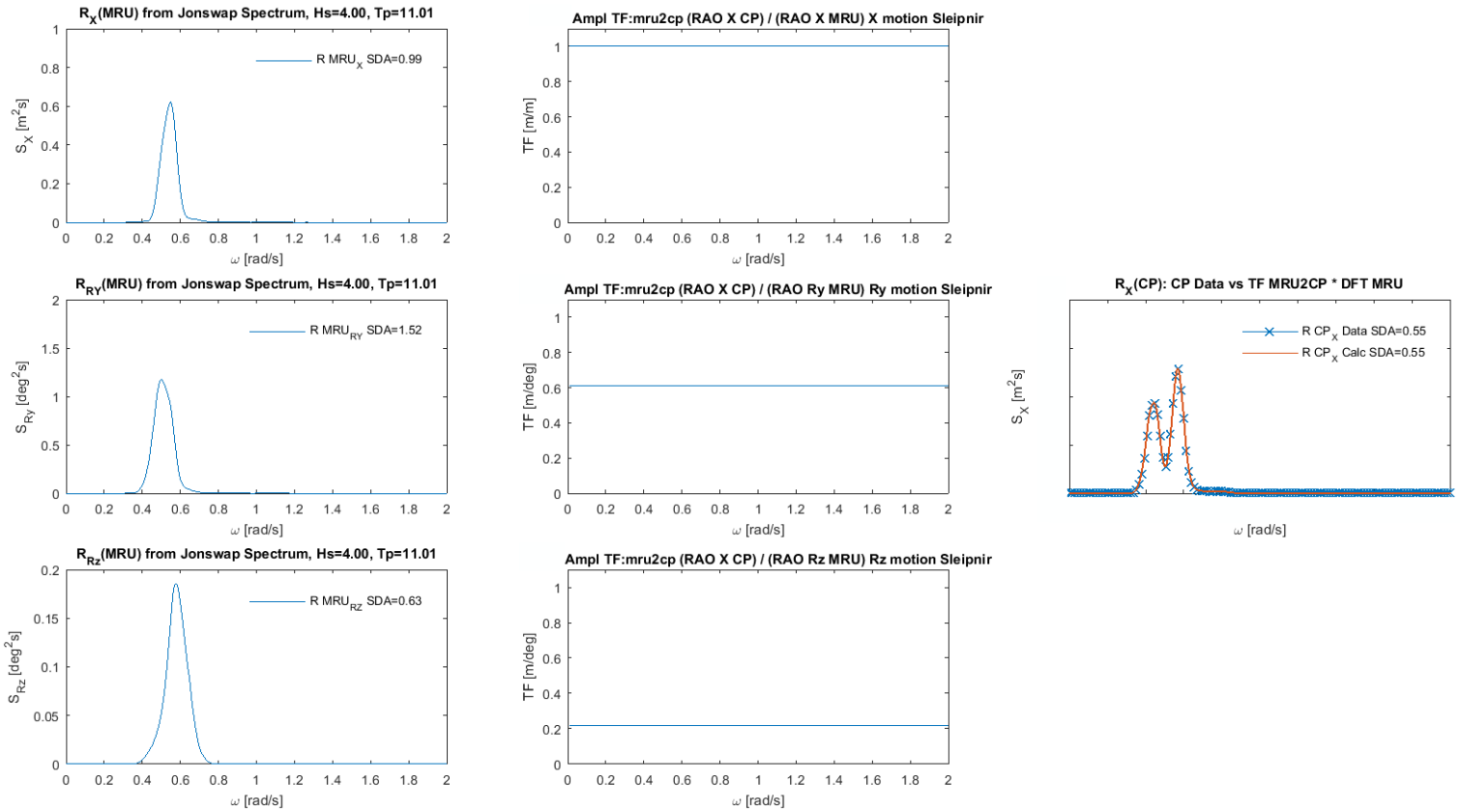


Figure 4.6: Response in Surge at the CP due to Surge, Pitch and Yaw at the MRU

To analyse the difference between the response of Surge at the control point with and without a contribution of Surge at the MRU, the phases between the contributing motions have to be checked. The phases of all required RAO's are shown in figure 4.7. From figure 4.7 the following can for example be found at 0.5 rad/s:

- Maximum Surge motion at MRU, gives maximum Surge motion at CP (in-phase) (red circle top left plot)
- Max positive Pitch motion at the MRU, gives a maximum negative Surge motion at the CP (-180° out-of phase) (red circle middle left plot)
- Max positive Yaw motion at the MRU, gives a maximum negative Surge motion at the CP (180° out-of phase) (red circle bottom left plot)
- Vessel Pitch at the MRU has a 48° phase shift with Surge at the MRU (red circle top right plot) at 0.5 rad/s
- Vessel Yaw at the MRU has a -165° phase shift with Surge at the MRU (red circle bottom right plot) at 0.5 rad/s

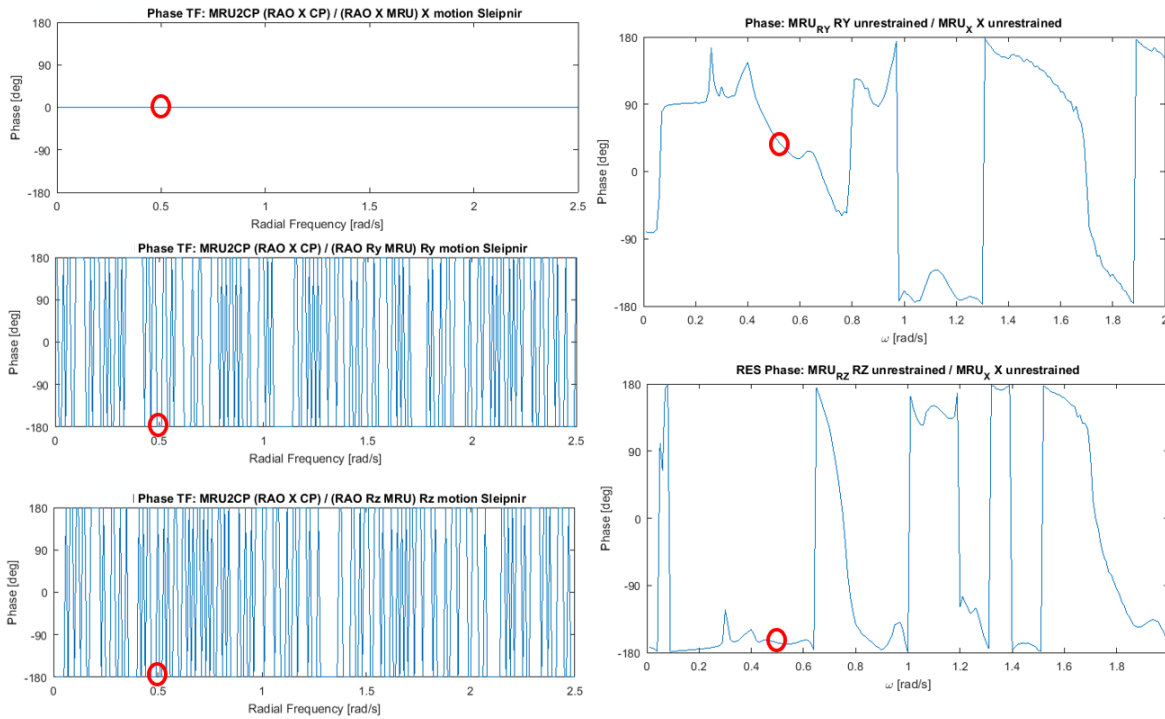


Figure 4.7: Phases of TFs, Surge, Pitch, Yaw at the MRU to Surge motion at the CP

This would result at 0.5 rad/s for the CP, assuming a maximum Surge ( $90^\circ$ ) at the MRU in:

- Max positive Surge at the MRU, gives max positive Surge at the CP
- Pitch  $48^\circ$  phase shift with Surge at the MRU result in a positive decreasing Pitch at the MRU ( $90+48=138^\circ$ )(red circle top right plot). This results in a  $138-180=-42^\circ$  is an negative decreasing Surge at the CP.
- Surge  $-165^\circ$  phase with Yaw at the MRU results in  $90-165=-75^\circ$  negative decreasing Yaw at the MRU. This results in  $-75+180=105^\circ$  positive decreasing Surge at the CP.
- The total contribution of the motions however depends on the amplitude transmissibility functions and the response in Surge, Pitch and Yaw at the MRU. From fig 4.6 it is found that there is less energy in Yaw of the vessel at the MRU than Pitch and Surge, so this motion will also influence the CP less.

Such an analysis can be used to explain how the response in Surge at the CP without contributions of Surge and Sway at the MRU in figure 4.5, top left figure magenta line at 0.5 rad/s shows a peak while the response in Surge at the CP with contributions of all degrees of freedom at the MRU (top left figure red line) shows a valley. This originates from that Surge and Pitch at the MRU give opposite contributions to Surge at the CP (negative decreasing vs positive decreasing Surge) . Therefore, not adding Surge motions at the MRU to find the Surge motion at the CP at 0.5 rad/s will results in different answers within the method. The magnitude of the difference depends on the respective amplitude transmissibility functions and the responses in the DOFs of the MRU.

### 4.3 Results jacket sensor

#### 4.3.1 $TF(MRU2JS) * RAO(W2MRU) = RAO(W2JS)$ [VT4]

To prove that the transmissibility functions between the MRU and the JS can correctly be obtained from RAO's extracted from Liftdyn, it must be shown that the restrained set of transmissibility functions [6x6] between MRU to jacket sensor (MRU2JS) multiplied with the unrestrained set of RAO's [6x1] from waves to MRU (W2MRU), result in the set of RAO's [6x1] from waves to jacket sensor (W2JS) (eq 4.4). To verify this, again simulations with the SDM model are done. In figure 4.8 it is shown that for all six degrees of freedom at the location of the jacket sensor the RAO, W2JS can be reconstructed. As can be observed, once again in every plot of figure 4.8 the orange line (TF MRU2JS \* RAO W2MRU) (almost) fully overlaps the blue line (RAO W2JS). There is a small error in the Surge and Pitch RAO at 0.28-0.3 rad/s which seems to originate from an error within Liftdyn. This should be further researched (fig 4.9). This proves that the transmissibility functions between the MRU(A) and the JS(B) which lay **not** on the same rigid body are correctly found [VT4].

$$TF_{DOF_{MRU}, DOF_{JS}} = \frac{RAO_{\zeta, DOF_{JS}}}{RAO_{\zeta, DOF_{MRU}}} \quad (4.4)$$

$$RAO_{\zeta, DOF_{JS}} = TF_{DOF_{MRU}, DOF_{JS}} \cdot RAO_{\zeta, DOF_{MRU}}$$

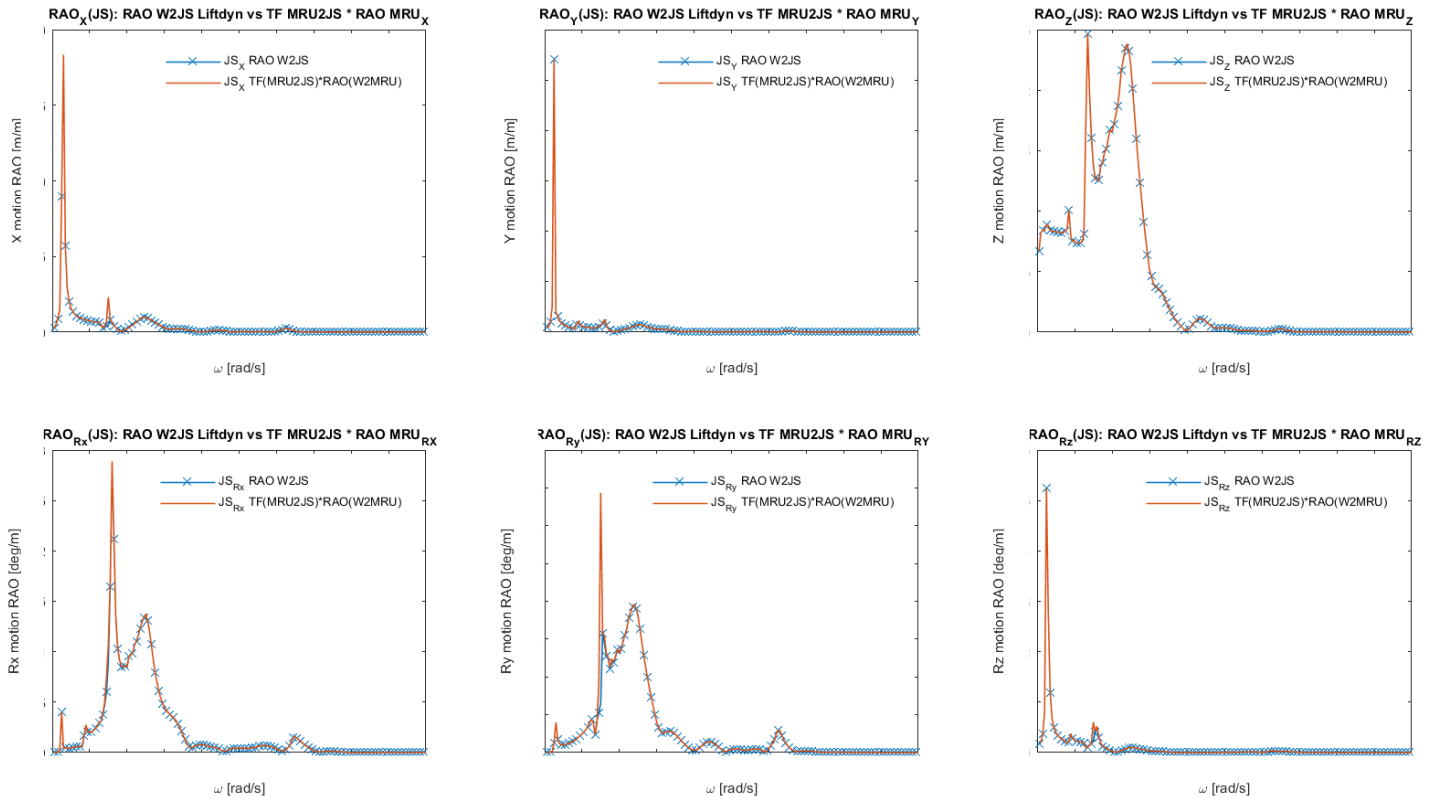


Figure 4.8: Reconstruction of  $RAO_{\zeta, DOF_{JS}}$  following 3.1[6]

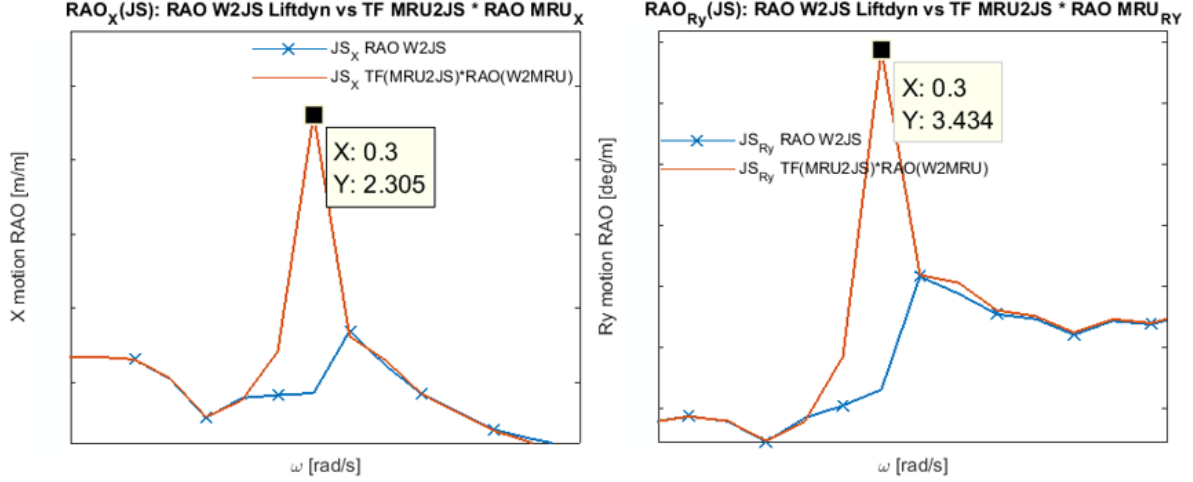


Figure 4.9: Small errors in Surge and Pitch TF from restrained RAO's at 0.28-0.3 rad/s

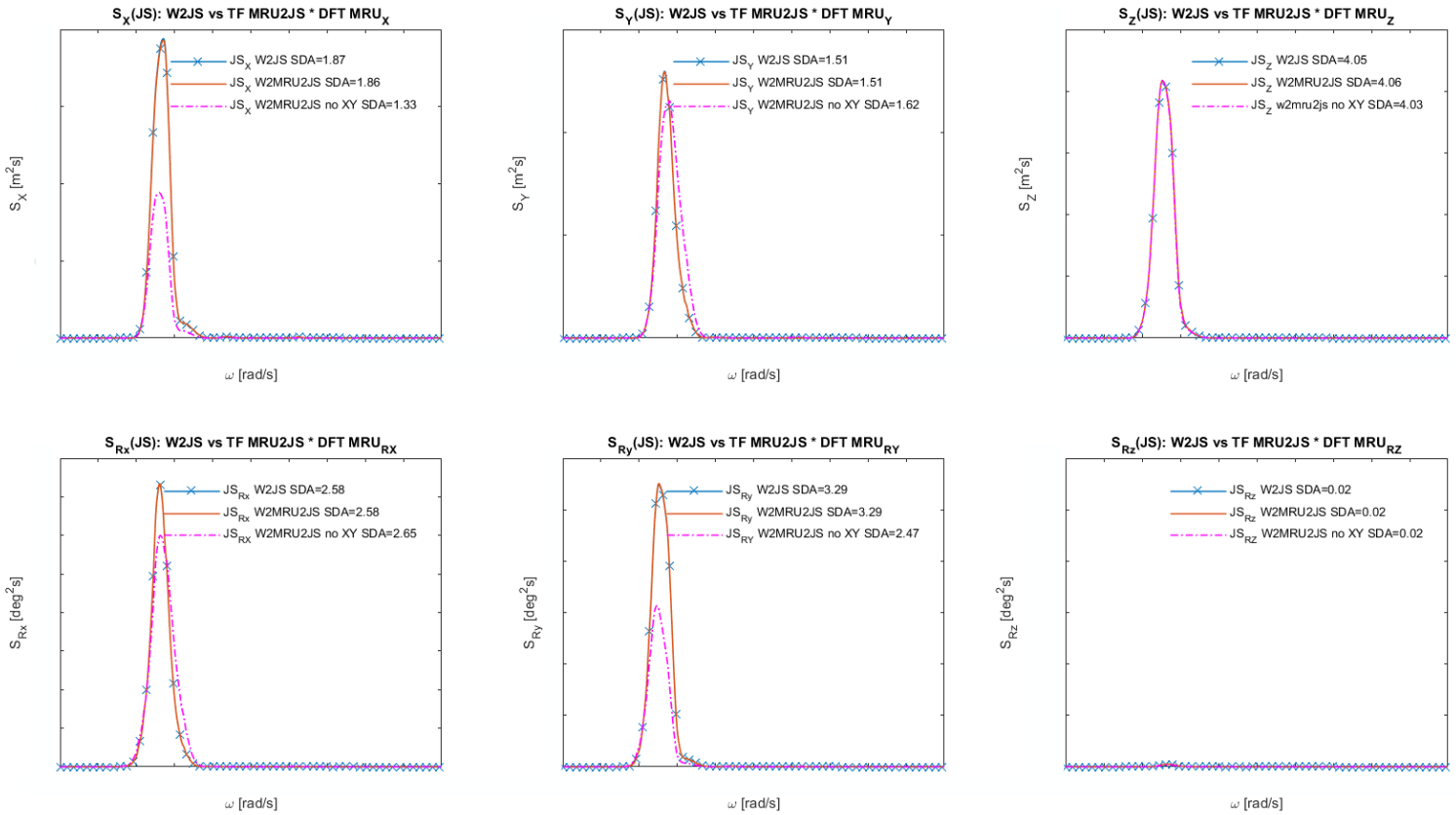
### 4.3.2 $S_{DOF_{JS}}$ from $S_{DOF_{MRU}}$ & TFs (MRU2JS) [VT5]

The proposed TF A2B Method in 3.6 is now finally used to find the responses of all six motions at the jacket sensor. To prove that the transmissibility functions between the MRU (A) and the jacket sensor (B) can be obtained from RAO's out of Liftodyn and find the correct responses at the jacket sensor, it must be shown that the response of all six motions at the jacket sensor **not** on the same rigid body as the MRU, found by using the restrained TF [6x6] (TF MRU2JS), is equal to the set of responses at the jacket sensor found by the unrestrained set of RAO's [6x1] from waves to the jacket sensor (W2JS) (eq 4.5).

$$S_{\zeta}(\omega) \cdot RAO_{\zeta, DOF_{JS}}^2 = S_{DOF_{JS}}(\omega) \quad (4.5)$$

$$DFT_{DOF_{MRU}}(\omega) \cdot TF_{DOF_{MRU}, DOF_{JS}} = DFT_{DOF_{JS}}(\omega) \xrightarrow{DFT2Spec} S_{DOF_{JS}}(\omega)$$

To verify this, simulations with the SDM model are done. In figure 4.10 the responses at the jacket sensor are shown for a relative wave direction of  $150^\circ$ . All six responses of the jacket sensor in figure 4.10 are within the wave frequency domain. This is expected as the input of the model currently is a Jonswap spectrum (figure 4.11) to represent the waves. It can be seen that there is no spectral density before 0.36 rad/s. This would then also result in no response in any motion of the vessel below this frequency, which is also what can be seen in all six plots of figure 4.10. What can also be seen is that the TF A2B Method W2MRU2JS (orange line) results in the same response in every degree of freedom as if the direct approach W2JS (blue line) would be used. The blue lines are not visible as the orange line (W2MRU2JS) is exactly on top of the blue line (W2JS). This is in line with the theory explained in 3.3.2. This proves that the transmissibility functions between the MRU (A) and the jacket sensor (B) can be used to find the correct response at the jacket sensor (B) which is **not** on the same rigid body [VT5].



A difference between the plots of the responses at the CP (figure 4.5) and the plots of the responses at the JS (figure 4.10) is the contribution of Surge and Sway of the vessel to Pitch and Roll motions at the JS. In the two bottom left plots of figure 4.10 the magenta lines which show the response without contribution of Surge and Sway of the vessel show a deviation of the orange lines. This shows that Surge and Sway motions of the vessel at the MRU influence the Pitch and Roll motions at the JS, respectively. This is a logical result as the jacket is suspended in one of the cranes, which makes it possible for the jacket to move in a pendulum like motion. A Surge motion of the vessel can Pitch the jacket and a Sway motion of the vessel can Roll the jacket. At the CP (fig 4.5) this is not possible as both the MRU and the CP are located on the same rigid body. The vessel therefore will Roll and Pitch the same amount at the MRU and the CP.

An interesting observation between the response in Yaw at the jacket sensor (figure 4.10, bottom right plot) and the response in Yaw at the control point (figure 4.5, bottom right plot) is that there is a bigger response of Yaw at the control point than at the jacket. A closer look to the transmissibility functions for the Yaw motion at the jacket sensor in figure 4.12 shows that in the wave energy domain (0.36 rad/s to 1 rad/s) obtained from the selected Jonswap spectrum (fig 4.3), there is almost no amplification by all six transmissibility functions.

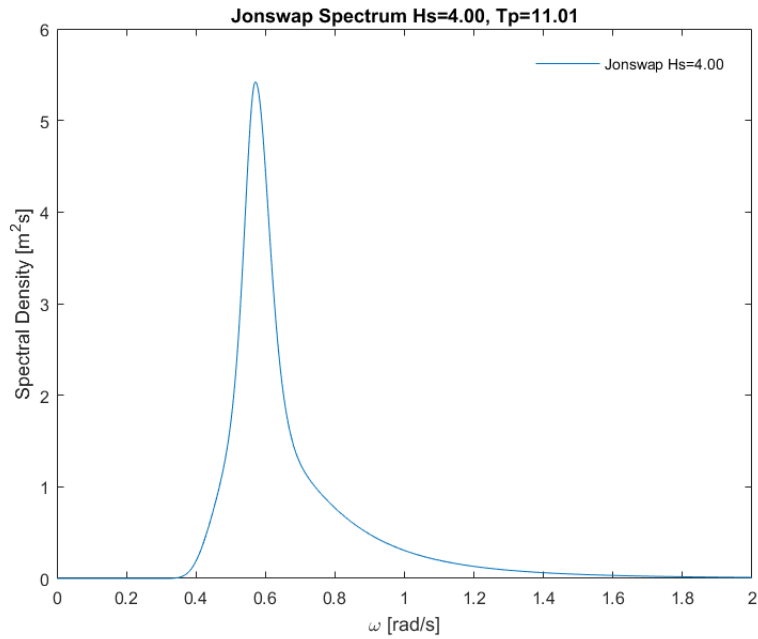


Figure 4.11: The Jonswap spectrum used as input for the SDM

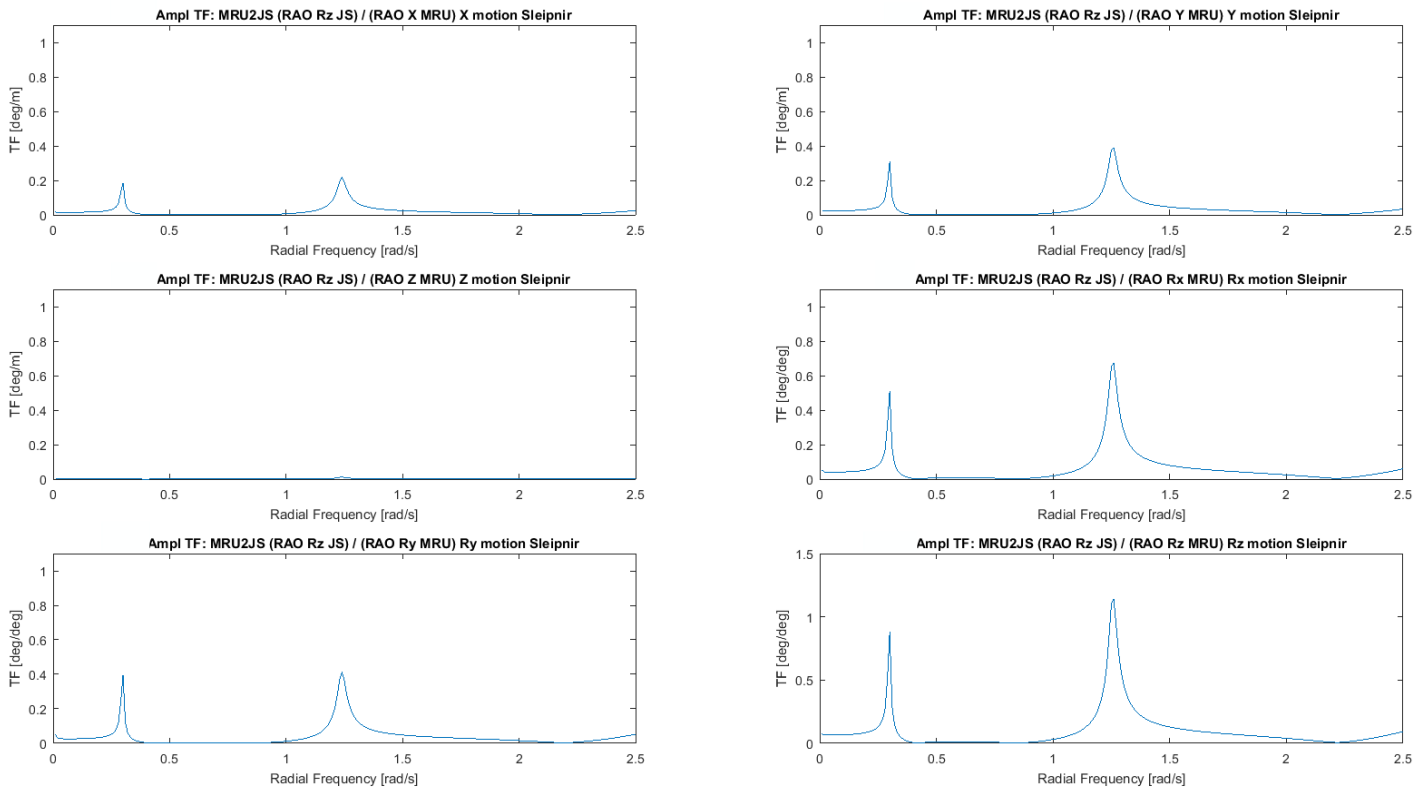


Figure 4.12: Transmissibility functions for the Yaw motion at the JS due to motions at the MRU

After further research, the cause of such a small Yaw response at the JS, is a restraint applied to the main block of the crane in the Liftdyn model. This restraint was applied as the suspended jacket would otherwise rotate many degrees within the model simulations. This is behaviour of the suspended jacket which doesn't reflect reality and was therefore modeled with this restraint. This however results in that the jacket cannot Yaw, as the rigging setup is not allowed to Yaw. This results in that the model cannot find any Yaw motion at the JS. The main block restraint is shown in figure 4.13.

When applying the TF A2B Method, care must be taken not to overlook hidden restraints in the Liftdyn model. The method can identify these restraints if a response at location B is practically zero and a bigger response is expected following the corresponding transmissibility functions and the responses at location A. It is therefore recommended to always perform a sanity check before applying this method.

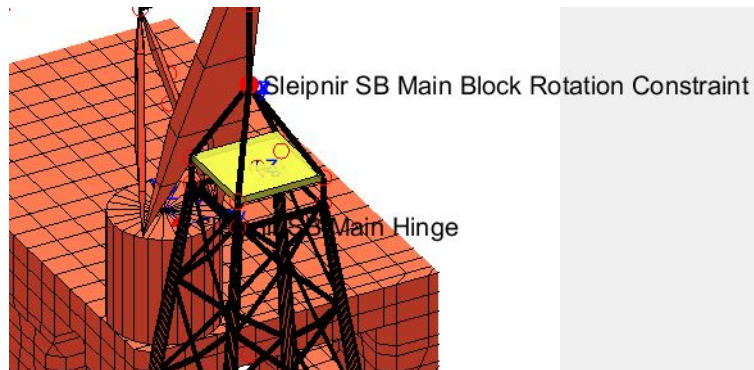


Figure 4.13: Yaw constraint at the SB main block of the crane

From an analysis of the transmissibility functions between the MRU and the JS in combination with the response at the MRU, it is found that the motions at the MRU that contribute most to a Surge motion at the jacket sensor are a Surge and Pitch motion at the MRU, with a smaller contribution of Yaw. The other motions at the MRU do also contribute, but in a much smaller extent. This is a logical result as motions at the MRU more easily excite in-plane motions at the JS. The transmissibility functions required for a Surge motion at the JS are shown in figure 4.14.

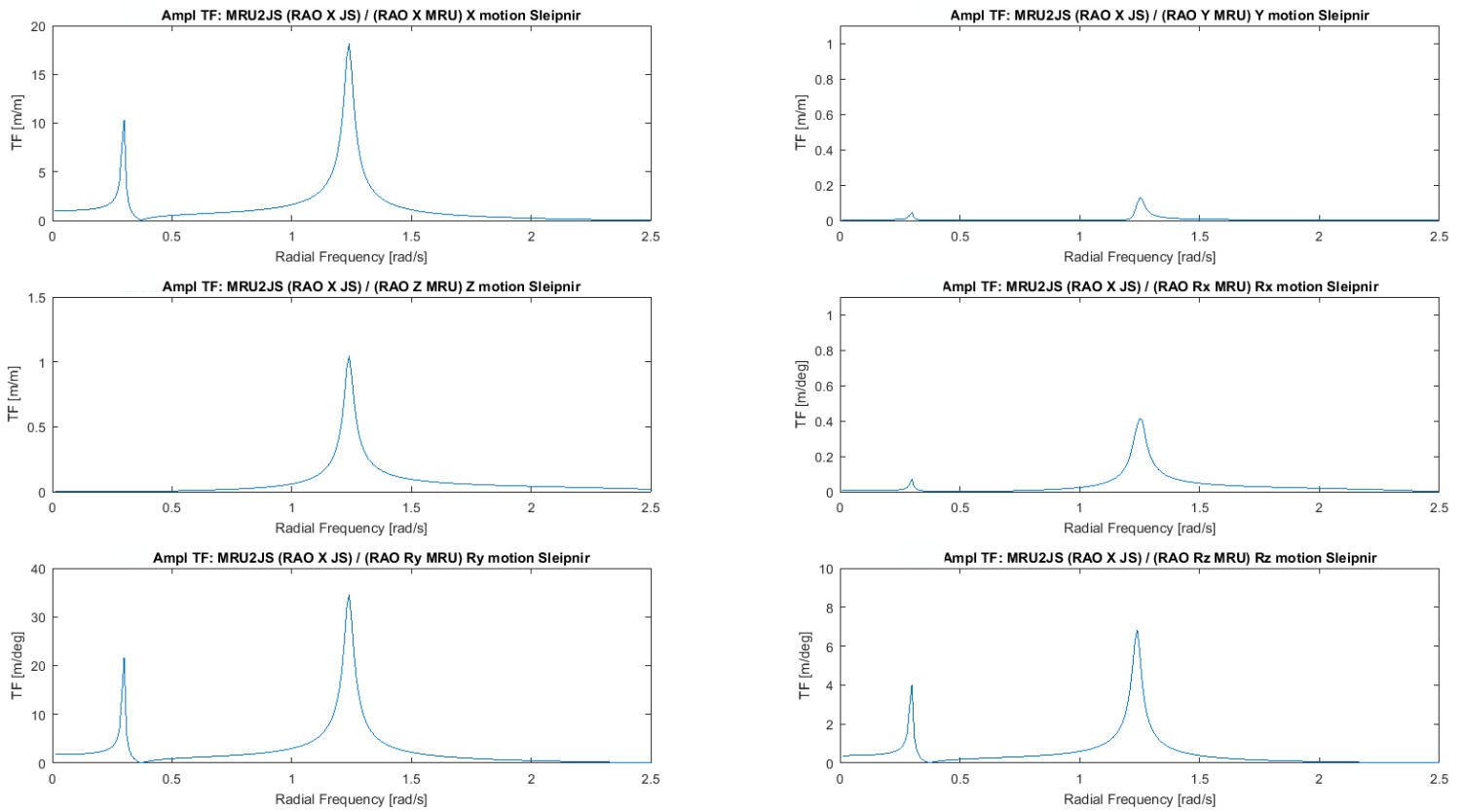


Figure 4.14: Transmissibility functions which contribute to a Surge motion at the JS

The Surge, Pitch and Yaw TF at the MRU to a Surge motion at the JS show the biggest amplification of motions over the frequency domain. These are the top left plot, bottom left and bottom right plot in figure 4.14 respectively. This however does not tell the full story as the responses at the MRU over the frequency domain also have to be taken into account. The Yaw RAO from waves to vessel is small within the wave frequency domain, resulting in a small Yaw response at the MRU of the vessel. Therefore, even though the TF between Yaw at the MRU and Surge at the JS is significant over the frequency domain, the Yaw motion almost doesn't affect the Surge motion of the jacket. All transmissibility functions required to obtain the response of a degree of freedom other than Surge at the jacket sensor from the motions at the MRU are found in Appendix E.

With the responses at the MRU and the strongest coupling TFs between the vessel motions to jacket Surge, again plots with the most contributing responses at the MRU to the Surge motion at the jacket sensor can be made. The most contributing motions at the MRU to a Surge motion at the JS are shown in figure 4.15.

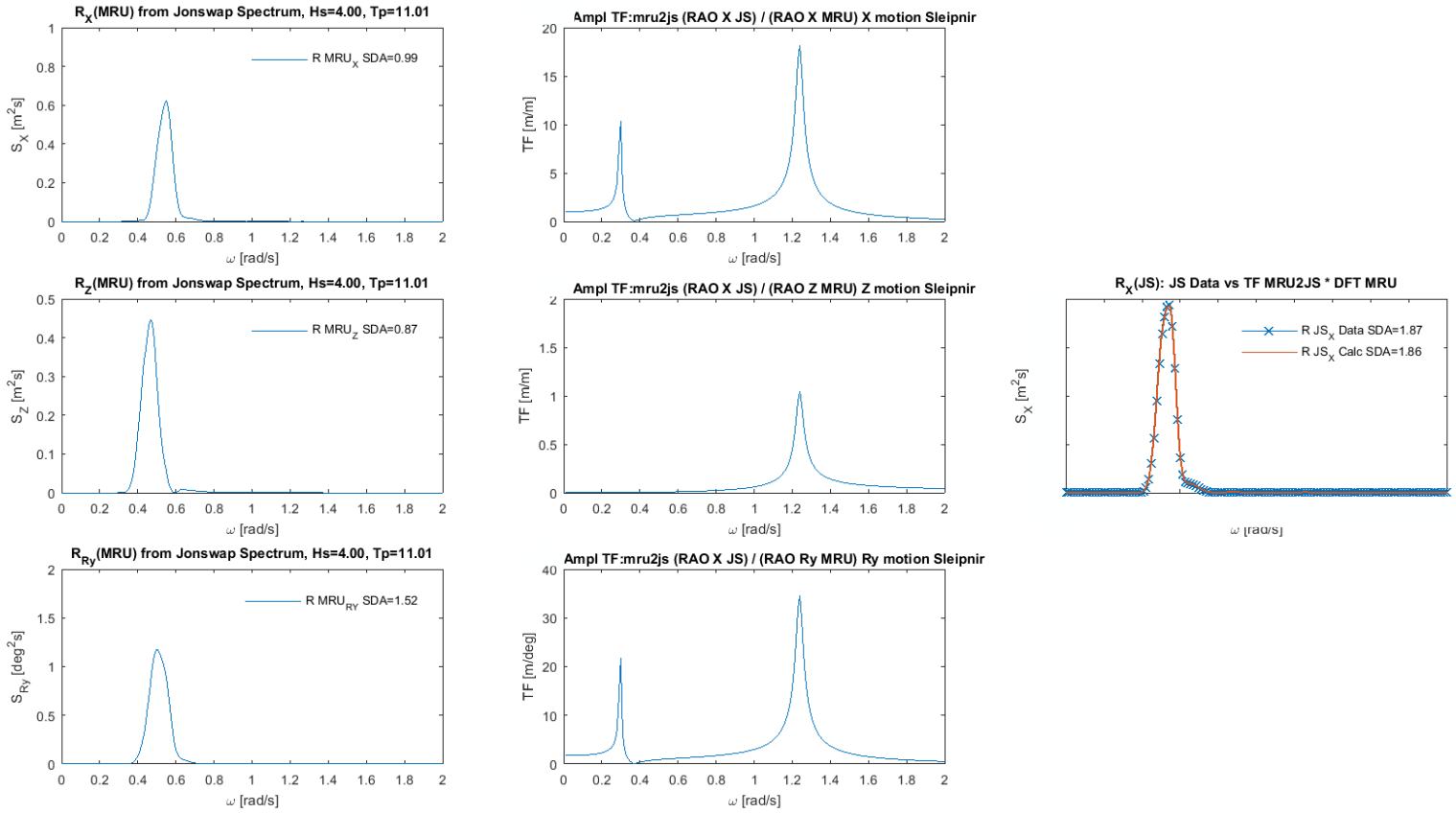


Figure 4.15: Main contributions to the Surge motion at the JS

### 4.3.3 Conclusion TF A2B Method

By performing the validation tests (sec 3.2) using the Synthetic Data Model (sec 3.6), it is shown that:

- The transmissibility functions (TFs) do not change much for different draft. [VT1]
- The TFs between the MRU(A) and the CP(B), which lay on the same rigid body are correctly found by the SDM using RAO's from Liftdyn. [VT2]
- The TFs between the MRU(A) and the CP(B) can be used to find the correct response at the CP(B). The CP(B) lays on the same rigid body as the MRU(A). [VT3]
- The TFs between the MRU (A) and the JS (B), which do **not** lay on the same rigid body are correctly found by the SDM. [VT4]
- The TFs between the MRU(A) and the JS(B) find the correct response at the JS(B). The JS(B) does **not** lay on the same rigid body as the MRU(A). [VT5]

Hereby, it is concluded that the TF A2B Method can correctly find motions at location B by using the motions of location A in combination with the corresponding transmissibility functions between A and B. Furthermore, it is validated that the TFs can be calculated by using RAO's obtained from Liftdyn. Specific deviations within the method can be fully explained by existing limitations of the Liftdyn model.

# Chapter 5: The Measured Data Model

Until now the proposed TF A2B Method is only used with the Synthetic Data Model. The calculated jacket motions resulting from simulated vessel motions at the MRU as input, in combination with the TFs from MRU to JS (MRU2JS) could be checked on correctness by the jacket motions resulting directly from the Jonswap Spectrum (W2JS) [VT4]. As both methods, directly (W2JS) and indirectly (W2MRU2JS) were dependent on the selected Jonswap Spectrum and linear theory, the resulting jacket motions by the two methods were exactly equal. Now, instead measured vessel motions at the MRU during the X suspended transport will be used as input to find the responses of all six degrees of freedom at the jacket sensor. The used model is therefore called the Measured Data Model (MDM). The data is provided by HMC for the unrestrained suspended jacket transport from site to Vats, both in Norway for the duration of 2 days. The measured vessel motions will be used to calculate the jacket motions with the MDM. These will be compared with measured jacket motions during the X transport, to verify how accurate the TF A2B Method is with real data. Within the Measured Data Model, the accuracy of the sensors at the MRU and JS become important, just as if modelled masses, damping and stiffness within the system are a correct representation of reality. Non-linearities within the system which are not fully captured by the linear TFs, calculated from the RAO's obtained from the Liftdyn model may also result in inaccurate calculated jacket motions. The goal of this chapter therefore is to validate the Liftdyn model of X. The Liftdyn model is validated if the results of the measured and calculated jacket motions match quite accurately. With this validation it is possible to extract the force RAO's at the boom pivots from Liftdyn which are required to find the stresses. An overview of the MDM is shown in figure 5.1.

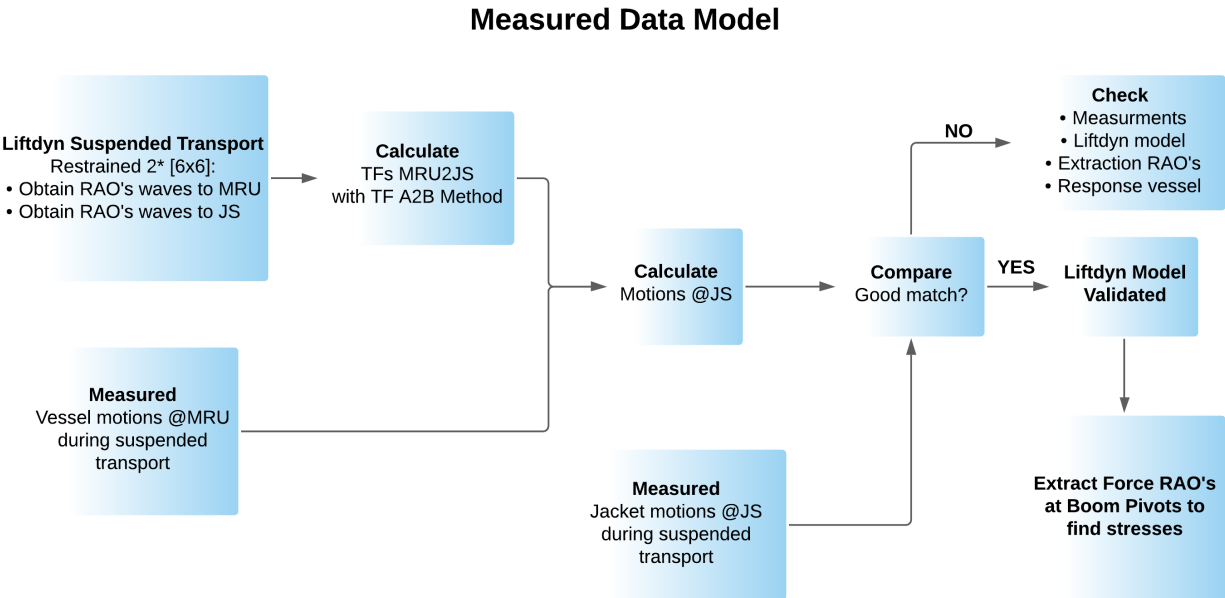


Figure 5.1: The Measured Data Model (MDM)

## 5.1 Background information X

Figure 5.2 shows the sailing route from site to Vats. The transport distance is 170 nautical miles to sheltered waters (Bokna Fjord). Sleipnir will still need to sail 40 nautical miles further in-shore to reach Vats. It is expected that the vessel behaves different in the Fjord than at open sea as there are less waves in the Fjord.

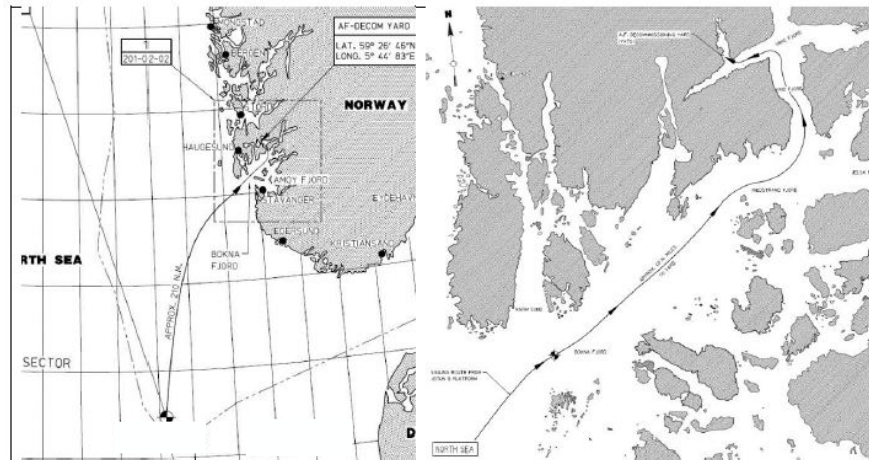


Figure 5.2: Sailing route from site to the decommissioning yard (Vats) [12]

## 5.2 Data selection X transport

The MDM mathematically given in appendix G is dependent on the measured vessel motions of Sleipnir. To be statistically more confident about the results, there are a few measures taken to improve the quality of the results.

A sample size with a minimum of 75 minutes of data is selected to be able to create a reliable spectrum capturing motions starting from 0.15 rad/s up to the upper limit defined by a low-pass filter set at 1.5 rad/s. The high-pass filter at 0.15 rad/s is applied to remove any energy close to 0 rad/s. Sensors frequently capture noise around 0 rad/s which creates an offset of the data which is incorrect. Especially when calculating Significant Double Amplitudes (SDAs) in the frequency domain this results in incorrect results. The high-pass filter set at 0.15 rad/s is still able to capture all prominent mode shapes of the system as these are found for frequencies higher than 0.15 rad/s. A rule of thumb frequently used by marine specialists within HMC, is that in order to create a reliable spectrum, 100-cycles of the lowest frequency that is assessed are required. For example: If the lowest frequency required has a 45s period ( $\omega = 0,14$  rad/s), approximately  $45 \cdot 100 = 4500s = 1,25h$  of data is required. Statistically results become less meaningful with a shorter duration.

The sampling speed of the sensor at the MRU is 1Hz (1s). The Nyquist frequency of the sensor is therefore 0.5Hz. This results in that until a frequency of  $\omega = \pi$  rad/s, signals can be captured. Following the rule of thumb used by marine specialists of HMC, a signal up to  $\frac{f_{sample}}{10} \geq f_{sig} = \frac{1}{10} = 0,1\text{Hz} = 0,628$  rad/s can be captured with full confidence. This is however in the middle of the wave frequency domain and that's why the low pass filter is set to 1.5 rad/s. There was no energy found for higher frequencies than 1.5 rad/s and if energy was found here this was statistically less reliable. The results between 0.628 rad/s and 1.5 rad/s should also be handled with more caution as they are statistically less reliable.

To obtain the most confidence that the model captures the motions of the jacket correctly, the best starting point of the analysis is to choose a suspended transport with the most notable vessel motions (Roll of the vessel of at least  $0.5^\circ$ , Pitch of at least  $0.2^\circ$ ). The suspended transport of X was therefore selected instead of other suspended transports, as bigger motions were measured during the suspended transport of X.

The selected sample for the analysis is a sample taken from the X Transport with the following characteristics:

- Start: -04-2021 11:00 UTC+2
- End: -04-2021 12:15 UTC+2

Other important data used in the model:

- Sampling rate jacket sensor: 0.2s
- Sampling rate motion sensor vessel: 1s
  - -> Up-sampling of the vessel motion sensor to 0.2s
- A high-pass filter applied at 0.15 rad/s to all motion measurements
- A low-pass filter applied at 1.5 rad/s to all motion measurements

The selected sample is shown between the red vertical lines in figure 5.3. In the top two plots notable Roll and Pitch motions of the vessel (Roll of the vessel of at least  $0.5^\circ$ , Pitch of at least  $0.2^\circ$ ) can be seen, respectively.

In the third plot it can be seen that the jacket is suspended as shown by the load in the crane. In the fourth plot the actual draft of 16.6m can be found and in the fifth and sixth plot it can be seen that Sleipnir is sailing in NNE direction to Vats with an almost constant speed of 4 m/s.

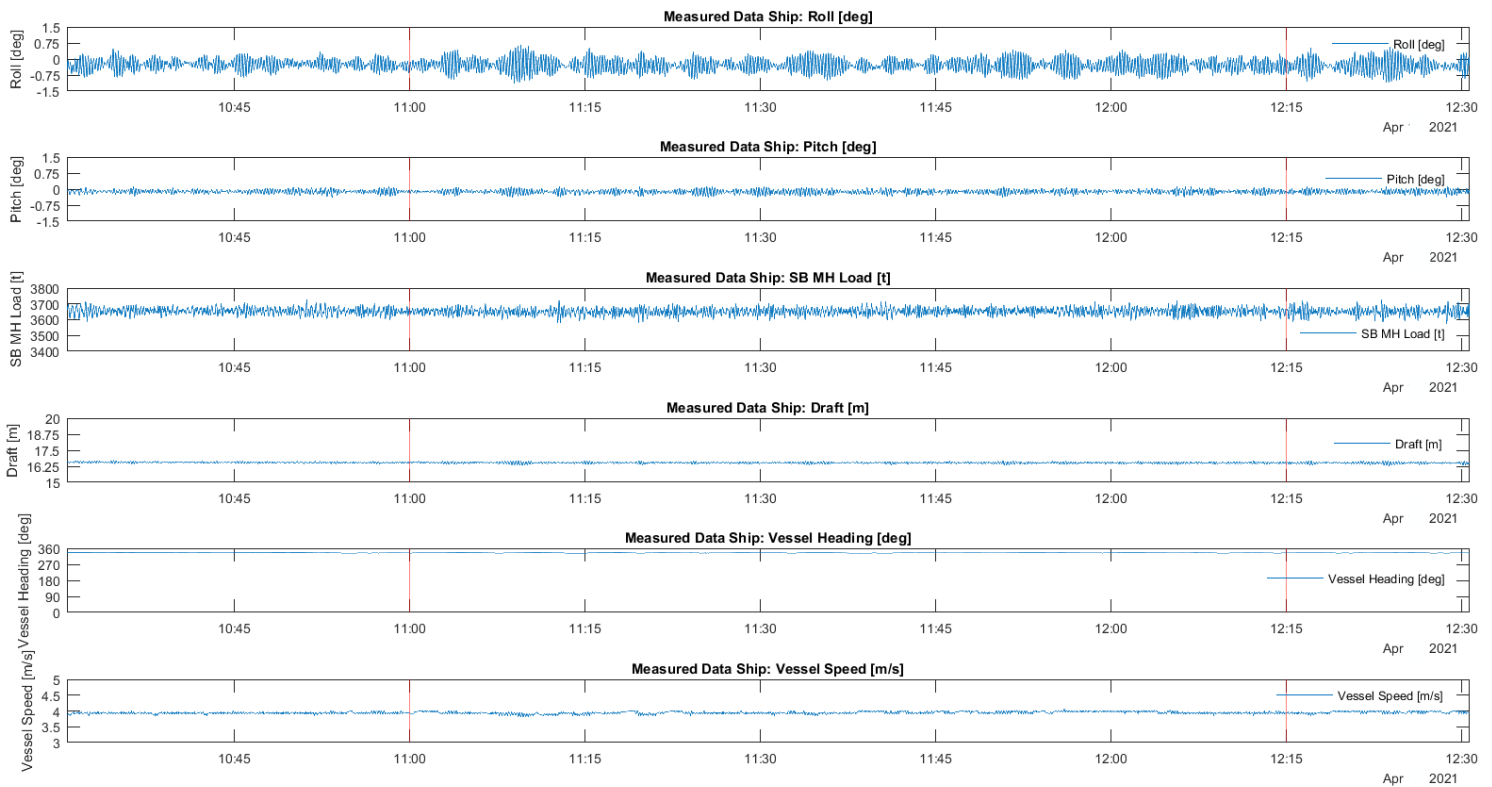


Figure 5.3: An overview of parameters during the X Transport and the selected sample between the red vertical lines

## 5.3 Data processing

### 5.3.1 Data pre-processing

All vessel motions measured during the X suspended transport are obtained from the Kognifai system of Sleipnir. This data comes from a different axis system as proposed in 2.1 (a right handed system with the Z axis downwards instead of upwards). Some measured vessel motions therefore had to be transformed, namely Heave, Pitch and Yaw. Sway is found differently as will be explained in 5.4.2.

All jacket measurements were obtained from the jacket sensor which for the X suspended transport was already positioned in the same way as the proposed axis system. Therefore, an axial transformation was not required. For the analysis of any other suspended transport the orientation of the axis system of the jacket sensor should be handled with caution and possible transformed to a right handed axis system with the Z axis pointing upwards. A picture of the jacket sensor is shown in figure 5.4 in which also the proposed axis system is found. In table 5.1 the measured parameters at the jacket sensor and some of the measured vessel parameters can be found.



Figure 5.4: A picture of the jacket sensor and the proposed axis system [13]

Vessel parameters	Unit	Jacket parameters	Unit
Heave	m	Acceleration X	$m/s^2$
Pitch	deg	Acceleration Y	$m/s^2$
Roll	deg	Acceleration Z	$m/s^2$
Gyro	deg	Rotational speed RX	m/s
Easting	m	Rotational speed RY	m/s
Northing	m	Rotational speed RZ	m/s
PS main hoist load	t	Pitch	deg
SB main hoist load	t	Roll	deg
Draft	m	Time	s
Vessel speed	m/s		

Table 5.1: Overview measured parameters during transport

The sensors measure the total acceleration in a degree of freedom. After double integrating the accelerations in a degree of freedom, the motion in that degree of freedom is found. This implies that not only motions due to first order wave loading are captured, but also low frequency motions due to for instance crane slew and high frequency motions until the Nyquist frequencies of the sensors can be captured (within the capabilities of the sensor). The sensor does not make any distinction in where a contribution to the response comes from. The downside is that it can become unclear where a contribution in the response of a DOF of the vessel or jacket comes from. The effects due to the forward speed of the vessel and any other non-linear effect due to the waves are already captured by using the measured vessel motions. The main advantage of using the measured vessel motions is therefore that any inaccuracy in the modeled translation from wave to vessel response is omitted.

All measured data should be checked for erroneous samples before filtering. Sometimes the sensors measure a single sample with a very high acceleration/motion. These have to be manually removed as these samples do not represent reality. It is easy to spot if a erroneous is still present in the filtered data as the spectral energy in the frequency domain then gives very high SDA values. For example, if the significant wave height is expected to be 1m then a calculated heave spectrum at the JS with a SDA of 12m probably originates from an erroneous sample with a very high vertical acceleration of the jacket sensor. After removing the erroneous sample results more realistic heave motions are expected  $\approx \leq 1m$ .

## 5.4 Vessel motions X

### 5.4.1 Pitch, Roll, Heave and Yaw vessel

Pitch, Roll, Heave and Yaw of Sleipnir can directly be obtained from the motion sensors at the MRU. For the selected time sample Roll and Pitch motions are found in figure 5.5 and Heave and Yaw of the vessel are found in figure 5.6. The plots on the left side of figures 5.5 & 5.6 show the motions in the time domain. The raw measurements are filtered with a band-pass filter. The filter shifts the signal to fluctuate around the 0 axis to make it easier to read the signal.

The plots on the right side of figures 5.5 & 5.6 show the motions in the frequency domain. A useful back test to check that the transformation from the time domain to the frequency domain went correctly is to check if the SDA in the time domain calculated as  $SDA = 4 \cdot \sigma$  is within 10% of the SDA calculated in the frequency domain as  $SDA = 4\sqrt{m_0}$ . For all jacket & vessel motions shown in this thesis this is the case. The vertical line shows the high-pass filter at 0.15 rad/s. There are three SDAs given:

- For the low frequency domain (LFD) 0.15 rad/s to 0.35 rad/s
- For the wave frequency domain (WFD) 0.35 rad/s and higher
- For the full frequency domain (FFD) from 0.15 rad/s and higher

This way it is easier to see in which part of the frequency domain most energy is found. The following can be found from figures 5.5 & 5.6:

- Roll (top plots fig 5.5): most energy in the wave frequency domain, with a smaller peak around 0.2 rad/s probably excited by some low frequency swell waves. Roll is the biggest rotational motion the vessel makes (SDA=1.09°).
- Pitch (bottom plots fig 5.5): most energy in the wave frequency domain, with a smaller peak around 0.25-0.26 rad/s in the lower frequency domain (SDA=0.34°).
- Yaw (top plots fig 5.6): almost no motion in Yaw. Low frequency noise is filtered out by the high pass filter. That there is almost no yaw motion is expected as the vessel is sailing in one direction (SDA=0.11°).
- Heave (bottom plots fig 5.6): most energy in the wave frequency domain, with a smaller peak at 0.27 rad/s in the lower frequency domain (SDA=0.64m).

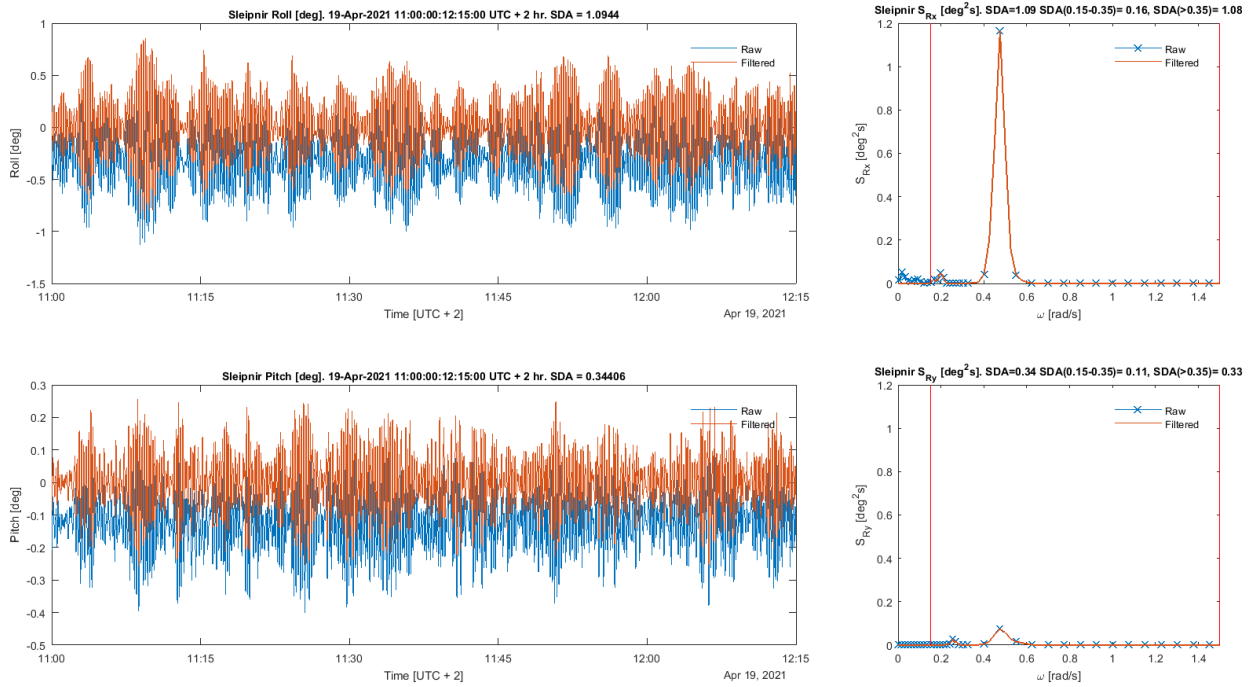


Figure 5.5: Roll & Pitch of the vessel

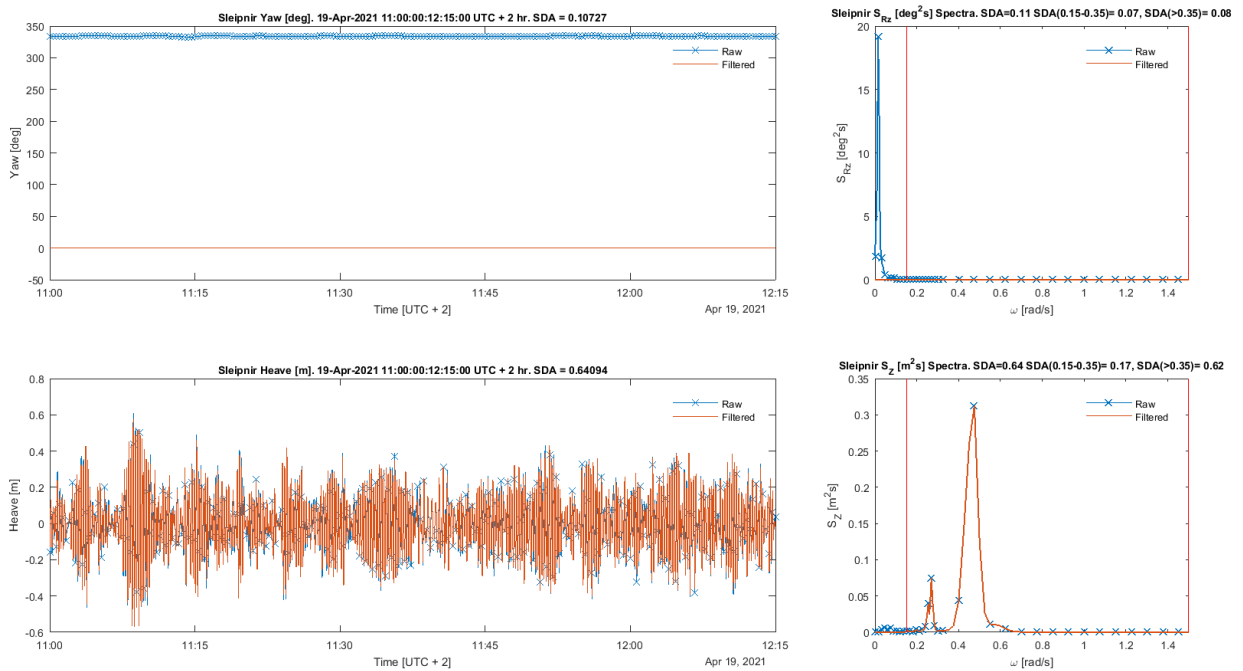


Figure 5.6: Yaw & Heave of the vessel

### 5.4.2 Surge & Sway of Sleipnir

Sleipnir's Surge and Sway are **not** directly measured at the MRU. A solution which has been examined is to use the Northing and Easting of the DP system in combination with the vessel heading of the vessel to obtain the Surge and Sway of Sleipnir. The Easting and Northing are obtained by 12 weighted measurements at the control point as in equation 5.1.

$$\begin{aligned} N &= \sum_{n=1}^{12} w_n * N_n \\ E &= \sum_{n=1}^{12} w_n * E_n \end{aligned} \tag{5.1}$$

The DP system records Easting and Northing at the CP of the vessel. In the right handed axis system described in 2.1, the Surge and Sway of the vessel at the CP can be found as in equation 5.2. The Surge of the vessel is a translation in the x-plane from a reference point, which is the location of the GPS sensor during transport. The Sway of the vessel is a translation in the y plane from the location of the GPS sensor. The GPS location of the vessel and sensor continuously change while sailing. As the motions of Sleipnir are mostly in the order of magnitude of dm and degrees (Roll & Pitch operational limits of  $\leq 1^\circ$  during X transport B [12]), it is important that the GPS sensor can accurately enough calculate the location of the vessel to obtain accurate measurements of Surge and Sway during the X suspended transport.

$$\begin{aligned} X_{cp} &= (N - N(1)) \cdot \cos(-H) + (E - E(1)) \cdot \sin(-H) \\ Y_{cp} &= (N - N(1)) \cdot \sin(-H) - (E - E(1)) \cdot \cos(-H) \end{aligned} \tag{5.2}$$

As all other vessel motions are measured at the MRU, the calculated Surge and Sway at the CP are translated to the MRU. This is done with the transformation matrix 3.7. This results in the Surge and Sway motions at the MRU shown in figures 5.7 & 5.8. As can be seen in figure 5.7, the Surge motion obtained from the GPS data is in the same order of magnitude of the other motions of the vessel (SDA=1m). There is however a lot of energy in the low frequency domain close to the high pass filter which can not be found for Roll, Pitch and Heave motions of the vessel.

It is therefore concluded that the Surge motion is not an accurate enough representation of the actual Surge of the vessel during the X transport. This results in that the Surge motion of the vessel is not taken into account for determining the motions of the jacket. This will especially influence the Surge and Pitch motion of the jacket and in a smaller extend the Heave motion of the jacket as in-plane motions have the strongest coupling. This is possible as all vessel motions in the model are uncoupled. Not taking into account a motion of the vessel therefore does not influence other contributions of the vessel to the jacket motions. It does however make the motions of the jacket less accurate as not all vessel motions are taken into account. How much less accurate the calculated jacket motions depends on the strength of the coupling between the vessel and jacket motions and how big the response of the contributing vessel motion was in the first place.

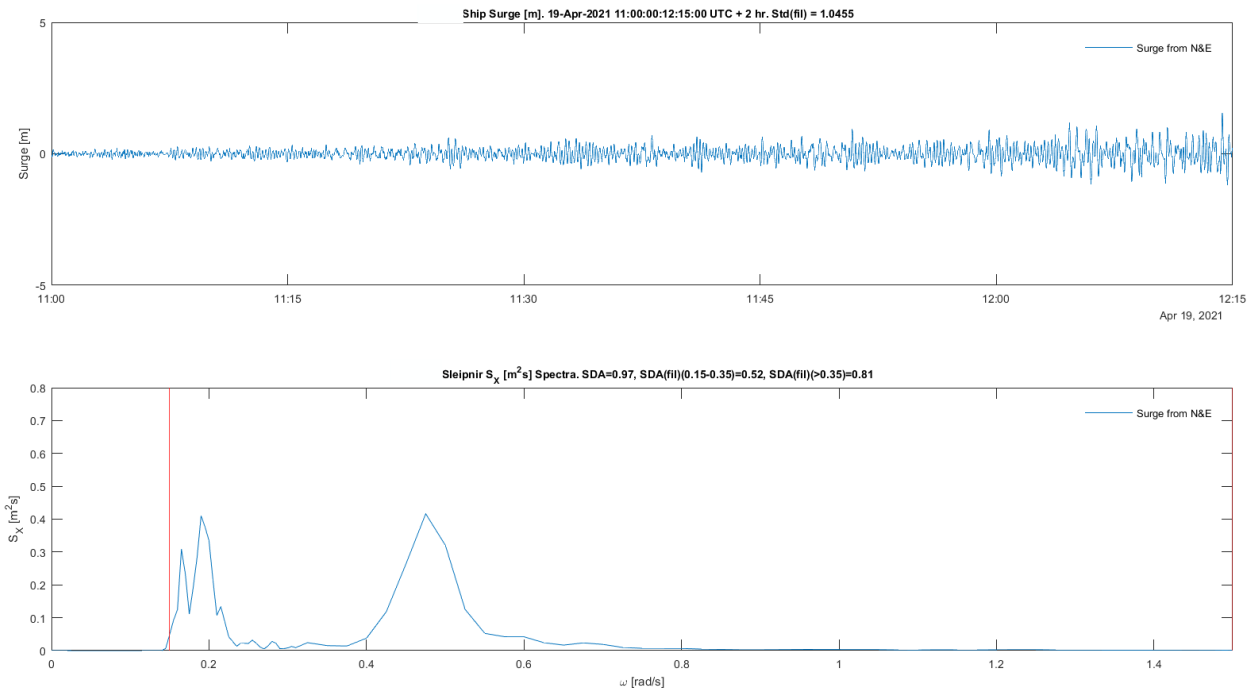


Figure 5.7: Surge at the MRU, obtained from GPS data

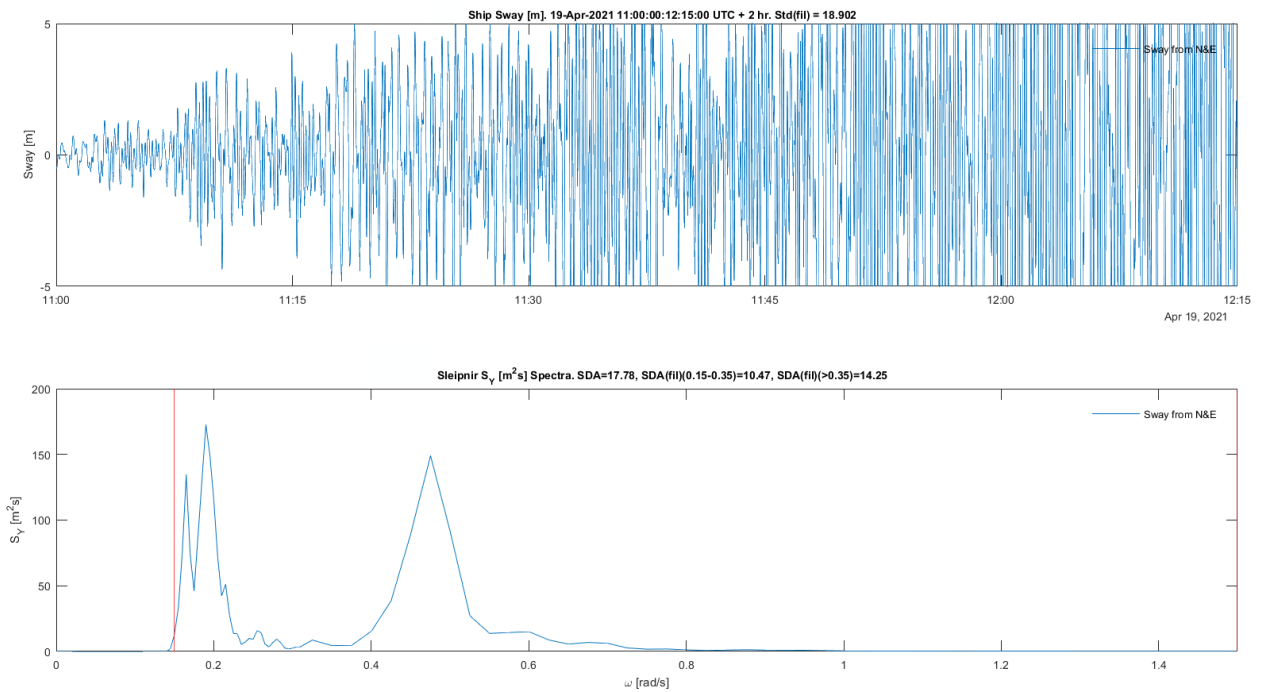


Figure 5.8: Sway at the MRU, obtained from GPS data

The Sway of the vessel shown in the plots of figure 5.8 is very inaccurate. The Sway motion obtained from the GPS data is not in the same order of magnitude as the other motions of the vessel but bigger. An SDA of 17.78 m vs SDA=1.09° for Roll and a SDA=0.64m for Heave of Sleipnir. Sway continuously increased within the sample by using this calculation method, even after removing the linear increase (de-trending). This increase of Sway in time can be seen in the top plot of figure 5.8.

It is therefore concluded that the Sway motion is not an accurate representation of the actual Sway of the vessel during the X suspended transport. This results in that the Sway motion of the vessel is not taken into account for determining the motions of the jacket.

This will especially influence the Sway and Roll motion of the jacket and in a smaller extend the Heave motion of the jacket. The main reason is that in-plane motions have a strong coupling which can be found from the transmissibility functions between the vessel and the jacket (appendix E). It is possible to remove a contribution of the vessel to the jacket motions as all vessel motions in the model are uncoupled. Not taking into account a motion of the vessel therefore does not influence other contributions of the vessel to the jacket motions but it does make the motions of the jacket less accurate as not all vessel motions are taken into account.

In total it is therefore concluded that the GPS sensor which measures the Easting and Northing of the vessel is not accurate enough to calculate the Surge and Sway motion of the vessel. It is therefore recommended that a more accurate sensor is installed which can calculate the Surge and Sway of the vessel at the MRU.



Figure 5.9: Left figure: waiting on weather Right figure: suspended X jacket

## 5.5 Jacket motions X

### 5.5.1 Roll, Pitch & Yaw

There are two options to obtain the Roll & Pitch motions of the jacket at the jacket sensor.

- Integrate rotational speeds obtained from the sensor
- Use the provided Roll & Pitch channels of the sensor

The provided Roll and Pitch channels of the motion sensor are used to check whether the integration of the jacket motions is done correctly within the Measured Data Model.

#### Roll jacket

In figure 5.10 the Roll of the jacket is shown. In the left plot the Roll motion is shown in the time domain and in the right plot in the frequency domain. The Roll directly obtained from the jacket sensor is plotted and the Roll motion found by the integration of the rotational Speed RX. The direct measured value (blue) is equal to the integrated value (red line) and are therefore on top of each other. This shows that the integration used in the scripts of the MDM works correctly. This integration method can therefore also be used to obtain the other jacket motions.

In the right plot the Roll motion is shown in the frequency domain. The vertical line shows the high-pass filter at 0.15 rad/s. There are three SDA's given, one for the whole frequency domain from 0.15 rad/s to 1.5 rad/s, one for the low frequency domain 0.15 rad/s to 0.35 rad/s and one for the wave frequency domain 0.35 rad/s to 1.5 rad/s. With an SDA of  $2.86^\circ$ , Roll is the biggest rotational motion of the jacket. It is excited mostly in the wave frequency domain, with a small peak at 0.31 rad/s in the low frequency domain. This is more than double the soft limit ( $1^\circ$ ) during the design phase of the project as defined in [12]. All limiting criteria during the X transport are found in appendix B.

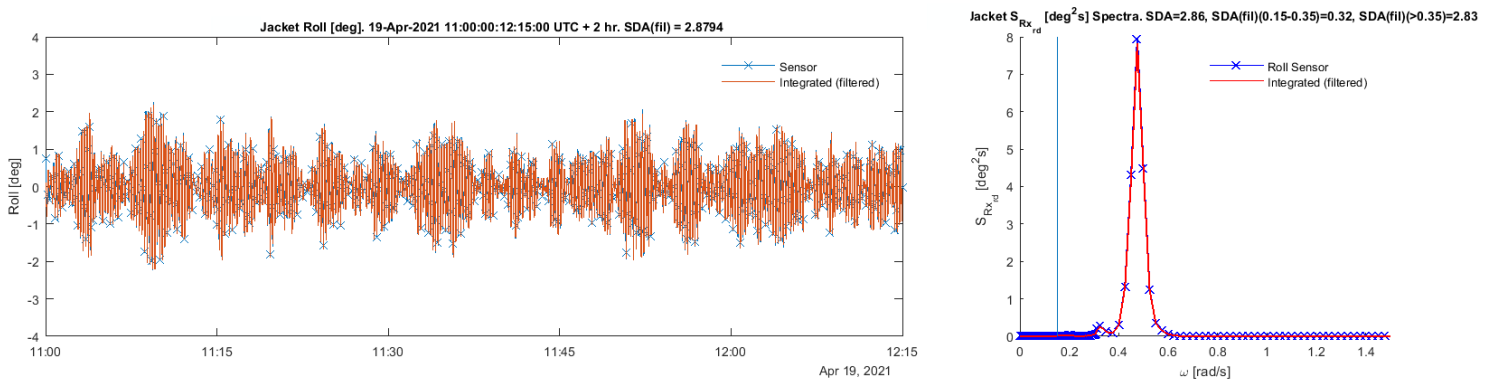


Figure 5.10: Roll of the jacket at the JS

### Pitch jacket

In figure 5.11 the Pitch of the jacket is shown. Again the Pitch directly found by the motion sensor (blue line) is equal to the Pitch found by the integration of the rotational speed  $R_y$  (red line). With an SDA of  $1.15^\circ$  Pitch is partly excited in the wave frequency domain but there is also excitation within the low frequency domain with a spectral peak  $0.27 \text{ rad/s}$  and an even bigger peak at  $0.31 \text{ rad/s}$ .  $1.15^\circ$  is approximately the soft limit ( $1^\circ$ ) defined during the design phase of the project [12].

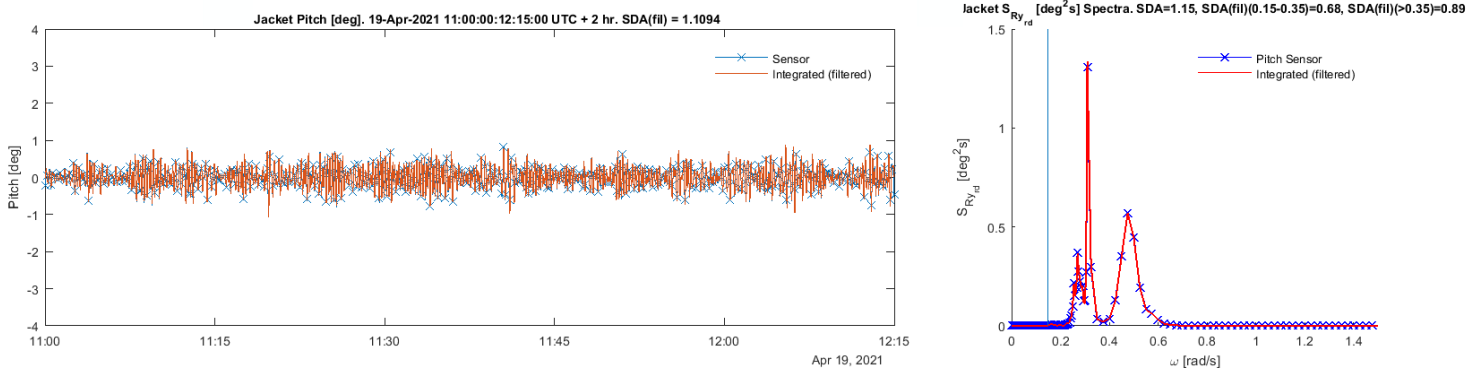


Figure 5.11: Pitch of the jacket at the JS

### Yaw jacket

In figure 5.12 the Yaw of the jacket is shown. Small Yaw motions are found in the wave frequency domain and in the low frequency domain with a second spectral peak around  $0.31 \text{ rad/s}$ . The Yaw motions ( $\text{SDA}=0.26^\circ$ ) also fall within the soft limit of  $1^\circ$  defined during the design phase of the project [12].

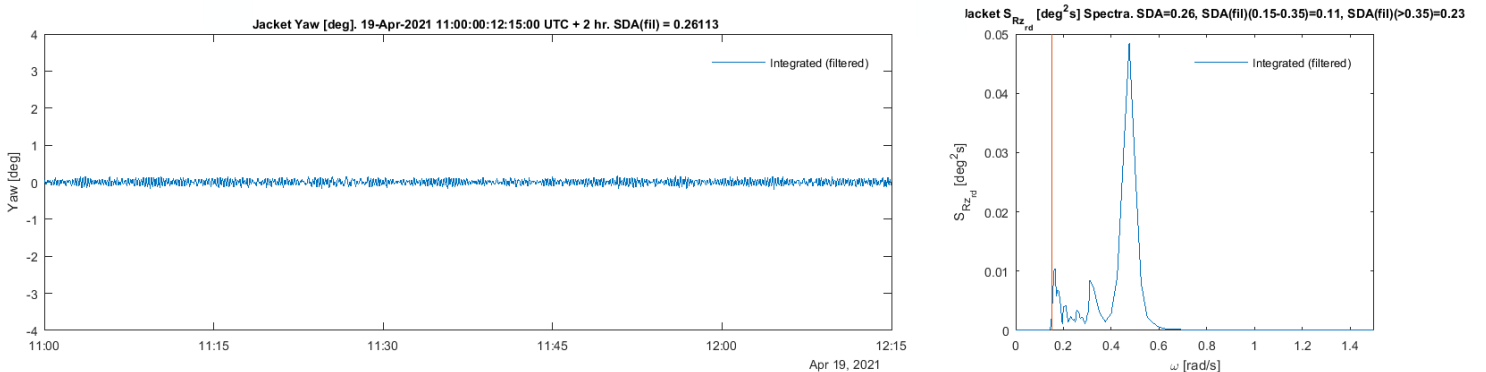


Figure 5.12: Yaw of the jacket at the JS

## 5.5.2 Surge, Sway & Heave jacket

The jacket sensor which is mounted on the jacket, measures accelerations in the X, Y and Z directions. To obtain Surge, Sway and Heave of the jacket the accelerations are integrated to velocities, which then again are integrated to obtain Surge, Sway and Heave of the vessel.

### Surge jacket

In figures 5.13 the Surge of the jacket is shown. With an SDA value of 1.33m, Surge is mostly excited in the wave frequency domain, but with spectral peaks at 0.27 rad/s and a bigger one at 0.31 rad/s, Surge of the jacket is also excited in the lower frequency domain.

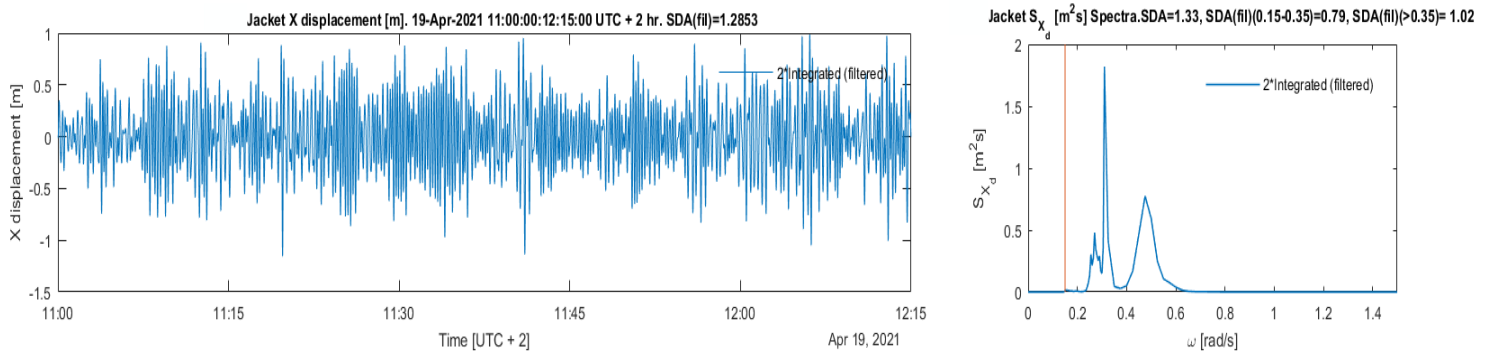


Figure 5.13: Surge of the jacket at the JS

### Sway jacket

In figures 5.14 the Sway of the jacket is shown. With an SDA value of 3.30m, Sway is the biggest translation of the jacket. Sway is mostly excited in the wave frequency domain (WFD), with again a small peak at 0.31 rad/s in the low frequency domain.

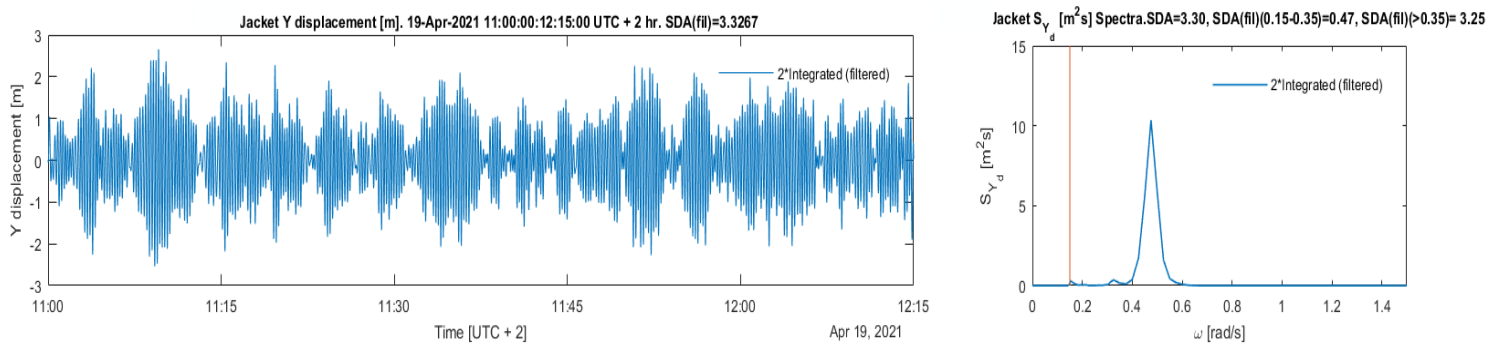


Figure 5.14: Sway of the jacket at the JS

## Heave jacket

In figures 5.15 the Heave of the jacket is shown. With an SDA value of 0.89m Heave is mostly excited in the wave frequency domain with a smaller spectral peak at 0.27 rad/s.

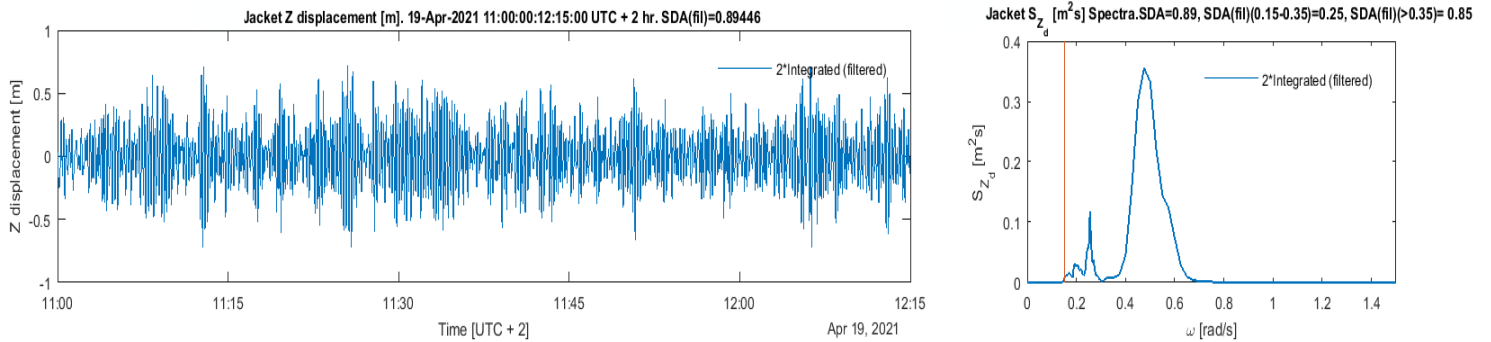


Figure 5.15: Heave of the jacket at the JS

It can be concluded that most of the jacket motions are found in the wave frequency domain. As the vessel is mostly excited by waves this is expected. There are also responses of the jacket found in the lower frequency domain around 0.27 and 0.31 rad/s which could originate from swell. These energy peaks are analysed in the next section by a mode shape analysis. An overview of all measured responses of the jacket are shown in appendix I. An overview of all SDA's is given in table 5.5.2.

Vessel	SDA LFD	SDA WFD	SDA FFD	Unit
Surge	-	-	-	m
Sway	-	-	-	m
Heave	0.17	0.62	0.64	m
Roll	0.16	1.08	1.09	deg
Pitch	0.11	0.33	0.34	deg
Yaw	0.07	0.08	0.11	deg
Jacket	SDA LFD	SDA WFD	SDA FFD	Unit
Surge	0.79	1.02	1.33	m
Sway	0.47	3.25	3.30	m
Heave	0.25	0.85	0.89	m
Roll	0.32	2.83	2.86	deg
Pitch	0.68	0.89	1.15	deg
Yaw	0.11	0.23	0.26	deg

Table 5.2: Overview off all SDA's during the X transport

## 5.6 Mode shape analysis

As the vessel is sailing it is mostly excited by the main excitation forces which are the waves in the wave frequency domain (WFD) (0.35 rad/s and up). To obtain a better understanding of why the system can move with less excitation outside of the WFD, a mode shape analysis can give more insights in the motions of the vessel and jacket.

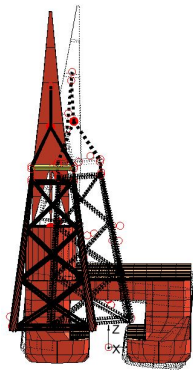
As already found by [1], there are low frequency domain mode (LFD) shapes ( $< 0.35$  rad/s) that induce pendulum like motions of the suspended jacket when excited. These pendulum motions should be handled with extra caution as these would easily affect the limiting criteria during suspended transport (appendix B).

For example, the horizontal x-motion at the bottom of the jacket should not exceed 5m, otherwise there is a bigger probability that the jacket clashes with Sleipnir as the distance between Sleipnir and the jacket is 8m [12]. The mode shapes can be obtained from Liftodyn. A full list of all mode shapes and indication of expected motions can be found in ???. In the LFD there were 3 peaks found with resulting motions of either the vessel or the jacket. These motions can be analysed by 6 mode shapes.

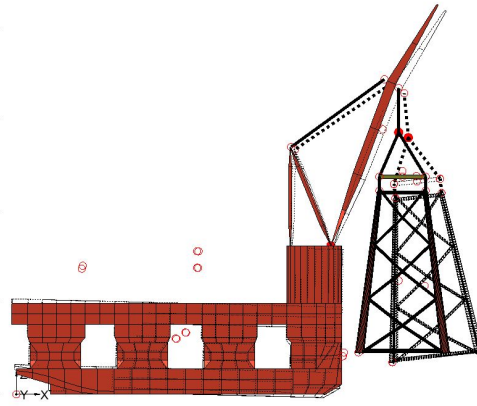
1. In the measured data a Roll motion of the vessel is found at approximately 0.18-0.2 rad/s (fig 5.5)(SDA LFD=0.16°). The closest mode shape has a natural frequency of 0.18 rad/s whilst a bit more motion in Roll of the vessel is found at 0.2 rad/s (fig 5.16a). This mode shape also suggests a Roll motion of the jacket which can also be found. Small frequency differences in mode shapes can originate from:
  - As only one sample of data is used (75 min), especially the low frequency motions (around 0.15 rad/s) found could be inaccurate as potentially not enough low frequency cycles are analysed. The biggest peak for Roll of the vessel now found at 0.2 rad/s could therefore also be somewhat lower or higher (0.18 rad/s) in the frequency domain as statistically the spectrum is less reliant with lower amount of cycles.
  - The panel method used within the diffraction analysis is not created for moving vessels. The potential coefficients require a correction with a lever arm  $\overline{OG}$  between CoG of the moving vessel(G) and the origin in the waterline value [5]. Besides this also an approximately steady flow potential has to be taken into account for a vessel with constant forward speed. Within the diffraction analysis these adjustments are not performed and also HMC's unproven way of adjusting the wave forces (and wave spectra) for forward speed is not taken into account. This can result in different added mass values at certain frequencies for a moving vessel. As the mode shapes are calculated by solving the eigenvalue problem  $eig(C, M + A(\omega)) = 0$ , the mode shapes for a sailing vessel can be found at somewhat different frequencies (0.01-0.02 rad/s) then for a stationary vessel.

- Within HMC it is also uncertain how accurate the diffraction analysis with damping lid is. This could lead to small changes differences in added mass with resulting small differences in mode shapes (0.01-0.02 rad/s)
- 2. The motions of the jacket and vessel found in the measured data around 0.26-0.27 rad/s are confirmed by mode shape fig 5.16b & 5.16c. The mode shapes show Heave & Pitch motions of the vessel and Heave, Surge & Pitch motions of the Jacket.
- 3. The motions of the jacket around 0.31-0.32 rad/s are confirmed by two mode shapes at 0.31-0.32 rad/s found in figure 5.16d & 5.16e. The mode shapes show clear pendulum modes with motions in all 6 degrees of freedom at the jacket sensor.

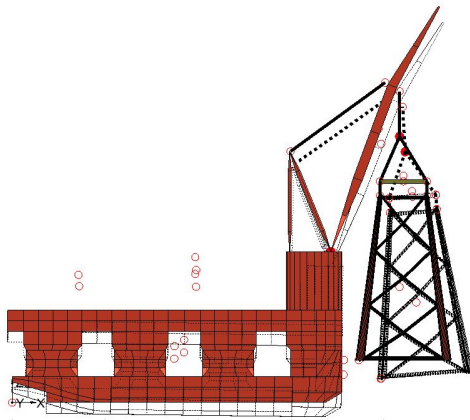
The sensors induce possible inaccuracies in the measured jacket and vessel motions. On the other side there are possible inaccuracies in the modelled hydrodynamic stiffness's and added masses which can originate from the forward speed problem and inconvenient draft problem. The results of the mode shape analysis however show that the abrupt peaks of the measured motions of the jacket and vessel can be found within an accuracy of 0.01 rad/s with the mode shapes from the model. This shows that these inaccuracies have a relatively small effect on the response of the vessel. This is however based on 1 sample and it is therefore recommended to take into account more samples.



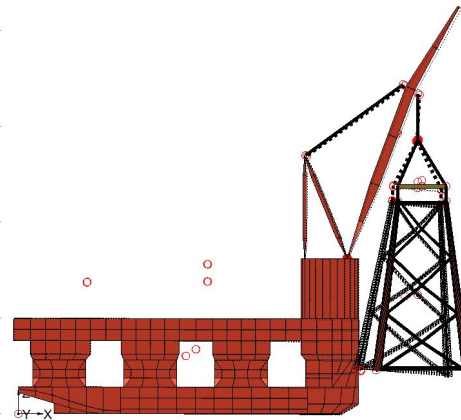
(a) Mode shape at  $T=34s$   $\omega=0.185$  rad/s.  
Mainly Sway and Roll Jacket.  
Vessel Roll



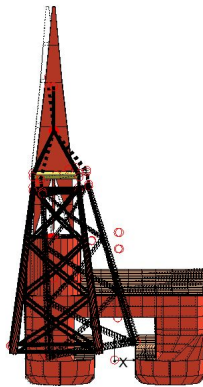
(b) Mode shape at  $T=24.09s$   $\omega=0.261$  rad/s.  
Mainly Heave, Pitch & Surge Jacket.  
Vessel Heave & Pitch



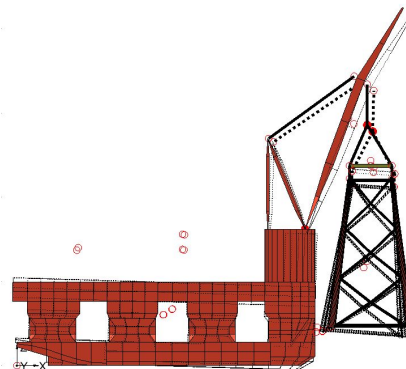
(c) Mode shape at  $T=23.27s$   $\omega=0.27$  rad/s.  
Mainly Heave, Pitch & Surge Jacket.  
Vessel Heave & Pitch



(d) Mode shape at  $T=19.99s$   $\omega=0.314$  rad/s  
Pendulum motion in x-plane jacket.  
Surge and Pitch of the vessel



(e) Mode shape at  $T=19.47s$   $\omega=0.323$  rad/s  
Pendulum motion in y-plane jacket.  
Sway and Roll of the vessel



(f) Mode shape at  $T=13.48s$   $\omega=0.466$  rad/s  
Pendulum motion in x-plane jacket.  
Surge and Pitch of the vessel

Figure 5.16: Important mode shapes X suspended transport

## 5.7 Model adjustment for real data MDM

The difference in input between the Synthetic Data Model (Jonswap spectrum) and the Measured Data Model (measured vessel motions) results in that the Synthetic Data Model described in section 3.6 has to be adjusted. In the Measured Data Model there is no verification point in the control point anymore, as there are no data measurements at the control point which could verify that the model finds the correct motions.

In the MDM there is no Jonswap spectrum required to simulate the vessel motions at the MRU (eq 3.12). Instead, the measured vessel motions at the MRU during the X transport are used. By knowing the motions of point A (mostly caused by the waves) the motions of point B are calculated without the need of having to know the exact sea state at every point of the transport (eq 3.1 [3]). Equation 3.12 therefore changes into equation 5.3.

$$S_{\zeta}(\omega) \xrightarrow{\text{Spec2DFT}} \begin{pmatrix} DFT_{\zeta} \\ DFT_{\zeta} \\ DFT_{\zeta} \\ DFT_{\zeta} \\ DFT_{\zeta} \\ DFT_{\zeta} \end{pmatrix} \cdot \begin{pmatrix} RAO_{\zeta, xMRU} \\ RAO_{\zeta, yMRU} \\ RAO_{\zeta, zMRU} \\ RAO_{\zeta, r xMRU} \\ RAO_{\zeta, r yMRU} \\ RAO_{\zeta, r zMRU} \end{pmatrix} = \begin{pmatrix} DFT_{xMRU} \\ DFT_{yMRU} \\ DFT_{zMRU} \\ DFT_{r xMRU} \\ DFT_{r yMRU} \\ DFT_{r zMRU} \end{pmatrix} \text{ changes in to } \begin{pmatrix} TT_{xmrU} \\ TT_{ymrU} \\ TT_{zmrU} \\ TT_{rxmrU} \\ TT_{rymrU} \\ TT_{rzmrU} \end{pmatrix} \xrightarrow{FT} \begin{pmatrix} DFT_{xmrU} \\ DFT_{ymrU} \\ DFT_{zmrU} \\ DFT_{rxmrU} \\ DFT_{rymrU} \\ DFT_{rzmrU} \end{pmatrix} \quad (5.3)$$

In equation 5.3, TT stands for time trace of the selected sample and FT for Fourier Transform. The time trace of the motion at the MRU should be used instead of the response spectrum in the frequency domain, as otherwise phase information is lost. Phase information is important as it tells if different vessel motions at the MRU contribute in- or out of phase to a degree of freedom at the jacket sensor. Therefore only at the last step in the Measured Data Model the motions may be transformed to the frequency domain, so that phase information is preserved in all intermediary steps.

The second adjustment to the model is that the calculated model responses at the jacket sensor found by using the measured vessel motions at the MRU are now compared to measured data at the jacket sensor, instead of being compared to simulated jacket responses found by using a Jonswap spectrum (W2JS). The time traces from a data sample of the measured motions at the jacket sensor are converted to the respective spectral responses of the six degrees of freedom, which then can easily be compared to the obtained model spectral responses of the six degrees of freedom at the jacket sensor. Equation 3.15 therefore transforms into equation 5.4. The MDM with measured vessel and jacket motions is given in appendix G.

$$\begin{array}{l} RAO_{\zeta, rz_{js}}^2 \cdot S_{\zeta} \rightarrow S_{x_{js}} \\ RAO_{\zeta, rz_{js}}^2 \cdot S_{\zeta} \rightarrow S_{y_{js}} \\ RAO_{\zeta, rz_{js}}^2 \cdot S_{\zeta} \rightarrow S_{z_{js}} \\ RAO_{\zeta, rz_{js}}^2 \cdot S_{\zeta} \rightarrow S_{rx_{js}} \\ RAO_{\zeta, rz_{js}}^2 \cdot S_{\zeta} \rightarrow S_{ry_{js}} \\ RAO_{\zeta, rz_{js}}^2 \cdot S_{\zeta} \rightarrow S_{rz_{js}} \end{array} \text{ changes in to } \begin{array}{l} TT_{x_{js}} \rightarrow S_{x_{js}} \\ TT_{y_{js}} \rightarrow S_{y_{js}} \\ TT_{z_{js}} \rightarrow S_{z_{js}} \\ TT_{rx_{js}} \rightarrow S_{rx_{js}} \\ TT_{ry_{js}} \rightarrow S_{ry_{js}} \\ TT_{rz_{js}} \rightarrow S_{rz_{js}} \end{array} \quad (5.4)$$

## 5.8 TF A2B Method with MDM X

With the proposed Measured Data Model in appendix G, the TF A2B Method can be used to find the motions of the jacket sensor by using the vessel motions measured at the MRU during the X suspended transport. The responses in the frequency domain of the six degrees of freedom at the jacket sensor calculated with all six vessel motions by the model and obtained from the motion measurements of the jacket sensor are shown in figure 5.17. All six plots show that the model **cannot** find the exact same responses as measured by the jacket sensor. The main reason for this is that the Surge and Sway motion of the vessel are very inaccurate as they are not directly measured at the MRU but are obtained from the GPS location of the vessel.

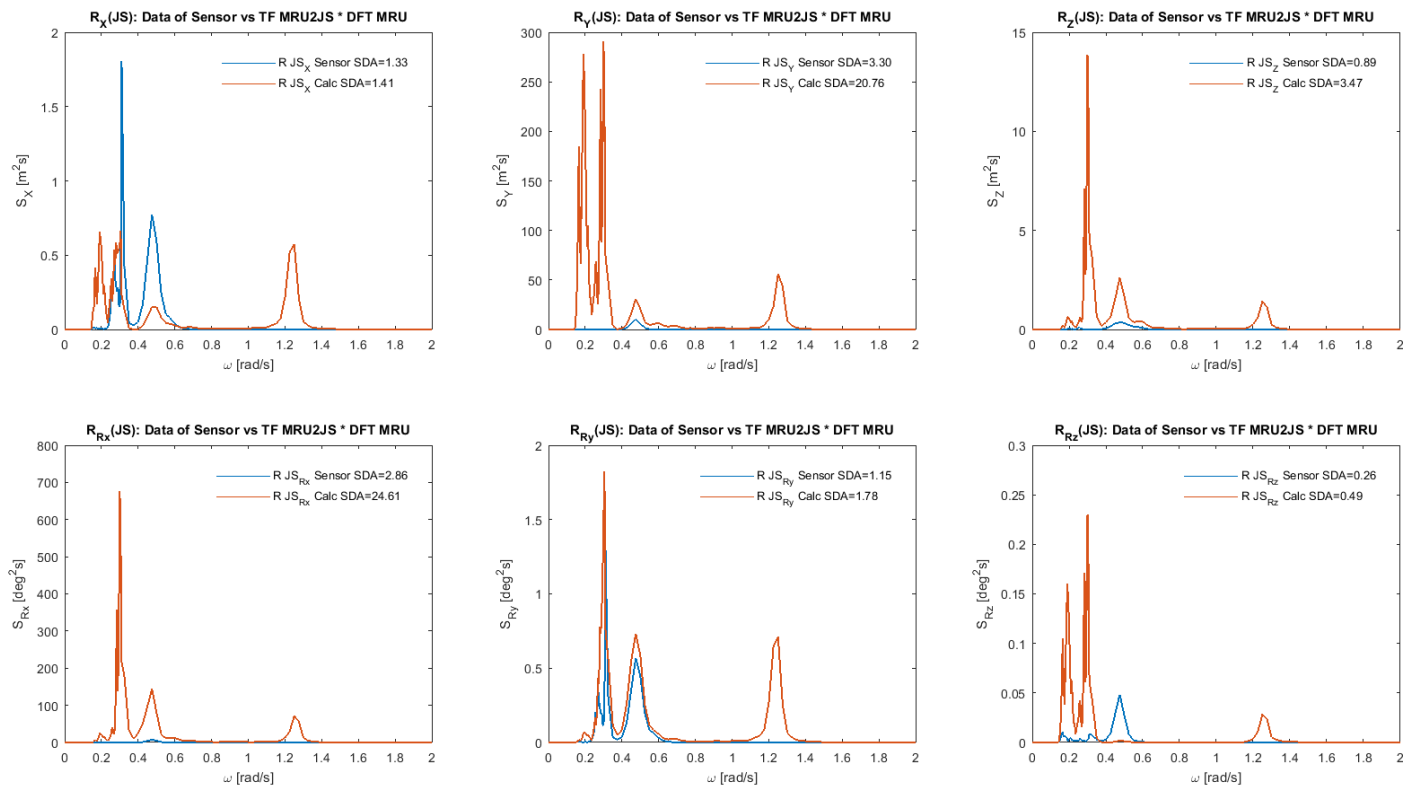


Figure 5.17: Incorrect responses all 6 DOF at jacket sensor by using all six vessel motions measured at the MRU.

A better result is found when omitting the Surge and Sway motions of the vessel. An overview of all responses of the jacket will be shown at the end of this chapter in figure 5.27. All responses calculated by the model without taking into account Surge and Sway of the MRU will be discussed one by one in the following sections.

### 5.8.1 Surge jacket

Surge jacket (fig 5.18): the model can find a bit less than half the SDA value (1.33m vs 0.58m) of the measured Surge motion of the jacket. This without taking the Surge motion of the vessel into account. What can be seen is that the low frequency peak at 0.27 rad/s can be found by the model, whilst the frequency peak at 0.31 rad/s cannot be found. As discussed in section 5.6, the mode shape found at 0.31 rad/s is a pendulum motion of the jacket in the x plane (fig 5.16e). The excitation of an x motion of the jacket at this frequency mostly comes from Pitch and Surge of the vessel. Without a correct Surge measurement this could explain why the peak at 0.31 rad/s cannot be found (fig E.1). The peak in the wave frequency domain is also significantly smaller.

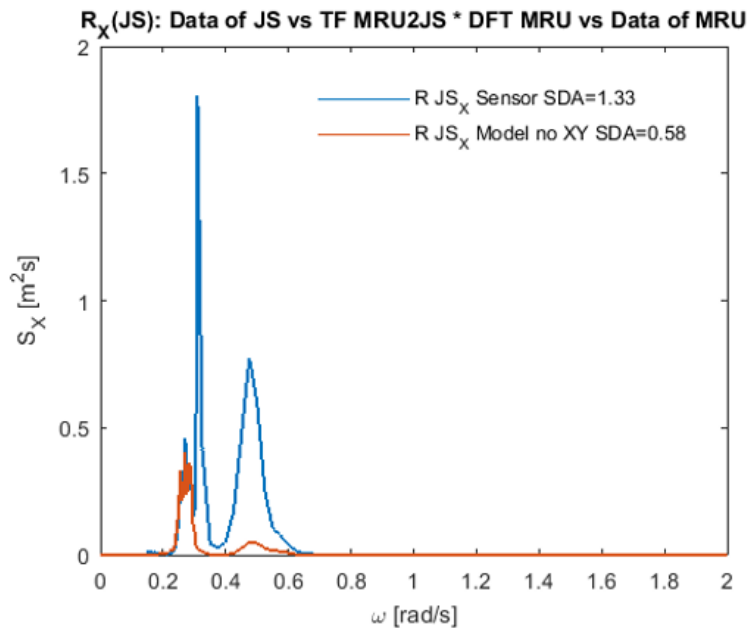


Figure 5.18: Surge response of the jacket at the jacket sensor calculated by using all measured vessel motions at the MRU, except Surge and Sway vs measured Surge at the jacket sensor

### 5.8.2 Sway jacket

Sway jacket (fig 5.19): the model cannot fully capture the Sway motion of the jacket without a Sway motion of the vessel. This can be seen by the SDA value of the model which is more than three times smaller than the measured SDA (3.30m vs 0.97m). The peak at 0.325 rad/s cannot be found for the y motion of the jacket. The mode shape with corresponds to this peak shows pendulum motions of the jacket in the y plane (fig 5.16e), but also shows Sway and Roll motions of the vessel. This can result in that this peak now cannot be found as Sway of the vessel is omitted. The peak in the wave frequency domain captured by the model shows resemblance with the measured peak as they are found at the same frequency. The modelled peak however again lacks captured energy. An accurate Sway measurement of the vessel is required to know if the peaks would be captured better as there is strong coupling in the y plane of the system (fig E.3).

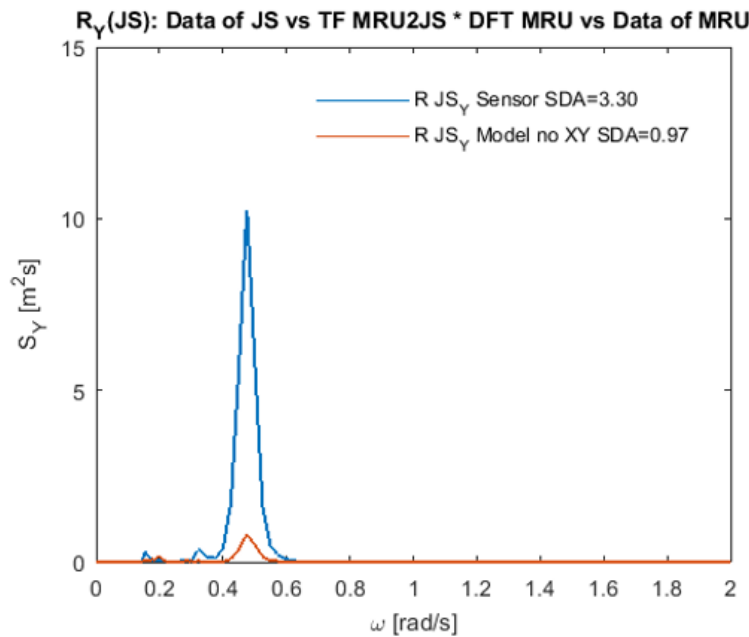


Figure 5.19: Sway response of the jacket at the jacket sensor calculated by using all measured vessel motions at the MRU, except Surge and Sway vs measured Surge at the jacket sensor

### 5.8.3 Heave jacket

Heave jacket (fig 5.20): the Heave motion found by the model (red line) does represent the measured heave motion fairly well (SDA=0.89m vs SDA=0.82m). All peaks are captured at almost the correct frequency. Interesting to see is that the z motion of the vessel (green line) is not the same as the calculated z motion of the jacket (red line) which shows that the proposed method does combine vessel motions fairly accurately.

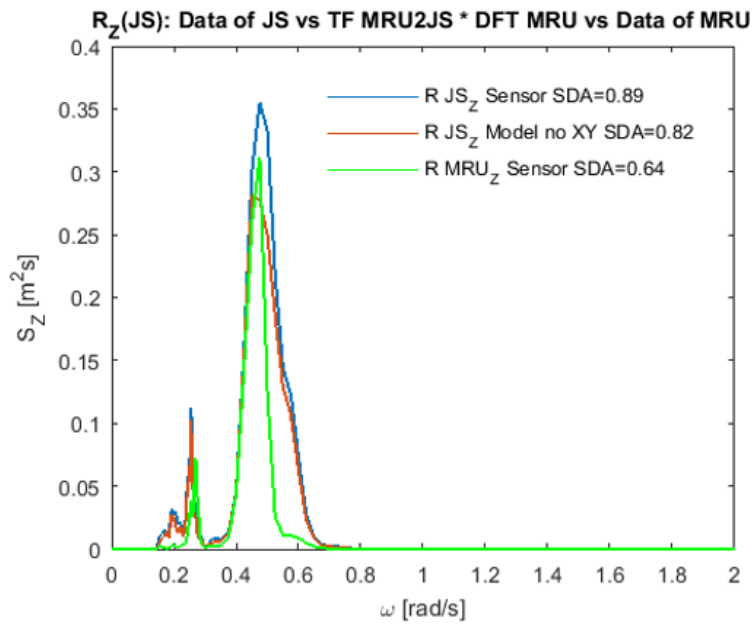


Figure 5.20: Heave response of the jacket at the jacket sensor calculated by using all measured vessel motions at the MRU, except Surge and Sway vs measured Heave at the jacket sensor vs measured vessel Heave

### 5.8.4 Roll jacket

Roll jacket (fig 5.21): the Roll motion of the jacket is captured fairly accurately ( $SDA=2.89^\circ$  vs  $SDA=2.00^\circ$ ). The model peak at 0.476 rad/s lacks strength which could be accounted for by an accurate Sway contribution of the vessel to the Roll motion at the jacket as there is strong coupling in the y plane (fig E.7). At 0.476 rad/s there is a mode shape excited of the vessel (fig 5.16f). This mode shape however does not really excite the vessel and jacket in the y-plane. The wave energy during the transport was however mostly between 0.35-0.6 rad/s. The main wave direction during the transport was approximately coming from NW and in combination with the vessel heading (to NNE) this results in a relative wave direction of approximately  $255^\circ$  (fig 2.2). This results in quarter beam waves which can excite the vessel in Roll and Pitch (green lines in fig 5.21 & 5.23). The RAO's from waves to Roll motion of the vessel and jacket are shown in the left plot of figure 5.22. These are not adjusted for forward speed (due to lack of time) and could also be not fully accurate due to shallow draft (sensitive damping lid), but do give an implication that there is significant amplification of Roll motion of the vessel and jacket in the wave frequency domain. Especially around 0.476 rad/s there is significant amplification in Roll. There is less damping in the y-plane of the vessel which explains the possibility of bigger motions in Roll than Pitch in the wave frequency domain. For this sample this is confirmed by the bigger measured Roll motion of the vessel (green line fig 5.21) in the wave frequency domain compared to the measured Pitch motion of the vessel (green line fig 5.23).

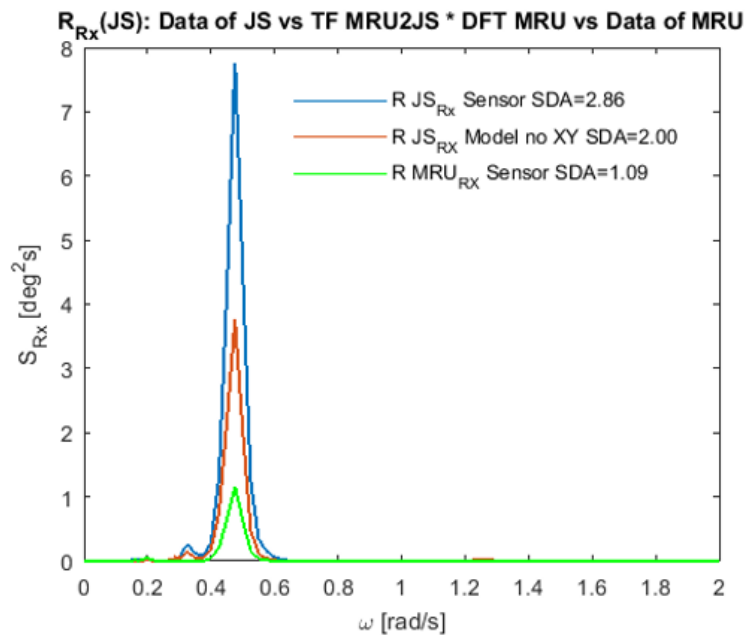


Figure 5.21: Roll response of the jacket at the jacket sensor calculated by using all measured vessel motions at the MRU, except Surge and Sway vs measured Roll at the jacket sensor vs measured vessel Roll

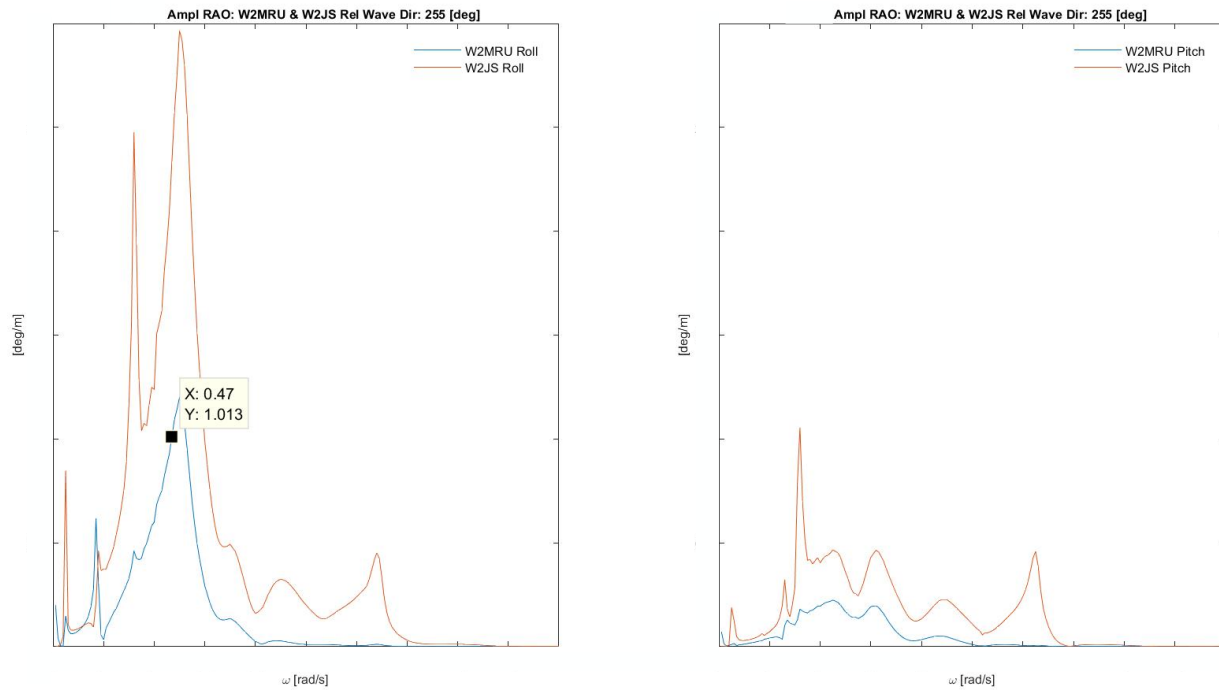


Figure 5.22: Left: RAO from waves to roll at the MRU and JS Right: RAO from waves to pitch at the MRU and JS

Further research is required to be sure that the peak at 0.476 rad/s for Roll of the jacket is coming from waves that induce vessel Sway, Heave and Roll motions of the vessel as these motions have the strongest coupling with Roll of the jacket (fig H.3). This can be tested by looking to more samples for which the wave direction was mostly coming from N or S so that mostly Surge and Pitch motions of the vessel are excited by the waves and no Roll and Sway. If the peak around 0.476 rad/s still exists for Roll motions of the jacket, there could be (non-linear) coupling between roll-pitch jacket motions for which the mode-shape at 0.476 rad/s which shows pendulum motions in x-plane of the jacket and vessel doesn't account for (fig 5.16f).

### 5.8.5 Pitch jacket

Pitch jacket (fig 5.23): the Pitch motion of the jacket is captured fairly accurately ( $SDA=1.15^\circ$  vs  $SDA=0.79^\circ$ ). The model peak at 0.476 rad/s lacks strength which could be accounted for by an accurate Surge contribution of the vessel to the Pitch motion at the jacket as coupling in the x plane (fig E.9) is expected and also shown by the respective mode shape (fig 5.16f). The mode shape in Surge-Pitch direction of the vessel isn't so strongly excited as there is a lot of damping in the Surge-Pitch direction. This damping originates from the fact that when a vessel sails a lot of water in front of the vessel has to be displaced which damps the motions of the mode shape. This is why the Pitch motion of the jacket and vessel are in the same order of magnitude as the Roll motion of the jacket and vessel within the wave frequency domain.

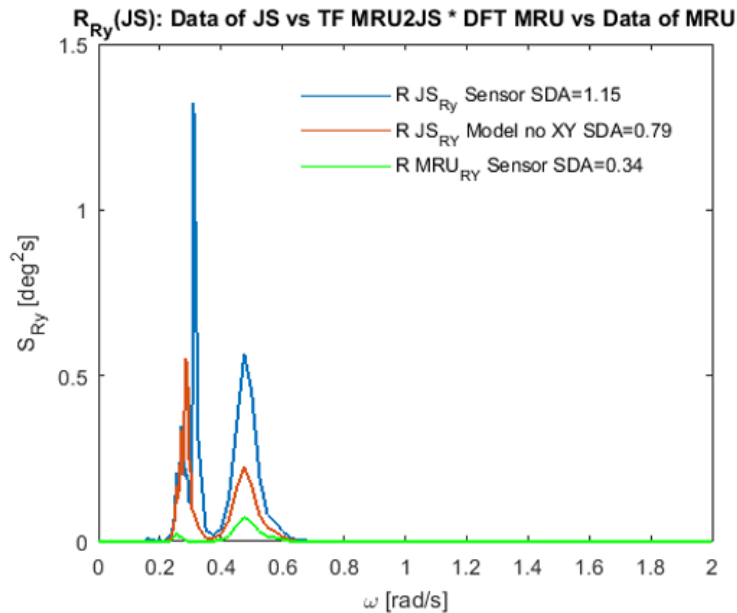


Figure 5.23: Pitch response of jacket at the jacket sensor calculated by using all measured vessel motions at the MRU, except Surge and Sway vs measured Pitch at the jacket sensor vs measured vessel Pitch

The model peak at 0.285 rad/s looks shifted in comparison to the peak of the measured data at 0.31 rad/s. A potential explanation is that the missing Surge motion of the vessel would be in anti-phase with the most dominant vessel motion contribution, Pitch. At the mode shape of 0.31 rad/s (fig 5.16f), the model expects that Pitch and Surge motions of the vessel are in anti-phase (?? mode shape 8, motion vessel in x and ry are both positive). A positive Pitch motion is however a negative Surge motion. To get a better understanding what happens at the frequencies 0.285 rad/s and 0.31 rad/s, the transmissibility functions for a Pitch motion at the jacket due to a Surge and a Pitch motion of the vessel can be inspected.

The top left plot in figure 5.24 shows that at 0.285 rad/s (red circle), Surge at the vessel would be mostly in anti-phase with the Pitch motion of the jacket. The same holds for the Pitch motion (bottom left plot red circle) at the vessel which would mostly be in anti-phase with a Pitch motion of the jacket. The Pitch motion of the vessel however also has a phase with the Surge motion of the vessel (right plot figure 5.24). This could result for example at 0.285 rad/s in:

- Assuming a maximum decreasing Surge of the vessel ( $90^\circ$ ) gives:
- Pitch motion at MRU with Surge vessel at MRU (from right plot fig 5.24 at red circle) =  $90+107= 197^\circ$ . Negative increasing Pitch
- Pitch motion vessel with Pitch jacket (from bottom left plot fig 5.24, red circle:  $167^\circ$  out of phase) gives =  $179+166=363^\circ$ . Gives a positive increasing Pitch at the jacket
- Surge motion vessel with Pitch at the jacket (from top left plot fig 5.24 red circle:  $166^\circ$  out of phase) =  $90+166= 256^\circ$ . Gives a negatively increasing Pitch at the jacket.
- Result: Adding an x motion of the vessel at the MRU to the model could result in a lower peak in the modeled Pitch motion of the jacket at 0.285 rad/s as Pitch and Surge of the vessel would give an contribution in opposite direction to the Pitch motion at the jacket. This would be in line with the measured data as at 0.285 rad/s a lower Pitch motion of the jacket is measured than shown by the calculated Pitch which doesn't take into account Surge.

At the mode shape 0.31 rad/s the contribution of Surge and Pitch of the vessel to the Pitch motion at the jacket would result in:

- Assuming a maximum decreasing Surge of the vessel ( $90^\circ$ ) gives:
- Pitch motion at MRU with Surge vessel at MRU (right plot fig 5.24 black square:  $103.6^\circ$ ). Phase shift between Pitch and Surge of the vessel =  $90+103.6= 193.6^\circ$ : negative increasing Pitch at the vessel.
- The correlation between the Pitch motion of the vessel and the Pitch of the jacket at the mode 5.24 (bottom left plot fig 5.24 blue circle: quick phase shift  $19^\circ$ ) =  $193.6+19= 212.6^\circ$ : negative increasing Pitch at the jacket.
- The correlation between the Surge motion of the vessel and the Pitch of the jacket at the mode 5.24 (top left plot fig 5.24 blue circle: quick phase shift  $12^\circ$ ) =  $90+12= 102^\circ$ : positive decreasing Pitch at the Jacket.
- Result: a Pitch and Surge motion at the MRU will let the jacket move in the same direction, so by adding a Surge motion at the MRU the peak at 0.31 rad/s would be amplified. The magnitude of contribution of the DOFs at the MRU to the total motion of Pitch at the jacket however depends on the amplitude transmissibility functions and phases in combination with the the response in mostly Surge and Pitch at the MRU.

Figure 5.25 shows the most contributing responses at the MRU with their respective TFs to Pitch. For all other jacket motions this is shown in appendix H. As the Surge motion is set to 0, not the full motion of Pitch can be captured. It is expected that a stronger peak in the model can occur at 0.31 rad/s if Surge of the vessel is taken into account due to it's strong coupling with Pitch at the jacket (fig 5.25, top middle plot). The calculated Pitch can then be closer to the measured Pitch at the jacket sensor. A conclusive answer can however only be given if a correct Surge motion measurement at the MRU is added to the model. It is therefore recommended that the MDM is tested when a vessel Surge (and Sway) sensor is installed.

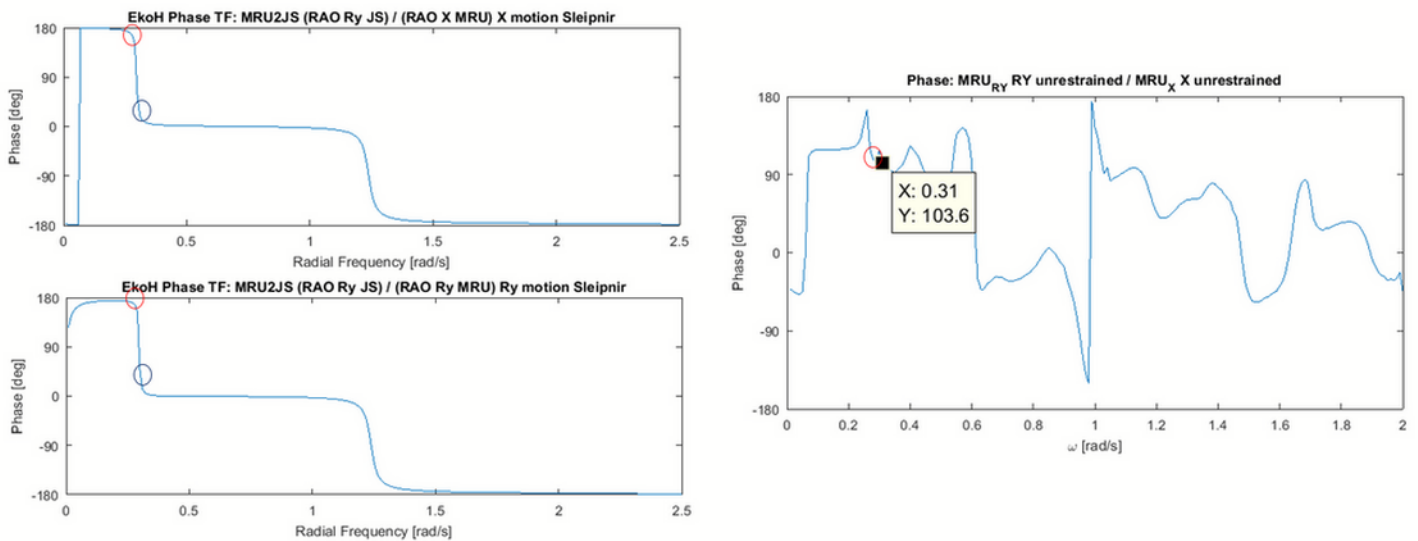


Figure 5.24: Phases of the TFs between vessel Surge & Pitch and the Pitch motion at the jacket sensor and phase between Pitch and Surge motion of the vessel

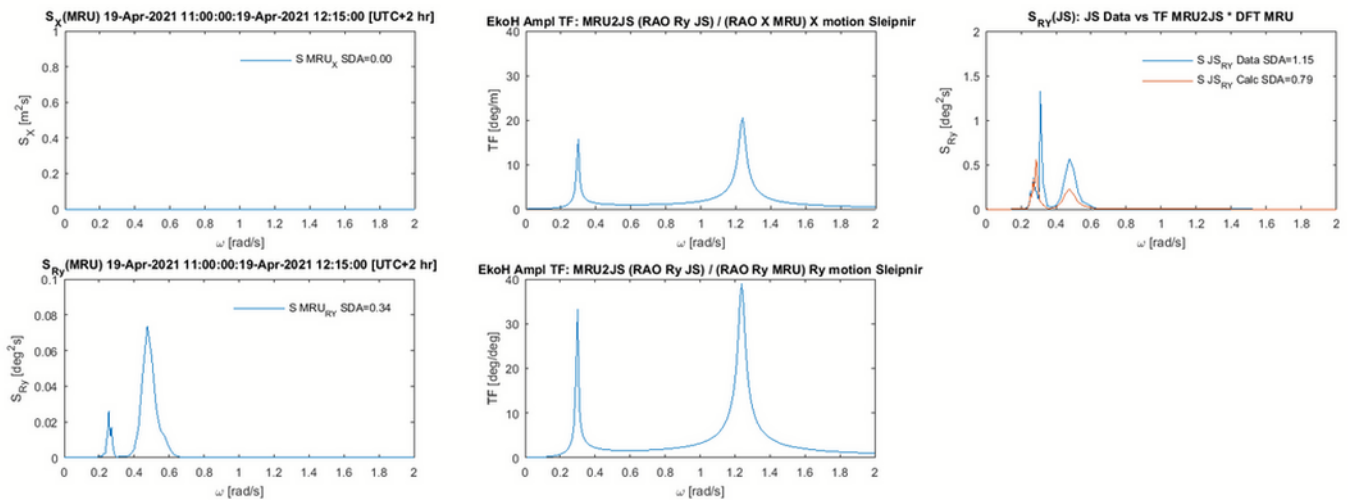


Figure 5.25: Contribution of vessel Surge & Pitch to Pitch at the JS

### 5.8.6 Yaw jacket

Yaw jacket (fig 5.26): the Yaw motion cannot be captured by the model due to the applied restraint in the main block of the crane which makes it impossible for the jacket to Yaw. In reality the reeving consists out of 80 lines, while the reeving of the jacket is now only modeled as 1 connector in Liftdyn. This makes the model susceptible to more Yaw than occurs in reality. A proposed solution would be to apply a spring instead of a constraint to make it possible for the jacket to Yaw, but the stiffness of this spring would be unknown. As can be seen in figure 5.26, the measured Yaw motions of the jacket are however small ( $SDA = 0.26^\circ$ ). Further research into a spring stiffness for the reeving in Yaw direction is required to model the Yaw motions correctly.

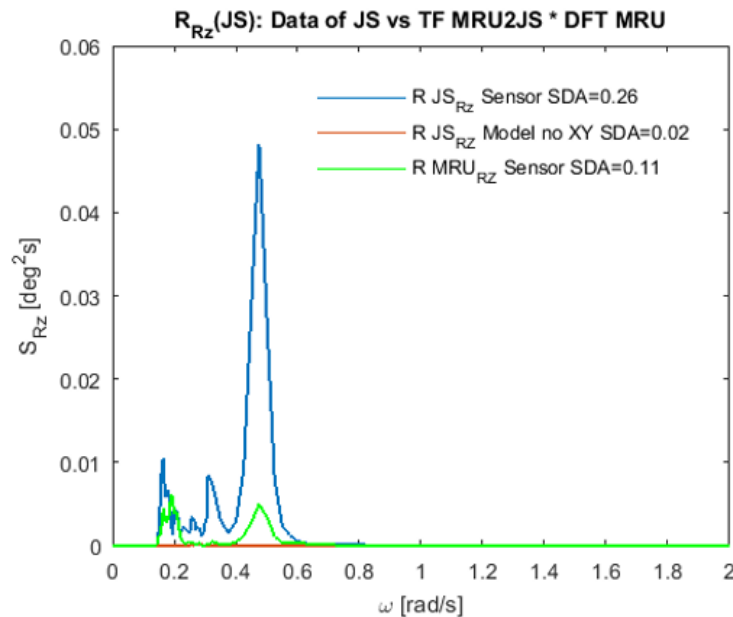


Figure 5.26: Yaw response of jacket at the jacket sensor calculated by using all measured vessel motions at the MRU except Surge and Sway vs measured Yaw at the jacket sensor vs measured Yaw vessel

### 5.8.7 MDM result X

In total the motions of, Heave, Pitch and Roll of the jacket can fairly well be described by the proposed method. Heave by the model is almost perfectly predicted (92%). Roll is predicted with an 70% accuracy and Pitch is predicted with an 69% accuracy. Even without the forced omission of Surge and Sway of the vessel, the accuracy of the method is still reasonably good. Without accurate measurements of Surge and Sway of the vessel, the total accuracy of the proposed method can however not be fully validated. There is confidence that adding Surge and Sway motions of the vessel could increase the accuracy of the method as the motion responses of the jacket calculated by the MDM are found at the same frequencies as the measured jacket motions. Almost all found measured vessel motions and all jacket motions coincide with mode shapes which are also found by the the model and can therefore be explained. A conclusive answer can however only be given until the method is tested with a correct Surge and Sway measurement at the MRU. All six jacket responses calculated with the vessel motions and found from the jacket sensor are shown together in figure 5.27.

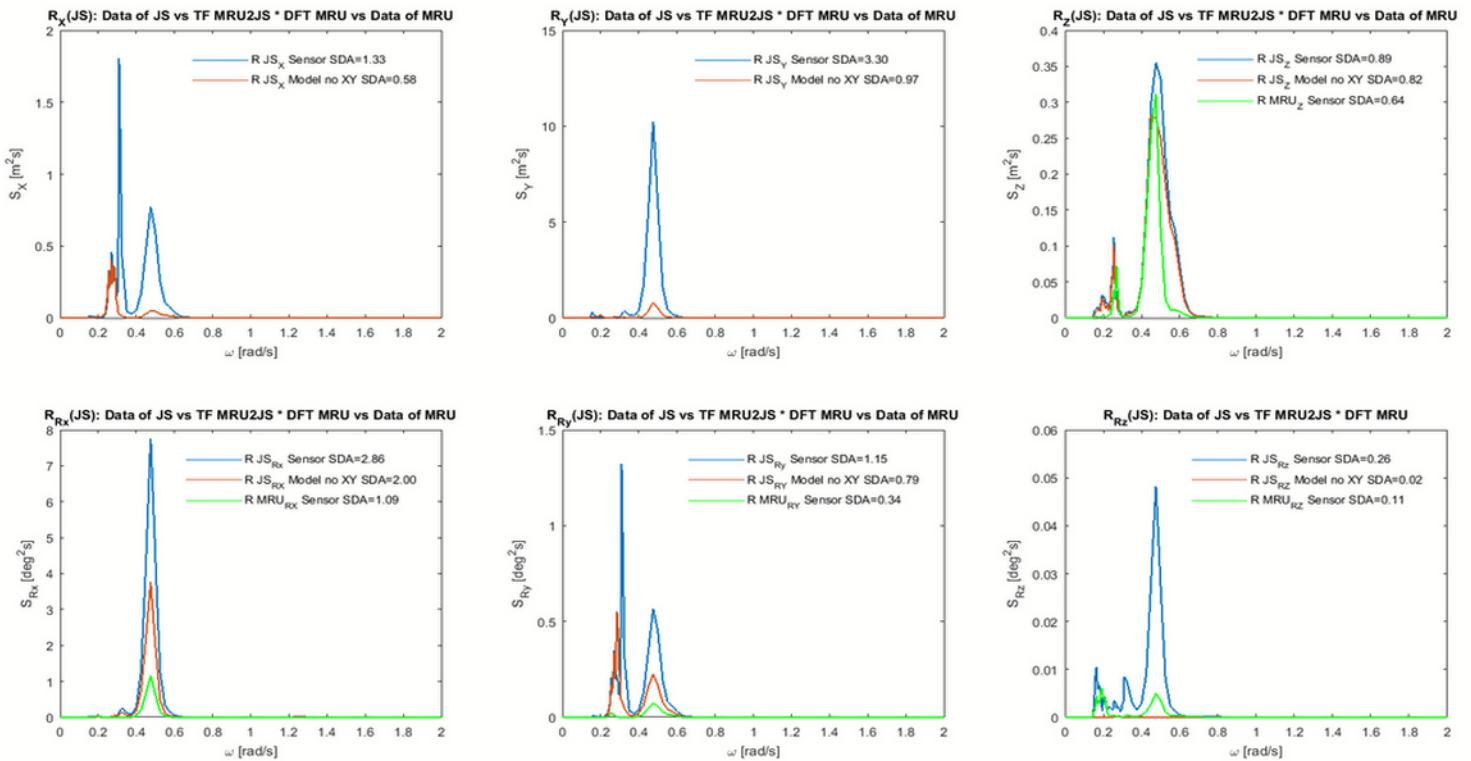


Figure 5.27: Responses all 6 DOF at the jacket sensor by using all vessel motions except Surge and Sway measured at the MRU vs measured jacket motions vs measured vessel motions

What remains important is to test the model with smaller vessel motions (Roll & Pitch  $< 0.5^\circ$ ). The vessel motions are the main excitation to the jacket motions, so it should be checked if the model can still find the jacket motions if the vessel motions are small. For an unrestrained suspended transport the transport of JotB can be used. Due to a lack of time in this thesis these time traces are not checked and are therefore recommendations for further research.

To be statistically more confident that a method works, also more than 1 time sample has to be inspected. As all Matlab scripts required to run the method are parametrically coded, only time traces have to be adjusted to check other samples from the same suspended transport. It is also possible to look at other suspended transports with the Matlab scripts. The extraction of data for other suspended transports is also parametrically coded, but then extra caution with the axis system of the jacket sensor and vessel motions is required. It would however be recommended test more samples after installing a surge and sway sensor at MRU of the vessel as otherwise still not the full accuracy of the method can be analysed.

# Chapter 6: Fatigue calculation input data

## 6.1 Fatigue Data Model

In chapter 5, it is concluded that with the current available data the jacket motions can accurately enough be described by the TF A2B Method with the Measured Data Model. There is confidence that by including measured Surge and Sway vessel motions which can be obtained from a to be installed Surge and Sway sensor at the MRU, the calculated jacket motions match the measured jacket motions of future suspended transports even better. These additions to the method must however first be tested in further research. The current available data is however good enough to assume with reservation that the Liftdyn model of the X Transport can accurately enough represent the X suspended transport.

With this validation it is also possible to extract force RAO's from the Liftdyn models. It is assumed that this information is also correct (indirectly proven). A more direct proof of forces resulting in stresses at the welds of the boom pivots is not possible as there are no strain gauges installed during the suspended transport. There are also no FEM models of the crane with suspended jacket available just as the information required to create such models for every transport. The points of interest in this report are the boom pivots of the crane for which the force RAO's can be obtained. To determine the stresses at the boom pivots of the crane the Fatigue Data Model is proposed. The Fatigue Data Model is shown in figure 6.1.

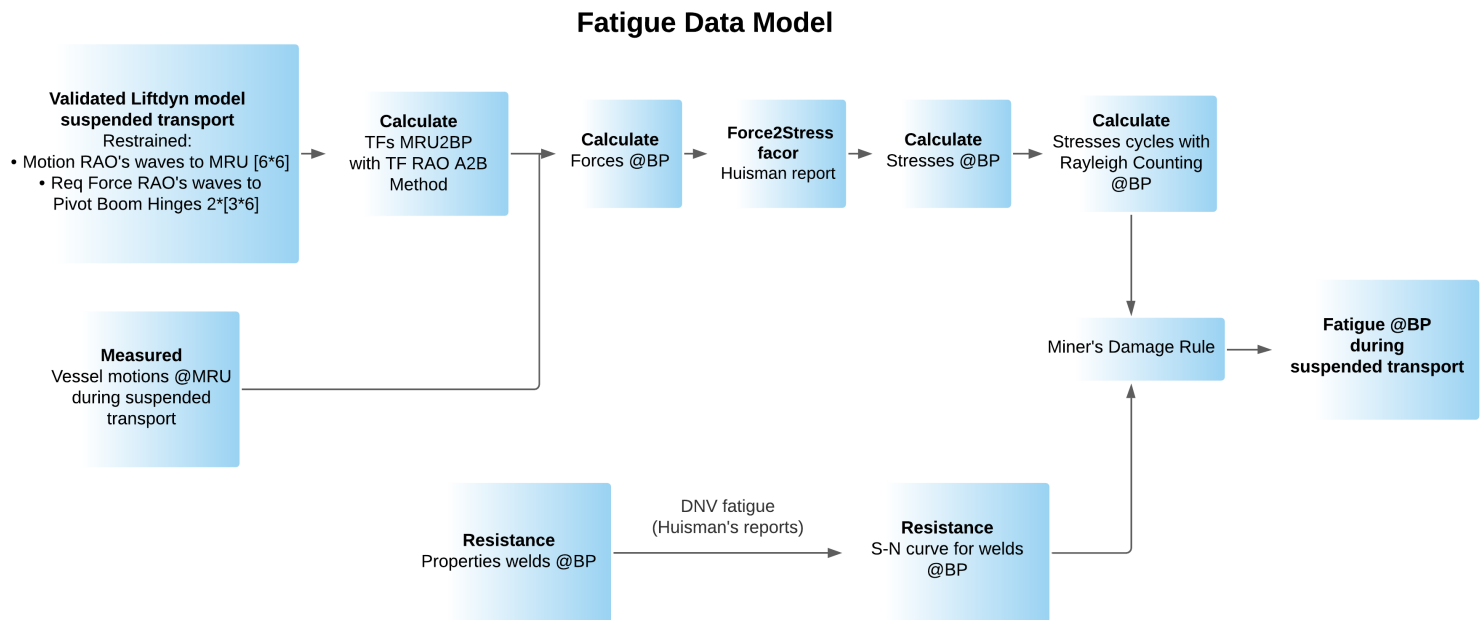


Figure 6.1: The Fatigue Data Model (FDM)

## 6.2 Forcing on welds boom pivots

Based on a previous extensive fatigue analysis by the crane manufacturer Huisman, the most critical weld in the boom is determined to be the weld between the pivot bush and the pivot leg. During a normal boom operation the boom can move freely up and down rotating around the boom pivots. The boom pivots are therefore assumed to be hinges and can freely rotate about the y-axis. Huisman's fatigue calculation is using FEM models of the cranes from which stress concentration factors (SCF) can be obtained which are used within the fatigue calculation. This method cannot be used within this research as it requires an extensive FEM model of the suspended transport for which a lot of data is not available, which Huisman also does not want to share.

Another method therefore has to be found which is able to assess the fatigue damage during suspended transport. A method will be proposed for the most critical fatigue elements: the welds of the crane boom pivots. It is assumed that the stresses in this point can be linearly scaled from the vertical crane load and side-way stress component on the crane boom due to the suspended jacket. Therefore, the fatigue method proposes that:

- The fatigue life and stress at the crane boom pivots can be calculated as function of the vertical load fluctuation.
- The fatigue life and stress at the crane boom pivots can be calculated as function of the side-lead load fluctuation.
- The fatigue life and stress at the crane boom pivots can be calculated as a combination of vertical and side lead load fluctuation.

## 6.3 Force distribution to the boom pivots

Exciting forces on the crane boom pivots are induced by the suspended jacket in the cranes during transport and inertia of the crane boom itself. The weight of the jacket induces a reaction force through the hoist wires to the suspension point of the crane boom. During the transport, the hoist wires are under an angle. Side-lead is the rotation angle of the hoist wires in lateral direction to the crane boom and off-lead is the rotation angle of hoist wires in longitudinal direction to the crane boom. The forces in the hoist wires can therefore be split up in vertical and horizontal forces. The off-lead, side-lead, suspension point, luffing wires, boom pivots, A frame and force decomposition are shown in figure 6.2. The jacket can move freely around the suspension point, so there are no moments in Roll, Pitch and Yaw direction at the suspension point. The vertical load fluctuation due to off-lead results in a vertical reaction force in the luffing wires which is transferred to the A frame of the crane and will therefore not go through the boom. The off-lead of the hoist wires also induces a force in  $F_x$ . The resultant axial force ( $F_x$ ) of the hoist wires and luffing wires is transferred through the crane boom, leading to axial loading of the boom pivots. The side-lead of the hoist wires induces an out of plane force  $F_y$ . This force cannot be taken by the luffing wires and will therefore go directly through the crane boom to the boom pivots.

The shear boom loading due to the side-lead of the hoist wires also creates a moment ( $M_z$ ) which results in a set of couple forces at the boom pivots. There is no moment in Pitch as the boom pivots are hinges which can rotate freely around the y axis. The forces are shown in figure 6.3. The forces and moment have to be transformed to stresses so that stress spectra at the pivots are obtained. With these stress spectra at the pivots then the cumulative fatigue can be calculated. The force RAO's at the boom pivots which are required to obtain the

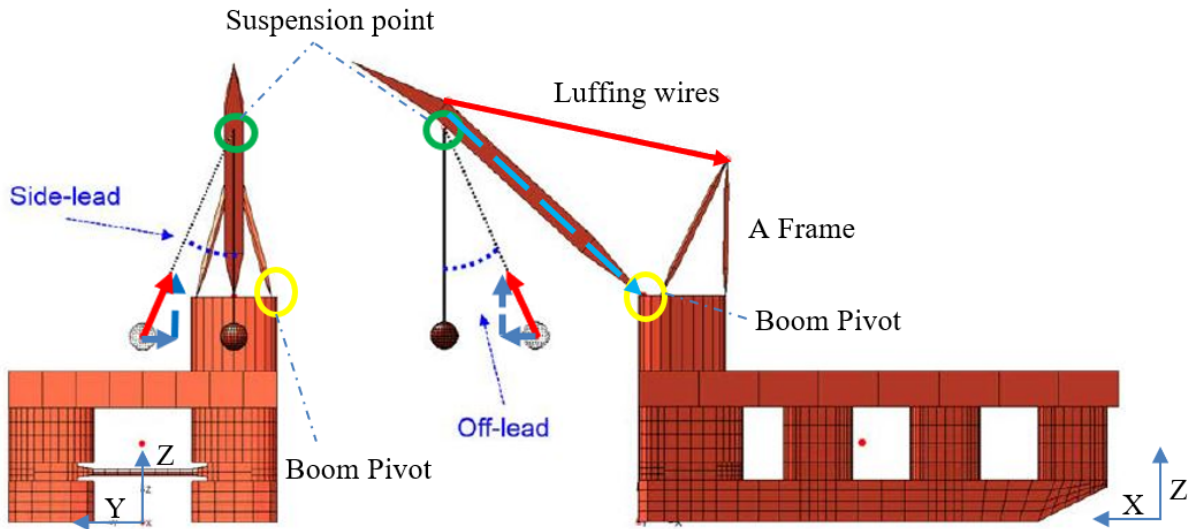


Figure 6.2: Off- & side-lead, decomposition of forces and the suspension point of the crane

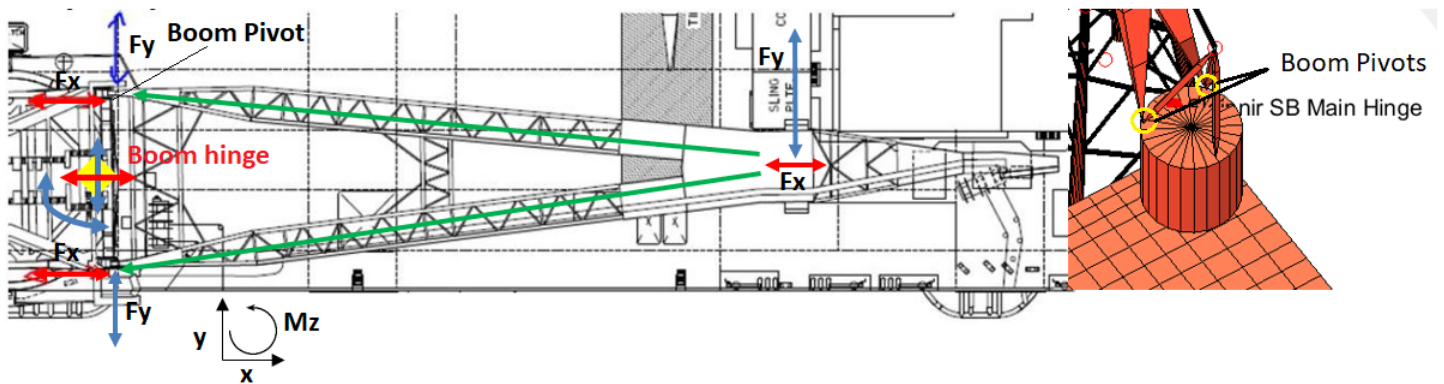


Figure 6.3: Axial and shear boom loading, transferred to the crane boom pivots resulting in  $F_x$  and  $F_y$  at the boom pivots

shear pivot loading & axial loading due to the load fluctuations of the suspended jacket are:

1. In-line force RAO  $F_x$
2. Perpendicular force RAO  $F_y$

## 6.4 TF A2B Method with Fatigue Data Model

To obtain the forces at the boom pivots again the TF A2B Method is used. This time the motions of the vessel at the MRU are used with transmissibility functions that translate the motions at the MRU to forces at the boom pivots of the crane. The boom pivots should however first be added in Liftodyn as two hinges. From [14] the locations of the boom pivots can be found for different slews and boom conditions. For a slew of 180° and boom-up condition (60°), the location of the pivots can be found as in table 6.1.

Item	Vessel PS crane			Vessel SB crane		
	CoG x	CoG y	CoG z	CoG x	CoG y	CoG z
Boom pivots	174 [m]	33.75 [m]	81 [m]	174 [m]	-33.75 [m]	81 [m]

Table 6.1: Location boom pivots [14]

As the Liftodyn model of the X suspended transport is validated, the force RAO's from waves to forces at the boom pivots can be taken. To obtain the transmissibility functions between vessel motions and the forcing at the boom pivots (BP), the TF A2B Method can be used. For a restrained vessel the transmissibility functions are obtained as:

1. The motions of the vessel are uncoupled by placing a restraint at the MRU (A) which restrains the vessel from moving in every motion, except for the motion which is chosen at the MRU (A).
2. This single motion at the MRU can then be used to describe the two required forces at the boom pivots.
3. To fully capture the two forces (Fx, Fy) at the BP, the restraint has to be changed six times, namely for every degree of freedom at the MRU (A). This will finally result in one 6x6 matrix with all motion RAO's at the MRU and two 2\* 2x6 matrices with the required forces at the boom pivots.
4. To obtain the transmissibility functions, from vessel motions at the MRU to forces at the boom pivots, the set of RAO's have to be divided as in equation 6.1.

$$TF_{SMRU2BP} = \begin{pmatrix} \begin{matrix} \text{Vessel unrestrained in X} \\ \frac{RAO_{\zeta, Fx_{BP}}}{RAO_{\zeta, x_{MRU}}} \\ \frac{RAO_{\zeta, Fy_{BP}}}{RAO_{\zeta, y_{MRU}}} \\ \frac{RAO_{\zeta, Fz_{BP}}}{RAO_{\zeta, z_{MRU}}} \end{matrix} & \begin{matrix} \text{Vessel unrestrained in Y} \\ \frac{RAO_{\zeta, Fx_{BP}}}{RAO_{\zeta, y_{MRU}}} \\ \frac{RAO_{\zeta, Fy_{BP}}}{RAO_{\zeta, y_{MRU}}} \\ \frac{RAO_{\zeta, Fz_{BP}}}{RAO_{\zeta, z_{MRU}}} \end{matrix} & \begin{matrix} \text{Vessel unrestrained in Z} \\ \frac{RAO_{\zeta, Fx_{BP}}}{RAO_{\zeta, z_{MRU}}} \\ \frac{RAO_{\zeta, Fy_{BP}}}{RAO_{\zeta, z_{MRU}}} \\ \frac{RAO_{\zeta, Fz_{BP}}}{RAO_{\zeta, z_{MRU}}} \end{matrix} & \begin{matrix} \text{Vessel unrestrained in Rx} \\ \frac{RAO_{\zeta, Fx_{BP}}}{RAO_{\zeta, rx_{MRU}}} \\ \frac{RAO_{\zeta, Fy_{BP}}}{RAO_{\zeta, rx_{MRU}}} \\ \frac{RAO_{\zeta, Fz_{BP}}}{RAO_{\zeta, rx_{MRU}}} \end{matrix} & \begin{matrix} \text{Vessel unrestrained in Ry} \\ \frac{RAO_{\zeta, Fx_{BP}}}{RAO_{\zeta, ry_{MRU}}} \\ \frac{RAO_{\zeta, Fy_{BP}}}{RAO_{\zeta, ry_{MRU}}} \\ \frac{RAO_{\zeta, Fz_{BP}}}{RAO_{\zeta, ry_{MRU}}} \end{matrix} & \begin{matrix} \text{Vessel unrestrained in Rz} \\ \frac{RAO_{\zeta, Fx_{BP}}}{RAO_{\zeta, rz_{MRU}}} \\ \frac{RAO_{\zeta, Fy_{BP}}}{RAO_{\zeta, rz_{MRU}}} \\ \frac{RAO_{\zeta, Fz_{BP}}}{RAO_{\zeta, rz_{MRU}}} \end{matrix} \end{pmatrix} \quad (6.1)$$

The Fatigue Data Model follows the same steps as the Measured Data Model:

- The DFT's of the motions at the MRU found from the time traces of the motions of the vessel can again be multiplied with the just obtained transmissibility functions to obtain the DFT's of the forces and moment at the boom pivots.
- These can just as in the MDM, be transformed to the spectral responses of the forces at the boom pivots. The part of the Fatigue Data Model (part 1) which is used to obtain the force spectra at the BP is mathematically given in appendix J. The full model is shown in figure 6.1.
- The main difference between the FDM compared to the MDM, is that there is no measured data which can validate the found spectral forces responses at the boom pivots. As the jacket motions with the MDM are validated, it is assumed that the found forces are also correct.

## 6.5 Rayleigh counting

### 6.5.1 Properties weld

To start counting the stress cycles with the Rayleigh counting method, first the force spectra from the samples have to be transformed to stress spectra. The properties of the welds are found from [15] and are as follows:

<i>STE690</i>	= Material type
$t_p$	= Plate thickness, 130 [mm]
$\sigma_y$	= Yield stress, 690 [ $\frac{N}{mm^2}$ ]
$\sigma_u$	= Ultimate tensile strength, 770 [ $\frac{N}{mm^2}$ ]
$L_w$	= Weld length, 1400 [mm]
$t_t$	= Throat size, 130 [mm]
<i>Type</i>	= Full penetration

### 6.5.2 Weld stresses

With the properties of the welds at the boom pivots, the stress spectra at the weld can be found. In [63], a force to stress factor is calculated from a weighted average load fluctuation which corresponded to a certain stress range. These stress ranges and load fluctuations originate from outsourced fatigue analyses of the cranes of Thialf during suspended transport. This force to stress factor can also be obtained from Huisman's suspended transport fatigue calculation [15].

As there are no detailed models of suspended transports with Sleipnir available, the best option to obtain the stresses in the welds of the boom pivots is to use a force to stress factor in which the weld stresses for a certain pivot load are obtained from Huisman's in depth fatigue analysis, see equation 6.2.

$$\sigma_w(\omega) = \frac{DAF_{actual}}{DAF_{Huisman}} \cdot F_{F2\sigma} \cdot \frac{F_{BP}}{2}(\omega) \quad (6.2)$$

Where:

$\sigma_w(\omega)$  = Stress spectrum at welds boom pivots

$\frac{DAF_{actual}}{DAF_{Huisman}}$  = Factor for different DAF

$F_{F2\sigma}$  = Force to stress factor from 6.2

$F_{BP}(\omega)$  = Force spectrum at boom pivot

In [15], the fatigue assessment is based on a suspended load of 10% of the allowable load at that radius found from the load curves of the cranes. A DAF of 1.1 and a side-lead of 1° is used in [15]. From the reduced weld stresses in [15] (LC 62, 63, 64) the force to stress factor can be calculated as shown in 6.2.

Load case	Weld load [kN]	Weld stress [MPa]	Weld stress reduced [MPa]	Allowable cycles	Fatigue life [yrs]
Off-lead					
Side-lead					
Combination					

Table 6.2: Fatigue analysis Huisman [15]

The weld are profiled and smoothed and therefore the weld stresses may be reduced as shown in 6.2. Membrane stress may be reduced following section section 7.2 [11]. For the welds of the boom pivots this is shown in appendix K.3. This can be done as in 6.3:

$$\sigma_{local\ reduced} = \sigma_{membrane} \cdot \alpha \quad (6.3)$$

$$\alpha = 0.47 + 0.17 \cdot (\tan\phi)^{0.25} \cdot \left(\frac{t_p}{r_w}\right)^{0.25}$$

$t_p$  = Thickness of the plate at which the main stresses are transferred, 130 mm

$r_w$  = Radius weld, 90 mm

$\phi$  = angle weld 45°

In [2] it is argued that the maxima of side lead and vertical load fluctuation rarely coincide. With the assumption of pendulum motions of the jacket this makes sense as maximum off-lead happens in the x-plane while maximum side-lead will happen in the y-plane. It can therefore be overly conservative.

A less conservative approach to the fatigue damage calculation of the combined vertical and side lead fluctuation would be to add the significant stress amplitude of one load with the maxima of the other load case.

With a relation of  $\sigma_{max} = 1.86 \cdot \sigma_{sign}$  the following load combinations are established:

- LC64A: maximum of vertical load fluctuation +  $\frac{1}{1.86}$  · maximum side-lead load fluctuation
- LC64B:  $\frac{1}{1.86}$  · maximum of vertical load fluctuation + maximum side-lead load fluctuation

This would result in the following:

Load case	Weld load [kN]	Weld stress [MPa]	Weld stress reduced [MPa]	Allowable cycles	Fatigue life [yrs]
LC 64A					
LC64B					

Table 6.3: Adjusted LC 64 obtaining less conservative weld stresses

For [15] this would increase the fatigue life. LC 64A results in the lowest fatigue life, for which the force to stress can be obtained by dividing the reduced weld stresses by the weld load, resulting in a stress factor. With the force to stress factor, stress spectra at the boom pivots during suspended transport can now be obtained from force spectra. The force spectra are obtained from the vessel motions at the MRU during suspended transport in combination with the transmissibility functions between vessel motions at the MRU and forces at the boom pivots.

### 6.5.3 Stress cycles

The stress cycles during transport can be obtained by dividing the complete transport in samples with the same duration. The duration of a sample for this transport is chosen to be at least 75 minutes, so that all motions of the system over 0.15 rad/s can be described with some confidence as at least 100 cycles of the low frequency vessel motions are observed.

The Rayleigh counting method assumes that the probability density of the stress range  $\sigma_r$  only depends on the zeroth spectral moment of the stress spectrum. The properties of the Rayleigh distribution are given as:

$$\begin{aligned}
 p_{RAY}(\sigma_r) &= \frac{\sigma_r}{4m_0} \cdot \exp\left(-\frac{\sigma_r^2}{8m_0}\right) \\
 m_n &= \int_0^\infty \omega^n \cdot S_{\sigma\sigma}(\omega) d\omega = n^{th} \text{ spectral moment of stress} \\
 \sigma_0 &= \sqrt{m_0} \\
 Cdf_{RAY}(\sigma_r) &= 1 - \exp\left(-\frac{\sigma_r^2}{8m_0}\right)
 \end{aligned} \tag{6.4}$$

The total number of stress cycles within the stress spectrum of a sample can be found from the total duration of the sample (here 4500s) and the zero crossing period  $T_2$  (eq 6.5):

$$\begin{aligned} N_{tot} &= \frac{D_{sample}}{T_2} \\ T_2 &= 2\pi \cdot \sqrt{\frac{m_0}{m_2}} \end{aligned} \quad (6.5)$$

The X suspended transport started at -04-2021 03:00 [UTC+2] and ended at -04-2021 04:30 [UTC+2]. The full duration is therefore 25,5h. This results in  $\frac{25.5}{1.25} = 20.4$  samples. Knowing the distribution of stress over the frequency domain for every sample, the number of cycles for every stress range  $\sigma_r$  can be found with the Rayleigh cumulative distribution function. The probability that a stress cycle in a sample is between a and b is given as  $Cdf_{RAY}(b(\omega)) - Cdf_{RAY}(a(\omega))$ . A bin is created at each data-point on the S-N curve. Assuming an equal bin-width ( $d\sigma_r$ ) the amount of cycles in a bin of a certain stress range  $\sigma_r$  is then calculated as 6.6:

$$N_{occurred}(\sigma_r) = N_{tot} \cdot [Cdf_{RAY}(\sigma_r + 0.5 \cdot d\sigma_r) - Cdf_{RAY}(\sigma_r - 0.5 \cdot d\sigma_r)] \quad (6.6)$$

The above requires the amount of bins to be sufficiently large such that the stress cycle amplitude within each bin can be considered constant. In [52] & [10] bin sizes of 1 MPa are taken. For durations less than the sample size the damage can be scaled down linearly. So an exposure of half the sample length will result in half the amount of damage.

## 6.6 Resistance weld

### 6.6.1 S-N curves

In the suspended transport fatigue analysis of Huisman, the welds at the boom pivots fall into detail class D, as given by [15]. The D-air curve selected for the boom pivots is given as [15]:

$$\begin{aligned} N_{low} &= 10^{\log(A_1) - m_1 \cdot \log(\Delta\sigma \cdot (\frac{t}{t_{ref}})^2)} \cdot 0.97 \\ N_{high} &= 10^{\log(A_2) - m_2 \cdot \log(\Delta\sigma \cdot (\frac{t}{t_{ref}})^2)} \cdot 0.97 \end{aligned} \quad (6.7)$$

With:

$$\begin{aligned} \log(A_1) &= 12.164 \\ m_1 &= 3, \text{ Low cycle logarithmic slope of S-N curve D in figure 6.4} \\ \log(A_2) &= 15.606 \\ m_2 &= 5, \text{ High cycle logarithmic slope of S-N curve D in figure 6.4} \\ t &= 130 \text{ mm} \\ t_{ref} &= 25 \text{ mm} \\ k &= 0.2 \text{ thickness exponent on fatigue strength as given in [11]} \end{aligned}$$

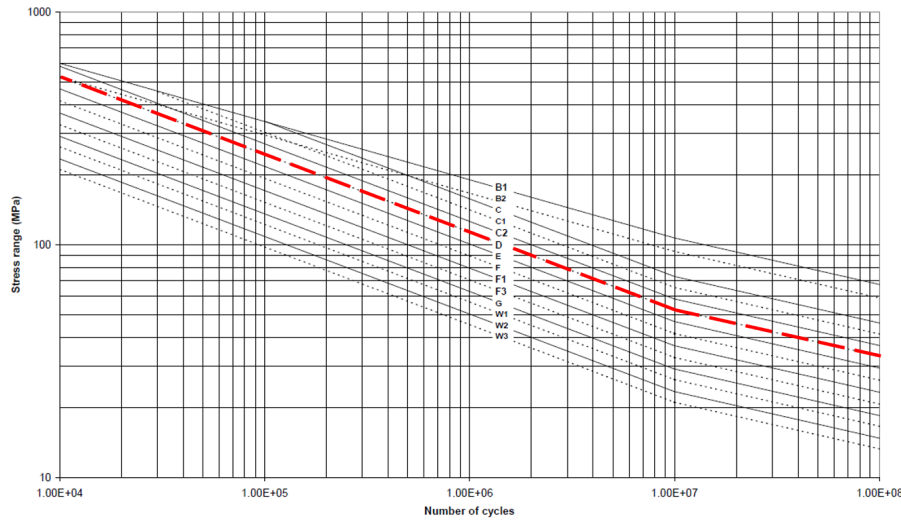


Figure 6.4: S-N curves in air as defined in [11] D-air curve in red

## 6.7 Damage during suspended transport

With Miner's damage rule finally the total fatigue damage during suspended transport can be calculated as Miner's damage rule gives the relation between all samples during transport. The rule is given in equation 6.8 [11]. The Design Fatigue Factor (DFF) used in [15] is 1.0.

$$D = \sum_{i=1}^k \frac{n_i}{N_i} \leq \eta \quad (6.8)$$

With:

$D$  = Accumulated fatigue damage

$k$  = Number of stress blocks

$n_i$  = Number of stress cycles in stress block  $i$  found by counting method

$N_i$  = Number of cycles to failure at constant stress range  $\Delta\sigma_i$  from S-N curve

$\eta$  = Usage factor, mostly 1 but may vary

= 1/design fatigue factor from DNVGL-OS-C101 Sec.6 Fatigue limit states [64].

The fatigue damage calculation with Miner's damage rule has to be performed for the most governing load case which is a fatigue life calculation due to stresses at the weld of the crane boom pivots due to the combination of off-lead and side-lead load fluctuation. For this load case all information is now available to calculate the total fatigue damage during suspended transport.

A road-map is now given to calculate the fatigue damage due to a suspended transport at the most prone fatigue location in the cranes. Due to the lack of time within this research, just a road-map is given for the fatigue calculations. The results of this fatigue calculation can in future work be compared with the scaling of the Huisman fatigue damage calculation to see if the currently used method by HMC is accurate enough.

In further research the modeled fatigue damage could also be compared to actual measured strains and calculated stresses obtained from strain gauges which would be installed at the welds of the boom pivots during suspended transport. With strain gauges at the boom pivots, the fatigue model which initially uses vessel motions as input to find forces at the boom pivots could be fully tested.

## Chapter 7: Conclusion & recommendations

This research investigates an accurate yet fast methodology which can be developed to calculate the crane fatigue damage incurred during suspended transports. The method uses measured vessel motions to obtain input for a fatigue damage calculation in the cranes during suspended transport. It is concluded that, in principle, vessel motions measurements can be used to provide input for a fatigue damage calculation of the cranes. The eligibility of the proposed TF A2B Method using RAO's obtained from Liftdyn is validated by performing validation tests with synthetic data using the Synthetic Data Model. With this model it is shown that the transmissibility functions between A and B are almost equal for different draft and therefore not dependent significantly on the hydrodynamic properties of the vessel. It is shown that the RAO's from waves to location B can be reconstructed by the RAO's from waves to location A multiplied with the TFs from A to B in which point A and B don't have to be on the same rigid body. It is also shown that the response of location B can be found by using a restrained set of TFs [6x6] in combination with the responses of the six motions at location A in which point A and B don't have to be on the same rigid body.

A Fatigue Data Model is proposed which can find the fatigue damage in the cranes during suspended transport by using measured vessel motions in combination with transmissibility functions which transform the measured vessel motions at the MRU into forces at the boom pivots of the crane(s). The required force RAO's at the boom pivots are obtained from Liftdyn models of the X suspended transport. The force RAO's are validated by showing that the proposed TF A2B Method can transform the measured vessel motions, Heave, Pitch, Roll and Yaw into six calculated jacket motions using the Measured Data Model. This resulted in a match of 30% for Sway, 44% for Surge and 92% for Heave. An approximate 70% accuracy match with the measured suspended jacket motions, Roll and Pitch during the X suspended jacket transport was found. In the system there is strong in-plane coupling of motions between the vessel and jacket. An approximate 70% accuracy match with the measured suspended jacket motions, Roll and Pitch is therefore a good result, taking into account that Surge and Sway vessel motions at the MRU were not accurately available and could therefore not be included in the model.

It is noted that the Yaw motion of the jacket could not be captured by the model due to the applied restraint in the main block of the crane which was placed to in the model to prevent the jacket from excessive Yaw. It is found that without accurate measurements of Surge and Sway of the vessel, the total accuracy of the proposed method cannot be fully validated. There is however confidence that adding Surge and Sway motions of the vessel could increase the accuracy of the Measured Data Model as the motion responses of the jacket calculated by the model are mostly found at the same frequencies as the measured jacket motions. Calculated motions at certain frequencies by the MDM which were not found by measured data can be partly explained by a phase shift analysis, by taking into account what would happen to the calculated response if Surge and Sway motions at the vessel would be added to the analysis. Besides this, all measured jacket motions coincide with mode shapes which are found by the the model and can therefore be explained.

The inaccuracies induced by the sensors and possible inaccuracies in the modelled hydrodynamic stiffness's and added masses which can originate from the forward speed problem and inconvenient draft problem, seem to be small (0.01 rad/s) as most measured abrupt peaks can be found by mode shapes. This is however based on 1 sample and it is therefore recommended to take into account more samples.

Within this research the measured vessel and jacket motions of the X unrestrained suspended transport are used to validate the TF A2B Method with the Measured Data Model. Fundamentally the proposed method can however be used to obtain any transmissibility function between point A and B. The two delivered models are both based on the theory of the TF A2B Method. The Synthetic Data Model is designed to handle synthetic data and the Measured Data Model is designed to handle measured data. The first part of the proposed Fatigue Data Model is an adjustment of the MDM, in which vessel motions are used to find forces at the boom pivots. This model is technically only different in the to be obtained RAO's from the Liftdyn model of a suspended transport, as the measured vessel motions during suspended transport are still used as input. Therefore, to estimate fatigue damage, only two data requirements are needed. The first requirement is that a correct Liftdyn Model of the suspended transport is created and the second requirement is that there are vessel motion measurements in all six degrees of freedom with an accuracy in the order of decimeters/degrees at a location on the vessel. The method can therefore also be used for restrained suspended transport in which the jacket is clammed to the vessel. This also results in that suspended transports with other vessels can be analysed. These situations are however yet to be validated by using measured vessel & jacket motions of past restrained suspended transports with Sleipnir and suspended transports with different SSCVs. Overall, the TF A2B Method shows positive results, but there are still a number of shortcomings that need to be addressed in further research.

It is found that the inconvenient draft problem and the forward speed problem are two problems which remain complicated. The last two theses about fatigue at HMC [52] [10] also investigated the inconvenient draft and forward speed problem. In this thesis therefore a method is proposed which omits these problems. Within the TF A2B Method many sub-steps had to be proven to verify whether the method works correctly. This resulted in that there was not enough time to do the fatigue damage calculations with the proposed Fatigue Damage Model. This is why only input for the Fatigue Data Model is delivered. This input is yet to be implemented in a to be made Matlab script of the Fatigue Data Model to validate if the TF A2B Method also works to find forces at the boom pivots in the correct order of magnitude. These forces can then be converted to stresses and stress cycles using the Fatigue Data Model as equations to do this are already delivered. The required S-N curve and other weld properties, just as Miner's damage rule are also delivered within the Fatigue Data Model. The stress cycles during suspended transport are the only required missing input to calculate the occurred fatigue damage at the boom pivots during a suspended transport. It is then also possible to compare the fatigue damage calculation found by the FDM with the scaling of the Huisman fatigue damage calculation to see if the currently used method by HMC is accurate enough.

Another option would be to let Huisman perform a fatigue calculation of the X suspended transport. The resulting fatigue damage found by the Fatigue Data Model can then more directly be compared to the result of Huisman as the same project is analysed.

To obtain accurate force RAO's and results with the proposed Fatigue Data Model it is most importantly recommended to Heerema Marine Contractors to install a motion sensor that can in the order of accuracy of decimeters capture the Surge and Sway motion of the vessel as this is currently missing input to the models. The most favourable location of this motion sensor would be the MRU of the vessel as all other vessel motions are already measured here. After the installation of this motion sensor at the MRU, it is advised to again measure the jacket motions during a future suspended transport. The TF A2B Method can then again be applied with the Measured Data Model, but now with all six measured vessel motions at the MRU. The real accuracy of the proposed method can then be evaluated which is required to validate if the Liftdyn model of the transport is an accurate representation of reality. The current results look promising but a final conclusion can only be given after validation of the method with all six measured vessel motions as input to the Measured Data Model.

Another recommendation would be to install strain gauges at the welds of the boom pivots of the cranes. One of the problems with the current method is that it does not directly validate if the found stresses at the boom pivots are correct. It is only proven that the model with some confidence can find the jacket motions. The only direct way to find the occurred strains at the boom pivots is to install strain gauges to measure the occurred strains. This would especially be helpful as then jacket motions and strains at the boom pivots are measured during the same future suspended transport. The stresses found by the FDM versus stresses found by the strain gauge can then be compared which makes it possible to fully validate all steps in the TF A2B Method with the to be tested Fatigue Data Model.

To better validate the TF A2B Method, certain validation tests are recommended:

- To be statistically more confident about the accuracy of the method more than 1 time sample has to be inspected. It is recommended to at least compare the model with 5 samples (75 min), preferably after installing the required motion sensor. Some longer time samples should also be analysed to get a better understanding of the low frequency motions of the vessel. To find the Yaw motions of the jacket it is recommended to apply a spring with a to be found spring stiffness instead of a constraint in the main block of the crane to make it possible for the jacket to Yaw.
- It is recommended to test the model with smaller vessel motions (Roll & Pitch  $< 0.5^\circ$ ). The vessel motions mostly determine the jacket motions, so it should be checked if the accuracy of the TF A2B Method decreases if the vessel motions are small. For an unrestrained suspended transport with smaller vessel motions samples from the other transports can be used.

- To validate if the TF A2B Method can be used for restrained suspended transport the method should be tested with recorded vessel and jacket motions of restrained suspended transports.
- To validate if the model can be used with other vessels it is advised to use the method with the MDM by taking recorded vessel and jacket motions of suspended transports with different vessels.

In general it would be recommended to evaluate if the chosen operational and environmental load cases selected at the start of Huisman's fatigue analysis are a correct representation of how the vessel is actually used. An expert within HMC noted that the assumed operational profile in which for example 34 lifts at 90% main hoist capacity a year is lifted is conservative, as 5 loads a year at maximum capacity would be as well. This in turn over-predicts the assumed accumulated fatigue damage in the cranes. As data like loads in the cranes during projects is measured on the vessel and every project is well documented, data processing is possible to obtain a better operational and environmental profile of Sleipnir. This can then be used by Huisman for a better fatigue assessment.

# Bibliography

- [1] P. Samudero, V. Capurso, and R. Zoontjes, “Crane suspended transportation - An effective way to remove offshore platforms,” in *Society of Petroleum Engineers - SPE Symposium: Decommissioning and Abandonment 2019*, Society of Petroleum Engineers, 2020.
- [2] Heerema Marine Contractors, “Sleipnir Crane Suspended Transport of Brent Alpha Jacket,” tech. rep., 2020.
- [3] Heerema Marine Contractors, “Liftdyn Theory Manual 8.1,” tech. rep., Leiden, 2017.
- [4] D. A. Russell, “Acoustics and Vibration Animations,” 2018.
- [5] J. M. J. Journée and W. W. Massie, *Offshore Hydromechanics*, vol. 47. 2002.
- [6] P. Groen and R. Dorrestein, “Zeegolven,” tech. rep., KNMI, 1976.
- [7] L. H. Holthuijsen, *Waves in oceanic and coastal waters*, vol. 9780521860284. 2007.
- [8] Heerema Marine Contractors, “Riding the Waves part 5: Hydrodynamics,” tech. rep., 2009.
- [9] Heerema Marine Contractors, “Presentation Encounter Frequency,” 2020.
- [10] Hötte S, *Fatigue Monitoring System of the J-Lay Tower on Heerema’s DCV Balder*. PhD thesis, Delft University of Technology, Delft, 2011.
- [11] DNV-GL, “DNVGL-RP-C203. Fatigue Design of Offshore Steel Structures,” *Standard, DNV GL, Høvik*, 2016.
- [12] Heerema Marine Contractors, “Sleipnir Crane-suspended Transport of Jacket-EKOH-M50 I0479-263-JA00-JT200-RP03 A,” tech. rep., 2020.
- [13] Tarka B.V., “MOSS DATALOGGER QUICK REFERENCE GUIDE,” tech. rep., 2020.
- [14] Huisman Equipment B.V., “Load Cases for Fatigue Analysis,” tech. rep., 2016.
- [15] Huisman Equipment B.V., “Additional Fatigue Study Transit with boom up,” tech. rep., 2019.
- [16] United Nations, “Convention on the Continental Shelf,” tech. rep., Geneva, apr 1958.
- [17] H. O. Bergesen, G. Parmann, and O. B. Thommessen, “United Nations Convention on the Law of the Sea (UNCLOS),” in *Yearbook of International Cooperation on Environment and Development 1998–99*, 2019.

- [18] B. J. Hoyle and W. S. Griffin, "International standards for removal of abandoned and disused offshore oil production platforms: negotiation and agreement," *OTC '89, PROC. 21ST ANNUAL OFFSHORE TECHNOLOGY CONF., HOUSTON, U.S.A., MAY 1-4, 1989, RICHARDSON, U.S.A., OFFSHORE TECHNOLOGY*, vol. 1 , 1989, 1989.
- [19] European Union, "OSPAR Convention," tech. rep., Paris, sep 1992.
- [20] H. O. Bergesen, G. Parmann, and O. B. Thommessen, "Convention on the Protection of the Marine Environment of the Baltic Sea Area (1992 Helsinki Convention)," in *Yearbook of International Cooperation on Environment and Development 1998–99*, 2019.
- [21] International Maritime Organization, "Guidelines and Standards for the removal of Offshore Installations and structures on the continental shelf and in the exclusive economic zone," tech. rep., oct 1989.
- [22] International Maritime Organization, "Convention on the Prevention of Marine Pollution by Dumping of Wastes and Other Matter," tech. rep., London, 1972.
- [23] United Nations, "Mediterranean Action Plan (MAP)," tech. rep., 1976.
- [24] United Nations, "Basel Convention on the control of transboundary movements of hazardous wastes and their disposal," tech. rep., Basel, 1989.
- [25] Euractiv, "Virus crisis threatens to set back oil platform decommissioning," oct 2020.
- [26] M. Hendrapati, J. Sumardi, J. Marthen, N. Anshar, H. Subhandi, and Y. Kristianto, "Offshore Installation Removal in the Interest of Navigation Safety from International Law Point of View," tech. rep., 2017.
- [27] Heerema Marine Contractors, "JotunB Crane Suspended Transport Report," tech. rep., 2020.
- [28] L. Pook, "Metal fatigue what it is, Why it matters," *Solid Mechanics and its Applications*, vol. 145, 2007.
- [29] A. J. Karlsen, "Fatigue in crane design," in *SAE Technical Papers*, SAE International, 1982.
- [30] Huisman Equipment B.V., "Fatigue Analysis Method," tech. rep., 2017.
- [31] B. Paul and P. Barkan, "Kinematics and Dynamics of Planar Machinery," *Journal of Mechanical Design*, vol. 102, no. 4, 1980.
- [32] R. Elling and A. McClinton, "Dynamic loading of shipboard cranes," (New York), pp. 174–177, Ocean 73, IEEE International Conference on Engineering in the Ocean Environment,, 1973.

- [33] J. W. Miles, "Stability of forced oscillations of a spherical pendulum," *Quarterly of Applied Mathematics*, vol. 20, no. 1, 1962.
- [34] J. Miles, "Resonant motion of a spherical pendulum," *Physica D: Nonlinear Phenomena*, vol. 11, no. 3, 1984.
- [35] M. H. Patel, D. T. Brown, and J. A. Witz, "OPERABILITY ANALYSIS FOR A MONOHULL CRANE VESSEL," *Royal Institution of Naval Architects (London), Supplementary Papers*, vol. 129, 1987.
- [36] P. K. Mukerji, "Hydrodynamic responses of derrick vessels in waves during heavy lift operation," in *Proceedings of the Annual Offshore Technology Conference*, vol. 1988-May, 1988.
- [37] J. A. Witz, "Parametric excitation of crane loads in moderate sea states," *Ocean Engineering*, vol. 22, no. 4, 1995.
- [38] G. F. Clauss and M. Vannahme, "An experimental study of the nonlinear dynamics of floating cranes," in *Proceedings of the 1999 Ninth International Offshore and Polar Engineering Conference (Volume 3), Brest, France, 30 May - 4 June 1999*, 1999.
- [39] K. Ellermann, E. Kreuzer, and M. Markiewicz, "Nonlinear dynamics of floating cranes," *Nonlinear Dynamics*, vol. 27, no. 2, 2002.
- [40] K. Ellermann, E. Kreuzer, and M. Markiewicz, "Nonlinear primary resonances of a floating crane," in *Meccanica*, vol. 38, 2003.
- [41] C. Chin, A. Nayfeh, and D. Mook, "Dynamics and control of ship-mounted cranes," (Long Beach), *Proceedings of the 39th Structures, Structural Dynamics, and Materials Conference*, 1998.
- [42] E. M. Abdel-Rahman and A. H. Nayfeh, "Pendulation reduction in boom cranes using cable length manipulation," *Nonlinear Dynamics*, vol. 27, no. 3, 2002.
- [43] T. E. Schellin, T. Jiang, and S. D. Sharma, "Crane ship response to wave groups," *Journal of Offshore Mechanics and Arctic Engineering*, vol. 113, no. 3, 1991.
- [44] M. M. Idres, K. S. Youssef, D. T. Mook, and A. H. Nayfeh, "A nonlinear 8-DOF coupled crane-ship dynamic model," in *Collection of Technical Papers - AIAA/ASME/ASCE/AHS/ASC Structures, Structural Dynamics and Materials Conference*, vol. 6, 2003.
- [45] F. J. McCormick and J. A. Witz, "Investigation into the parametric excitation of suspended loads during crane vessel operations," *Underwater Technology*, vol. 19, no. 3, 1993.

- [46] N. Sun, T. Yang, Y. Fang, Y. Wu, and H. Chen, "Transportation control of double-pendulum cranes with a nonlinear quasi-pid scheme: Design and experiments," *IEEE Transactions on Systems, Man, and Cybernetics: Systems*, vol. 49, no. 7, 2019.
- [47] B. Riemann, "Grundlagen für eine allgemeine Theorie der Functionen einer veränderlichen complexen Grösse," tech. rep., 1851.
- [48] A.-L. Cauchy, "CALCUL INTÉGRAL. – Considérations nouvelles sur les intégrales définies qui s'étendent à tous les points d'une courbe fermée, et sur celles qui sont prises entre des limites imaginaires," in *Oeuvres complètes*, 2011.
- [49] G. Green, "22. An Essay on the Application of mathematical Analysis to the theories of Electricity and Magnetism," *Journal fur die Reine und Angewandte Mathematik*, vol. 1852, no. 44, 1852.
- [50] H. Versteeg, W. Malalasekera, G. Orsi, J. H. Ferziger, A. W. Date, and J. D. Anderson, *An Introduction to Computational Fluid Dynamics - The Finite Volume Method*. 1995.
- [51] M. D. Haskind, "The Exciting Forces and Wetting of Ships in Waves," *Izvest Akademii Nauk SSSR, Otdelenie Tekhnicheskikh Nauk*, vol. 7, 1957.
- [52] Rentoulis I, *Improvement of fatigue damage prediction for the Balder J-lay tower during transits*. PhD thesis, Delft University of Technology, Delft, 2016.
- [53] H. Schlichting and K. Gersten, *Boundary-Layer Theory*. 2016.
- [54] A. E. Veldman, "Matched asymptotic expansions and the numerical treatment of viscous-inviscid interaction," *Journal of Engineering Mathematics*, vol. 39, no. 1, 2001.
- [55] C. Li, "Numerical Investigation of a Hybrid Wave Absorption Method in 3D Numerical Wave Tank," *Computer Modeling in Engineering & Sciences*, vol. 107, no. 125-153, 2015.
- [56] X.-b. Chen, "Hydrodynamics in offshore and naval applications - part I," *6th International Conference on Hydrodynamics*, no. 1993, 2004.
- [57] D. Benasciutti and R. Tovo, "Rainflow cycle distribution and fatigue damage in gaussian random loadings," 2004.
- [58] I. Rychlik, "On the 'narrow-band' approximation for expected fatigue damage," *Probabilistic Engineering Mechanics*, vol. 8, no. 1, 1993.
- [59] P. M. Wirsching and M. C. Light, "FATIGUE UNDER WIDE BAND RANDOM STRESSES," *ASCE J Struct Div*, vol. 106, no. 7, 1980.
- [60] M. A. Miner, "Cumulative Damage in Fatigue," *Journal of Applied Mechanics*, vol. 12, no. 3, 1945.

- [61] M. L. Kaminski, "Sensing and understanding fatigue lifetime of new and converted FPSOs," in *Offshore Technology Conference, Proceedings*, vol. 3, 2007.
- [62] H. Eskandari and H. S. Kim, "A theory for mathematical framework and fatigue damage function for the S-N plane," in *ASTM Special Technical Publication*, vol. STP 1598, 2017.
- [63] Heerema Marine Contractors, "Thialf Crane Fatigue During Jacket suspended transport," tech. rep., 2018.
- [64] DNV-GL, "DNVGL-OS-C101: Design of Offshore Steel Structures," *Standard*, DNV GL, Høvik, April, 2015.

# Appendices

## Appendix A Potential theory

The mass continuity equation describes the mass transport through the faces of an body element. In it's most basic form the mass continuity equation describes the mass transport through the edges of a block, which can be seen in figure A.1.

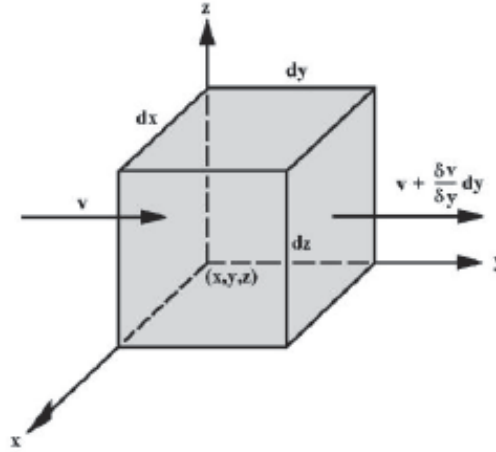


Figure A.1: Mass transport through faces block, only showing y-component of velocity [5].

In mathematical form the Continuity equation is given as equation in A.1.

$$\frac{\delta \rho}{\delta t} + \frac{\rho u}{\delta x} + \frac{\rho v}{\delta y} + \frac{\rho w}{\delta z} = 0 \quad (\text{A.1})$$

Combined with the assumption that the fluid is treated as being in-compressible, there is a constant density  $\rho = \text{constant}$ , the Continuity equation A.1 simplifies into equation A.2. In which u, v and w are velocity components along the x-, y- and z- axes respectively.

$$\frac{\delta u}{\delta x} + \frac{\delta v}{\delta y} + \frac{\delta w}{\delta z} = 0 \quad (\text{A.2})$$

A velocity potential is a mathematical expression in which the velocity component in a point in the fluid in any chosen direction is the derivative of this potential function in that point to the chosen direction. This can best be explained by the change in potential of two certain points. The increase of potential between point A and B in figure A.2 can be described as in equation A.3. From equation A.3 it follows that the increase of the potential doesn't depend on the integration path used between point B and A.

$$\Delta \Phi_{A \rightarrow B} = \int_A^B \vec{V} \cdot \vec{ds} = \int_A^B (u \cdot dx + v \cdot dy + w \cdot dz) = \int_A^B \left( \frac{\delta \Phi}{\delta x} dx + \frac{\delta \Phi}{\delta y} dy + \frac{\delta \Phi}{\delta z} dz \right) = \int_A^B d\Phi = \Phi(B) - \Phi(A) [5] \quad (\text{A.3})$$

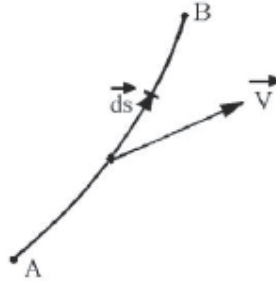


Figure A.2: Definition velocity potential [5].

From equation A.3 it also follows that potential lines between two points have the characteristic that  $\Phi = \text{constant}$ . This will result in 3D rectangular coordinates in equation A.4.

$$d\Phi = u \cdot dx + v \cdot dy + w \cdot dz \quad (\text{A.4})$$

From equation A.3 and A.4 it follows that the velocity components  $u$ ,  $v$  and  $w$  can be described by the potentials as in equation A.5.

$$u = \frac{\delta\Phi}{\delta x} \quad v = \frac{\delta\Phi}{\delta y} \quad w = \frac{\delta\Phi}{\delta z} \quad (\text{A.5})$$

A potential flow therefore describes the velocity field as the gradient of a scalar function, the velocity potential. There are two main requirements which have to be satisfied before potential theory can be used.

- The flow satisfies the Laplace Equation (eq A.6)
- The flow is characterized by an irrotational velocity field. The irrotationality of a potential flow is the result of the curl of the gradient of a scalar always being equal to zero. Ergo, a moving fluid undergoes no net rotation with respect to a chosen coordinate axes from one instant to other.

The Laplace equation for an in-compressible fluid follows from the continuity equation A.2 and the definition of the velocity potentials A.5. This Laplace Equation for an in-compressible fluid is given in A.6.

$$\frac{\delta^2\Phi}{\delta x^2} + \frac{\delta^2\Phi}{\delta y^2} + \frac{\delta^2\Phi}{\delta z^2} = 0 \quad (\text{A.6})$$

With potential flow theory also streamlines can be defined. Streamlines are lines which show the direction in which a mass-less fluid element will travel at any point in time. The rate of flow remains constant when a water particle follows its streamline. This also results in that the volume of flow between any two streamlines can be found as the difference between the stream function values of these two stream lines. If two stream lines come closer together the velocity must increase whilst if two stream lines diverge the velocity must decrease. This follows from the continuity of the in-compressible flow defined by equation A.2. A streamline is therefore defined as  $\Psi = \text{constant}$ . As no flow takes place across streamlines the derivative of a streamline in 2D rectangular coordinates is given as in equation A.7.

$$d\Psi = u \cdot dy - v \cdot dx \quad (\text{A.7})$$

### A.0.1 Properties potential flow

Some useful properties of potential flow are:

- In potential flow theory streamlines and potential flow lines are orthogonal: streamlines and potential lines always cross each other at right(90 degrees) angles. In mathematical form this results in A.8.
- There is no drag force in potential flow. This is the result of the assumption that there is no viscosity. Thin boundary layers as a result of viscous forces are therefore neglected. This results in that there is no friction drag on streamlined objects and on bluff bodies additionally there is no flow separation and a low-pressure wake behind the object, which leads to form drag [53] [54].
- There is a circulation required to generate a lift force.

$$u = \frac{\delta\Phi}{\delta x} = \frac{\delta\Psi}{\delta y} \quad v = \frac{\delta\Phi}{\delta y} = -\frac{\delta\Psi}{\delta x} \quad (\text{A.8})$$

Potential theory is commonly used to describe flow patterns as due to its linearity, superposition of flow pattern components can be used to generate more complex flow patterns. This can be seen in figure A.3. In this figure, a uniform flow is combined with a Source (flow radiating outwards) and a Sink (inward radial flow). The flow from source to sink stays inside the bold ellipse whilst the constant current flow stays outside the ellipse and passes around it. Physically this could be interpreted as that the ellipse could be replaced by an impermeable object as a ship hull in a uniform flow. Engineer and physicist W.J.M. Rankine extended this approach by including additional, matched pairs of sources and sinks along the x -axis in the uniform flow. Using relatively weaker source-sink pairs near the ends of the shape make these edges more pointed. As these shapes somewhat resemble a horizontal slice of a ship these shapes were named Rankine ship forms. These Rankine ship forms are still used in flow computations as they are quite simple to run with potential flow software.

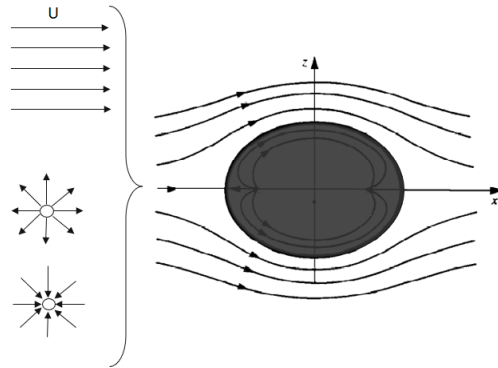


Figure A.3: Superposition of a uniform flow, sink and source potential [8].

## Appendix B Limiting criteria X transport

Dynamic limits	Limit in 3 hr SMPM	Remarks
Hs	4 [m]	Design sea state restricted transport

Table B.1: Limiting criteria X transport

# Appendix C TFs independent of draft

## C.1 TFs independent of draft using the MRU and the CP

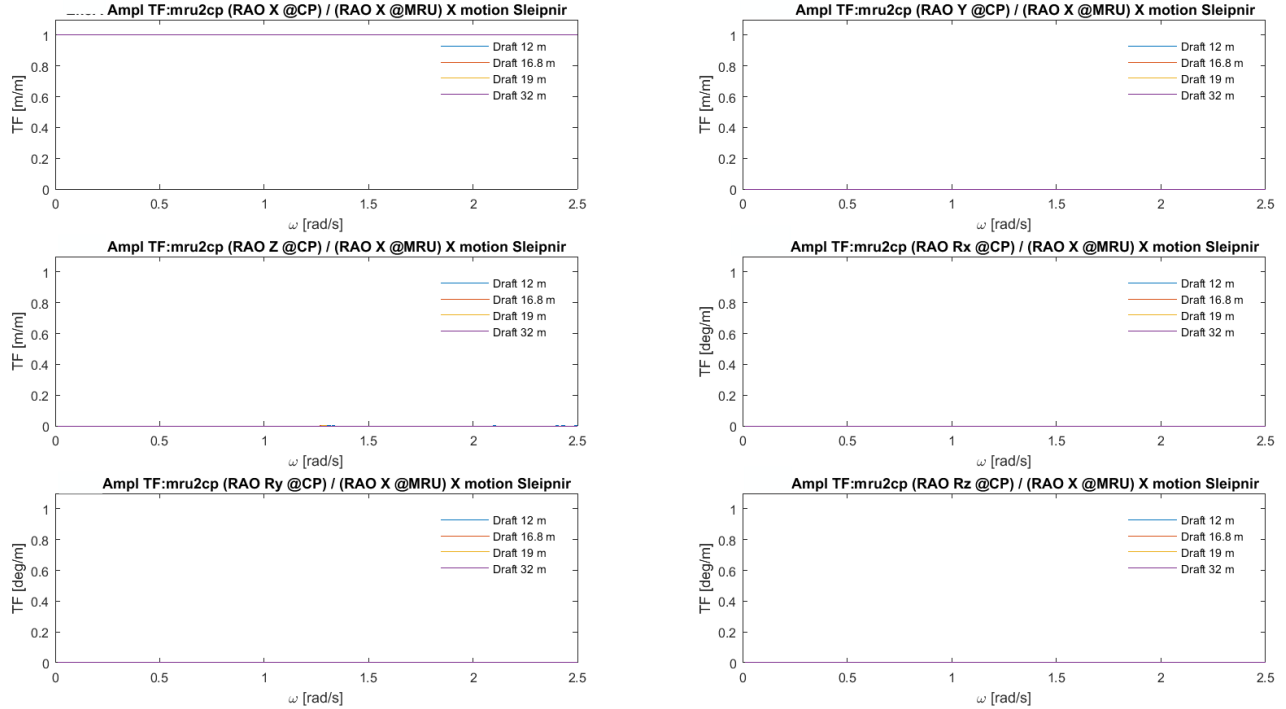


Figure C.1: The TFs for all six dof at the CP(B) due to a Surge motion of the vessel at the MRU(A)

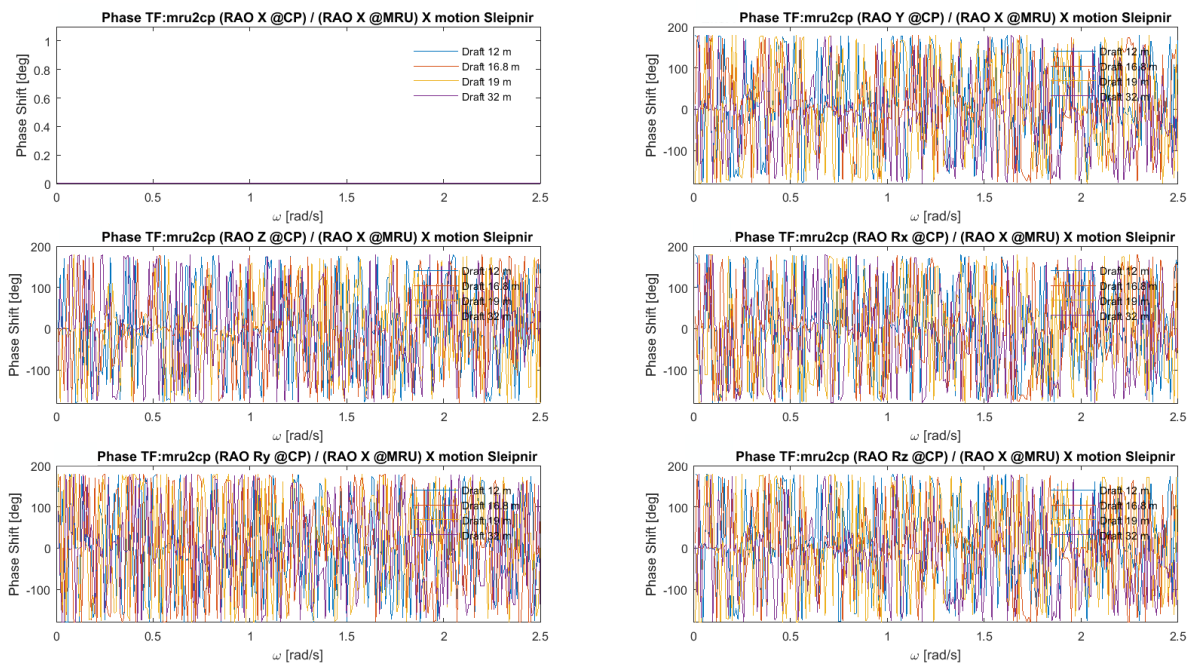


Figure C.2: The TFs phases for all six dof at the CP(B) due to a Surge motion of the vessel at the MRU(A)

### C.2 TFs independent of draft using the MRU and the JS

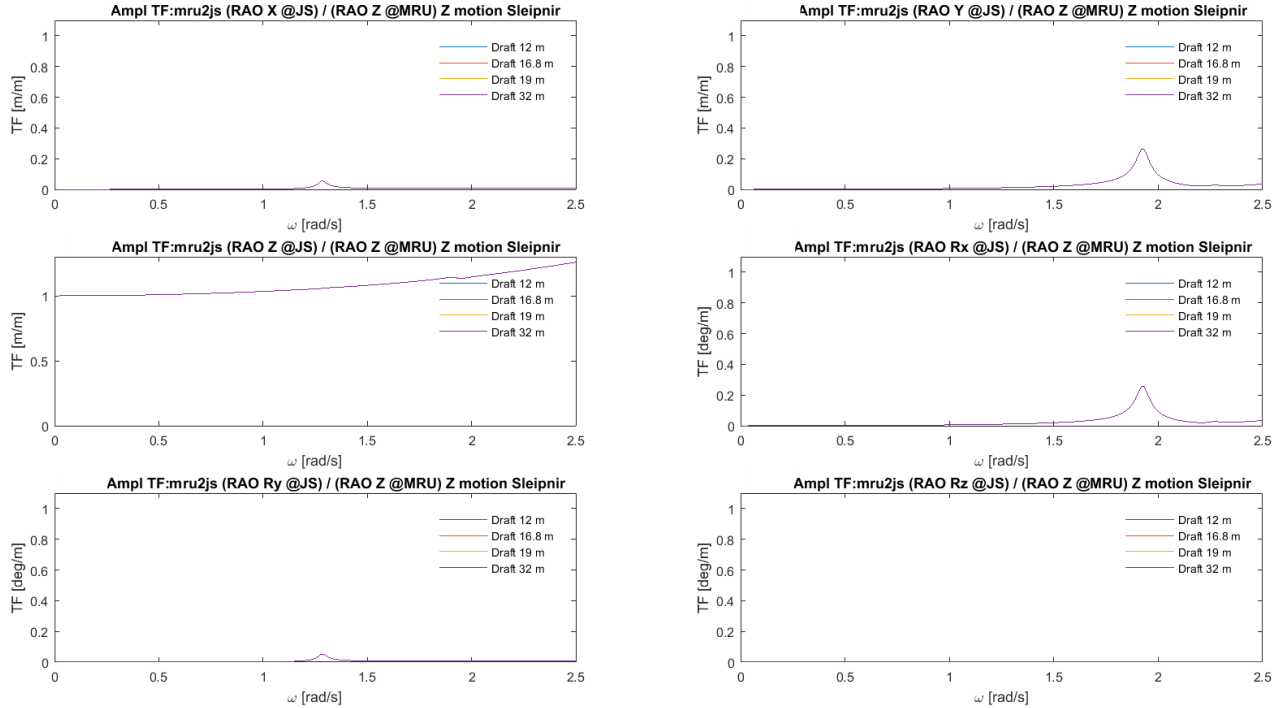


Figure C.3: The TFs for all six dof at the JS(B) due to a Heave motion at the MRU(A)

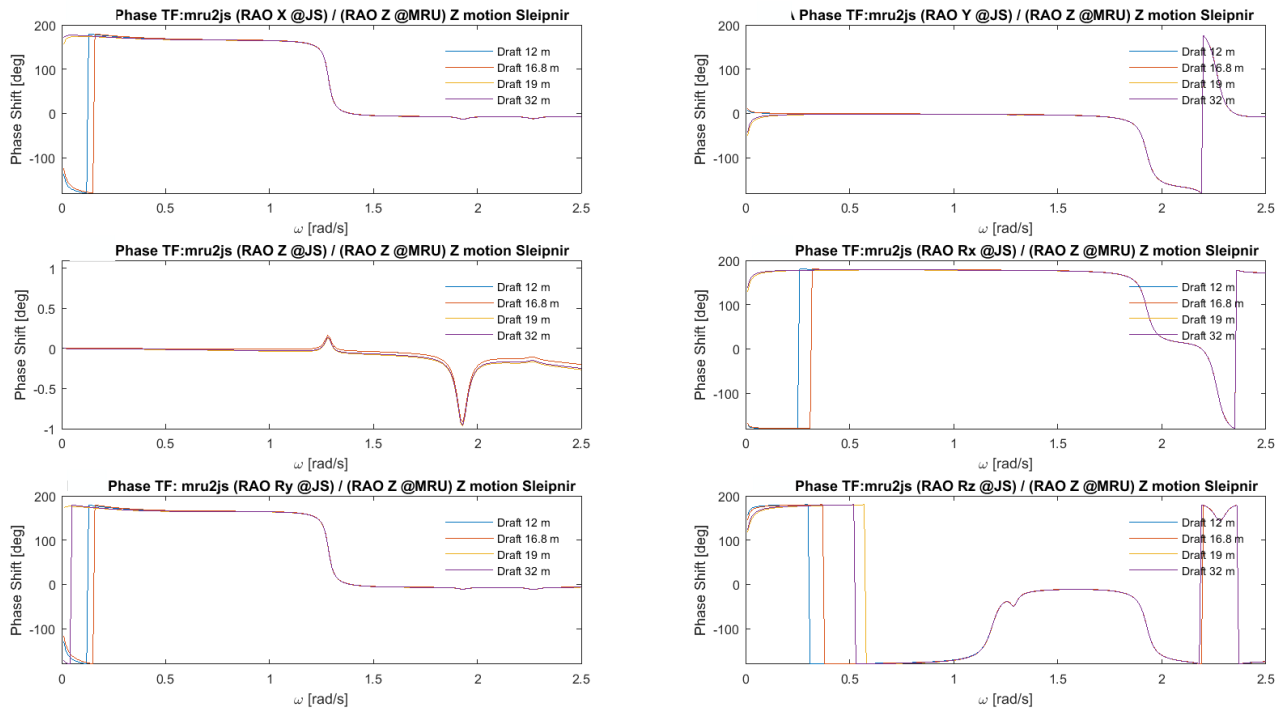


Figure C.4: The TFs phases for all six dof at the JS(B) due to a Heave motion at the MRU(A)

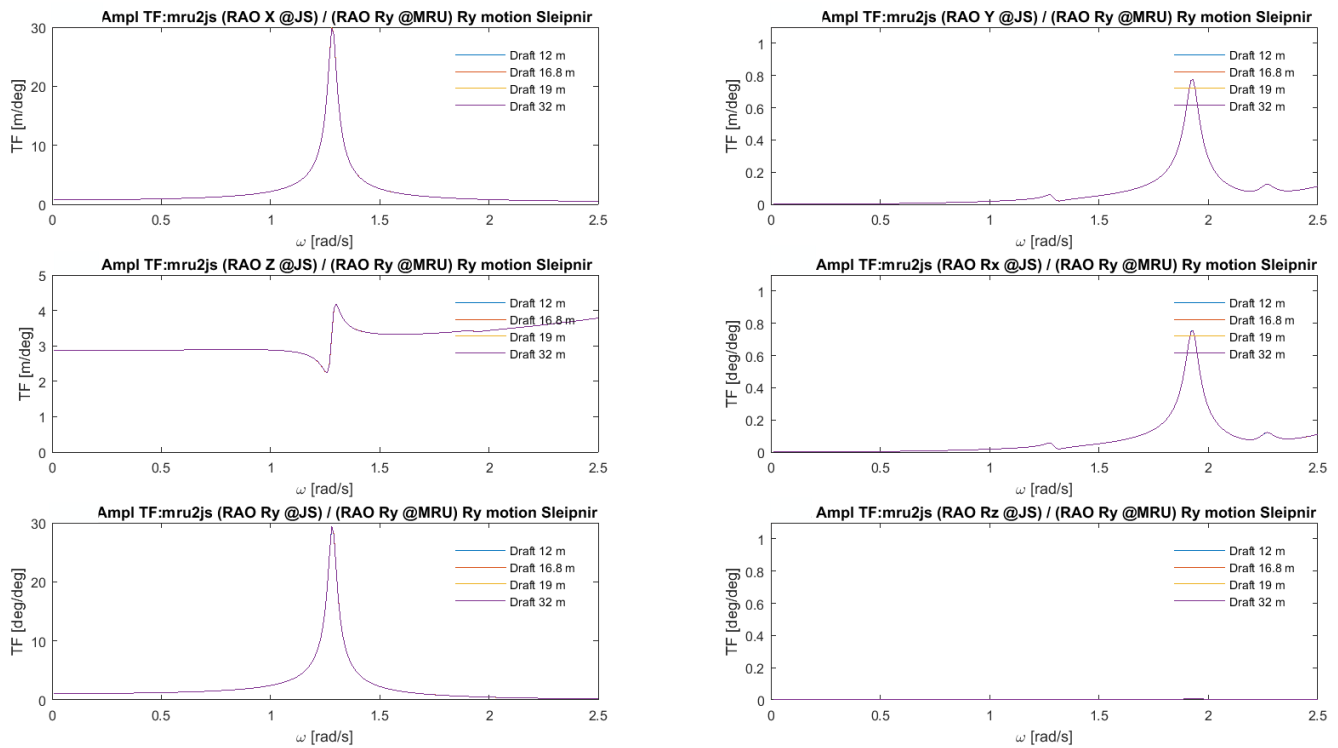


Figure C.5: The TFs for all six dof at the JS(B) due to a Pitch motion at the MRU(A)

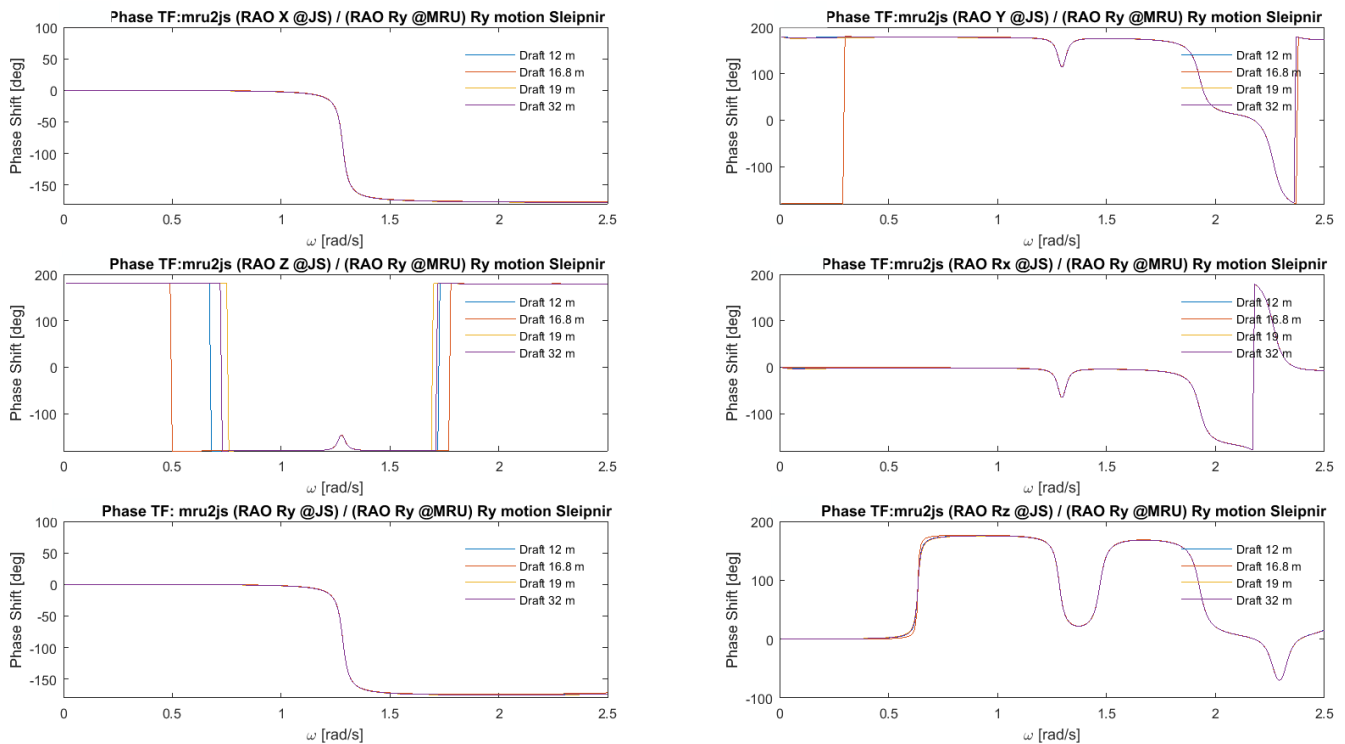


Figure C.6: The TFs phases for all six dof at the JS(B) due to a Pitch motion of the vessel at the MRU(A)

# Appendix D Synthetic Data Model X

## D.1 Synthetic Data X: TFs MRU2CP

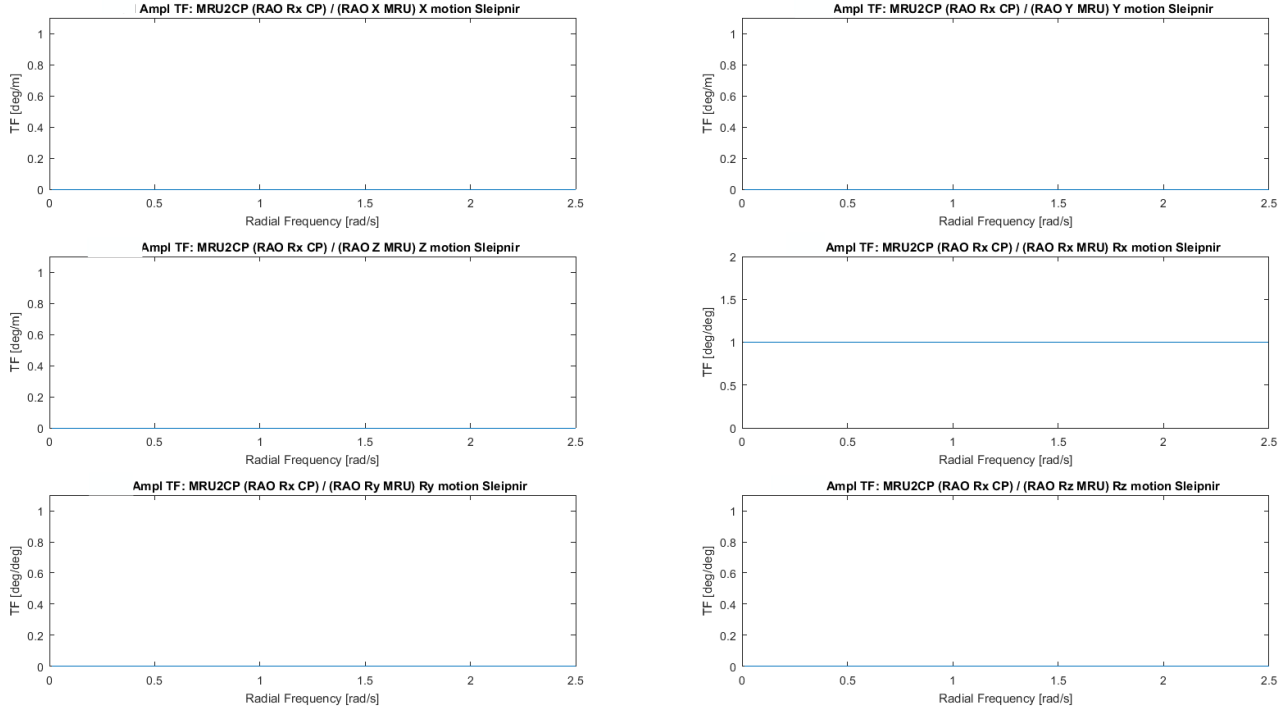


Figure D.1: TFs required for the response of RX at the control point

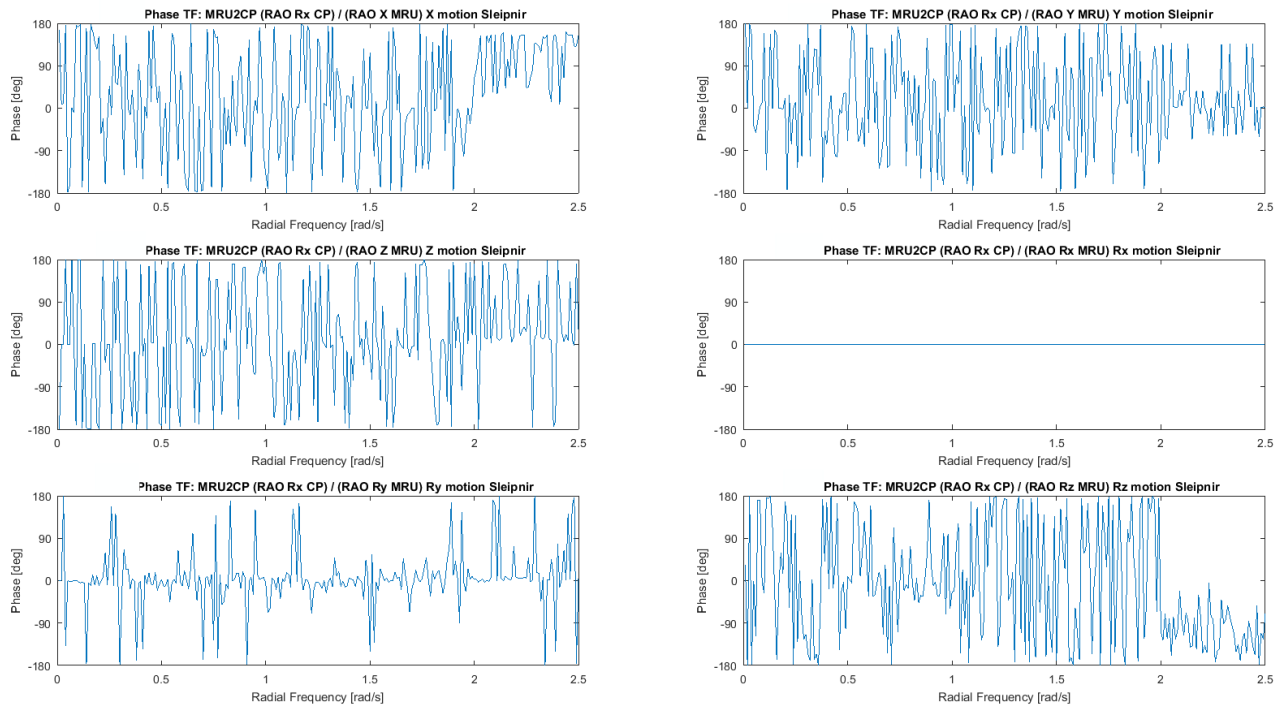


Figure D.2: Phases of the TFs required for the response of RX at the control point

## D.2 Synthetic data: responses control point

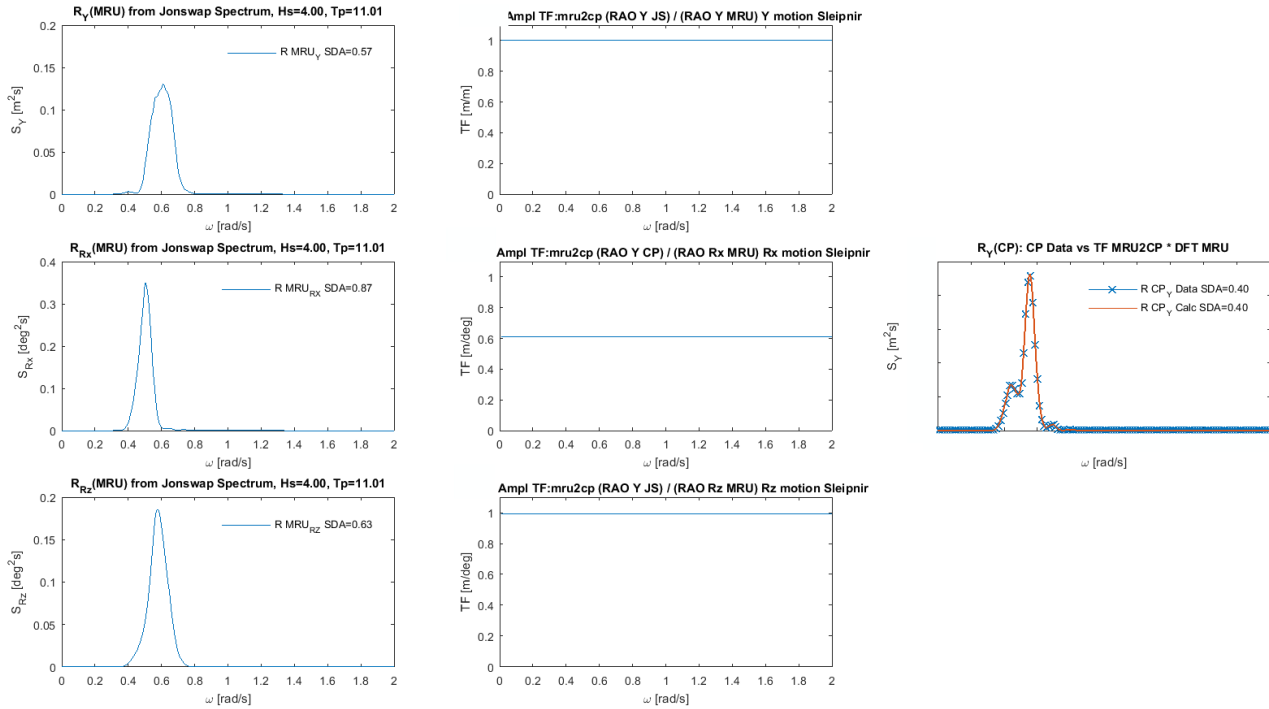


Figure D.3: Response in Sway at the control point due to Sway, Roll and Yaw at the MRU

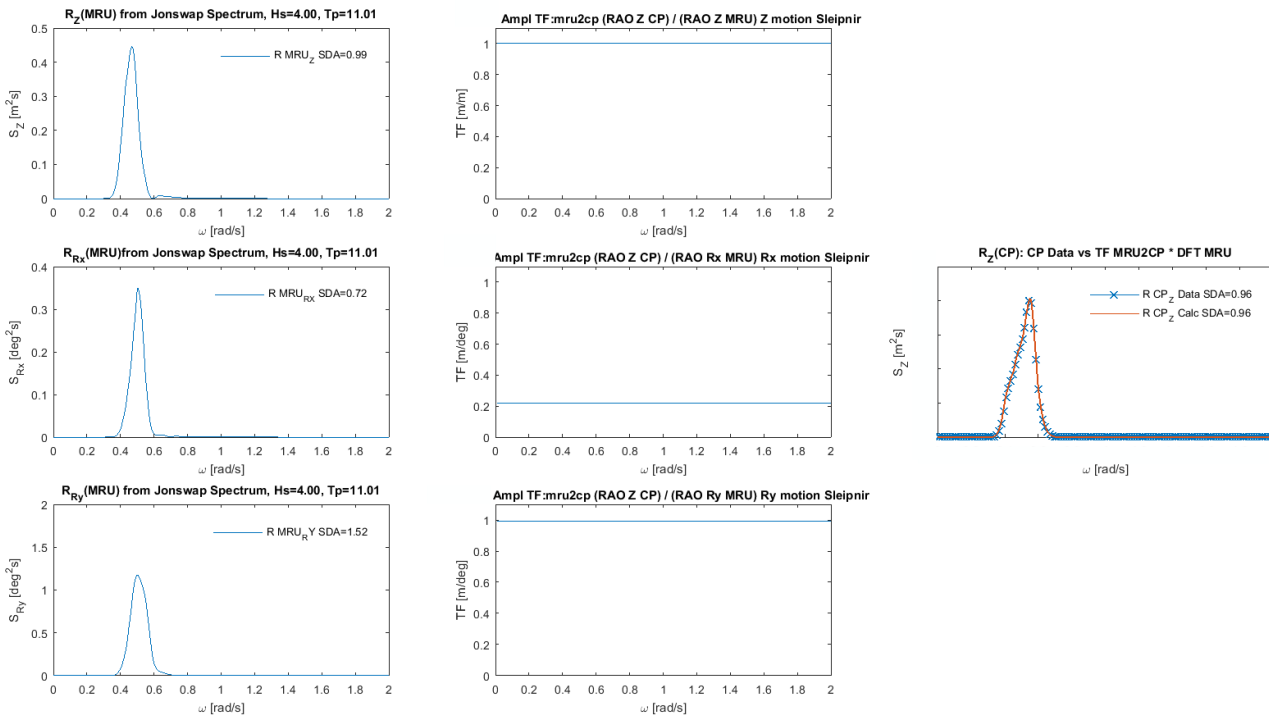


Figure D.4: Response in Heave at the control point due to Heave, Roll and Pitch at the MRU

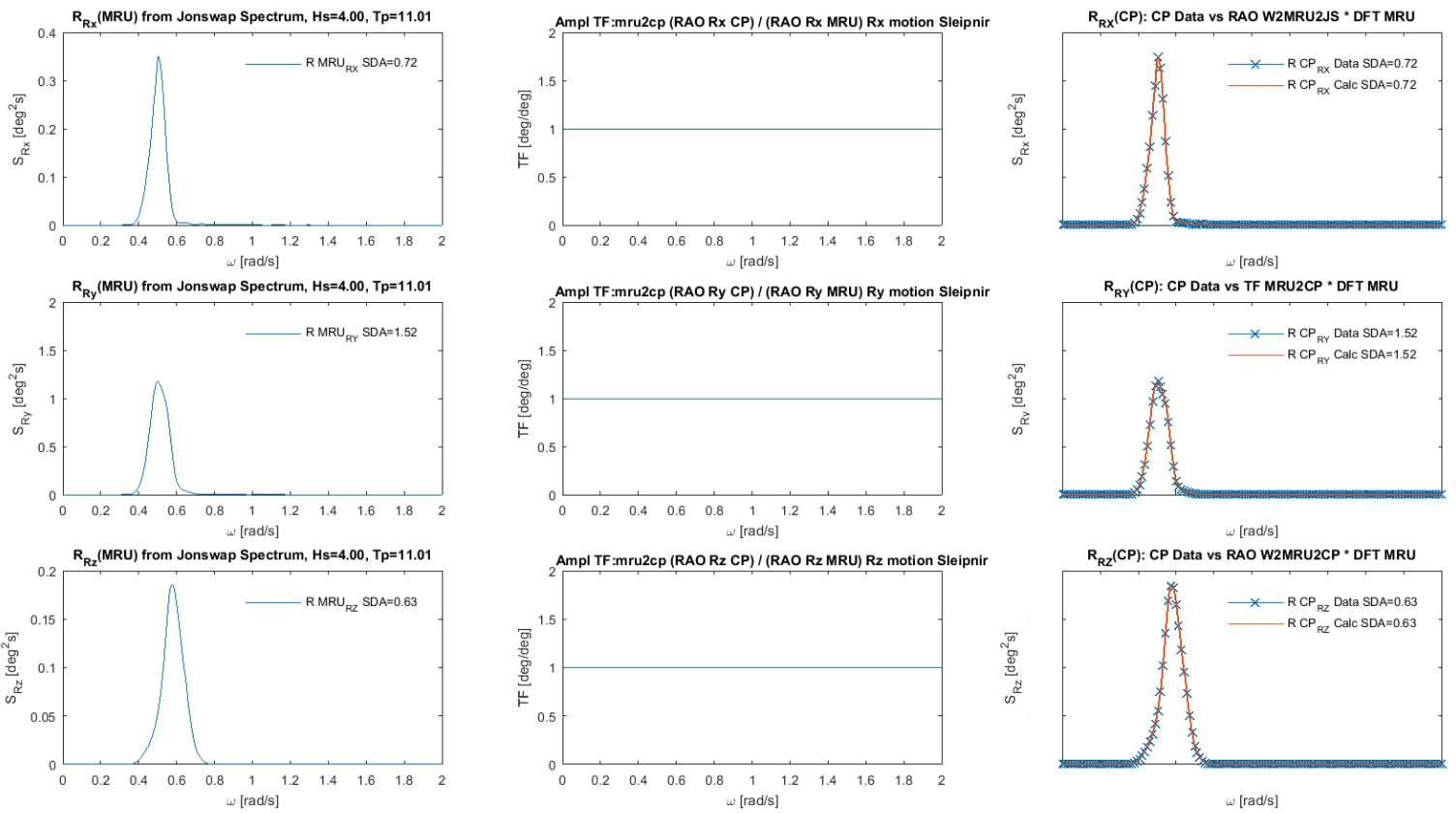


Figure D.5: Responses in Roll, Pitch and Yaw at the control point due to Roll, Pitch and Yaw at the MRU respectively

# Appendix E TFs MRU2JS X

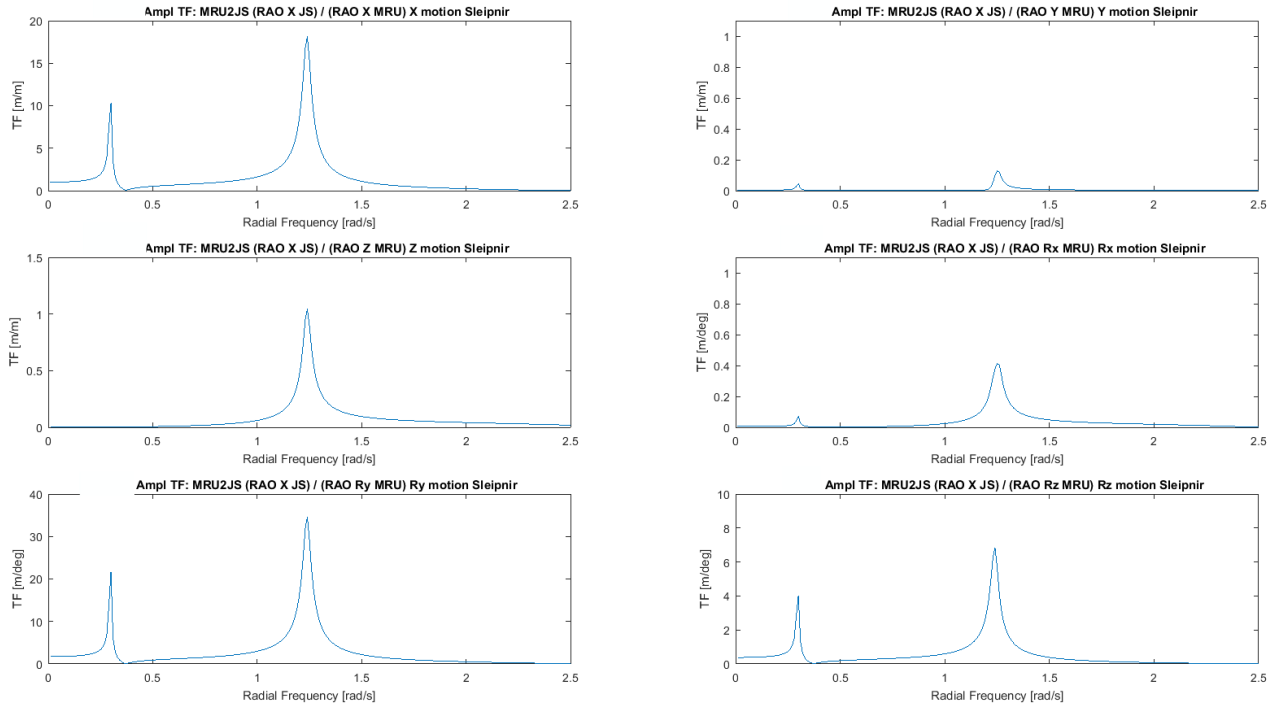


Figure E.1: TFs required for the response of X at the jacket sensor

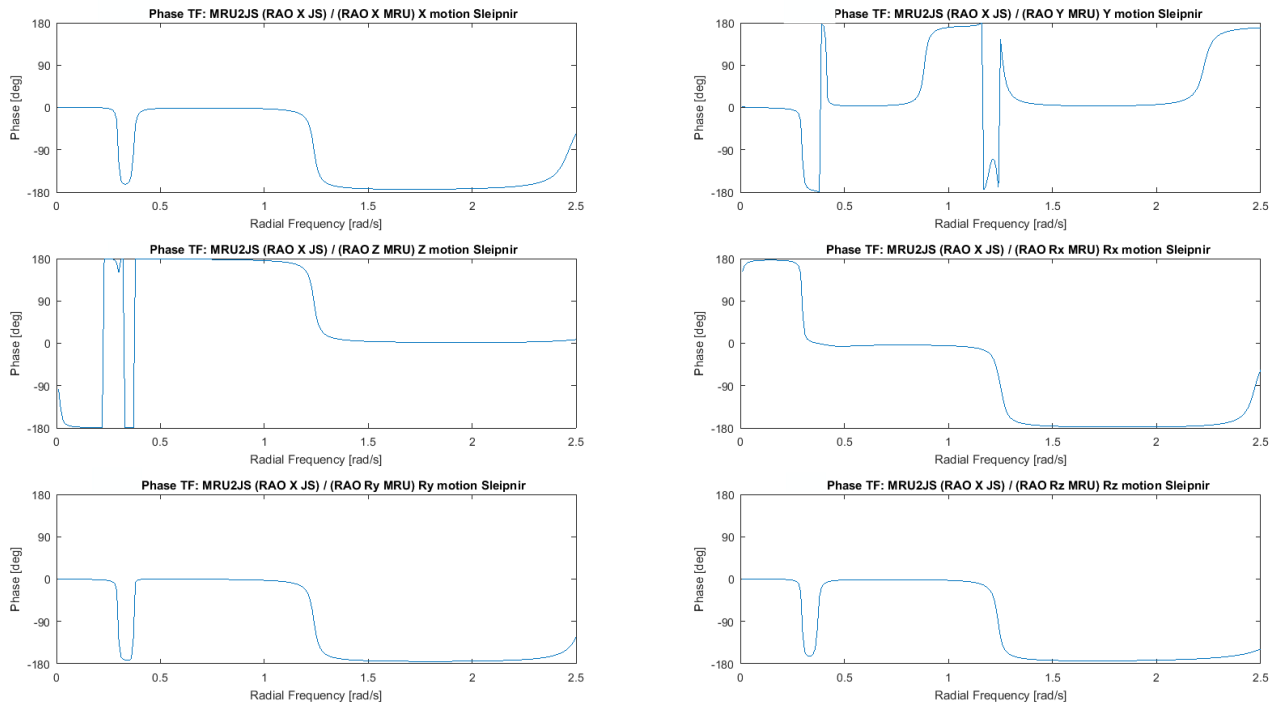


Figure E.2: Phases of the TFs required for the response of X at the jacket sensor

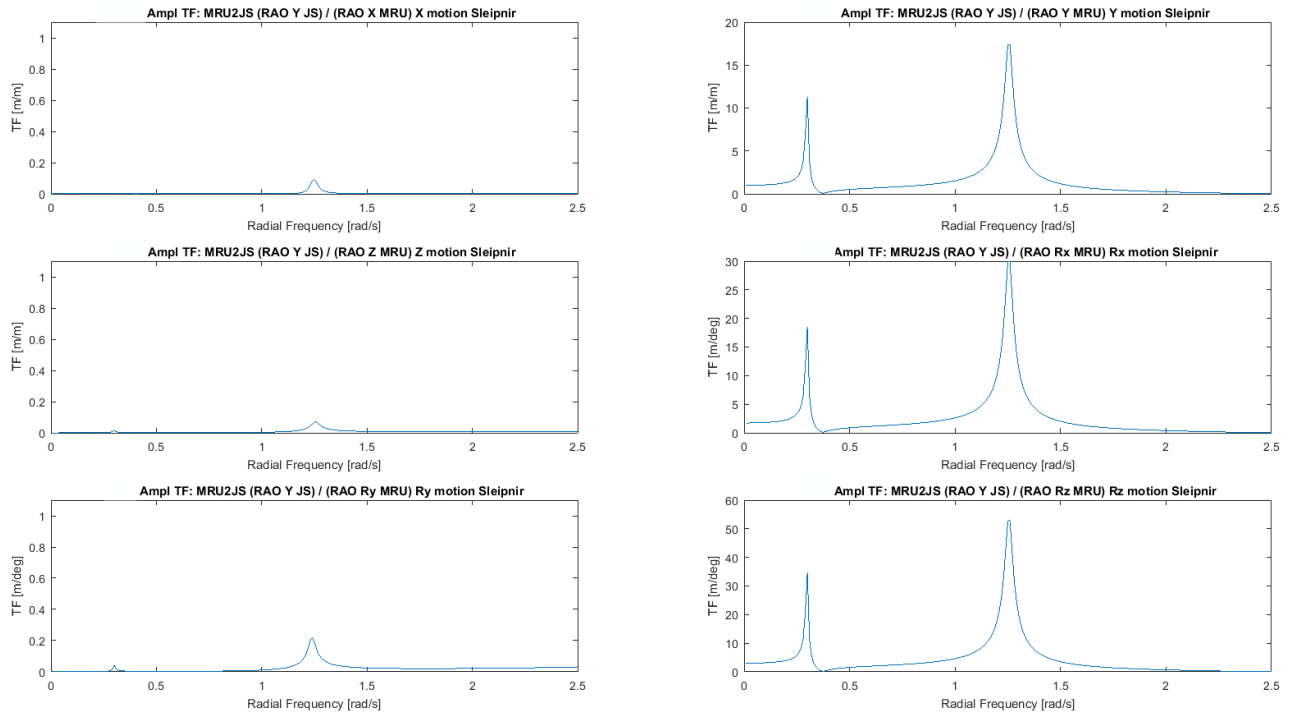


Figure E.3: TFs required for the response of Y at the jacket sensor

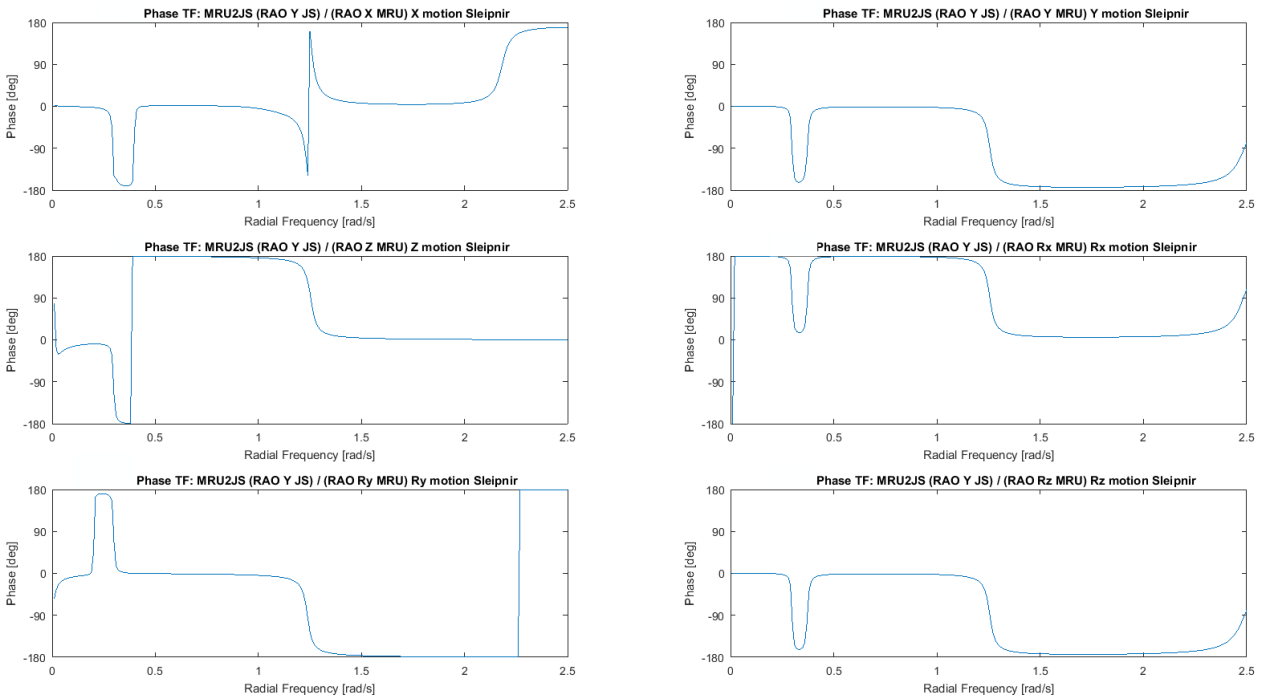


Figure E.4: Phases of the TFs required for the response of Y at the jacket sensor

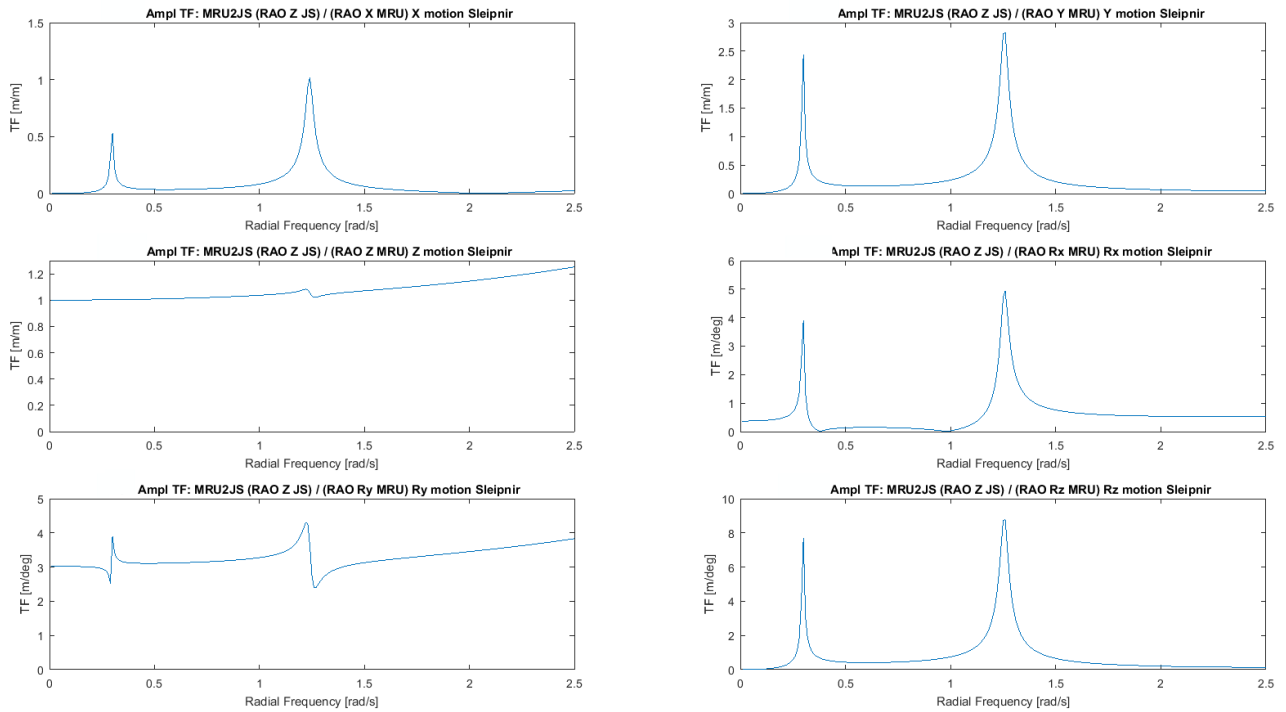


Figure E.5: TFs required for the response of Z at the jacket sensor

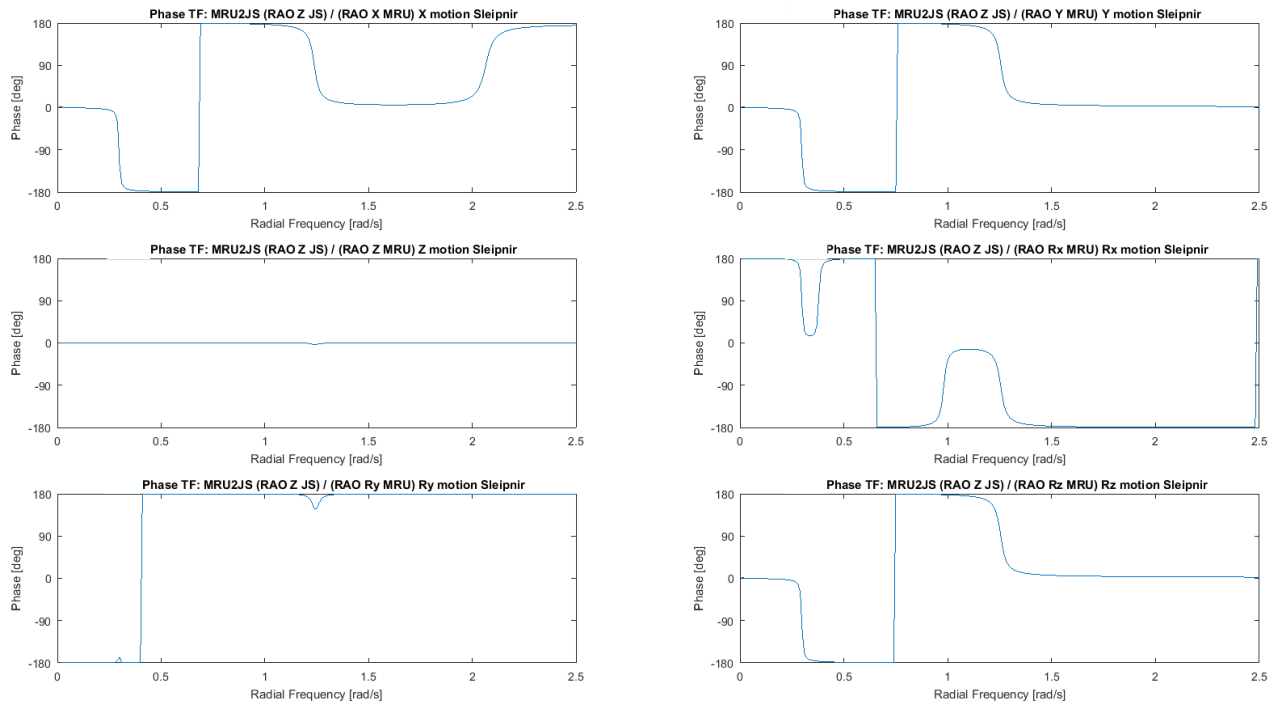


Figure E.6: Phases of the TFs required for the response of Z at the jacket sensor

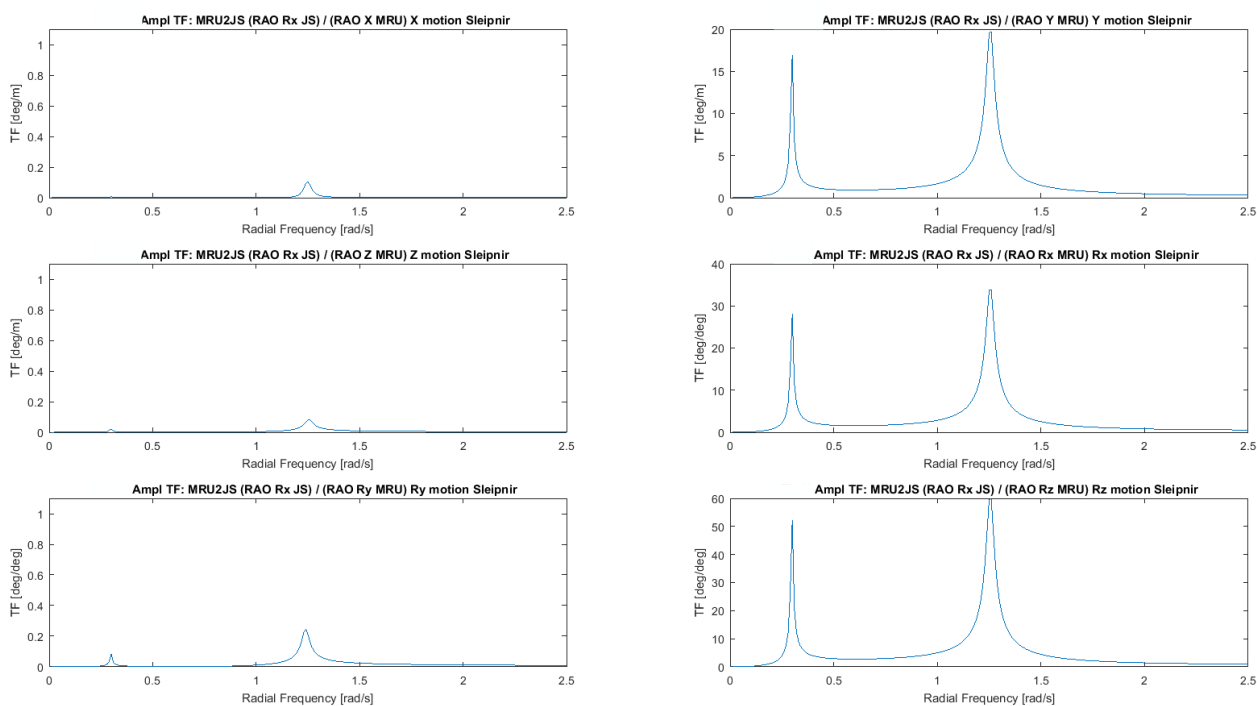


Figure E.7: TFs required for the response of RX at the jacket sensor

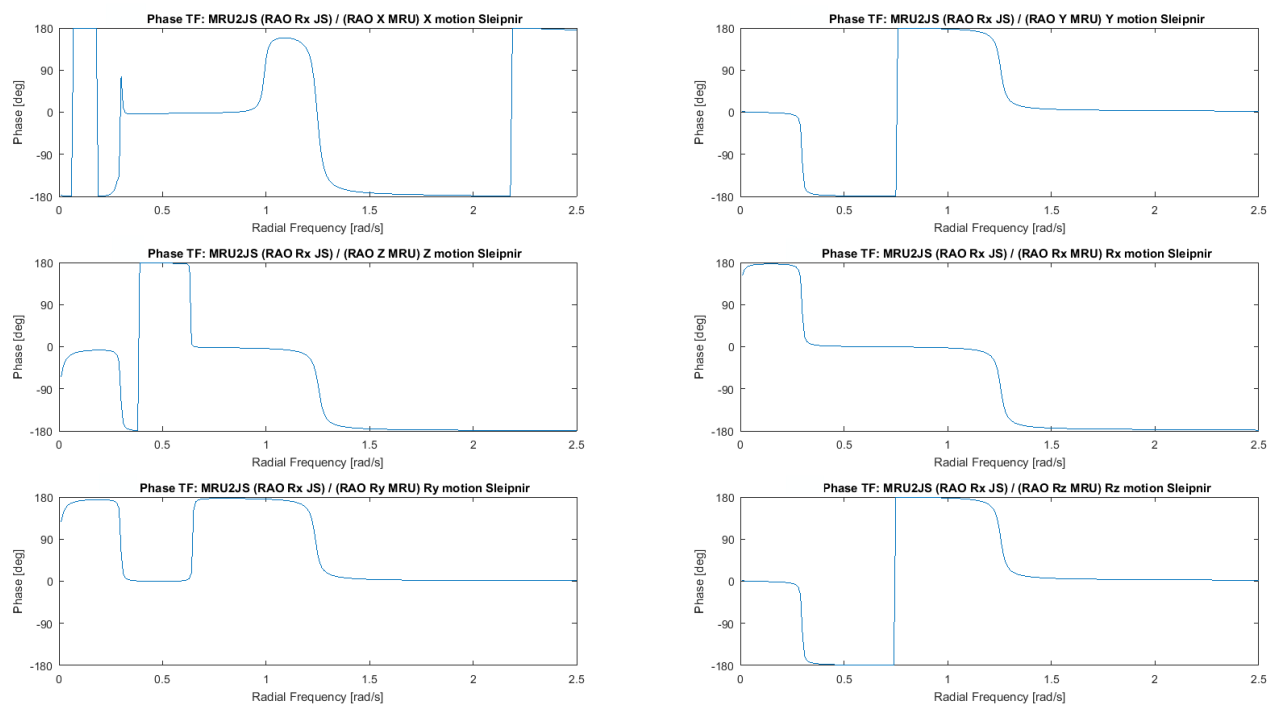


Figure E.8: Phases of the TFs required for the response of RX at the jacket sensor

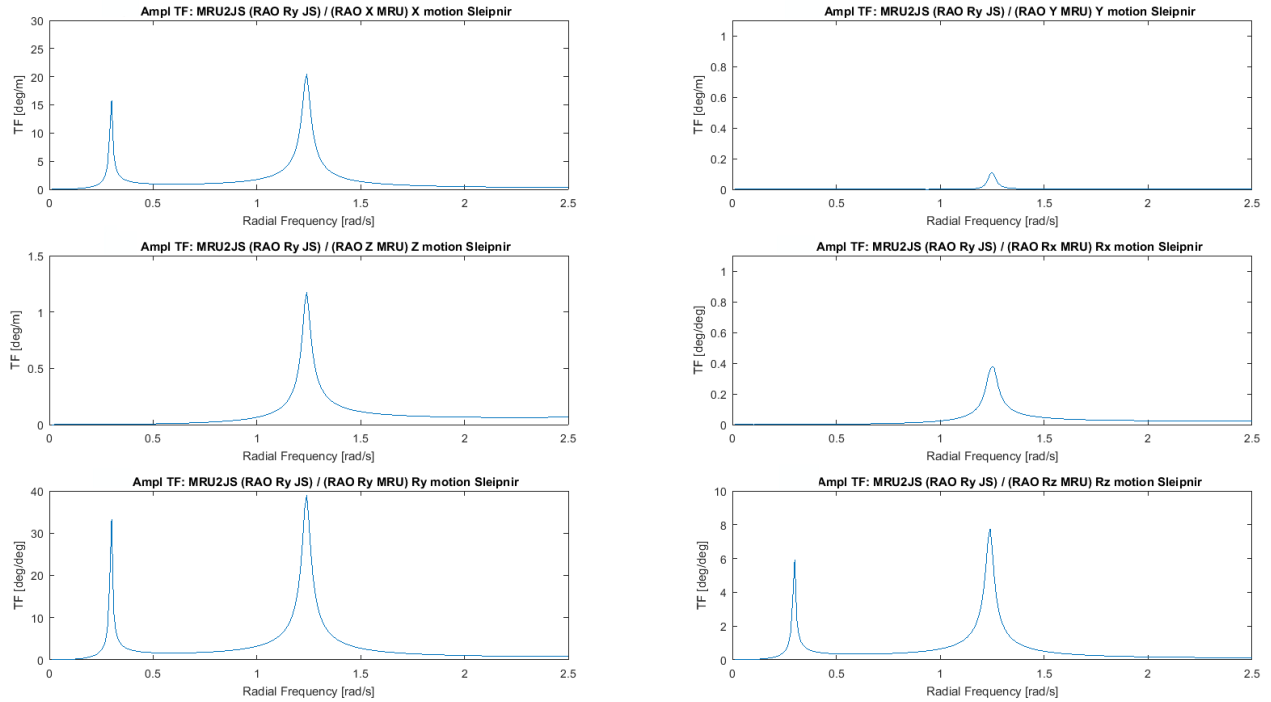


Figure E.9: TFs required for the response of RY at the jacket sensor

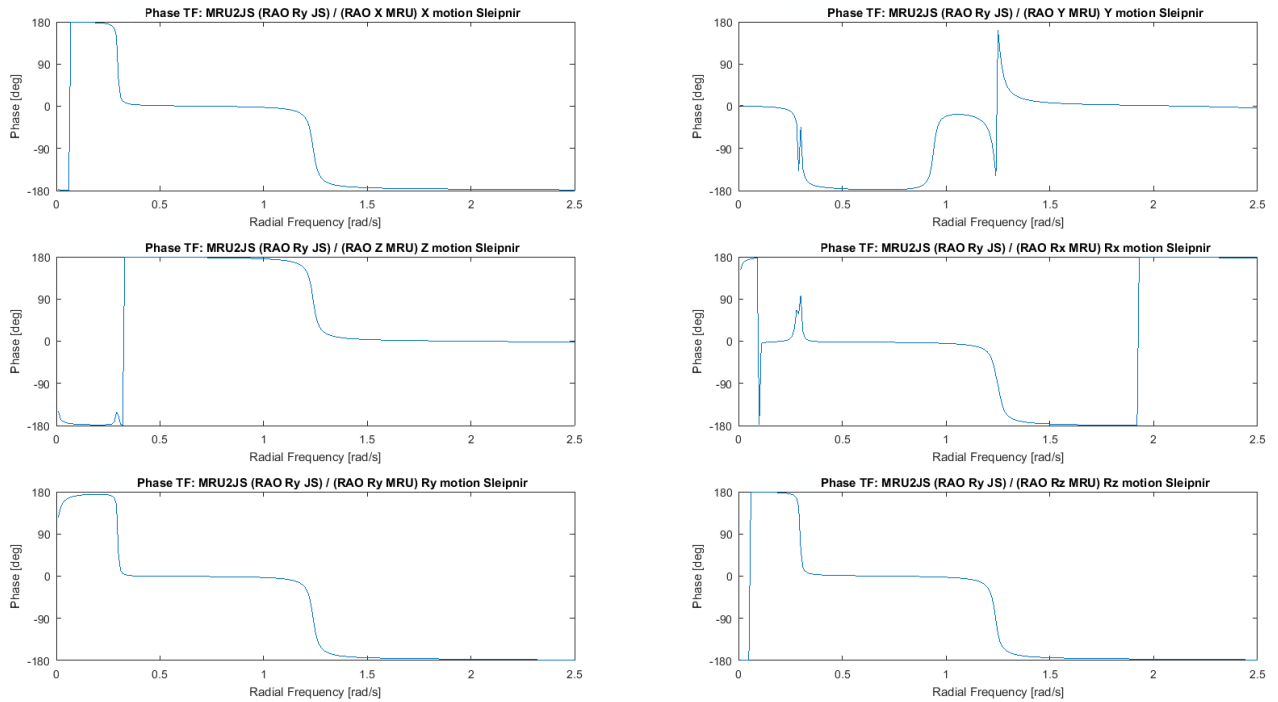


Figure E.10: Phases of the TFs required for the response of RY at the jacket sensor

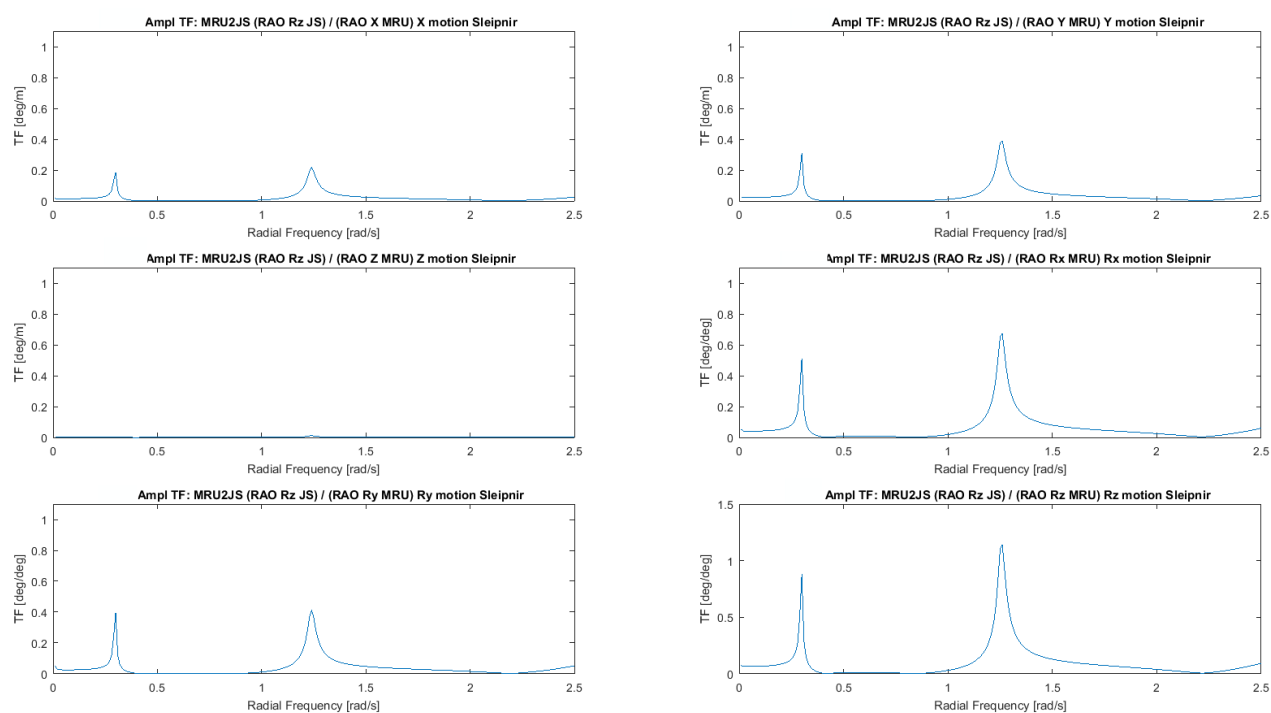


Figure E.11: TFs required for the response of RZ at the jacket sensor

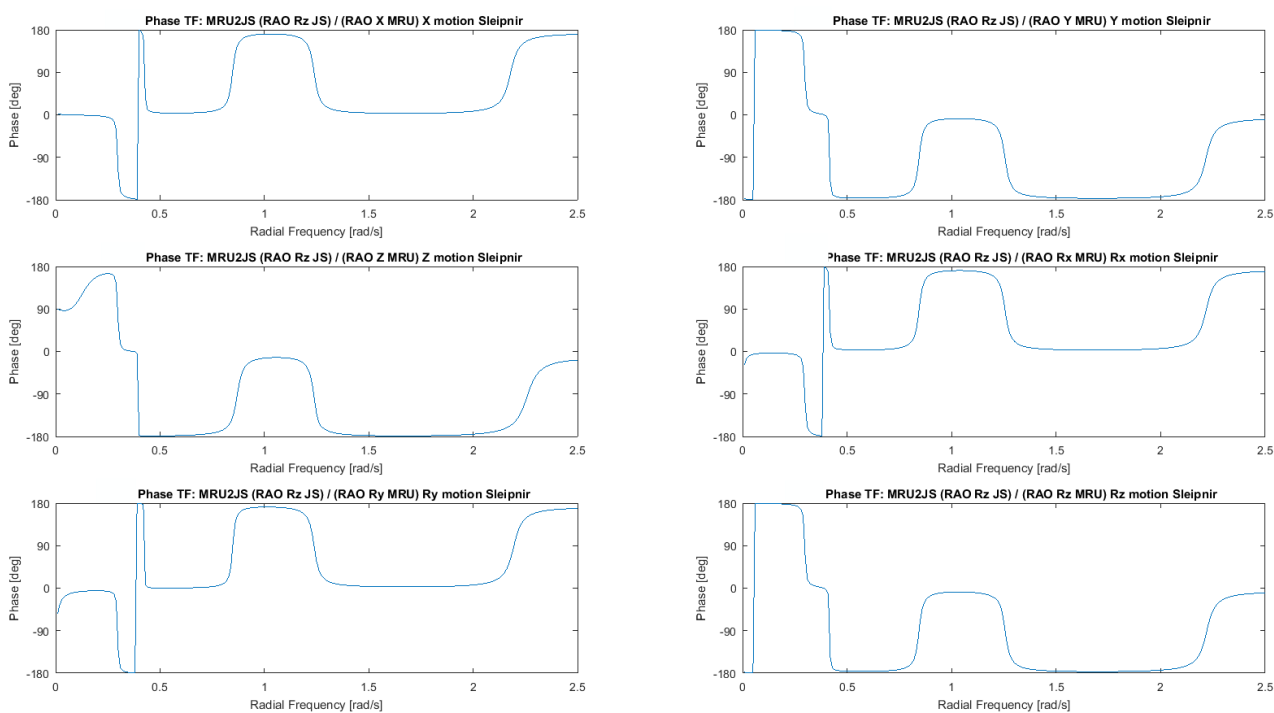


Figure E.12: Phases of the TFs required for the response of RZ at the jacket sensor

# Appendix F Synthetic data: response jacket sensor

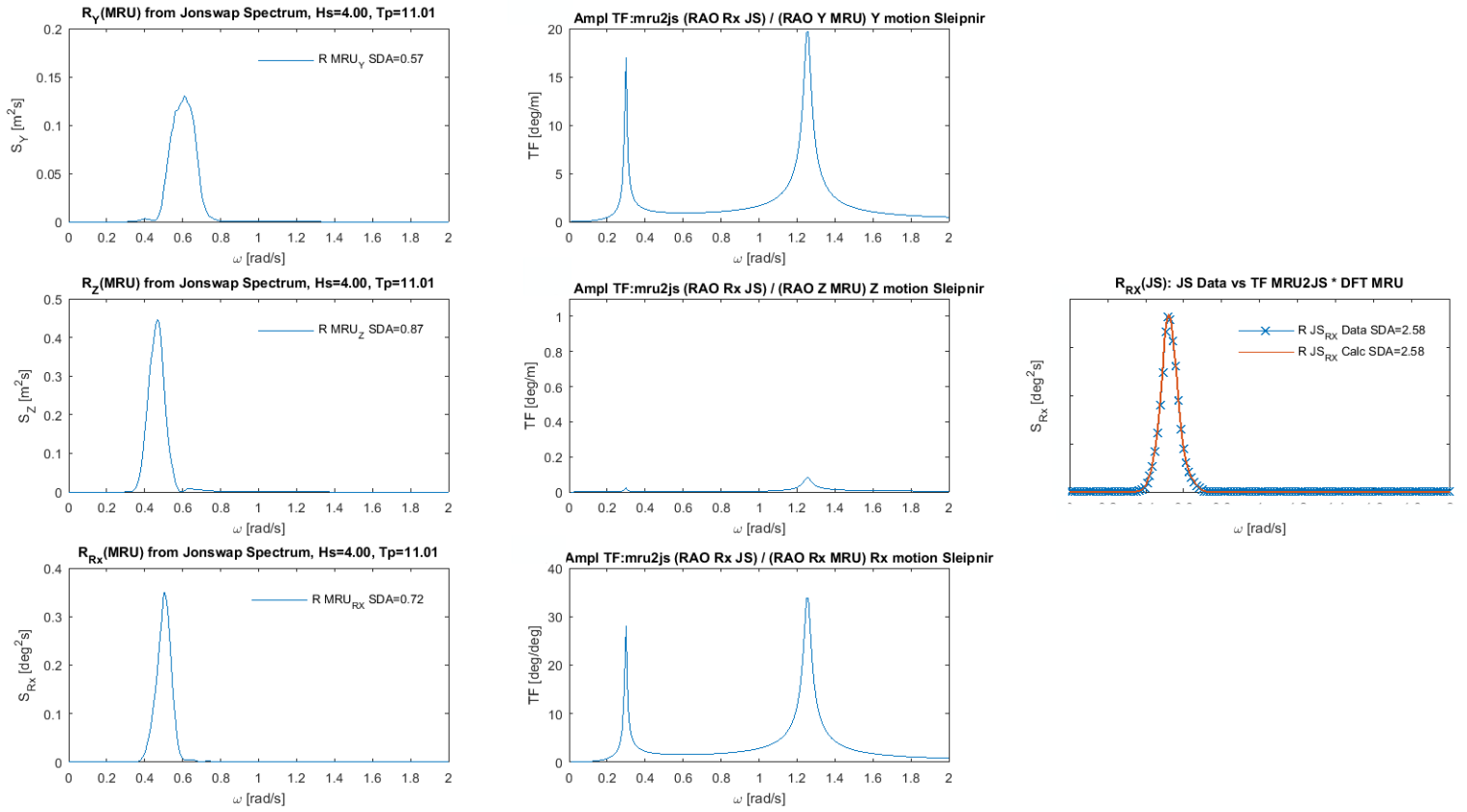


Figure F.1: Responses in Roll at the jacket sensor due to Sway, Heave and Roll at the MRU

## Appendix G MDM model X

$$\begin{pmatrix} TT_{x_{mru}} \\ TT_{y_{mru}} \\ TT_{z_{mru}} \\ TT_{rx_{mru}} \\ TT_{ry_{mru}} \\ TT_{rz_{mru}} \end{pmatrix} \xrightarrow{\text{FourierTransform}} \begin{pmatrix} DFT_{x_{mru}} \\ DFT_{y_{mru}} \\ DFT_{z_{mru}} \\ DFT_{rx_{mru}} \\ DFT_{ry_{mru}} \\ DFT_{rz_{mru}} \end{pmatrix} \quad (\text{G.1})$$

$$TF_{SMRU2JS} = \begin{pmatrix} \text{Vessel unrestrained in X} & \text{Vessel unrestrained in Y} & \text{Vessel unrestrained in Z} & \text{Vessel unrestrained in Rxx} & \text{Vessel unrestrained in Ryy} & \text{Vessel unrestrained in Rzz} \\ \frac{RAO_{\zeta, x_{js}}}{RAO_{\zeta, x_{mru}} RAO_{\zeta, y_{js}}} & \frac{RAO_{\zeta, x_{js}}}{RAO_{\zeta, y_{mru}} RAO_{\zeta, y_{js}}} & \frac{RAO_{\zeta, x_{js}}}{RAO_{\zeta, z_{mru}} RAO_{\zeta, y_{js}}} & \frac{RAO_{\zeta, x_{js}}}{RAO_{\zeta, rx_{mru}} RAO_{\zeta, y_{js}}} & \frac{RAO_{\zeta, x_{js}}}{RAO_{\zeta, ry_{mru}} RAO_{\zeta, y_{js}}} & \frac{RAO_{\zeta, x_{js}}}{RAO_{\zeta, rz_{mru}} RAO_{\zeta, y_{js}}} \\ \frac{RAO_{\zeta, x_{mru}}}{RAO_{\zeta, z_{js}}} & \frac{RAO_{\zeta, y_{mru}}}{RAO_{\zeta, z_{js}}} & \frac{RAO_{\zeta, z_{mru}}}{RAO_{\zeta, z_{js}}} & \frac{RAO_{\zeta, rx_{mru}}}{RAO_{\zeta, z_{js}}} & \frac{RAO_{\zeta, ry_{mru}}}{RAO_{\zeta, z_{js}}} & \frac{RAO_{\zeta, rz_{mru}}}{RAO_{\zeta, z_{js}}} \\ \frac{RAO_{\zeta, x_{mru}}}{RAO_{\zeta, rx_{js}}} & \frac{RAO_{\zeta, y_{mru}}}{RAO_{\zeta, rx_{js}}} & \frac{RAO_{\zeta, z_{mru}}}{RAO_{\zeta, rx_{js}}} & \frac{RAO_{\zeta, rx_{mru}}}{RAO_{\zeta, rx_{js}}} & \frac{RAO_{\zeta, ry_{mru}}}{RAO_{\zeta, rx_{js}}} & \frac{RAO_{\zeta, rz_{mru}}}{RAO_{\zeta, rx_{js}}} \\ \frac{RAO_{\zeta, x_{mru}}}{RAO_{\zeta, ry_{js}}} & \frac{RAO_{\zeta, y_{mru}}}{RAO_{\zeta, ry_{js}}} & \frac{RAO_{\zeta, z_{mru}}}{RAO_{\zeta, ry_{js}}} & \frac{RAO_{\zeta, rx_{mru}}}{RAO_{\zeta, ry_{js}}} & \frac{RAO_{\zeta, ry_{mru}}}{RAO_{\zeta, ry_{js}}} & \frac{RAO_{\zeta, rz_{mru}}}{RAO_{\zeta, ry_{js}}} \\ \frac{RAO_{\zeta, x_{mru}}}{RAO_{\zeta, rz_{js}}} & \frac{RAO_{\zeta, y_{mru}}}{RAO_{\zeta, rz_{js}}} & \frac{RAO_{\zeta, z_{mru}}}{RAO_{\zeta, rz_{js}}} & \frac{RAO_{\zeta, rx_{mru}}}{RAO_{\zeta, rz_{js}}} & \frac{RAO_{\zeta, ry_{mru}}}{RAO_{\zeta, rz_{js}}} & \frac{RAO_{\zeta, rz_{mru}}}{RAO_{\zeta, rz_{js}}} \\ \frac{RAO_{\zeta, x_{mru}}}{RAO_{\zeta, y_{mru}}} & \frac{RAO_{\zeta, y_{mru}}}{RAO_{\zeta, y_{mru}}} & \frac{RAO_{\zeta, z_{mru}}}{RAO_{\zeta, z_{mru}}} & \frac{RAO_{\zeta, rx_{mru}}}{RAO_{\zeta, rx_{mru}}} & \frac{RAO_{\zeta, ry_{mru}}}{RAO_{\zeta, ry_{mru}}} & \frac{RAO_{\zeta, rz_{mru}}}{RAO_{\zeta, rz_{mru}}} \end{pmatrix} \quad (\text{G.2})$$

$$\begin{pmatrix} DFT_{mru6dof \rightarrow x_{js}} \\ DFT_{mru6dof \rightarrow y_{js}} \\ DFT_{mru6dof \rightarrow z_{js}} \\ DFT_{mru6dof \rightarrow rx_{js}} \\ DFT_{mru6dof \rightarrow ry_{js}} \\ DFT_{mru6dof \rightarrow rz_{js}} \end{pmatrix} = \begin{pmatrix} DFT_{x_{mru}} \\ DFT_{y_{mru}} \\ DFT_{z_{mru}} \\ DFT_{rx_{mru}} \\ DFT_{ry_{mru}} \\ DFT_{rz_{mru}} \end{pmatrix} \cdot TF_{SMRU2JS} \quad (\text{G.3})$$

$$\begin{pmatrix} DFT_{mru6dof \rightarrow x_{js}} \\ DFT_{mru6dof \rightarrow y_{js}} \\ DFT_{mru6dof \rightarrow z_{js}} \\ DFT_{mru6dof \rightarrow rx_{js}} \\ DFT_{mru6dof \rightarrow ry_{js}} \\ DFT_{mru6dof \rightarrow rz_{js}} \end{pmatrix} \xrightarrow{DFT2Spec} \begin{pmatrix} S_{mru6dof \rightarrow x_{js}} \\ S_{mru6dof \rightarrow y_{js}} \\ S_{mru6dof \rightarrow z_{js}} \\ S_{mru6dof \rightarrow rx_{js}} \\ S_{mru6dof \rightarrow ry_{js}} \\ S_{mru6dof \rightarrow rz_{js}} \end{pmatrix} \quad DFT2Spec : \quad \begin{aligned} \zeta_{dof_{js}} &= \frac{\|DFT_{dof_{js}}\|}{N} \\ S_{dof_{js}} &= \frac{\zeta_{dof_{js}}^2 \cdot \Delta\omega}{2} \\ \epsilon &= \angle(DFT_{dof_{js}}) \cdot \frac{180}{\pi} \end{aligned} \quad (\text{G.4})$$

$$\begin{pmatrix} S_{mru6dof \rightarrow x_{js}} \\ S_{mru6dof \rightarrow y_{js}} \\ S_{mru6dof \rightarrow z_{js}} \\ S_{mru6dof \rightarrow rx_{js}} \\ S_{mru6dof \rightarrow ry_{js}} \\ S_{mru6dof \rightarrow rz_{js}} \end{pmatrix} \approx \begin{pmatrix} S_{x_{js}} \\ S_{y_{js}} \\ S_{z_{js}} \\ S_{rx_{js}} \\ S_{ry_{js}} \\ S_{rz_{js}} \end{pmatrix} \leftarrow \begin{matrix} TT_{x_{js}} \\ TT_{y_{js}} \\ TT_{z_{js}} \\ TT_{rx_{js}} \\ TT_{ry_{js}} \\ TT_{rz_{js}} \end{matrix} \quad (\text{G.5})$$

# Appendix H MDM model responses jacket X

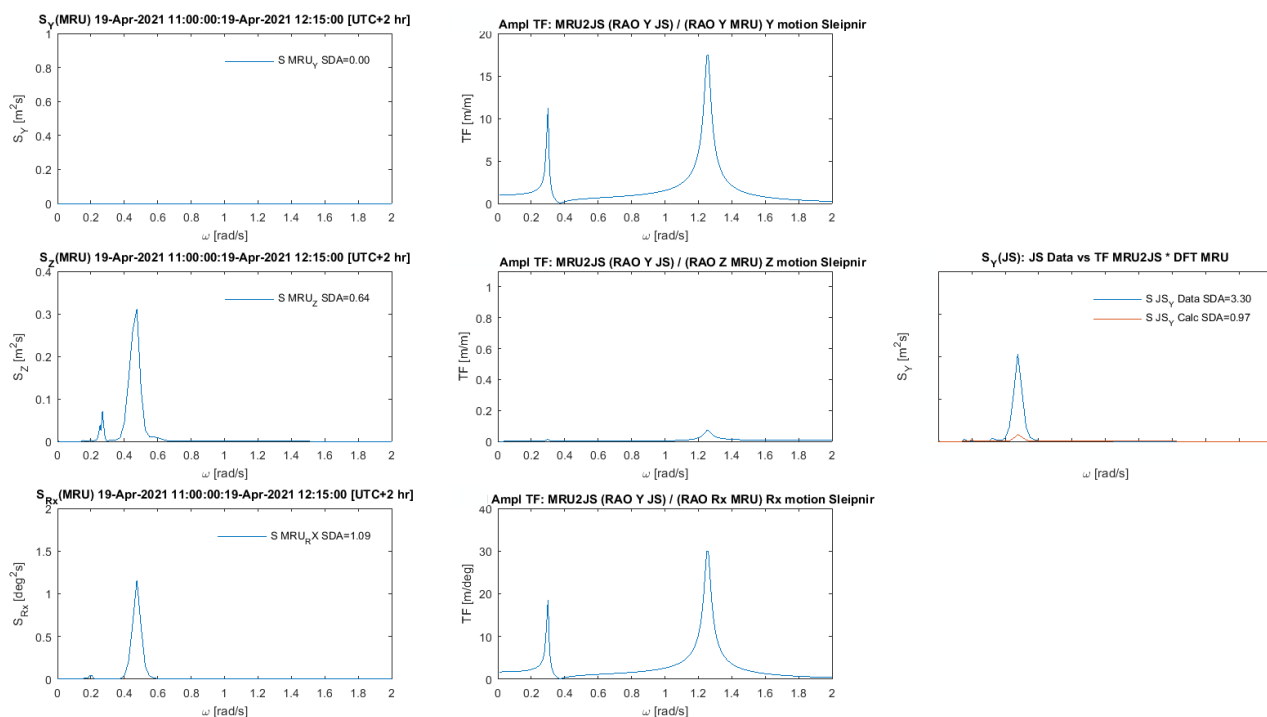


Figure H.1: MDM jacket Sway due to most contributing vessel motions vs measured Sway jacket

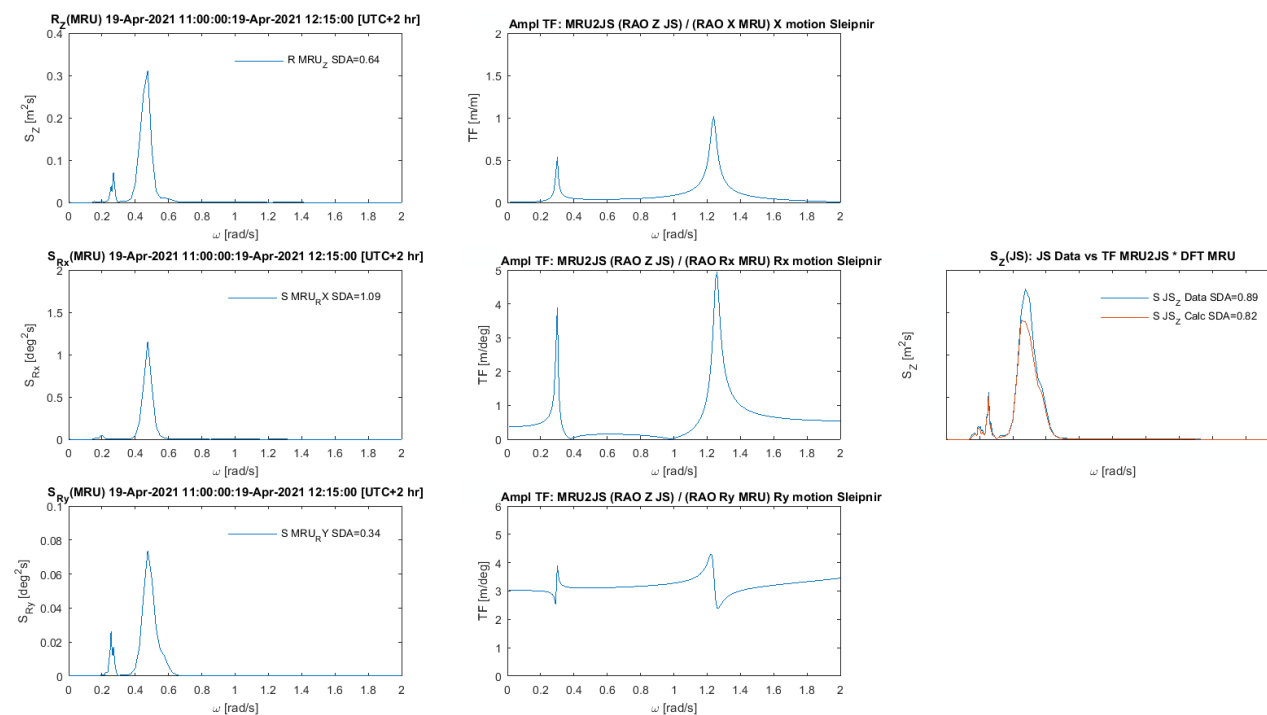


Figure H.2: MDM jacket Heave due to most contributing vessel motions vs measured Heave jacket

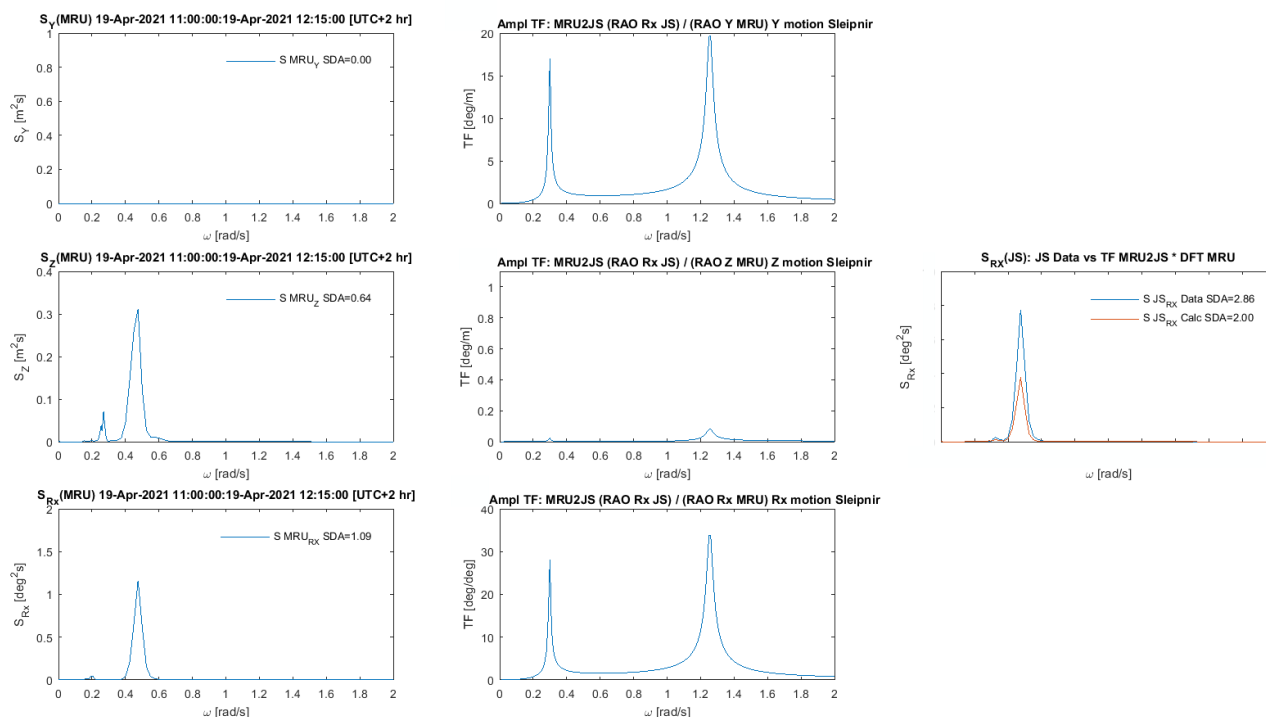


Figure H.3: MDM jacket Roll due to most contributing vessel motions vs measured Roll jacket

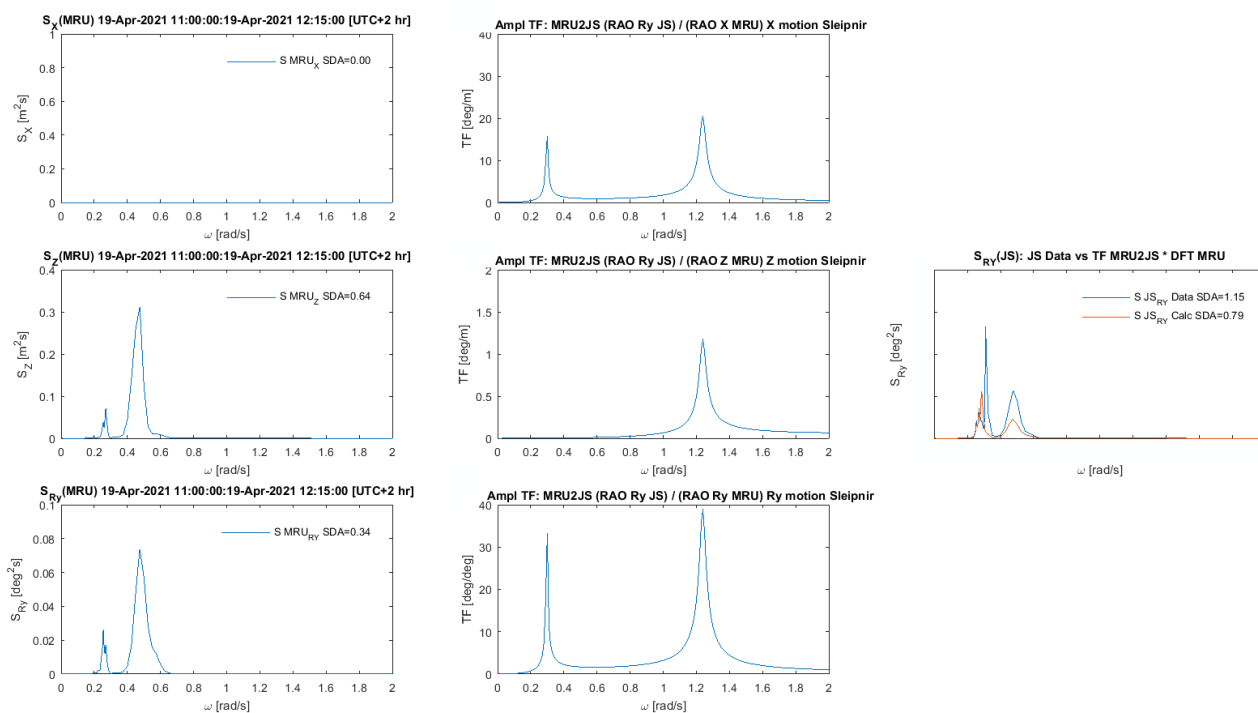


Figure H.4: MDM jacket Pitch due to most contributing vessel motions vs measured Pitch jacket

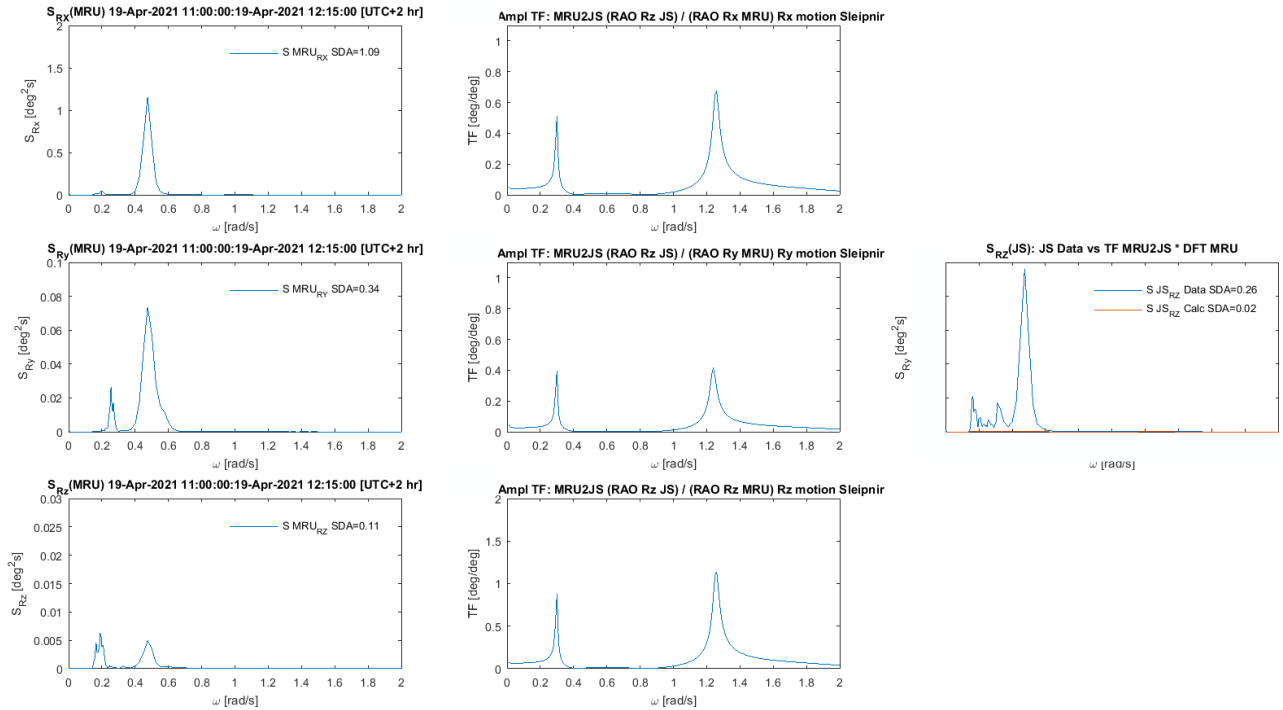


Figure H.5: MDM jacket Yaw due to most contributing vessel motions vs measured Yaw jacket

# Appendix I Overview measured motions jacket

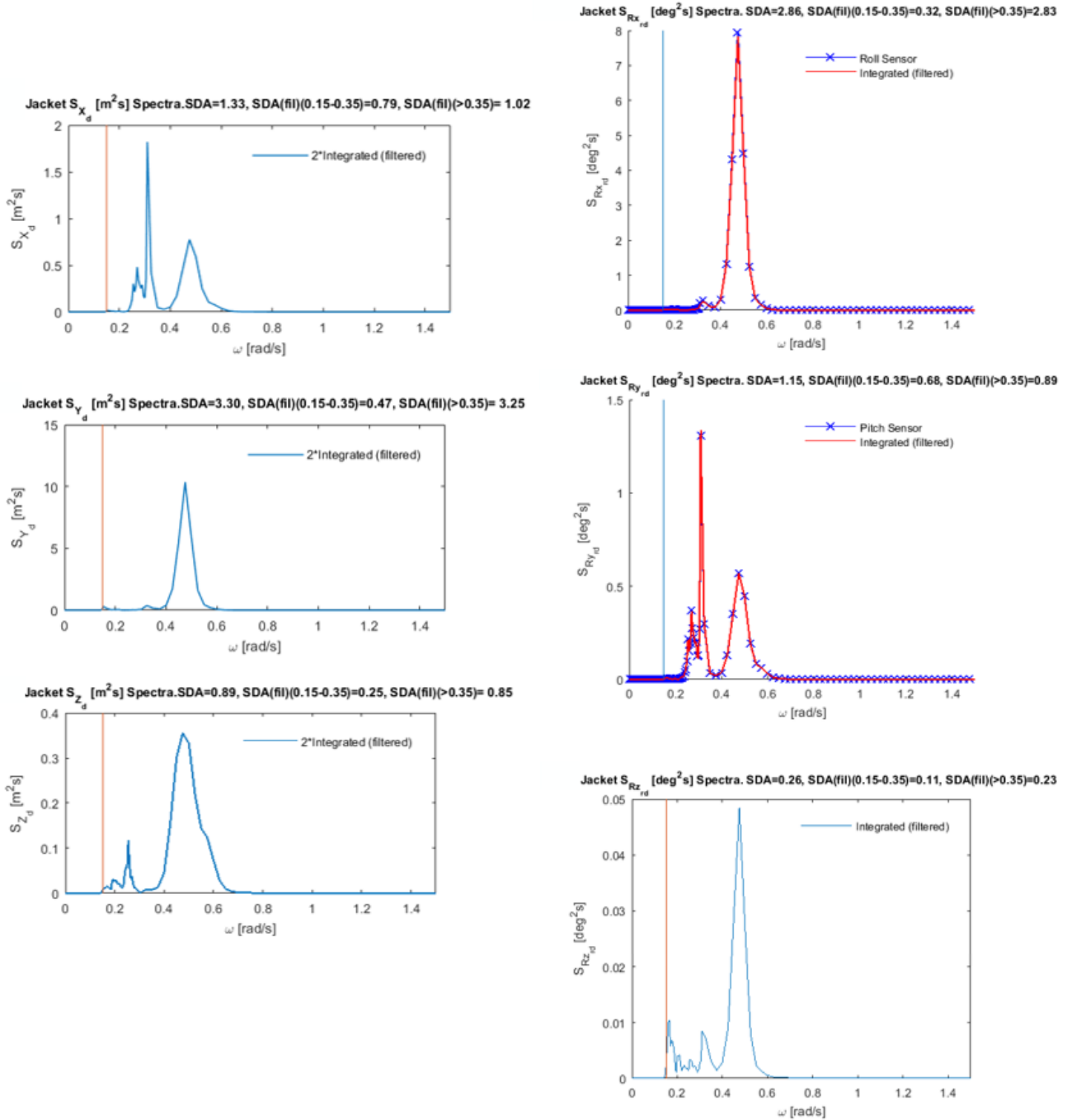


Figure I.1: Overview of all measured jacket motions

## Appendix J FDM model X part 1

$$\begin{pmatrix} TT_{x_{mru}} \\ TT_{y_{mru}} \\ TT_{z_{mru}} \\ TT_{rx_{mru}} \\ TT_{ry_{mru}} \\ TT_{rz_{mru}} \end{pmatrix} \xrightarrow{\text{FourierTransform}} \begin{pmatrix} DFT_{x_{mru}} \\ DFT_{y_{mru}} \\ DFT_{z_{mru}} \\ DFT_{rx_{mru}} \\ DFT_{ry_{mru}} \\ DFT_{rz_{mru}} \end{pmatrix} \quad (\text{J.1})$$

$$TFsMRU2BP = \begin{pmatrix} \begin{array}{c} \text{Vessel unrestrained in X} \\ \frac{RAO_{\zeta, Fx_{BP}}}{RAO_{\zeta, xMRU}} \\ \frac{RAO_{\zeta, Fy_{BP}}}{RAO_{\zeta, yMRU}} \\ \frac{RAO_{\zeta, xMRU}}{RAO_{\zeta, Mz_{BP}}} \\ \frac{RAO_{\zeta, Mz_{BP}}}{RAO_{\zeta, xMRU}} \end{array} & \begin{array}{c} \text{Vessel unrestrained in Y} \\ \frac{RAO_{\zeta, Fx_{BP}}}{RAO_{\zeta, yMRU}} \\ \frac{RAO_{\zeta, Fy_{BP}}}{RAO_{\zeta, yMRU}} \\ \frac{RAO_{\zeta, yMRU}}{RAO_{\zeta, Mz_{BP}}} \\ \frac{RAO_{\zeta, Mz_{BP}}}{RAO_{\zeta, yMRU}} \end{array} & \begin{array}{c} \text{Vessel unrestrained in Z} \\ \frac{RAO_{\zeta, Fx_{BP}}}{RAO_{\zeta, zMRU}} \\ \frac{RAO_{\zeta, Fy_{BP}}}{RAO_{\zeta, zMRU}} \\ \frac{RAO_{\zeta, zMRU}}{RAO_{\zeta, Mz_{BP}}} \\ \frac{RAO_{\zeta, Mz_{BP}}}{RAO_{\zeta, zMRU}} \end{array} & \begin{array}{c} \text{Vessel unrestrained in Rx} \\ \frac{RAO_{\zeta, Fx_{BP}}}{RAO_{\zeta, rxMRU}} \\ \frac{RAO_{\zeta, Fy_{BP}}}{RAO_{\zeta, rxMRU}} \\ \frac{RAO_{\zeta, rxMRU}}{RAO_{\zeta, Mz_{BP}}} \\ \frac{RAO_{\zeta, Mz_{BP}}}{RAO_{\zeta, rxMRU}} \end{array} & \begin{array}{c} \text{Vessel unrestrained in Ry} \\ \frac{RAO_{\zeta, Fx_{BP}}}{RAO_{\zeta, ryMRU}} \\ \frac{RAO_{\zeta, Fy_{BP}}}{RAO_{\zeta, ryMRU}} \\ \frac{RAO_{\zeta, ryMRU}}{RAO_{\zeta, Mz_{BP}}} \\ \frac{RAO_{\zeta, Mz_{BP}}}{RAO_{\zeta, ryMRU}} \end{array} & \begin{array}{c} \text{Vessel unrestrained in Rz} \\ \frac{RAO_{\zeta, Fx_{BP}}}{RAO_{\zeta, rzMRU}} \\ \frac{RAO_{\zeta, Fy_{BP}}}{RAO_{\zeta, rzMRU}} \\ \frac{RAO_{\zeta, rzMRU}}{RAO_{\zeta, Mz_{BP}}} \\ \frac{RAO_{\zeta, Mz_{BP}}}{RAO_{\zeta, rzMRU}} \end{array} \end{pmatrix} \quad (\text{J.2})$$

$$\begin{pmatrix} DFT_{mru6dof \rightarrow Fx_{bp}} \\ DFT_{mru6dof \rightarrow Fy_{bp}} \\ DFT_{mru6dof \rightarrow Mz_{bp}} \end{pmatrix} = \begin{pmatrix} DFT_{x_{mru}} \\ DFT_{y_{mru}} \\ DFT_{z_{mru}} \\ DFT_{rx_{mru}} \\ DFT_{ry_{mru}} \\ DFT_{rz_{mru}} \end{pmatrix} \cdot TFsMRU2BP \quad (\text{J.3})$$

$$\begin{pmatrix} DFT_{mru6dof \rightarrow Fx_{bp}} \\ DFT_{mru6dof \rightarrow Fy_{bp}} \\ DFT_{mru6dof \rightarrow Mz_{bp}} \end{pmatrix} \xrightarrow{DFT2Spec} \begin{pmatrix} S_{mru6dof \rightarrow Fx_{bp}} \\ S_{mru6dof \rightarrow Fy_{bp}} \\ S_{mru6dof \rightarrow Mz_{bp}} \end{pmatrix} \quad DFT2Spec : \quad \begin{array}{l} \zeta_{dof_{bp}} = \frac{\|DFT_{dof_{bp}}\|}{N} \\ S_{dof_{bp}} = \frac{\zeta_{dof_{bp}}^2 \cdot \Delta\omega}{2} \\ \epsilon = \angle(DFT_{dof_{bp}}) \cdot \frac{180}{\pi} \end{array} \quad (\text{J.4})$$

# Appendix K Additional information

## K.1 Liftdyn background information

Software Description Sheet

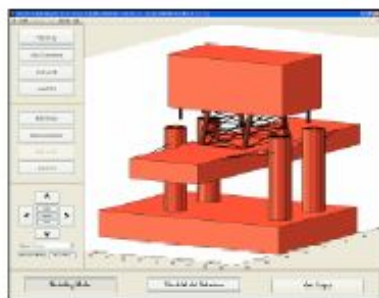
### LIFTDYN

*Multibody hydro-dynamic analysis in the frequency domain*

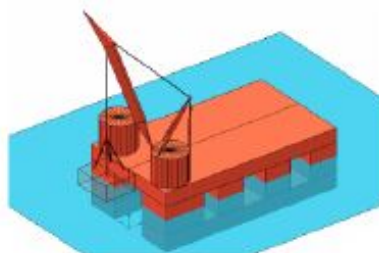


The possible risks and the workability of an offshore operation in a particular sea condition are determined by the motion response of the crane vessel, the lifted object and the cargo barge during various stages of the lift procedure. In addition, the forces in the hoisting arrangement or the possible impact between the lifted object and the cargo barge might be limiting the lift operation.

LIFTDYN is an in-house developed computer code that is designed to model and solve general linear hydrodynamic problems in the frequency domain. The program features a graphical user interface enabling visual checking options.



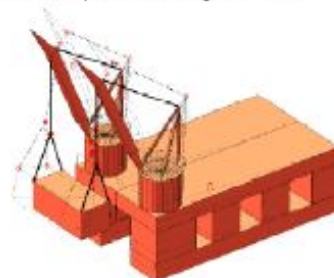
The program can solve systems consisting of rigid bodies connected to each other or to the earth by springs, dampers and hinges. In this way, all linear dynamic systems can be modeled irrespective of the number of bodies or connectors.



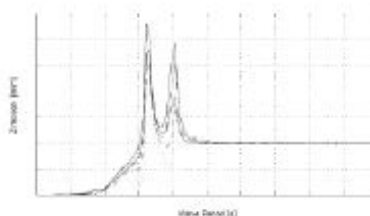
The bodies may have frequency dependent (added) mass and damping, and frequency

dependent exciting forces, which can be calculated with any diffraction code. Linear damping may be added to represent the viscous damping not calculated by the diffraction analysis code.

The calculation procedure includes animation of the structural mode shapes, which give insight in the hydrodynamic behavior of the system and can be used to optimize lift arrangements, etc.



The resulting Response Amplitude Operators (RAO) calculated by LIFTDYN can be post-processed to a motion, velocity or acceleration RAO at any desired point relative to any other point. A RAO of the force in a connector can also be generated. A generated RAO can be used to produce the significant response in a specific seastate. Furthermore, limiting criteria can be defined to obtain operability curves indicating the maximum allowable wave height as a function of the spectral period.



The results of LIFTDYN can be exported to other applications, i.e. to perform a weather downtime assessment taking into account actual motion limits, or for motion prediction during the offshore execution.

Figure K.1: Background Information on Liftdyn

## K.2 WAMIT background information

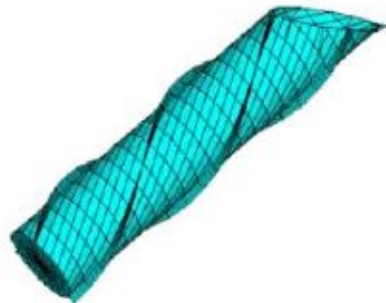
Software Description Sheet

### WAMIT

*Multibody radiation diffraction program*

WAMIT® is an advanced set of tools available for analyzing wave interactions with offshore platforms and other structures or vessels created by the Massachusetts Institute of Technology (MIT). Since the announcement of Version 1 in 1987, WAMIT has gained widespread recognition for its ability to analyze complex structures with a high degree of accuracy and efficiency. Over the subsequent years WAMIT has been licensed to more than 100 industrial and research organizations worldwide. Upgrades have been issued at approximately two-year intervals, with many enhancements.

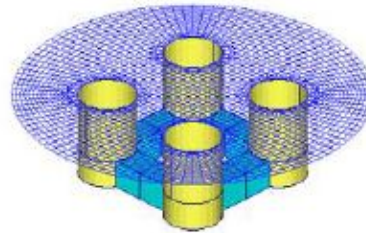
WAMIT is a computer program based on the linear and second-order potential theory for analyzing floating or submerged bodies, in the presence of ocean waves. The boundary integral equation method (BIEM), also known as the panel method, is used to solve for the velocity potential and fluid pressure on the submerged surfaces of the bodies. Separate solutions are carried out simultaneously for the diffraction problem, giving the effects of incident waves on the body, and the radiation problems for each of the prescribed modes of motion of the bodies. These solutions are then used to obtain the relevant hydrodynamic parameters including added-mass and damping coefficients, exciting forces, response-amplitude operators (RAO's), the pressure and fluid velocity, and the mean drift forces and moments. The second-order module, Version 6S, provides complete second-order nonlinear quantities in addition.



Heerens Marine Contractors



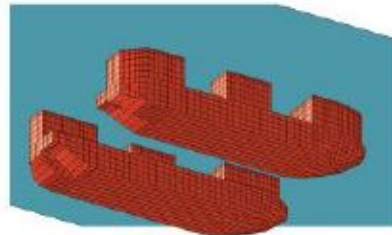
WAMIT includes several unique options to facilitate its application in the most effective manner. In addition to the conventional low-order method, where the geometry is represented by small quadrilateral panels and the velocity potential is assumed constant on each panel, a powerful higher-order method is also available based on the representation of the potential by continuous B-splines and with a variety of options to define the geometry of the body surface approximately or exactly.



When multiple bodies are considered the hydrodynamic interactions between the bodies are included in the computations, without approximation. In addition to the conventional six degrees of rigid-body motion WAMIT also enables the user to define additional generalized modes to represent a wide variety of physical phenomena including hydroelastic deformations, motions of hinged structures, various types of wave-energy converters, damping of gap and moonpool resonances, wavemakers, etc.

More information can be found on the WAMIT website:

[www.wamit.com](http://www.wamit.com)



Version 2010.09.26/MAE

Figure K.2: Background Information on WAMIT

### K.3 Weld profiling

The membrane- and bending stress [ $\sigma_{\text{membrane}}$  &  $\sigma_{\text{bending}}$ ] may be reduced, equation B1, when the welds are profiled and smoothed [3] with the given dimensions at figure B.1.

The reduction factors  $\alpha$  and  $\beta$  are given in equations B2 and B3 respectively. The thickness [T] is taken from the plate at which the main stresses are transferred.

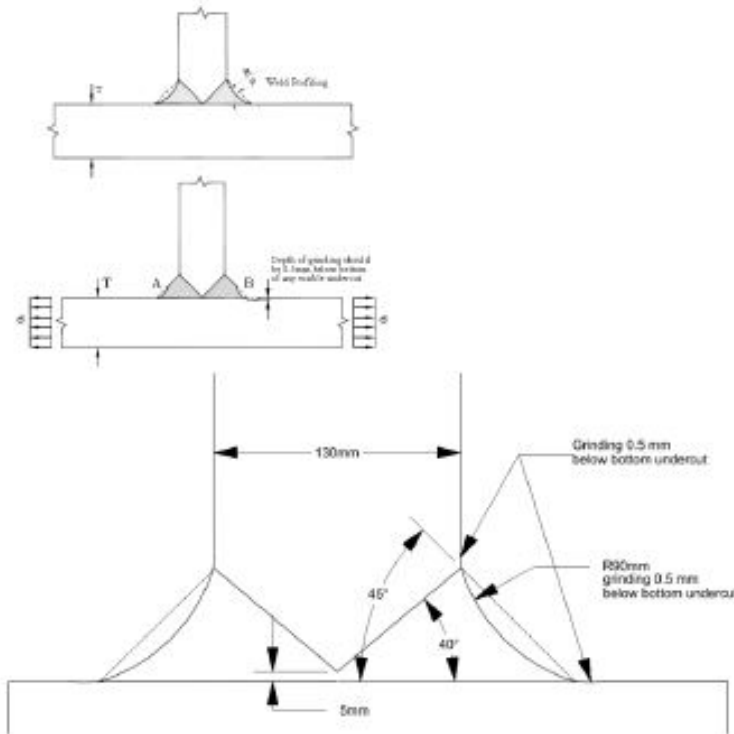


Figure B.1 – Weld profiling and smoothing. Right: symbol indication at typical detail, Left: dimensions weld, T=130mm, R=90mm,  $\varphi=45^\circ$ .

$$\sigma_{\text{local reduced}} = \sigma_{\text{membrane}} \cdot \alpha + \sigma_{\text{bending}} \cdot \beta \quad (\text{Equation B1})$$

$$\alpha = 0.47 + 0.17(\tan \varphi)^{0.25} (T/R)^{0.25} \quad (\text{Equation B2})$$

$$\beta = 0.60 + 0.13(\tan \varphi)^{0.25} (T/R)^{0.25} \quad (\text{Equation B3})$$

Figure K.3: Weld profiling for the welds of the boom pivots [15]